ornl

ORNL/TM-13648

OAK RIDGE NATIONAL LABORATORY

LOCKHEED MARTIN

Heavy Vehicle Propulsion System Materials Program Semiannual Progress Report for October 1997 Through March 1998

Prepared for
U.S. Department of Energy
Assistant Secretary for
Energy Efficiency and Renewable Energy
Office of Transportation Technologies

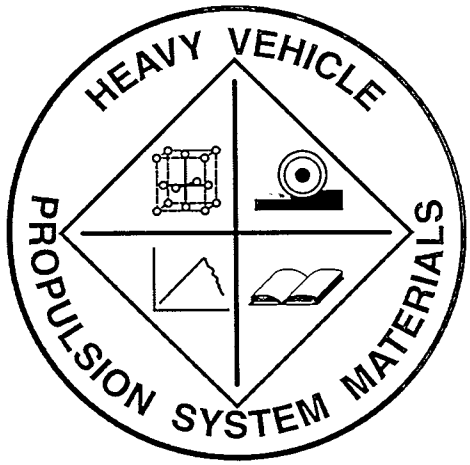

MANAGED AND OPERATED BY
LOCKHEED MARTIN ENERGY RESEARCH CORPORATION
FOR THE UNITED STATES
DEPARTMENT OF ENERGY

ORNL-27 (3-96)

DISCLAIMER

Portions of this document may be illegible in electronic image products. Images are produced from the best available original document.

ORNL/TM-13648

Metals and Ceramics Division

HEAVY VEHICLE PROPULSION SYSTEM MATERIALS PROGRAM SEMIANNUAL PROGRESS REPORT FOR OCTOBER 1997 THROUGH MARCH 1998

D. R. Johnson
Program Manager

Date Published: June 1998

Prepared for
U.S. Department of Energy
Assistant Secretary for Energy Efficiency and Renewable Energy
Office of Transportation Technologies
EE 04 02 000

Prepared by the
OAK RIDGE NATIONAL LABORATORY
Oak Ridge, Tennessee 37831-6285
managed by
LOCKHEED MARTIN ENERGY RESEARCH CORP.
for the
U.S. DEPARTMENT OF ENERGY
under Contract DE-AC05-96OR22464

REPORTS PREVIOUSLY ISSUED

ORNL/TM-9325	Period March 1983-September 1983
ORNL/TM-9466	Period October 1983-March 1984
ORNL/TM-9497	Period April 1984-September 1984
ORNL/TM-9673	Period October 1984-March 1985
ORNL/IM-9947	Period April 1985-September 1985
ORNL/TM-10079	Period October 1985-March 1986
ORNL/TM-10308	Period April 1986-September 1986
ORNL/TM-10469	Period October 1986-March 1987
ORNL/TM-10705	Period April 1987-September 1987
ORNL/TM-10838	Period October 1987-March 1988
ORNL/TM-11116	Period April 1988-September 1988
ORNL/TM-11239	Period October 1988-March 1989
ORNL/TM-11489	Period April 1989-September 1989
ORNL/TM-11586	Period October 1989-March 1990
ORNL/TM-11719	Period April 1990-September 1990
ORNL/TM-11859	Period October 1990-March 1991
ORNL/TM-11984	Period April 1991-September 1991
ORNL/TM-12133	Period October 1991-March 1992
ORNL/TM-12363	Period April 1992-September 1992
ORNL/TM-12428	Period October 1992-March 1993
ORNL/TM-12674	Period April 1993-September 1993
ORNL/TM-12778	Period October 1993-March 1994
ORNL/TM-12924	Period April 1994-September 1994
ORNL/TM-13046	Period October 1994-March 1995
ORNL/TM-13219	Period April 1995-September 1995
ORNL/TM-13262	Period October 1995-March 1996
ORNL/TM-13395	Period April 1996-September 1996
ORNL/TM-13467	Period October 1996-March 1997
ORNL/TM-13562	Period April 1997-September 1997

Research sponsored by the U.S. Department of Energy, Assistant Secretary for Energy Efficiency and Renewable Energy, Office of Transportation Technologies, as part of the Heavy Vehicle Propulsion System Materials Program, under contract DE-AC05-96OR22464 with Lockheed Martin Energy Research Corporation.

CONTENTS

HEAVY VEHICLE PROPULSION SYSTEM MATERIALS PROGRAM
SEMIANNUAL PROGRESS REPORT
FOR OCTOBER 1997 THROUGH MARCH 1998

SUMMARY AND INTRODUCTION

The purpose of the Heavy Vehicle Propulsion System Materials Program is the development of materials: ceramics, intermetallics, metal alloys, and metal and ceramic coatings, to support the dieselization of class 1-3 trucks to realize a 35% fuel-economy improvement over current gasoline-fueled trucks and to support commercialization of fuel-flexible LE-55 low-emissions, high-efficiency diesel engines for class 7-8 trucks.

The Office of Transportation Technologies, Office of Heavy Vehicle Technologies (OTT OHVT) has an active program to develop the technology for advanced LE-55 diesel engines with 55% efficiency and low emissions levels of 2.0 g/bhp-h NOx and 0.05 g/bhp-h particulates. The goal is also for the LE-55 engine to run on natural gas with efficiency approaching that of diesel fuel. The LE-55 program is being completed in FY 1997 and, after approximately 10 years of effort, has largely met the program goals of 55% efficiency and low emissions. However, the commercialization of the LE-55 technology requires more durable materials than those that have been used to demonstrate the goals. Heavy Vehicle Propulsion System Materials will, in concert with the heavy duty diesel engine companies, develop the durable materials required to commercialize the LE-55 technologies.

OTT OHVT also recognizes a significant opportunity for reduction in petroleum consumption by dieselization of pickup trucks, vans, and sport utility vehicles. Application of the diesel engine to class 1, 2, and 3 trucks is expected to yield a 35% increase in fuel economy per vehicle. The foremost barrier to diesel use in this market is emission control. Once an engine is made certifiable, subsequent challenges will be in cost; noise, vibration, and harshness (NVH); and performance.

The design of advanced components for high-efficiency diesel engines has, in some cases, pushed the performance envelope for materials of construction past the point of reliable operation. Higher mechanical and tribological stresses and higher temperatures of advanced designs limit the engine designer; advanced materials allow the design of components that may operate reliably at higher stresses and temperatures, thus enabling more efficient engine designs. Advanced materials also offer the opportunity to improve the emissions, NVH, and performance of diesel engines for pickup trucks, vans, and sport utility vehicles.

The principal areas of research are:

Cost Effective High Performance Materials and Processing
Advanced Manufacturing Technology
Testing and Characterization
Materials and Testing Standards

COST EFFECTIVE HIGH PERFORMANCE MATERIALS AND PROCESSING

Cost-Effective Smart Materials for Diesel Engine Applications

J. O. Kiggans, Jr., T. N. Tiegs,
F. C. Montgomery, L. C. Maxey, and H. D. Kimrey
Oak Ridge National Laboratory
Oak Ridge, TN 37831

B. Mikijelj
Ceradyne, Inc.

A. W. Suman
Eaton Co

Objective / Scope

There are several objective of this project. The first object is to evaluate the cost-effectiveness and maturity of various "Smart Materials Technologies," which are under consideration for diesel engine applications, such as fuel injection systems. The second objective is to work on materials development problems which exist with selected "Smart Materials" systems, to enable these materials to be incorporated into working actuators. At the present, a third objective is to fulfill DOE milestones for the reaction-bonded silicon nitride materials project and to fulfill CRADA obligations which still exist with Ceradyne, Inc. and Eaton Co.

Smart Materials

Activity 1

The first activity in this project has been the review of available literature on smart materials, and in particular, materials for actuator applications. The data gathered from books, scientific articles, Ph.D. thesis from universities, patents, and company brochures, will be used to develop a plan of action for the project. This information gathering activity has included visit a to TRS Ceramics, Inc, an manufacturer of piezoelectric materials. Future visits are planned to other manufacturers of PZT and magnetostrictive materials. Other plans include developing CRADA projects with manufactures of actuator materials. The accumulated information has been summarized in two small white paper studies.

Paper Study 1:

The term "Smart Materials" has been widely used to describe materials that have both sensing and actuator capabilities.[1] Most prominent among these materials include piezoelectric materials, electrostrictive materials, shape memory alloys, and magnetostrictive materials. A number of recent reviews and books have highlighted the flurry of activity in this area in the last few years by American, Japanese , and European companies, and research organizations. [2-5]

Applications which have surfaced in patents regarding piezoelectric, electrostrictive, and magnetorestricive materials involve the use these materials for actuator functions, where precise, fast, controlled displacement is needed. Companies, including General Motors, Ford, Caterpillar, in the U. S., and Toyota, Nissan, and Honda, in Japan, have registered numerous patents for the use of piezoelectric materials for applicators in devices that range from active suspension systems for automobiles, to fuel injection actuators.[2,6] Depending

on the selection of the smart material and the type of actuator, displacements ranging from micrometer to millimeters are possible, at response speeds of 0.1 msec and faster. This compares to the fastest electric actuator, which exhibits a response time of 100 msec, for typical millimeter displacements. The bottom line is that actuators made through proper design from various smart materials can have 1000 fold higher speeds than equivalent electrical devices.[4]

Besides speed, the primary issues for implementing smart materials into actuators for diesel engines are cost, reliability, ease of manufacture (including the safety of the materials components), and cycle lifetime of the actuator.[7,8] In addition, more specific factors must be considered, such as size of the actuator, sensitivity to environmental conditions (such as high humidity and temperature), and amount of force needed to produce the desired action.[4] Comparisons by most companies and researchers have reached the conclusion that piezoelectric materials are the best selection of materials for actuators. Magnetostictive actuators have received considerable interest, but are not commonly used, due to several limitations. These include the extremely high cost of the commercially available magnetorestrictive material, Terfenol-D; the loss of the magnetic properties at low temperatures; the brittle nature of Terfenol-D; and the limited life-cycle of Terfenol-D (in the range 10^6-10^7 cycles).[9,10]

Given the fact that PZT actuators appear to be the most likely candidate for smart actuators in diesel engines, several problems have prevented PZT actuators from entering the market place. The most important is the high cost of many of the actuators which is related to the manufacturing. To date, most actuator designs have been multilayer devices. A multilayer actuator requires electroding of each surface of up to two hundred layers of ceramic material, along with making electrical connections between layers and to the power supply. Alternate actuator designs are under consideration to lower the costs associated with these complex actuators.[5]

A second source of the high cost associated with piezoelectric actuators is the cost of the electrode materials. The silver-palladium electrodes commonly used for present piezoelectric devices are not cost-effective. Nickel and copper electrodes are desired, however piezoelectric ceramic elements that can be fired to around 900°C in non-oxidizing conditions are needed before copper and nickel can be used. Research projects are underway to find new piezoelectric compositions that can be sintered at lower temperatures in the inert atmospheres dictated by the use of copper and nickel electrodes.[3,4]

Besides costs, another problem associated with prototype piezoelectric actuators is their long-term reliability and durability. Single-layer, high displacement, piezoelectric devices are limited to from between 10^5 - 10^6 cycles, and multilayer actuators to between 10^7 - 10^8 cycles. These projected life-cycles are not acceptable for diesel applications. However, such lifetimes could be acceptable if the actuators are changed on routine intervals, as is done with items such as air filters. Since the fatigue of piezoelectric devices has been found to be associated with the electrode- ceramic interfaces within actuator devices, work needs to be done on alternate electrode - ceramic materials combinations.

The final major problem associated with piezoelectric materials is the presence of lead in the materials, such as the most commonly used PZT (lead zirconate titanate) and PMN (lead magnesium niobate) compositions. The presence of lead increases the cost associated with fabrication of the devices due to special handling conditions for lead compounds and in the recycling of the materials after use. Research into alternative piezoelectric materials is underway in some laboratories, and is sure to be an important research area in future years.[3]

Although the problems associated with the manufacture of piezoelectric actuators are large, the potential pay-off for the entry of the devices is enormous. High speed actuators for fuel injections systems for diesel engines will lead to significant fuel savings, reductions in pollutants, and lowering of diesel engine noise. The intent of this project is to address some of these problems associated with piezoelectric and possibly magnetorestrictive actuators, in order to allow their introduction into the diesel engine market.

References

1. R. E. Newnham, "Molecular Mechanisms in Smart Materials," MRS Bulletin, 22 (5), 20-34, 1997.

2. S. L. Swartz, T. R. Shrout, and T. Takenaka, "Electronic Ceramics R&D in the U. S., Japan, Part 1: Patent History," Am. Ceram. Soc. Bull., 76 (7), 59-65, 1997.

3. S. L. Swartz, T. R. Shrout, and T. Takenaka, " Electronic Ceramics R&D in the U. S., Japan, Part 2: Japanese View," Am. Ceram. Soc. Bull., 76 (8), 51-55, 1997.

4. K. J. Uchino, Piezoelectric Actuators and Ultrasonic Motors, ed. H. L. Tuller, Kluwer, Boston, Mass., 1997.

5. K. Uchino and S. Takahashi, "Multilayer Ceramic Actuators," Current Opinion in Solid State & Materials Science," 1, 698-705, 1996.

6. S. Abe, T. Igashira, Y. Sakakibara, and F. Kobayashi, "Development of Pilot Injection System Equipped with Piezoelectric Actuator for Diesel Engine," JSAE Review, 15, 201-208, 1994.

7. T. Sakai, M. Ishikiriyama, Y. Terai, and R. Shimazaki, " Improvement in the Durability of PZT Ceramics for Actuator, Toyota Technical Review, 42 (2), 56-62, 1993.

8. C. T. Sun and J. Z. Jiang, "Fatigue Behavior of Piezoelectric Ceramics," Proc. of Int. Soc. Opt. Eng. (SPIE), 3040, 129-159, 1997.

9. K. Prajapati, R. D. Geenough, and A. Wharton, "Magnetic and Magnetoelastic Response of Stress Cycled Terfenol-D," J. Appl. Phys., 81 (8), 5719 - 5721, 1997.

10. M. Goodfriend, "Materials Breakthrough Spurs Actuator Design," Machine Design, 63 (6), 1991.

Paper Study 2:

Information on "conventional actuators" and "smart-fast actuators is summarized in Tables 1 and 2. [1,2] Table 1 shows that conventional actuators typically exhibit large force and travel characteristics; however, response times are in the ms range. Table 2 shows that smart actuators have limited travel, but they can exhibit response times less than a ms and can have high force capability. Additional data in the tables discusses the benefits and problems associated with the different actuator types.

Information given in Tables 2 indicates that the three most likely candidates for smart actuators for diesel applications are magnetostrictive TERFENOL-D actuators, piezoelectric actuators, and voice-coil actuators. Several companies were contacted for company

product information. Manufacturers of piezoelectric materials and actuators include Piezo Systems, Inc., Token America, Polytech PI, TRS Ceramics, Inc., Active Control eXperts, Inc., and EdO Corporation. Etrema Products, Inc. is the primary U. S. manufacturer of TERFENOL-D magnetostrictive powders and actuators. BEI Sensors and Systems Company is a primary manufacturer of voice-coil actuators. All indications to this point are that none of the presently manufactured piezoelectric and magnetostrictive devices are capable of the combination of properties needed for diesel fuel injection. Devices that are on hand also have limited data related to product reliability (cycle life-time under load), and no data for product operation under conditions that would be expected for diesel engine applications.

References

1. K. Uchino, Piezoelectric Actuators and Ultrasonic Motors, Kluwer Academic Publishers, London, 1997.
2. EuduraTEC Systems Corporation web page, info@euduratec.com

Activity 2

PZT powders have been ordered from American Piezo Ceramics, Inc. to prepare piezoelectric test which will be used for base-line studies

Electronic equipment needed for measurements in the base-line studies has been identified. Additional purchases will be made of needed equipment. Plans for the project include fabrication of an actuator test apparatus for reliability tests.

Figure 1 is a schematic of a basic system which is envisioned for measuring the output performance (free deflection, blocked force, and resonant frequency) of test actuator devices. One important part of this apparatus is a device for measurement of actuator piston displacement. Basic parameters for selecting a measurement device include a total measurement range of 1.5 mm, a resolution of 0.1 μm, and measurement speed of 3 KHz. A Philtec, Inc. Model D20-M fiber optic displacement sensor was chosen as the cheapest technology for meeting these criteria.

During the survey of company products, several items were identified which can serve as good base line devices to evaluate what is available for diesel actuator applications. Piezoelectric materials, a piezoelectric actuator kit, and software for design of piezoelectric actuators were ordered from Piezo Systems, Inc. Several multilayer PZT devices are under consideration for testing. A TERFENOL-D actuator was ordered from Etrema Products, Inc. These actuator devices will be evaluated at ORNL.

Activity 3

Due to the toxicity of the lead present in PZT materials, discussions were made with health safety personnel about work-place requirements. Lab space has been identified for the present project. Work will take place primarily in certified hood areas, and in some cases, in a designated glove box. Separate furnaces are being set up for the binder burnout and sintering the PZT materials.

Activity 4

The fourth major activity was preliminary work in the fabrication PZT materials. A dispersion study with two powder types, APC 840 and APC 850. Both as received and powders heated in air to 500°C to remove binders were evaluated. APC 840 is commonly known as PZT-4, DOD-I, and Navy 1. APC 850 is commonly known as PZT-5A, DOD-II , and Navy II. Both powder types are produced by a number of manufacturers. Both powders have high curie temperatures > 300 °C and were designed for actuator applications. The objective of the present activity was to determine the proper dispersants for making stable slurries of the APC 840 and APC 850 in water, with an ultimate goal of forming piezoelectric preforms using gelcast forming methods. Presently, piezoelectric materials are commonly made using tape casting methods utilizing organic solvents. Processing in water offers a safer more environmentally sound method of forming piezoelectric materials, while gelcasting allows one to form very strong ceramic green bodies with much lower binder additions than is possible with tape casting.

The following procedure was used for the sedimentation tests conducted with the two piezoelectric powders. Dispersants chosen for the dispersion-sedimentation studies included polyvinylpyrrolidone MW 10,000 (Aldrich Chemicals), Darvan 821A (R. T. Vanderbilt Co.), polyethylene imine MW 2000 (Polysciences Inc.), Duramax 3005 (Rohm and Hass), Duramax 3019 (Rohm and Hass), and Darvan 821A plus PVP 10,000. Dispersants were used at either 0.05 wt % or 0.5 wt % concentration. Stock dispersant solutions were adjusted with tetramethyammonium hydroxide (TMOH) or acetic acid to pH values between 8 and 10, as suggested by Dr. Jim Adair of the University of Pennsylvania, who has worked extensively on the chemistry and rheology of aqueous solutions of barium titanate. A fixed volume of the pH adjusted dispersant solution was added to a 50 cc HDPE centrifuge tube. Two vol % of the test powder was then added to the dispersant solution to give a final volume of 10 ml. The mixture was then sonicated 20 sec with a Fischer ultrasonic probe. The slurry was allowed to equilibrate for 60 m, the pH was readjusted, and the slurry re-sonicated for 30 s. The slurry was then transferred to a 15 ml transparent polystyrene centrifuge tube. The sedimentation behavior of the slurry was recorded over a 21 day period. Figure 2 shows a schematic of the test fixture used for the measurement of the sedimentation. The test required the sample tube to be lined up against a white background with a vertical line behind the line of sight to the tube. The opacity measurement recorded for each sample represents the percent of the line blocked from view by the opaque settling slurry.

Figure 3 is a line graph of a dispersion of APC 840 showing the change in opacity over time with the listed dispersants at the lower dispersant concentration. Opacity as defined in Figure 2 as the height of the opaque slurry divided by the total liquid height (multiply result times 100 to express as per cent). The data show that Darvan 821A, Duramax 3005, and Darvan 821A plus PVP 10,000 had longer sedimentation times, and thus higher opacities, than the polyvinylpyrrolidone MW 10,000 and polyethylene imine MW 2000. Graphs (not shown) similar to Figure 3 were created for both the APC 840 and the APC 850 powders.

Figures 4 and 5 are single time point bar graphs of opacity treatment for APC 840 and APC 850 powders at the 4 day time point, showing a comparison of the sedimentation of as received and powders with the binder burn out treatment. Each bar in this graph is identified by a three letter-number designator. The first letter is a designator for the dispersant type, the middle number is the adjusted pH of the slurry, and the next letter, C or D, refers to concentrated, 0.5 wt % dispersant concentration or dilute, 0.05 wt % dispersant concentration, respectively. If the powder is treated for binder burn out, it is designated as calcined. For example, A8C data bar (shown above a Darvan 821A dispersant label) is the opacity level for powder dispersed with Darvan 821A, at pH 8, and

at he concentrated dispersant level. The data in Figure 4 indicates that powders having the binder burn out step exhibited much quicker settling than as received powders. This may be due to agglomeration or changes in the powder that resulted during the treatment. The data also shows that for the as received powders, differences in the settling behavior were not related to the pH value of the dispersant solution; the Darvan 821A, Duramax 3005, and the Duramax 3019 were equally effective for dispersing the 840 powder; and the higher concentration of dispersant was more effective than the dilute dispersant. Since the data with the 840 powder showed that the concentrated dispersant was more effective for dispersion, experiments with the APC powder were conducted at only the 0.5 wt % (concentrated) level. Data in Figure 5 indicates that once again the Darvan 821A, Duramax 3005, and the Duramax 3019 were all equally effective as dispersants.

Following these dispersion tests, the supernatant liquids from the centrifuged dispersions were stored for future studies to indicate whether lead leached from the powders during the dispersion process in water. Future work includes tests for volumes loading characteristics of the two piezoelectric powders, and tests to determine whether green preforms can be fabricated from these PZT powders using gelcast techniques.

Activity 5

A capital equipment request for Fiscal Year 2000 was written and submitted for review. The request includes details for a actuator test facility, which will include five computer controlled actuator test systems which each include a data acquisition system to allow life-time reliability testing. Key personnel needed for equipment set-up, software development, and operation responsibilities have been identified.

Improved (SRBSN) Materials

This is the final report necessary to meet milestones listed for the "Cost-Effective SRBSN Project.". During the present reporting period, modulus, strength, and toughness measurements were made on 3 by 4 by 45 mm MOR bars, which were made from nitrided and sintered SRBSN materials. Table 3 lists the sample compositions of the materials. A "C" or "F" in the sample number indicates that samples were fabricated from the "coarse powder" or the "fine powder," respectively, collected from separate collection points of a Niro spray dryer. Table 4 lists data for the samples. Included is data for material formed in previous studies using gelcast methods. Several observations can be made concerning the data present in Table 4. The first observation is that higher strength and toughness values were obtained for materials sintered for 10 h. The same results were observed for the gelcast SRB-1 material, and was unrelated to how the materials were formed. Second, the strengths of the materials made in the present study were lower than the SRB-1 gelcast materials. This is not surprising, since studies have shown that gelcast preforms of silicon, silicon nitride, and alumina materials have more uniform microstructures, which results in higher strengths in sintered materials. Third, SRB 32 and the SRB 33 SRBSN materials prepared from the "fine" spray dried powders, had higher strengths than samples made from the "coarse" fraction, while the toughness values were similar. This result indicates that the fine powders pressed more uniformly than did the coarse powders. The observation points to the need to carefully control the size of the spray-dried granules. A fourth observation is that much better properties were obtained from materials made from the high yittria compositions (8% Y_2O_3-4% Al_2O_3 -0.2% Cr_2O_3), SRB 32 and SRB 33, than for the other compositions. The toughness of the SRB 34 (6% Y_2O_3-6% Al_2O_3 - 0.2% Cr_2O_3) was much lower than SRB 32 and SRB 33 materials of comparable densities. The strength of the SRB 35 (6% Y_2O_3-6% $MgAl_2O_4$ -0.2% Cr_2O_3) was lower than SRB 32 and 33 materials. The SRB 36 and 36 samples, containing the cerium oxide and mixed-

lanthanide sintering aids, were much more difficult to sinter than the yittria- containing materials. The lower densities resulted in lower strength and toughness values.

In summary, the data from this last study reinforces the need for choice of optimal powder granule sizes of the spray dried powders used for SRBSN materials . In addition, optimal sintering times during the final processing of the materials are necessary to achieve high densities, along with high strength and toughness values. The study indicates that more work is needed to maximize properties of SRBSN materials made from spray dried powders containing cheaper, rare earth sintering aids. This data completes the research activities in the "Cost Effective SRBSN Project."

Ceradye Inc. CRADA - Biljana Mikijelj

The CRADA with Ceradyne Inc. has involved two activities: the evaluation of gelcast technologies for forming Ceradyne SRBSN materials, and the evaluation of microwave heating for the nitrdation of Ceradyne silicon preforms. During this reporting period, two batches of microwave nitrided SRBSN Ceradyne parts were shipped to Ceradyne for sintering operations. The densification behavior and mechanical properties of these parts will be determined by Ceradyne. These data will be compared to data for materials nitrided at Ceradyne. This data will help evaluate if microwave nitridation is a viable technology for consideration by their company. In addition, a final procedure for gelcasting Ceradyne silicon powders was written and sent to Ceradyne.

Eaton Corporation CRADA Completion

Four activities were undertaken during the present reporting period to fulfill CRADA obligations to Eaton Co. The first activity was the preparation of a written procedure for gelcast forming of Eaton powders. This task has been completed and a draft document sent to Eaton.

The second activity of this CRADA was to nitride Eaton "green" parts by microwave and conventional graphite furnace methods used at ORNL. The first experiment in this activity was a nitridation of Eaton silicon parts using microwave heating. Prior to the microwave nitridation, the parts had binders removed by a 1°C/m heat to 500 °C. Figure 6 shows silicon parts, as placed in a silicon nitride crucible and surrounded by fiber board insulation in a 2.45 GHz microwave cavity. Parts were heated in N_2 4-vol % H_2 gas to 600°C and then the supply gas was switched to N_2. The peak nitridation temperature was 1350° C. The heating cycle was 13 h. The parts appeared to nitride uniformly with an average weight gain of 62.7 %. The weight change of for sample, 1350°C MWF, is shown in Figure 7. Figure 8 is a photograph of nitrided valve seats from this microwave nitridation. The second experiment in the second activity was a comparison scale-up nitridation of valve seats in a graphite element furnace. Figure 9 is a photograph of the set-up used for this nitridation test. Since one of the main difficulties of nitriding the green silicon valve seats is the handling of parts during loading, the air burn out of parts prior to nitridation was omitted. The parts were heated at 1°C per minute to 600° C in N_2 to remove volatile binders, followed by a normal nitridation cycle. Once again, the peak temperature for nitridation was 1350° C, with a total heating cycle of 13 h. Figure 2 shows an average weight gain of 62.9 % for sample group 1350°C GF. Figure 10 is a photograph of a few of the samples after nitridation showing a silicon carbide (SiC) layer on some samples. The SiC layer was probably due to the interaction of the silicon in the samples with residual carbon resulting from the volatile binders in the crucible.

The third activity of this CRADA was a series nitridation - sintering experiments. These experiments were performed in a graphite furnace with vacuum capability, in order to remove carbon materials from the sample crucibles during binder volatilization. Figure 11 is a photograph of one of the crucibles used for nitridation and subsequent sintering. The photo shows nitrided and sintered samples on a "Crystar" SiC plate, which was supported by silicon nitride (Si_3N_4) porous beads (3M Co.). In other experiments, samples were also covered by a layer of the porous beads for atmosphere control during sintering. Previous, in-house experiments have demonstrated that Si_3N_4 parts packed in Si_3N_4 powders during sintering steps had less weight losses. The concept explored here was to use beads, instead of powders. Powder packing can result in melted silicon parts during nitridation, however beads have been shown to be a cover material that does not trap too much of the exothermic heat of nitridation. In experiment 1, performed without a bead cover, the sample group, designated 1750°C-B in Figure 2, had an average weight change of 51.6 %. This lower weight gain, versus 62.9% for nitridation alone, is a combination of a nitridation weight gain plus a sintering weight loss, here a 11.3 % weight loss. Sample group 1750°C+B, which were covered with the porous beads had a weight gain of 56.5 %, showing the atmosphere protection of the bead cover. Figure 12 is a graph of the sintering behavior of the two groups of samples. The 1750°C-B samples had an average densities of 94.5 % (based on a 3.4 g/cm^3 theoretical density) and the 1750°C+B group had average densities of 93.0 %. It is believed the 1750°C+B group had the lower densities because the weight losses are associated with silica volatalization and resulted in materials with higher specific densities. This would give an apparent lower density to the parts covered by the beads. Since the densification at 1750° C was lower than desired, nitridation-sintering runs were made at 1775°C and 1800° C with and without bead cover. The nitridation weight gains for these runs are given in Figure 2, with +B and -B disignating the packing arrangement of with or without bead cover, respectively . The data show that the bead cover prevents weight loss at the higher 1775 and 1800° C temperatures. Data in Figure 12 shows that the densification at 1775° C was higher for the -B group, however at 1800° C there was no difference observed in the densities for the two packing arrangements. To evaluate the effect of the sintering temperatures and packing arrangements on the sample properties, simple load failure tests were performed on the samples. The round valve seats were placed on their outer rim in an Instron 4465 Materials Testing System. The samples were then compressed by the Instron until failure of the rings and the load at failure recorded. Figure 13 is summary of the data obtained. The results for the three sets of samples processed in the vacuum graphite furnace at 1775 and 1800°C show that the bead cover was detrimental to strength. Only minor differences were seen in strengths of the samples processed without a bead cover at the two test temperatures.

The last activity performed for the Eaton CRADA was an exploration of the use of gas pressure nitrogen for nitridation and sintering of silicon preforms. Work has been done by other research groups on gas pressure nitridation and of silicon preforms, and extensive work has been done at ORNL gas pressure sintering of Si_3N_4, so it seemed logical to test how a combination of gas pressure nitridation and sintering would benefit processing of the Eaton silicon valve seats. In this experiment the samples containing binder were placed on a SiC plate in graphite crucible. The samples were heated to 600°C in vacuum for binder removal and then heated to 1350°C in 100 psig N_2 gas pressure for nitridation. The pressure was removed and the samples then heated to 1775°C for 30 m. The pressure was then raised to 100 psig and the samples heated to 1850° C for sintering. The total heating cycle minus cool down was 8.3 h. Figures 7, 12, and 13 shows data for weight gain, densities, and load to failure for these 1850° C OPF samples. The data show that the weight loss was similar to the samples processed at 1800° C, the density of 99 % T. D. was higher than all other sample groups, and the average strength of 347 lb was significantly higher than any other group of samples. Gas pressure nitridation and

sintering appears to have a potential for rapid processing of valve seats with improved strength.

Status of Milestones

Ceradyne, Inc. and Eaton Co. CRADAs have been completed. Other milestones on schedule.

Travel

Travel by J. O. Kiggans to Penn. State University, Oct. 21-24, to attend a short course, "Smart Actuators." Tour of Materials Research Laboratories of Penn. State to view piezoelectric processing facilities.
Tour of TRS Ceramics. Inc. of State College, a manufacturing facility of capacitors and piezoelectric devices. Discussions with Tom Shrout, president of TRS Ceramics, concerning piezoelectric actuators for diesel engines.

Travel by J. O. Kiggans and T. N. Tiegs, Oct. 28-29, to Dearborn, MI. for poster presentations at the "Annual Automotive Customers' Coordination Meeting".
Discussions at CCM meeting with Andy Suman of Eaton Co. concerning ongoing CRADA work.
Visit to Detroit Diesel , Oct. 29, for discussions with Yury Kalish and Debra Dobson, to discuss the "Smart Materials for Diesel Engines" project.

Publications

Publication of the poster, "SRBSN for Diesel Engine Applications" in "The Preprints of the Annual Automotive Technology Development Customers Coordination Meeting."

Table 1: Conventional Actuators

Drive Source	Name	Displacement Range	Displacement Accuracy	Generative Force	Response Speed	Benefits	Problems
Air pressure	Rotary motor	Rotation	----------	5 kgm	10 sec	lower cost than hydraulic less power than hydraulics mature technology	----------
	Pressure cylinder	100 mm	100 µm	10^{-2} kg/mm^2	10 sec	lower cost than hydraulics less power than hydraulics mature technology	----------
Oil - hydraulic pressure	Rotary motor	Rotation	----------	10 kgm	0.2 to 1 sec	mature technology high power	higher cost higher maintenance pump life - 800 h
	Pressure cylinder	1000 mm	10 µm	10 kg/mm^2	1 sec	mature technology high power	higher cost higher maintenance
Electricity	AC servo motor	Rotation	----------	----------	100 msec	mature technology	----------
	DC servo motor	Linear or Rotation	----------	----------	10 msec	mature technology	----------
	Stepper motor	1000 mm	10 µm	30 kg	100 msec	Accurate locks in position mature technology	low loads

Table 2. Fast Actuator Types

Drive Source	Name	Displacement Range	Displacement Accuracy	Generative Force	Response Speed	Benefits	Problems
Electricity	Voice Coil motor (BEI Sensors & Systems)	1 mm	0.1 µm	30 kg	1 msec	mature technology linear characteristics zero hysteresis high power to weight	low force for higher speed devices
	Piezoelectric multilayer (Tokin)	0. 001 to 0.04 mm	0 .01 µm	80 kg	0.1 msec	mature technology low voltage large displacment	high cost expensive power supply hysteresis aging 10^{11} cycle life
	Piezoelectric bimorph bender (Piezo Systems)	1 mm	1 µm	0.07 kg	1 ms	higher displacment	hysteresis aging high voltage (0.1 to 1 kv) expensive power supply 10^5 cycle life
	Electrostrictive (TRS Ceramics)	1.5 % strain	1 µm	device dependent	1 µsec 1 msec	higher displacment vs PZT multilayer high speed	high cost expensive control system low temperature use
	Magnetostrictive Terfenol-D (Etrema)	0. 001 to 0.07 mm	0 .01 µm	90 kg	1 µsec 1 msec	large displacement high speed low voltage (12 V)	high cost expensive control system
	Electrorheological device (not commercial)	----------	----------	----------	0.1 msec	high speed	high cost high voltage nonlinear control unstable fluids immature technology
	Magnetorheological device (Rheonetics)	----------	----------	22 kg	< 10 msec	more stable fluid low voltage (12 v)	high cost fluid
Heat	Shape memory alloys (TiNi Alloy)	mm to cm 3-4 % strain	----------	device dependent	0.2 sec	on-off device large strain high power to weight	slow cycle time limited applications hysteresis difficult to machine

Table 3. SRB Compositions

Sample #	Sample Type	Composition
SRB 32C1	DP, IP from SD Coarse Powder	Si met.+ Seed -8% Y_2O_3-4% Al_2O_3 -0.2% Cr_2O_3
SRB 32F1	DP, IP from SD Fine Powder	Si met.+ Seed -8% Y_2O_3-4% Al_2O_3 -0.2% Cr_2O_3
SRB 33C1	DP, IP from SD Coarse Powder	Si met.- Seed -8% Y_2O_3-4% Al_2O_3 -0.2% Cr_2O_3
SRB 33F1	DP, IP from SD Fine Powder	Si met.- Seed -8% Y_2O_3-4% Al_2O_3 -0.2% Cr_2O_3
SRB 34C1	DP, IP from SD Coarse Powder	Si met.+ Seed -6% Y_2O_3-6% Al_2O_3 -0.2% Cr_2O_3
SRB 35C1	DP, IP from SD Coarse Powder	Si met.+ Seed -6% Y_2O_3-6% $MgAl_2O_4$ -0.2% Cr_2O_3
SRB 36C1	DP, IP from SD Coarse Powder	Si met.- Seed -10.7 % CeO_2-2.1 % Al_2O_3 -0.2% Cr_2O_3
SRB 37C1	DP, IP from SD Coarse Powder	Si met.- Seed -10.9 % Lanthanide mix -2.1 % Al_2O_3
SRB 1	GC, IP from TM Powder	Si met.+ Seed -9% Y_2O_3-3% Al_2O_3

DP = die press
IP = isopress
SD = spray dried
Si met = Elkem metallurgical grade Si Lot # 49485
Seed = LC10 Si_3N_4
GC = gelcast
Lanthanide mix = La_2O_3 (41.3%), CeO_2 (5.4%), Other Rare Earths (20.8%), CaO (0.2%)
TM = turbomilled

Table 4. Summary of densities and mechanical properties of nitrided and sintered SRBSN materials fabricated from spray dried powders by die press methods.

Sample #	Sintering* Time (h)	Theoretical Density (%)	Youngs Modulus	Fast Fracture Strength (MPa)	Toughness (MPa$\sqrt{}$ m)
SRB 32C1	10	97.0	281	517	6.7
SRB 32C2	2	95.0	264	510	5.2
SRB 32F1	10	97.4	284	679	6.6
SRB 33C1	10	97.0	283	647	6.3
SRB 33C2	2	94.8	264	469	5.1
SRB 33F1	10	97.4	285	687	6.3
SRB 34C1	10	96.9	279	560	5.6
SRB 35C1	10	97.4	281	529	6.7
SRB 36C1	10	94.6	265	549	5.8
SRB 37C1	10	92.7	275	550	4.4
SRB 1	10	98.7	292	747	6.8
SRB 1	2	98.7	289	542	6.1

*All samples except SRB 36 and SRB 37 were sintered at 1800°C. SRB 36 and SRB 37 were sintered at 1750°C.

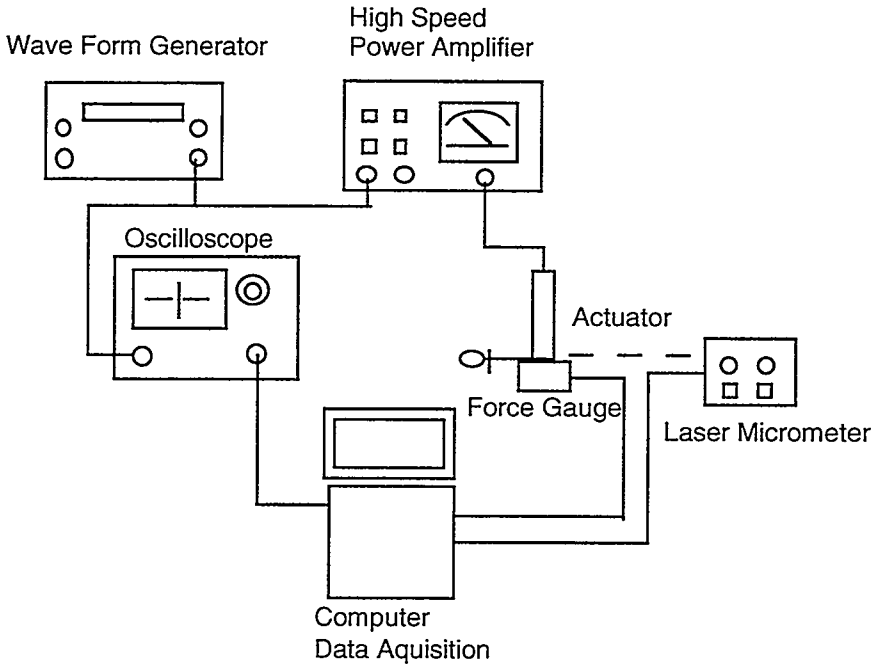

Figure 1. System Block

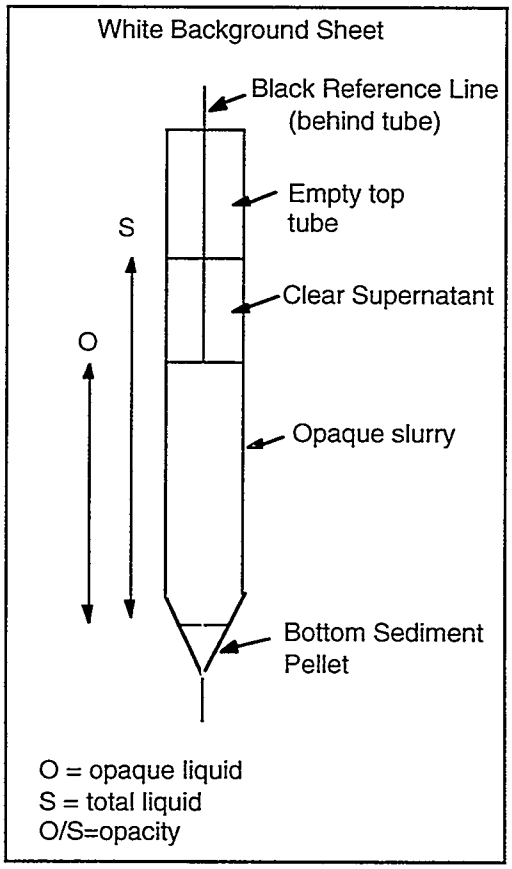

Figure 2. Sedimentation measurement schematic

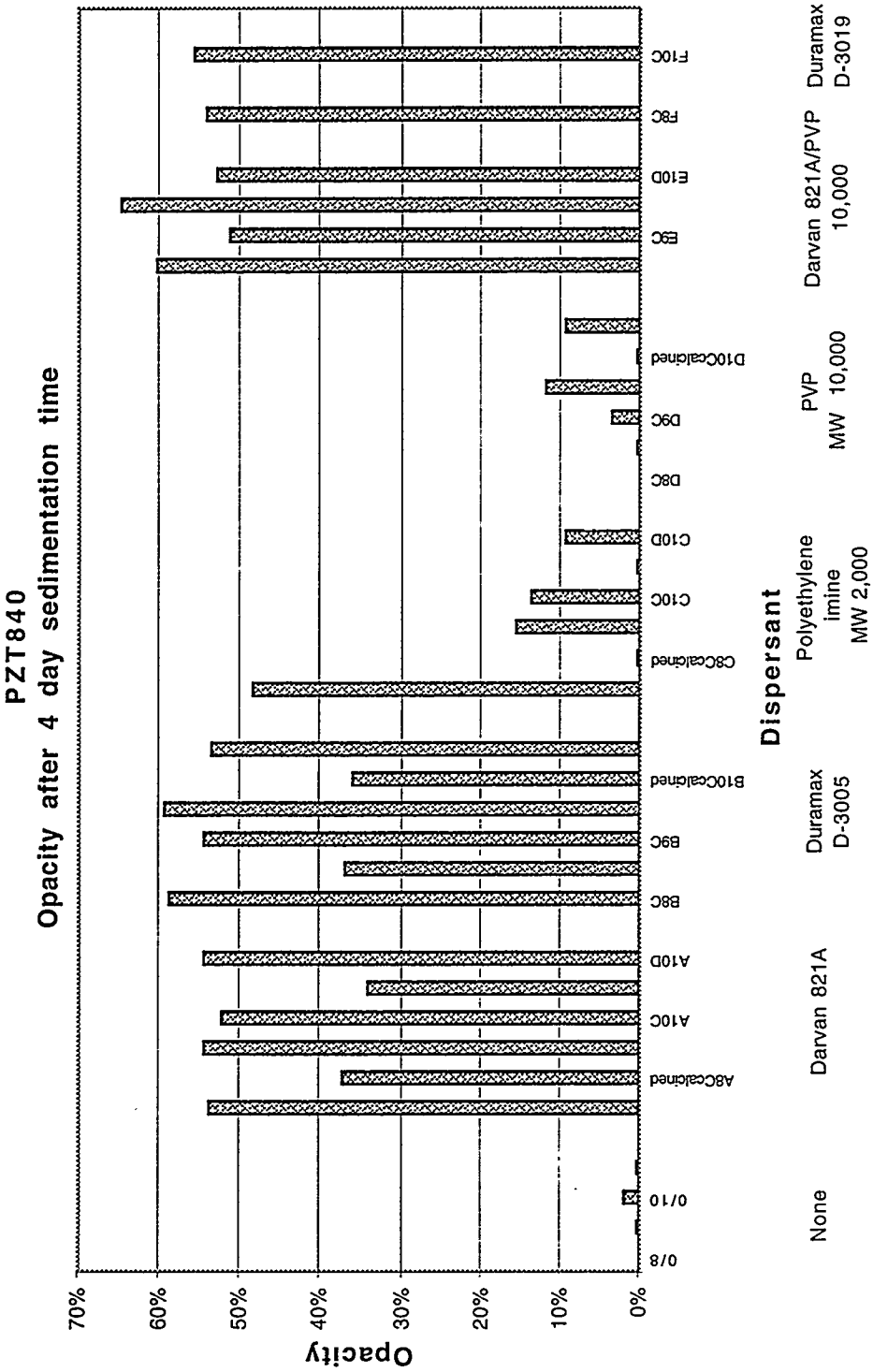

Figure 4. Sedimentation behavior of APC 840 Powder with various dispersants

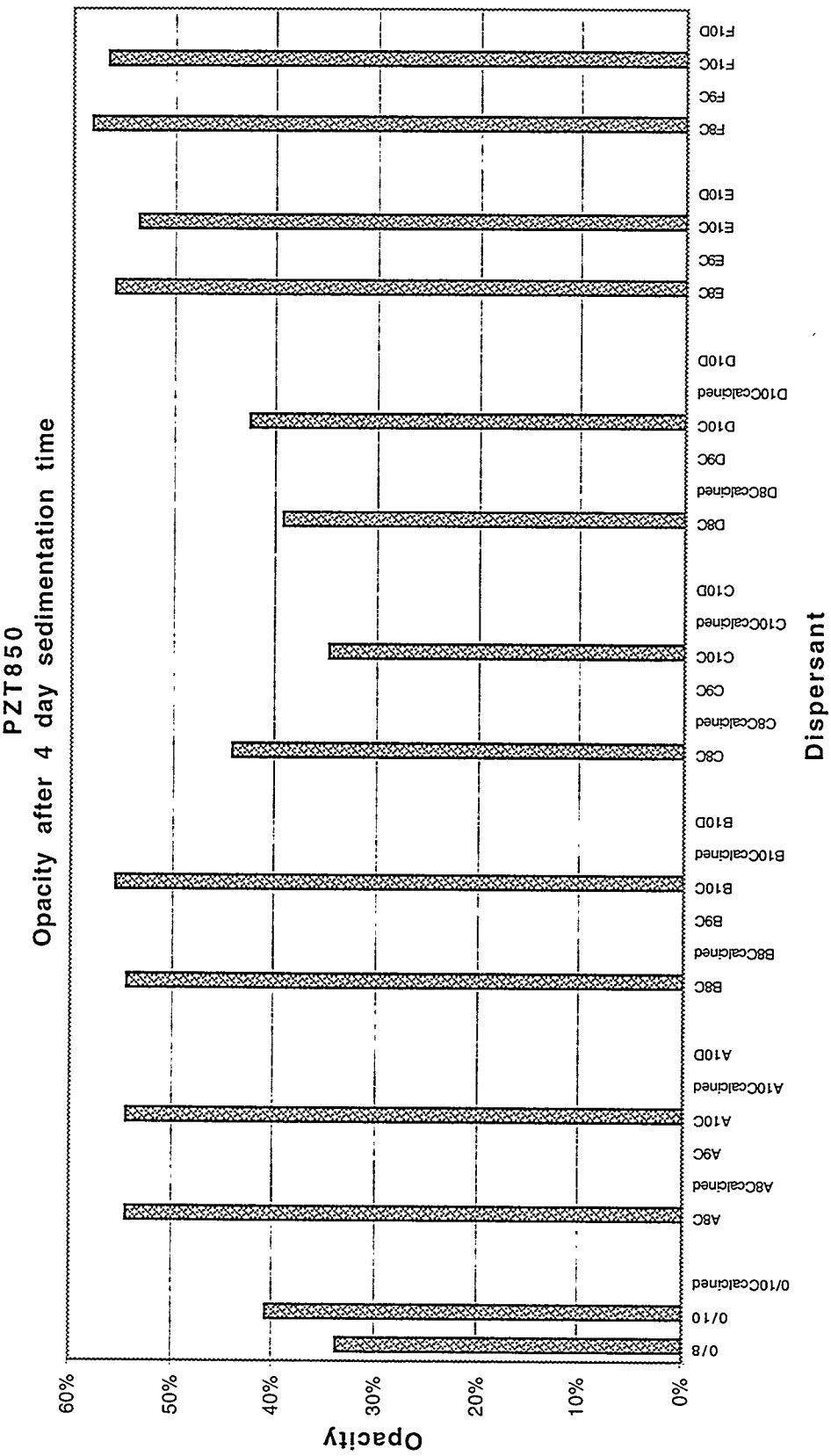

Figure 5. Sedimentation behavior of APC 850 Powder with various dispersants

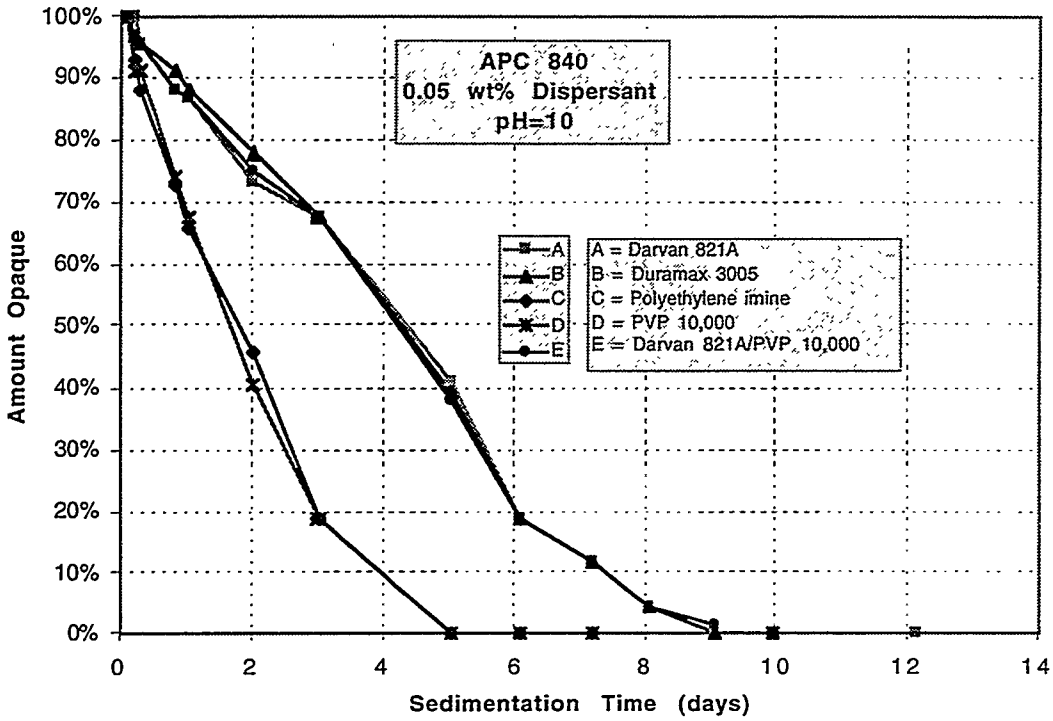

Figure 3. Sedimentation analysis of APC 840 powder for various dispersants at pH10.

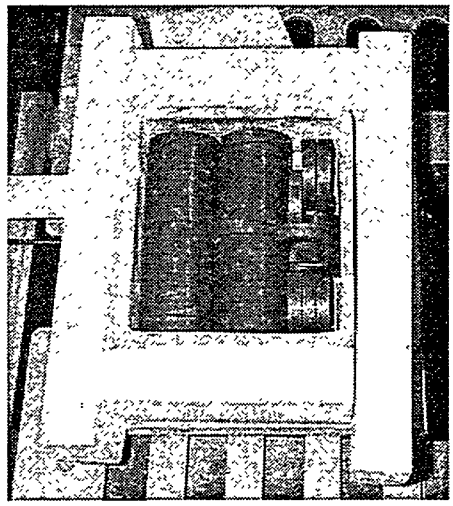

Figure 6. Set-up for the nitridation of Eaton silicon valve seat parts.

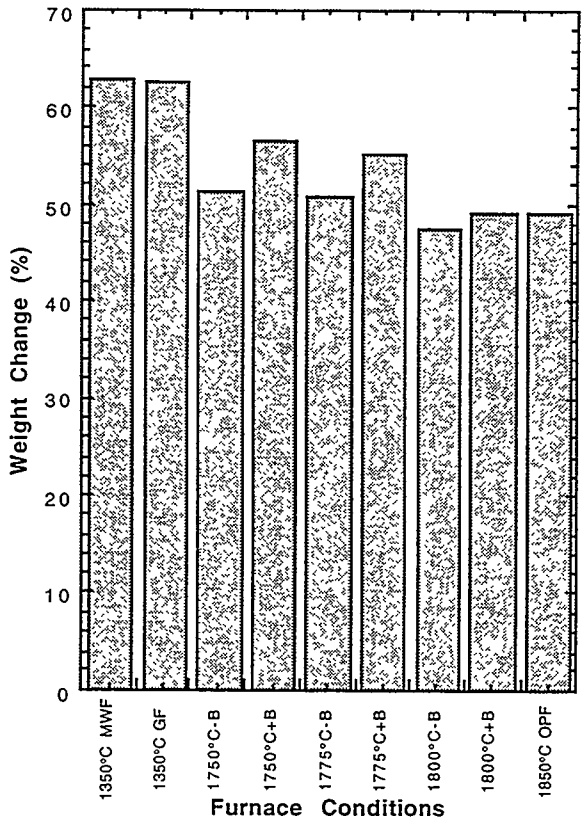

Figure 7. Weight change for silicon valve seats processed by different furnace conditions.

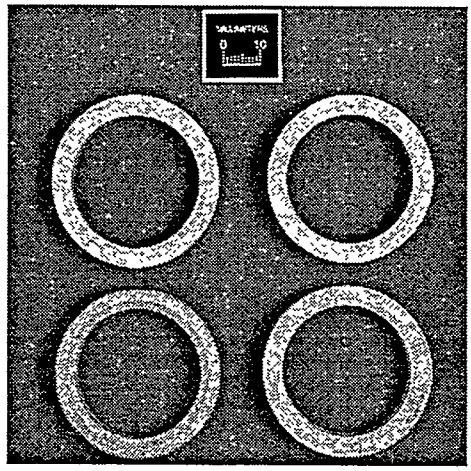

Figure 8. Photograph of several of the microwave nitrided valve seats.

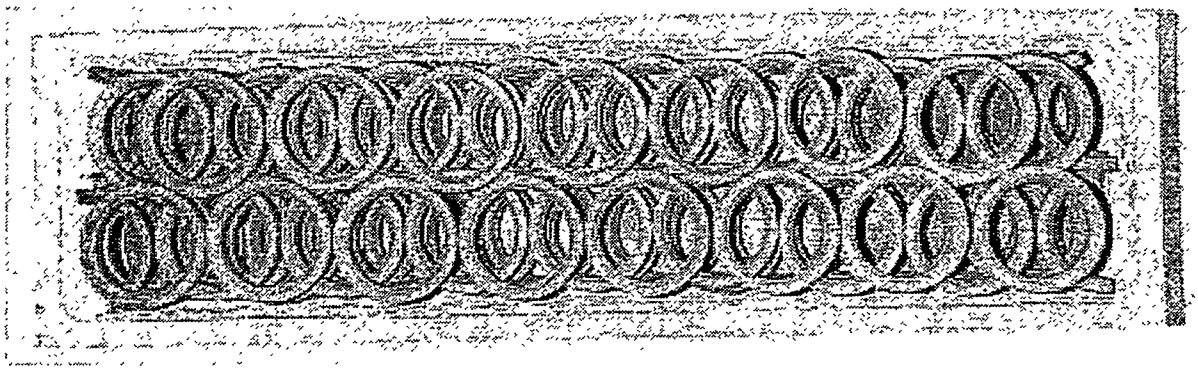

Figure 9. Photograph of the graphite crucible and silicon valve seats prior to nitridation.

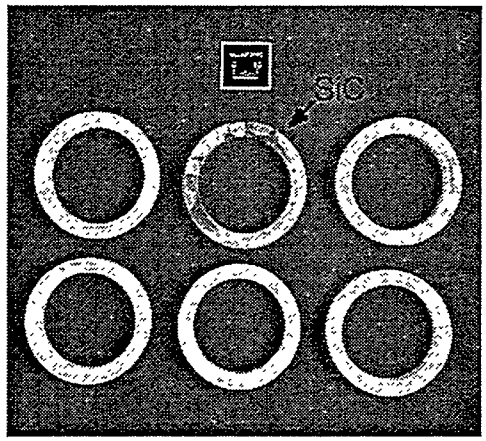

Figure 10. Photograph of valve seats after nitridation in a graphite furnace.

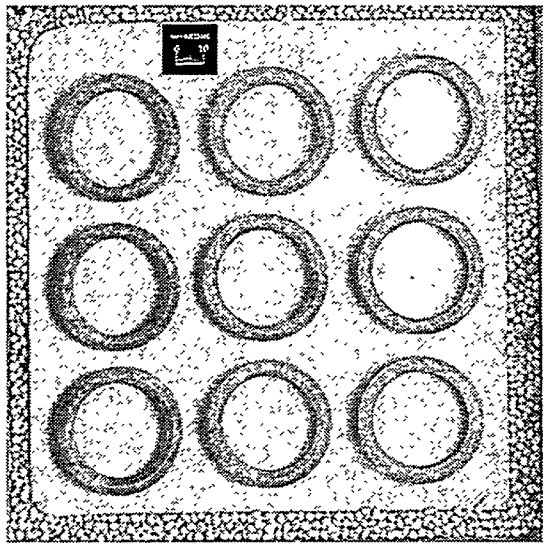

Figure 11. Photograph of nitrided valve seats in a graphite crucible used for one step nitridation and sintering runs (without silicon nitride bead cover).

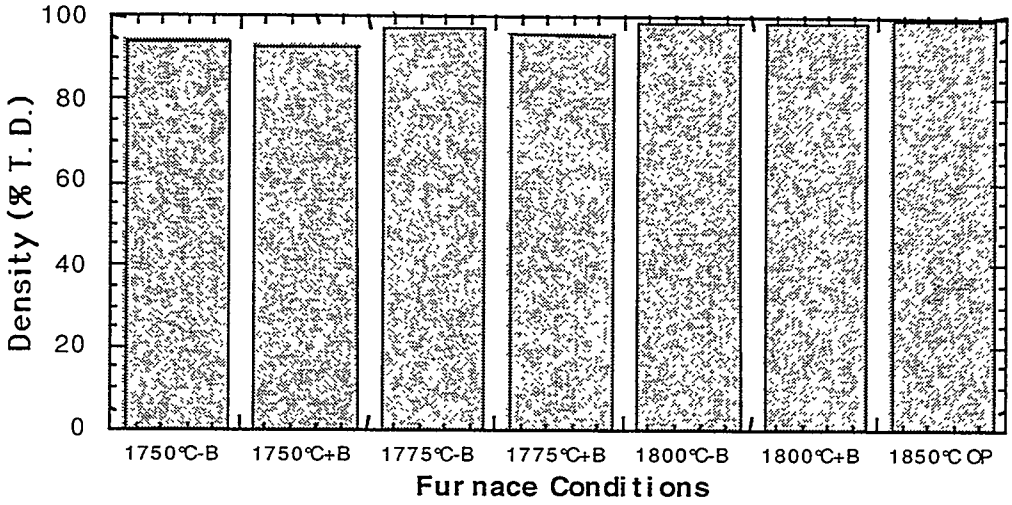

Figure 12. Densities for silicon valve seats processed by different furnace conditions.

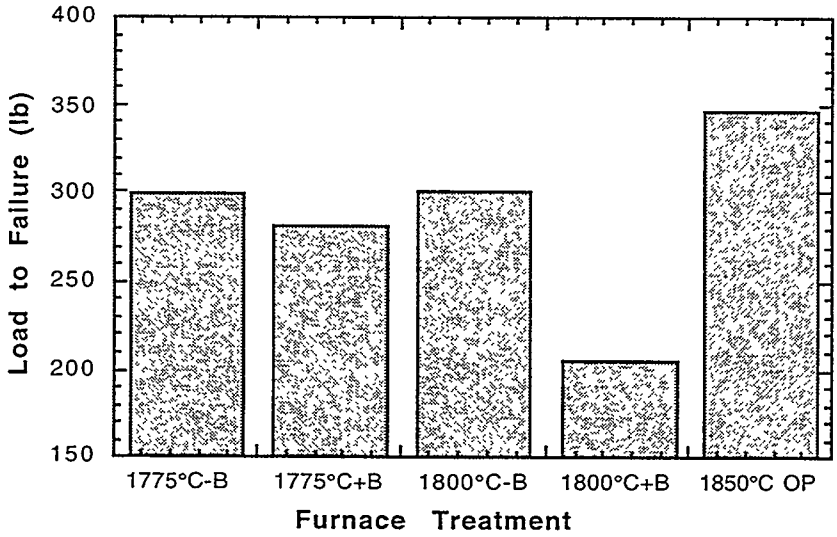

Figure 13. Load to failure data for compression test of valve seats processed by different furnace conditions

LOW COST-HIGH TOUGHNESS CERAMICS

T. N. Tiegs, F. C. Montgomery, P. A. Menchhofer, D. L. Barker, and P. F. Becher
Oak Ridge National Laboratory
Oak Ridge, TN 37831

Objective/Scope

Significant improvement in the reliability of structural ceramics for advanced diesel engine applications could be attained if the critical fracture toughness (K_{Ic}) were increased without strength degradation. Early results from ORNL research showed that significant increases in fracture toughness could be achieved by manipulating the microstructure to promote toughening mechanisms such as crack bridging. Excellent properties were obtained in this manner for the alumina and mullite matrix systems reinforced with SiC whiskers. In silicon nitride, mechanical property improvements were achieved by promoting acicular or elongated grain growth and these provided significant toughening on the same order as the whisker reinforced materials. Currently, the project is initiating studies on toughening of ceramics by two methods: microstructure development in oxide-based ceramics, and incorporation of ductile intermetallic phases.

Technical Highlights

In-Situ Toughening of Oxide-Based Ceramics by Microstructure Development

Microstructure manipulation has been used to increase the fracture toughness of ceramics for many years. Mainly, this has been done in the silicon nitride-based systems where growth of acicular grains has been encouraged. Recently, oxide-based ceramics have been studied to achieved the same type of results observed with silicon nitride. Initially, Al_2O_3 was investigated, however, mullite has also been examined.[1-9]

The oxide-based ceramics have several benefits as compared to the non-oxide systems. Lower costs should be obtained because of the lower powder costs and the capability for sintering in air atmospheres at ambient pressures and temperatures $\leq$1750°C. The materials are also more inherently stable in oxidizing environments. Silicon nitride materials, on the other hand, have higher associated powder costs, and require sintering in inert gas furnaces at high temperatures ($\geq$1750°C) and possibly gas overpresssure. While the mechanical properties and temperature capabilities for the silicon nitride materials are generally higher, for many diesel engine applications the properties of the oxides are more than adequate. Thus, because of the large potential, a study is being initiated to develop in-situ toughened oxide-based ceramics.

To begin, mullite will be examined as the matrix because of its low thermal conductivity and expansion characteristics. Seeding of mullite has been shown to produce microstructures with anisotropic grain growth similar to that observed with in-situ reinforced silicon nitride.[8,9] However, to date, the experiments have been exploratory in nature and no mechanical properties have been reported for these materials. Consequently, samples are being prepared to produce mullite with the desired microstructures for mechanical property testing to determine their suitability for diesel engine applications.

At the present time, mullite seeds are being produced that will then be added back to pure matrix raw materials. The seeds are being fabricated by a gel method using commercially available Al_2O_3 and SiO_2 precursors.[10] The different compositions of the mullite seeds are

shown in Table 1. Initial x-ray and DTA/TGA results show that the mullitization reaction occurs at ≥1350°C for pure mullite precursors and slightly lower temperatures for the Fe and Cr doped materials. The optimum conditions for seed fabrication are being determined.

Preliminary morphological results are encouraging and indicate anisotropic grain growth is most prominent with the Fe-doped samples. An example is shown in Fig. 1. In addition to the samples shown in Table 1, other dopants will be tried to determine their effects on grain growth.

Preliminary sintering results on seeded compositions are shown in Table 2. As indicated, the addition of the Fe-based seeds inhibited the densification of the gel-derived mullite. These particular seeds had a average particle size of ~30 μm and were considerably larger that the starting mullite powder. These larger, lower surface area particles significantly decreased the driving force for sintering. Consequently, at the present time the most recent batches of seeds are being processed to reduce the average particle size to <0.5 μm.

Also shown is the densification behavior of a commercially available mullite powder. This powder sintered poorly in comparison to the gel-derived materials and currently new sources of commercial materials are being explored.

Aluminide-Bonded Ceramics

Previous studies examined composites based on a matrix consisting of a hard carbide or boride phase coupled with an aluminide (e.g., Ni_3Al, FeAl) binder phase.[11-13] Initial results showed that these composites have exceptional properties. For instance, fracture toughness values comparable to the very high values obtained in the best commercial cobalt-bonded WC composites can be achieved in the aluminide-bonded carbides. Such extensive toughening is obtained by local plastic deformation in the aluminide phase which means these materials can exhibit very high mechanical reliability (e.g., Weibull modulus > 20 in preliminary studies). In addition, these composites can also exhibit extremely high fracture strengths (e.g., in excess of 1 GPa), and these strength levels are retained at temperatures up to 1000°C.

The physical properties of these composites can be tailored by careful selection of matrix and binder, and amounts of each. For instance in the TiC-Ni_3Al system, the thermal expansion coefficients can also be tailored (ranging from ~ 7 to 15 x 10^{-6}/°C) by modifying the respective volume contents of different components. The expansion can also be varied by altering the binder phase composition. In addition, the aluminide binder phases provide good oxidation and corrosion resistance.

These materials should be amenable to low cost, industrially viable fabrication routes (i.e. pressureless-sintering of complex shapes). Both direct vacuum-sintering of mixtures of carbide and Me_xAl mixtures and reaction sintering where MeAl + Me mixtures are substituted for Me_3Al powders will be developed. Preliminary results indicate a melt-infiltration–liquid phase sintering process is also a viable fabrication method. It is attractive because the extent of shrinkage during densification can be minimized, and thus, near-net-shape parts or ones requiring minimal machining are thus possible. In addition, the aluminide powder size range is not a factor with the infiltration process as it is with the sintering of powder mixtures. In each process, the equipment requirements and processing conditions are identical to those presently used in industry. Finally, these cermets also exhibit good electrical conductivity allowing them to be machined by electrical discharge

machining (EDM) processes; a substantial additional benefit in the manufacture of complex shapes.

Because the properties of the aluminide-bonded ceramics are attractive for diesel engine applications, development of these materials is being started. Issues to be studied include the fabrication of parts using cost-effective processing, effect of alloying elements on the properties and fabrication of near-net-shape parts for testing.

Initially, a study will be done to examine the sintering behavior of the aluminide-bonded ceramics at high binder contents. Most of the previous work on ABC's was done at binder contents of 10-30 vol. %. However, higher binder contents on the order of 30-50 vol. % are necessary for these composites to match the thermal expansion of steel. A comparison of thermal expansion for the TiC-based composites is shown in Fig. 2.

At the present time, samples are being prepared by three different methods: (1) sintering with pre-alloyed gas-atomized Ni_3Al or FeAl powders, (2) reaction sintering with fine elemental powders to form Ni_3Al in-situ, or (3) infiltration of TiC preforms with pre-alloyed gas-atomized Ni_3Al. The experimental plan is shown in Table 2. Besides the densification behavior, the samples will be characterized for strength, fracture toughness, and thermal expansion. The microstructure will also be evaluated.

Other areas of interest in the development of ABC's that will be done in the near future include:

1. Alternate methods to produce materials by infiltration techniques will be investigated. Previous work has shown infiltration produces materials with fine grain sizes and superior properties. Variations on the method will be systematically examined that will give a wide range of infiltration temperatures from ~700°C up to >1400°C. Current infiltration temperatures are 1300-1400°C.

2. Examine the effect of alloy composition on final properties. It is will known that the properties of these intermetallic aluminides can be altered significantly by alloying with other elements, such as Fe, Cr, Mo, Zr, W and others. The goal would be to increase the strength, fracture toughness, thermal expansion and corrosion resistance of the materials. This would allow tailoring of the properties of the composites to specific applications.

3. Investigate the use alternate ceramic reinforcement phases and combinations of phases. Alternate ceramics would include TiN, VC. Mo_2C, TiB_2 and others.

Status of Milestones

On schedule.

Communications/Visits/Travel

Travel by T. N. Tiegs to the American Ceramic Society Meeting in San Francisco, CA, October 13-15, 1997 to present a paper entitled "Effect of ß-Nucleation Conditions on Mechanical Properties of GPS Si_3N_4."

Travel by T. N. Tiegs to the Customer's Coordination Meeting in Dearborn, MI, October 27-29, 1997 to present a poster entitled "Development of High Toughness Silicon Nitride."

Travel by T. N. Tiegs to the American Ceramic Society Meeting in Cocoa Beach, FL, January 20-23, 1998 to present a paper entitled "Comparison of Sintering Behavior and Properties of Aluminide-Bonded Ceramics."

Travel by T. N. Tiegs to Las Vegas, NV, December 9-10, 1997 to attend a Program Coordination Meeting for the Metal Powder Industries Federation 1998 International Conference on Powder Metallurgy and Particulate Materials.

Problems Encountered

None.

Publications

T. N. Tiegs, P. A. Menchhofer, K. P. Plucknett, P. F. Becher, C. B. Thomas and P. K. Liaw, "Comparison of Sintering Behavior and Properties of Aluminide-Bonded Ceramics." Ceram. Eng. Sci., (to be published).

References

1. M. M. Seabaugh, I. H. Kerscht and G. L. Messing, "Texture Development by Templated Grain Growth in Liquid-Phase-Sintered α-Alumina," J. Am. Ceram. Soc., 80[5]1181-1188(1997).

2. A. Kebbede, G. L. Messing and A. H. Carim, "Grain Boundaries in Titania-Doped α-Alumina with Anisotropic Microstructure," J. Am. Ceram. Soc., 80[11]2814-2820(1997).

3. D. E. Garcia, J. Wendorff, R. Janssen and N. Claussen, "Formation of Needle-Like Grains in Al_2O_3," pp. in Ceram. Eng. Proc.,

4. J. Tartaj and G. L. Messing, "Anisotropic Grain Growth in α-Fe_2O_3-Doped Alumina," J. Europ. Ceram. Soc., 17, 719-725 (1997).

5. J. A. Salem, J. L. Shannon and R. C. Bradt, "Crack Growth Resistance of Textured Alumina," J. Am. Ceram. Soc., 72[1]20-27(1989).

6. D. Brandon, D. Chen and H. Chan, "Control of Texture in Monolithic Alumina," Mater. Sci. Eng., A195, 189-196 (1995).

7. D. S. Horn and G. L. Messing, "Anisotropic Grain Growth in TiO_2-Doped Alumina," Mater. Sci. Eng., A195, 169-178 (1995).

8. S.-H. Hong, W. Cermignani and G. L. Messing, "Anisotropic Grain Growth in Seeded and B_2O_3-Doped Diphasic Mullite Gels," J. Europ. Ceram. Soc., 16, 133-141 (1996).

9. T. J. Mroz and J. W. Laughner, "Microstructures of Mullite Sintered From Seeded Sol-Gels," J. Am. Ceram. Soc., 72[3]508-509(1989).

10. S. P. Chaudhuri and S. K. Patra, "Preparation and Characterization of Transition Metal Ion Doped Mullite," Brit. Ceram. Trans., 96 [3] 105-111 (1997).

11. K. P. Plucknett, T. N. Tiegs, P. A. Menchhofer, P. F. Becher and S. B. Waters, "Ductile Intermetallic Toughened Carbide Matrix Composites," Ceram. Eng. Proc., 17[3]314-321 (1996).

12. T. N. Tiegs, K. P. Plucknett, P. A. Menchhofer and P. F. Becher, "Development of Nickel Aluminide Cermets," pp. 339-357 in Internat. Symp. Nickel and Iron Aluminides, ASM International, Metals Park, OH (1997).

13. R. Subramanian and J. H. Schneibel, "Processing of Iron-Aluminide Composites Containing Carbides or Borides," J. Metals, 49[8]50-54(1997).

Table 1. Summary of mullite seed compositions for anisotropic grain growth experiments.

Specimen No.	Dopant[a]	Dopant Level	Alumina Source	Silica Source
ITM-1	None	--	Versal 850	Ludox HS-40
ITM-2	None	--	Versal 850	Ludox AS-40
ITM-Cr-1	Cr	21.5	Versal 850	Ludox HS-40
ITM-Cr-2	Cr	0.7	Versal 850	Ludox HS-40
ITM-Cr-3	Cr	0.7	Versal 850	Ludox AS-40
ITM-Cr-4	Cr	7.2	Versal 850	Ludox AS-40
ITM-Fe-1	Fe	7.2	Versal 850	Ludox AS-40
ITM-Fe-2	Fe	0.7	Versal 850	Ludox AS-40
ITM-Sr	Sr	7.2	Versal 850	Ludox AS-40
ITM-Sr	Sr	5.2	Versal 850	Ludox AS-40
ITM-Y	Y	7.2	Versal 850	Ludox AS-40
ITM-Y	Y	5.8	Versal 850	Ludox AS-40

[a] Added as either chrome acetate, iron nitrate, strontium carbonate or yttrium nitrate.

Table 2. Initial results on sintering of seeded mullite compositions for anisotropic grain growth.

Mullite Type	Matrix	Seed Content (wt. %)	Sintering Conditions (°C/h) Density (g/cm³) 1600/3	Density (g/cm³) 1600/15	Density (g/cm³) 1650/3
ITM-2		None	2.70	2.82	2.85
ITM-2		2% ITM-Fe-1	2.40	2.63	2.72
Baikowski*		None	2.06	2.41	2.49

* Baikowski Corp., High purity mullite.

Table 3. Experimental plan to compare the sintering behavior and properties of aluminide-bonded ceramics by different processing methods.

Specimen No.	Binder Type	Binder Content (vol. %)	Fabrication Method[a]
DC-10	Ni_3Al (IC-50)	30	S/PA
DC-11	Ni_3Al (IC-50)	40	S/PA
DC-12	Ni_3Al (IC-50)	50	S/PA
DC-13	Ni_3Al	30	RS/E
DC-14	Ni_3Al	40	RS/E
DC-15	Ni_3Al	50	RS/E
DC-16	Ni_3Al (IC-50)	30	I/PA
DC-17	Ni_3Al (IC-50)	40	I/PA
DC-18	Ni_3Al (IC-50)	50	I/PA
DC-19	Fe-40Al	30	S/PA
DC-20	Fe-40Al	30	RS/E
DC-21	Fe-40Al	30	I/PA

[a] S/PA - Sintering with pre-alloyed powders; RS/E - Reaction sintering with elemental powders; I/PA - Infiltration with pre-alloyed powders.

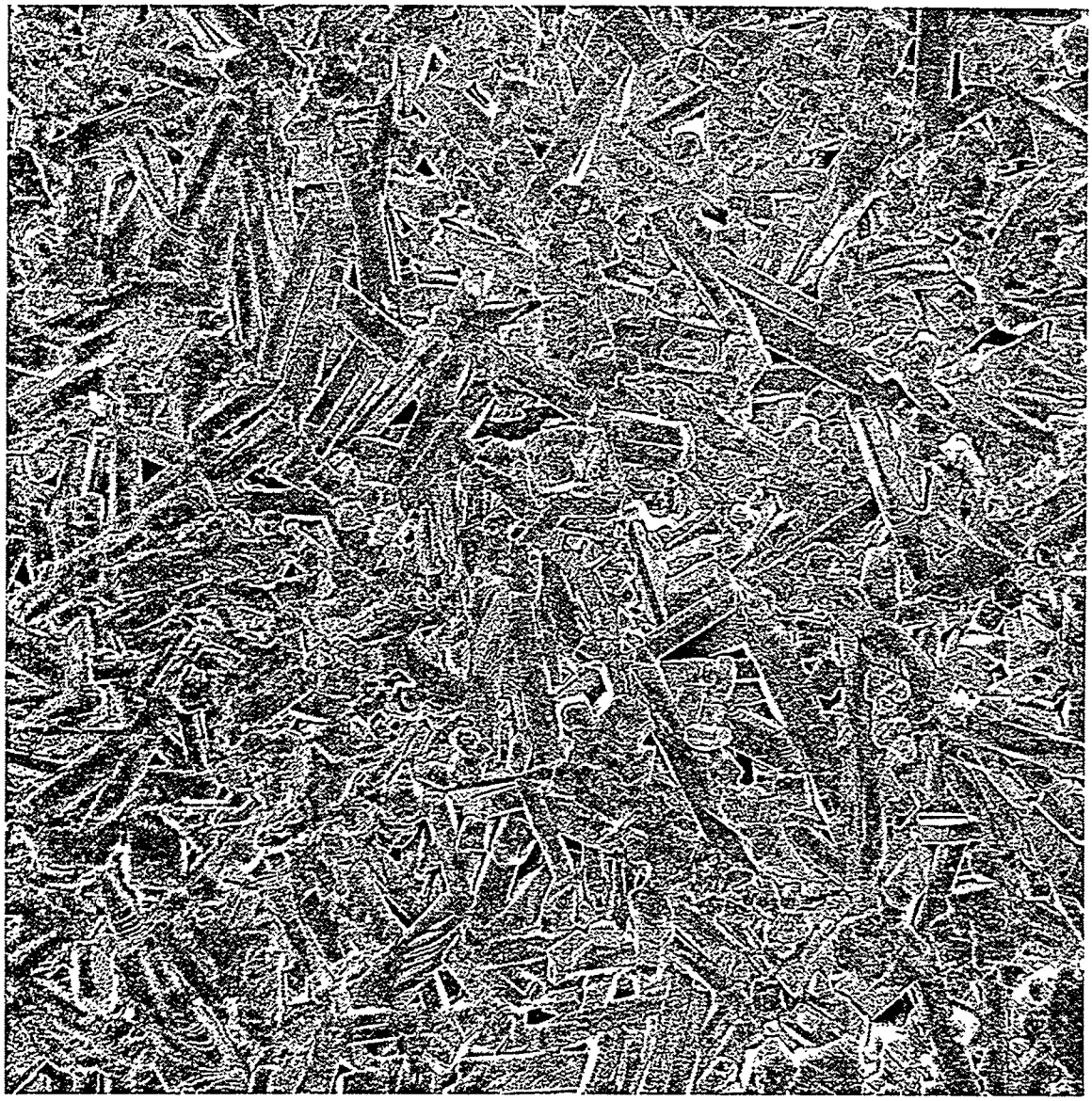

Fig. 1. Initial results on Fe-doped mullite composition exhibiting anisotropic grain growth.

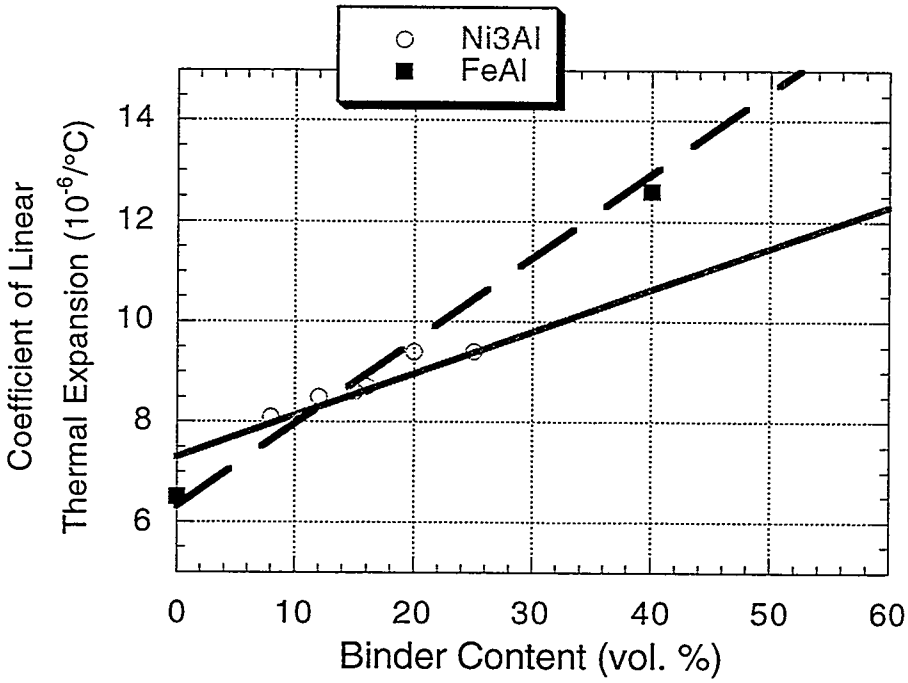

Fig. 2. Thermal expansion characteristics of TiC-based composites with Ni_3Al or FeAl binders.

Cost Effective Sintering of Silicon Nitride Ceramics (SIU-C)-
D. E. Wittmer, Southern Illinois University, Carbondale, IL 62901

Objective/Scope

The purpose of this work is to investigate the potential of cost effective sintering of Si_3N_4 through the development of continuous sintering techniques and the use of lower cost Si_3N_4 powders and sintering aids. The addition of a recent task has added the objective of investigating the cost effective sintering of advanced carbides and cermets.

Technical Highlights

Task 1. Refine Economic Model and Design for Chosen Furnace Configuration

This task was completed as reported in a previous semiannual report.

Task 2. Continue evaluation of sintering parameters on properties of selected Si_3N_4 compositions

Prototype Belt Furnace

The Model 44-BF belt furnace has been operating with the tungsten hot zone installed for over 3 years (>3500 hours) of high-temperature operation without any major problems with the furnace. Several advanced ceramics compositions have been successfully sintered including: silicon nitride formulations containing alumina and rare earth oxide sintering aids, SiAlON, AlN, WC, SiC and some mixed alunina/zirconia oxides. Specific furnace modifications have been suggested to Centorr Vacuum Industries to improve the operation of the next generation furnace for commercialization. Also, the addition of a debinding chamber or continuous debinding is being investigated as part of the latest contract modification.

Since its installation at SIUC, the belt furnace has been in operation using the tungsten element hot zone and shield package. The furnace was moved and installed in SIUC campus's new engineering annex. The presently installed tungsten hot zone will be replaced with the graphite hot zone in late May or early June to conduct research on new composites and carbides.

During this reporting period, an attempt was made to map out the furnace thermal cross-section and determine the respective heating rates for various belt speeds. This work is continuing. Also the effect of heating rate on a standard formulation has been initiated. Since the furnace is capable of being operated with one or two of the three zones either off or at a reduced temperature. It is possible to affect both the heating and

cooling rate during sintering. This would make it possible to develop specific phases during both heating and cooling which would affect both the sinterability of the material and the development of microstructures and crystalline phases on cooling. It is expected that this area will develop into a new task area for the next funding phase and would hold special attraction for processing bonded carbides which are typically sintered in vacuum batch furnaces.

Industrial Collaboration/Affiliation

Industrial collaboration/affiliation is an important aspect of this program to allow transfer of continuous sintering technology to transportation related industry and also to allow industry to evaluate continuous sintering as a viable cost effective method of sintering their products, without the investment which would otherwise be required.

Advanced Ceramics, Inc.

Advanced Ceramics, Inc. (ACI is a Division of Coors) has been included in our group of industrial collaborators. We have been working with them and Advanced Refractories Technologies to develop processing methods for ART's recently introduced silicon nitride powder.

During this reporting period, work was initiated with ACI in the processing and sintering of their compositions which utilize a new ART silicon nitride powder. The as-received powder is much larger and has a wider particle size distribution than any of the other commercially available silicon nitride powders that are known to be sinterable.

Initially we conducted a turbomilling study to determine the amount of time required to achieve a particle size and distribution similar to any of the commercial powders. Both tungsten carbide and silicon nitride media were used initially. The tungsten carbide appeared to reduce the particle size quite rapidly, but produced unacceptable amounts of contamination. After 16 hours of turbomilling using silicon nitride media, the particle size and distribution of the ART silicon nitride was similar to that of the Starck M-11 grade, and after 21 hours of turbomilling with the silicon nitride media, the particle size distribution was similar to the Ube E-10. The particle size results, after turbomilling for 21 hours, are shown in Figure 1. The turbomilled material was delivered to ACI for spray drying and sintering but did not produce acceptable results. The problems with the particle size and morphology were discussed with Roger Storm at ART and they are currently working with their partner to reduce the initial particle size.

More recently, the ART powder has been processed by turbomilling to try to reduce its particle size and improve its sinterability. Also, 50/50 blends of the ART silicon nitride have been made with commercial powders from H. C. Starck (thanks to Dale Lathrop of H. C. Starck for gratis samples of M-11 and ST grades of silicon nitride) and Ube E-10. This will be discussed in more detail in the evaluation of low cost powders.

Allied Signal, Inc.

No new work was completed for Allied Signal, Inc. and notice that all silicon nitride research directed at this collaboration has been transferred or suspended. Future work will depend on the availability of materials from Allied Signal.

Eaton Corporation

ORNL is in the process of microwave nitriding some of Eaton's SRBSN. Continuous sintering of the microwave nitrided SRBSN will be conducted at SIUC when received. Eaton has indicated an interest in increasing the scope of the program at SIU-C to include assistance in the processing and sintering of their SRBSN materials. However, due to program reviews that are in progress, no additional materials have been received at SIU or ORNL.

Kennametal, Inc.

During this reporting period, Kennametal, Inc. has been included as one of our industrial collaborators. As reported in previous reports, it has been demonstrated that a commercial silicon nitride, Kyon 3000, could be continuously sintered in the belt furnace at SIUC. Kennametal processed 250 test bars of Kyon 3000 which were continuously sintered at SIU and then HIPed by Kennametal. Following their evaluation, some of these test bars were sent to ORNL for mechanical property testing and appear to have high temperature properties exceeding other silicon nitride materials tested by ORNL. This work is expected to lead to further collaboration between Kennametal, ORNL and SIUC. We are presently in the process of outlining a new initiative with Kennametal which should involve one of the diesel engine companies.

Norton Advanced Ceramics

The additional funds that were requested by NAC to continue investigations involving sintering warpage and consistency of the exhaust valves under the ACMT contract have still not yet been approved. It is expected that final approval of the contract extension will take place during the next reporting period and work can proceed on studying the influence of a modified sintering environment on the valve acceptability. This work will be completed before the tungsten hot zone is installed. Additional valves may be sintered after the graphite hot zone is installed to make a comparison.

Task 3. Continue Evaluation of Low Cost Si_3N_4 Powder

Starck M-11 and Shin-Etsu Silicon Nitride Powders

The work on this task has been summarized in an MS thesis by Mr. Magnus Holgesson, "The Effects of Milling Media on the Properties of Turbomilled Silicon Nitride." The results of this work were also presented at "Fine Powder Processing '97", an International Conference on Fine Grinding, Classification, and Agglomeration Science and Technology, Penn State, Sept. 15-17, 1997. This concludes this portion of the work initiated for this task.

Starck Baysinid and ART, Inc. Silicon Nitride Powders

Because of the lack of consistent sintering results for the Starck M-11 powder, Starck has provided a 5 kg sample of their new Baysinid grade of silicon nitride for our evaluation. This material has been prepared in the A3Y9 composition as will be discussed.

During this reporting period, 10 kgs of ART, Inc. (Lot 4) silicon nitride were also received for our evaluation. This powder was included in our characterization, milling and sintering evaluations. Collaboration with ACI was also initiated to investigate ART silicon nitride as a low cost alternative to other commercially available powders.

The 10 kgs of ART, Inc. (Lot 4) Si_3N_4 was turbomilled with and without sintering aids. The preliminary sintering results were not satisfactory, because of the larger starting particle size of the as-received powder. This material because of its excellent crystallinity has proven to be a challenge to process without remnant large particulate. Because of this, we have chosen to investigate it as a possible extender for the higher cost Starck and UBE powders. This was accomplished by adding the ART Si_3N_4 as a 50/50 blend to the other commercially available powders in the A3Y9 formulation, as indicated in Table I. These powders were turbomilled in the A3Y9 formulation for the following: 100% ART (Fig. 2); 100% Ube E-10 (Fig. 3); 100% Starck M-11 (Fig. 4); 100% Starck ST (Fig. 5); 50/50 ART/Ube (Fig. 6); 50/50 ART/Starck ST (Fig. 7) and 50/50 ART/M-11 (Fig. 8).

These formulations were turbomilled to produce equivalent particle size, as measured by the Horiba 910 analyzer. The formulations containing the ART powder alone took longer turbomilling time to reach the same average particle size as the other powders. The 100% ART required 21 hours of turbomilling to reach an average particle size of 0.5 microns (compared with the other commercial powders which took about 1 hour), while the powder blends required about 6 hours of milling.

Following turbomilling, 9 cm diameter by 6 mm thick disks were pressure cast, dried, isopressed to 55Ksi and then continuously sintered at 1750°C and 1790°C for 2 hours. Following sintering the density and weight loss for each formulation were determined and are given in Table II. Representative disks were then sent out for machining into test bars, after which the test bars were evaluated for density, flexural strength, Vickers hardness (5 kg load), and fracture toughness by both the indentation

and strength methods. Representative samples will be plasma etched and the microstructures will be determined by SEM during the next reporting period.

The preliminary density and strength results (based on limited data) are given in Table III. As expected the 100% UBE A3Y9 had the highest density and strength. The 100% Starck ST A3Y9 had the next highest density but the 100% Starck M-11 A3Y9 had the third highest density but was second in strength. The 100% ART A3Y9 had the lowest density and the lowest strength.

The powder blends gave densities marginally lower that the for the commercial powders, however the strength values were much lower for the blends than anticipated. The ART/Starck M-11 blend had the highest density, while the ART/UBE blend had the lowest density and strength. Also, the strengths observed were considerably lower than would be predicted by a general rule of mixtures, but are about 20% higher than achieved for the 100% ART A3Y9. This would indicate that the strength limiting flaws were not affected significantly by the additional milling. The reason for these low strength values is currently being investigated, but is assumed to be due to large particulate from the as-received ART that remains following turbomilling.

Table IV gives the results obtained for hardness and fracture toughness (both indentation and strength methods). The results for the commercial powders in the A3Y9 formulation are the typical values obtained for this formulation and sintering conditions. All of the ART blends had lower fracture toughness than expected. This again is most likely due to the remnant large particulate.

Task 4. Design and Construct Prototype Belt Furnace

This task has been completed.

Status of Milestones

1.	Refine Economic Model and Design for Chosen Furnace Configuration	Completed
2.	Continue Evaluation of Sintering Parameters on Properties of Selected Si_3N_4 Compositions	On Schedule Continuing
3.	Continue Evaluation of Low Cost Si_3N_4 Powders	On Schedule Continuing
4.	Design and construct prototype belt furnace	Completed

Problems Encountered

None

Publications

D. E. Wittmer and P. M. Holgesson, "The Effect of Milling Media on the Properties of Turbomilled Silicon Nitride Slurries," **Fine Powder Processing '97**, to be published in 1998.

Presentations

D. E. Wittmer and P. M. Holgesson, "The Effect of Milling Media on the Properties of Turbomilled Silicon Nitride Slurries," presented at "Fine Powder Processing '97", an International Conference on Fine Grinding, Classification, and Agglomeration Science and Technology, Penn State, Sept. 15-17, 1997.

Table I. A3Y9 Formulations Being Investigated

Designation and ID Key	ART	Starck M-11	Starck ST	UBE
ART	100%			
ST		100%		
SM			100%	
UBE				100%
ASM	50%	50%		
AST	50%		50%	
AU	50%			50%

Table II. Sintering Results for A3Y9 Formulations

Comp.	1750°C for 2 h		1790°C for 2 h	
	Bulk Density (g/cc)	Wt. Loss %	Bulk Density (g/cc)	Wt. Loss %
ART	3.20	3.51	3.22	4.56
ST	3.26	2.03	3.27	3.11
SM	3.24	1.87	3.26	2.72
UBE	3.27	2.16	3.28	2.26
ASM	3.19	3.51	3.24	3.94
AST	3.24	4.04	3.26	4.23
AU	3.18	3.64	3.22	3.81

Table III. Density and Strength Results for A3Y9 Formulations

Comp.	1790°C for 2 h	
	Bulk Density Machined Bars (g/cc)	Four-Point Flexural Strength (MPa)
ART	3.21	526 +/-68
ST	3.28	814 +/- 91
SM	3.27	859 +/- 86
UBE	3.29	953 +/- 52
ASM	3.21	630 +/- 33
AST	3.25	644 +/- 60
AU	3.22	624 +/- 77

Table IV. Hardness and Fracture Toughness Results for A3Y9 Formulations

Composition	Sintered at 1790°C for 2 h		
	Vickers Hardness 5 kg load (kg/mm^2)	Fracture Toughness ($MPa\text{-}m^{1/2}$)	
		Indentation	Strength
ART	1290	5.0	4.7
ST	1280	5.2	5.9
SM	1300	5.4	6.4
UBE	1330	5.4	6.5
ASM	1254	5.2	5.5
AST	1380	5.2	5.5
AU	1280	5.2	5.5

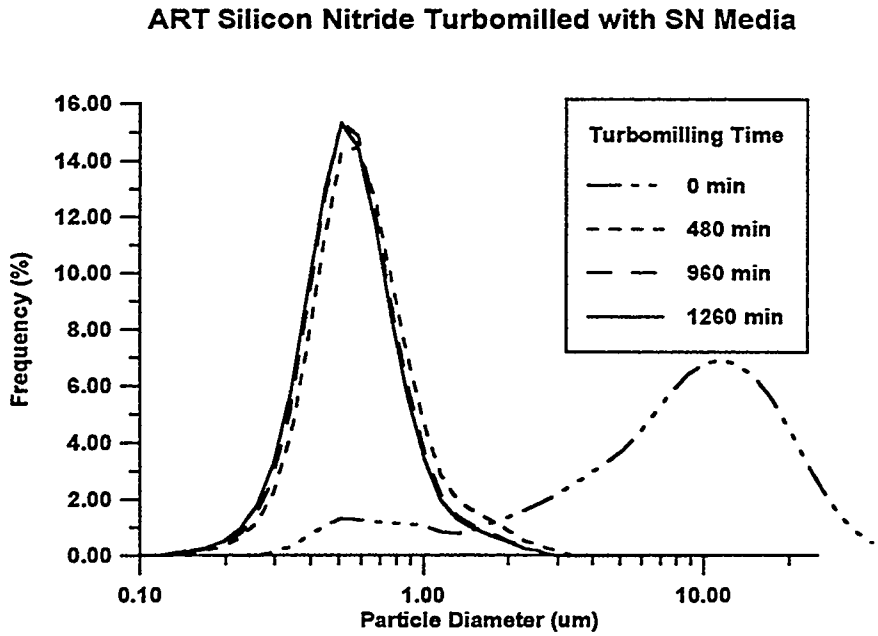

Figure 1. Particle size distribution for ART silicon nitride: As-received and turbomilled for 480, 960 and 1260 min.

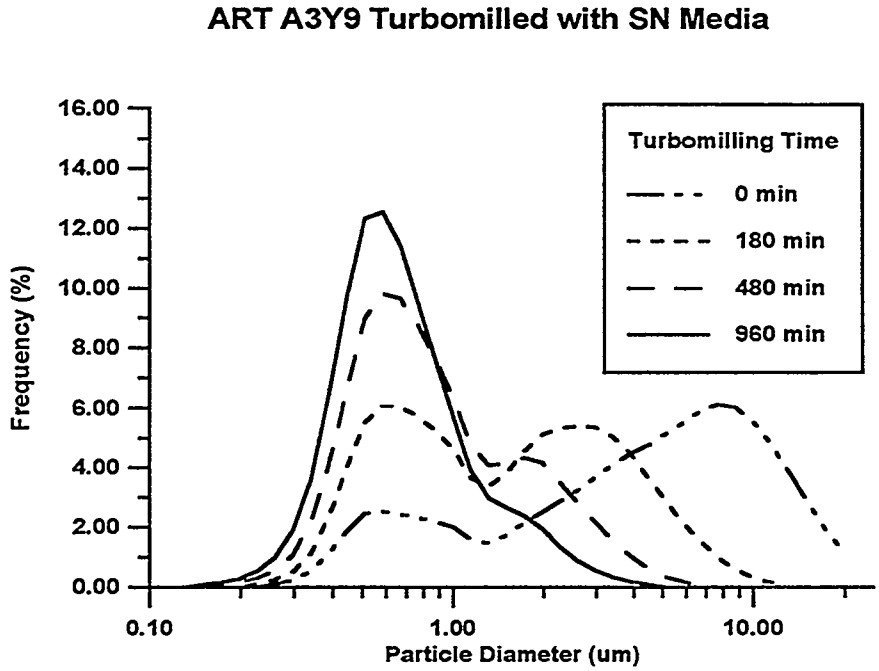

Figure 2. Particle size distribution for ART A3Y9: As-received and turbomilled for 180, 480 and 960 min.

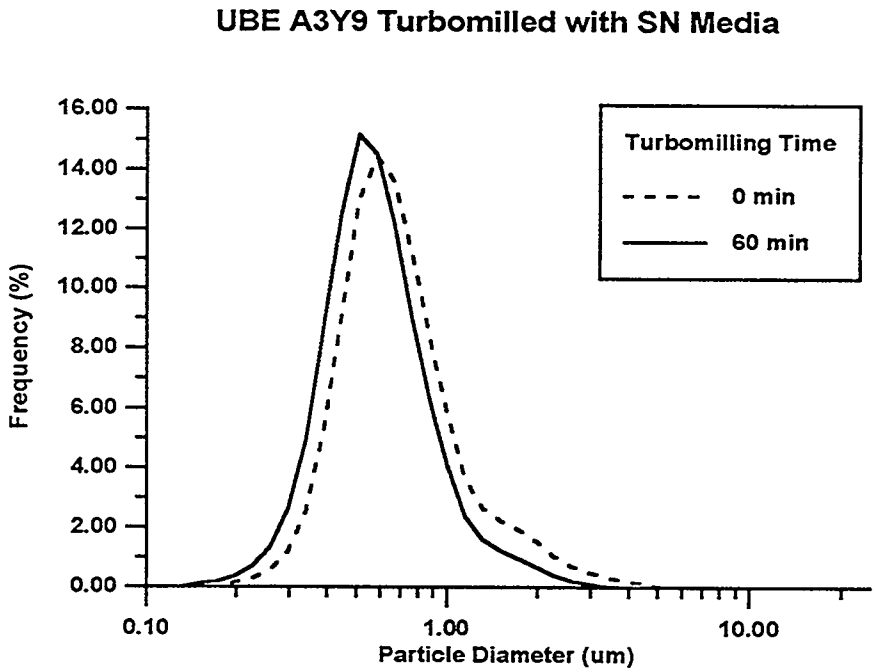

Figure 3. Particle size distribution for 100% Ube A3Y9: As-received and turbomilled for 60 min.

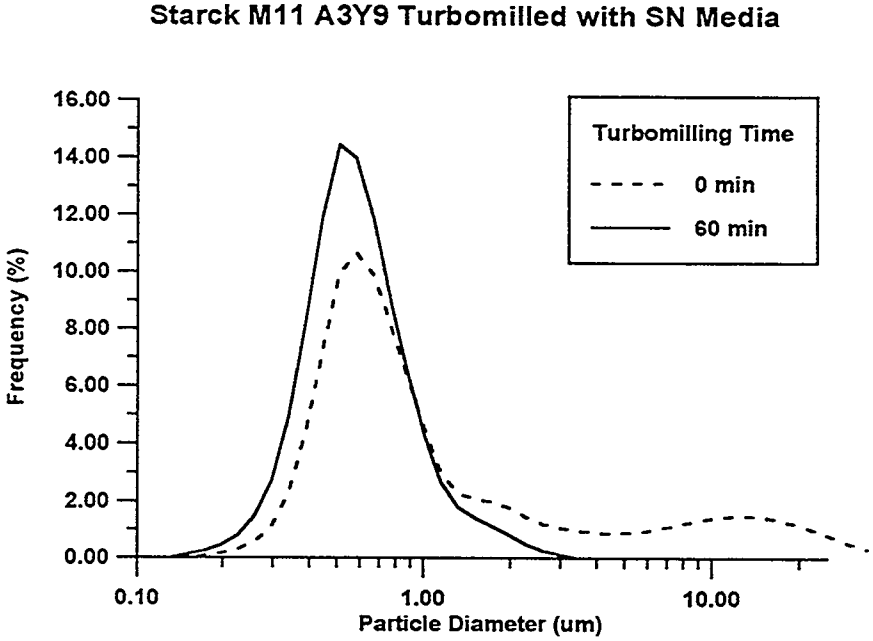

Figure 4. Particle size distribution for 100% Starck M-11: As-received and turbomilled for 60 min.

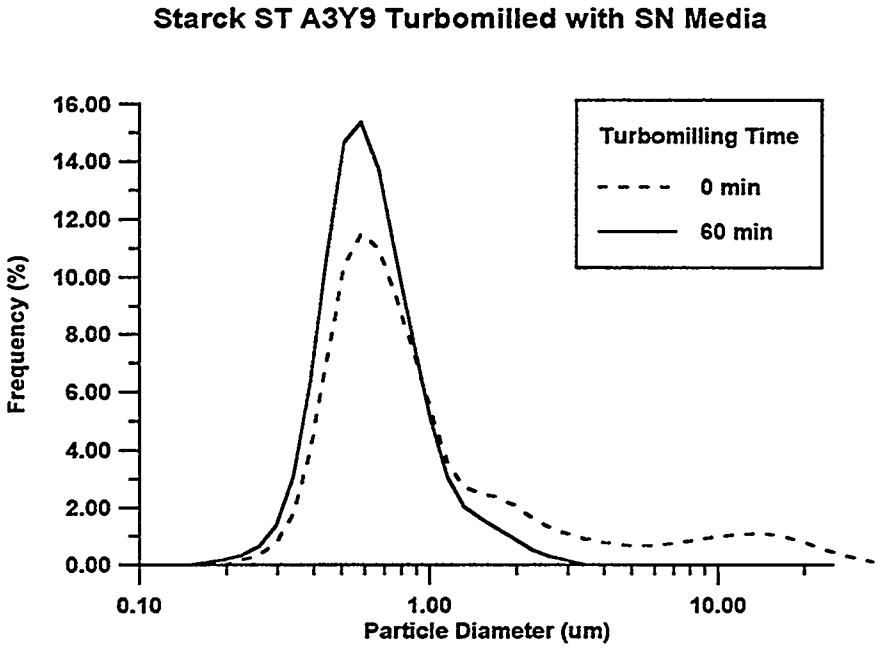

Figure 5. Particle size distribution of 100% Starck ST A3Y9: As-received and turbomilled for 60 min.

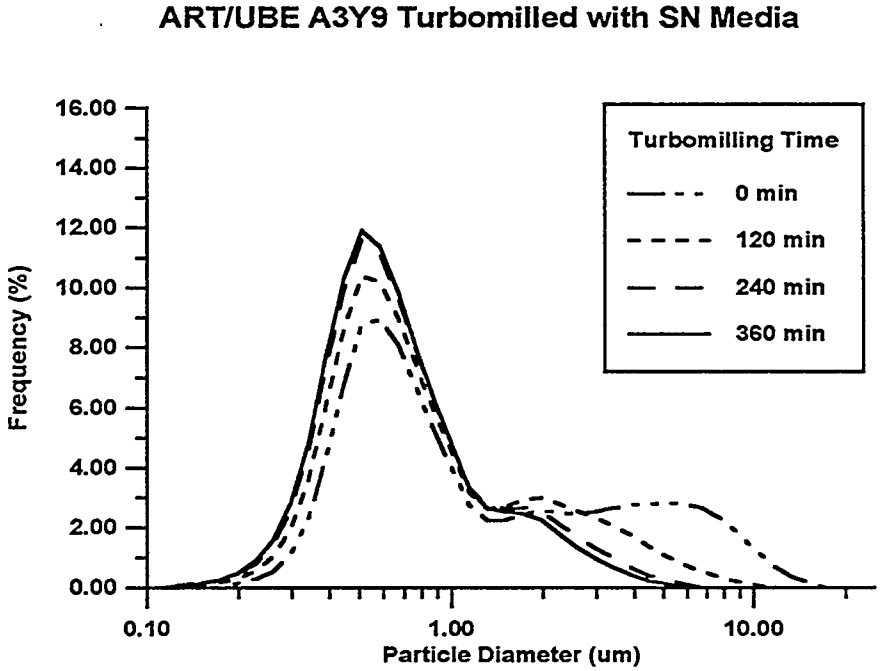

Figure 6. Particle size distribution of 50/50 ART/Ube E-10 A3Y9: As-received and turbomilled for 120, 240, and 360 min.

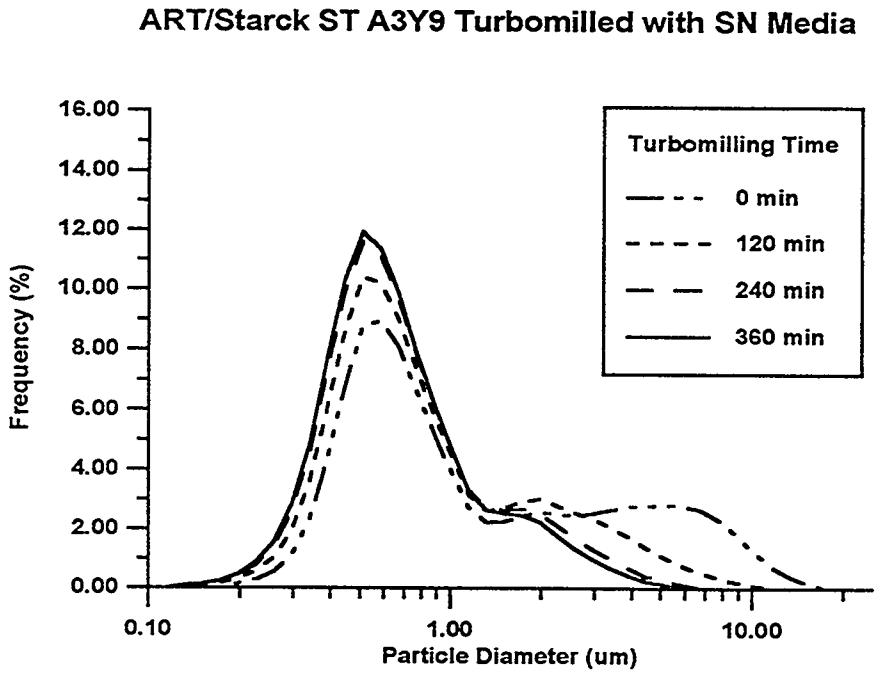

Figure 7. Particle size distribution of 50/50 ART/Starck ST A3Y9: As-received and turbomilled for 120, 240 and 360 min.

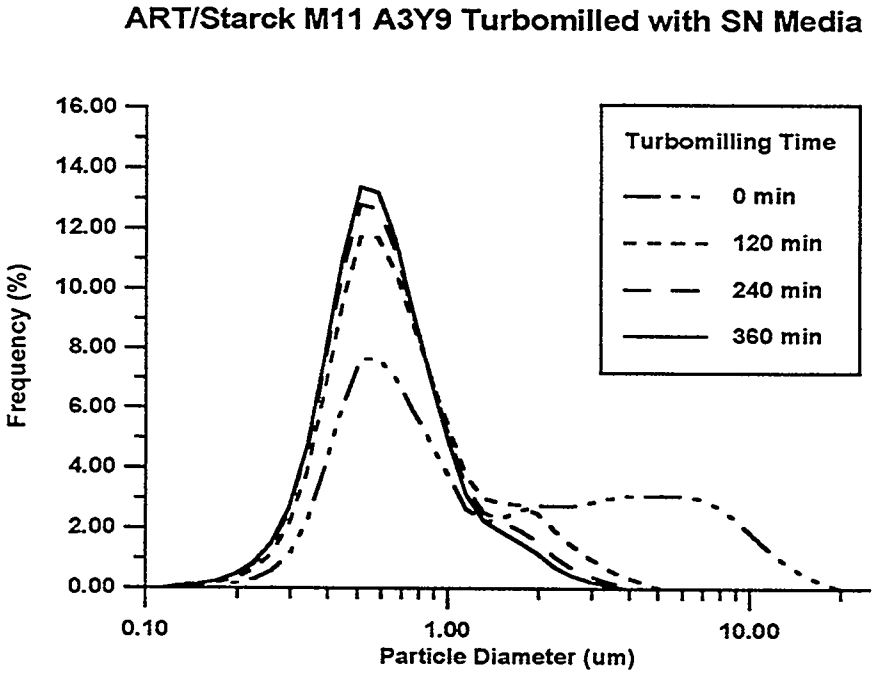

Figure 8. Particle size distribution of 50/50 ART/Starck M-11 A3Y9: As-received and turbomilled for 120, 240 and 360 min.

CHARACTERIZATION AND TESTING OF LOW-EXPANSION CERAMIC MATERIALS

V. M. Vaubert, K. Breder, and D. P. Stinton

Objective/Scope

Insulated exhaust portliners are needed in advanced diesel engines to increase engine efficiency by increasing the combustion temperatures and reducing the combustion heat that is lost through the head and into the water cooling system. Low-expansion materials have a potential for this application due to their very low thermal conductivity, extraordinary thermal shock resistance, and reduction of attachment stresses. Thermal shock resistance is critical because the complex shape of the portliners requires that they be cast into the metallic cylinder head. Functioning exhaust portliners are inaccessible after they are cast into cylinder heads, hence, must not require maintenance for the life of the head (~1 million miles). A contract has been placed with LoTEC, Inc. to develop cost-effective processes for the fabrication of portliners. LoTEC is investigating $Ba_{1+x}Zr_4P_{6-2x}Si_{2x}O_{24}$ (BS-25) and $Ca_{1-x}Sr_xZr_4P_6O_{24}$ (CS-50). Oak Ridge National Laboratory (ORNL) is assisting with the characterization and evaluation of the above compositions.

Technical Highlights

Casting of low-expansion ceramic portliners into cast iron requires a compliant layer that insulates the portliner from the high temperatures and absorbs clamping stresses that are created by the metal as it cools. Clamping stresses result because the coefficient of thermal expansion (CTE) of the metal is many times more than that of the ceramic. Straight-wall portliners have been successfully cast into aluminum without any compliant layer because of the low aluminum melting point. An investigation to evaluate the effect of three different portliners, two types of compliant layers and casting metal, on the casting behavior of ceramic portliners continued this period. The three variations of low-expansion portliners are a BS-25 material with a CTE of $1x10^{-6}$/°C, a low-modulus CS-50 material with a CTE of $3x10^{-6}$/°C, and a high-strength CS-50 material with a CTE of $3x10^{-6}$/°C. The two compliant layers being examined are a very porous, low-expansion ceramic that is fabricated at LoTEC and a fibrous material that is purchased commercially.

Aluminum cast CS-50 high modulus, CS-50 low-modulus and BS-25 portliners have been analyzed by computed tomography to reveal any cracking of the ceramic liner due to thermal shock or compression by the cast metal. Iron-cast, CS-50 medium density port-liners with compliant layer, were also scanned to detect cracks in the ceramic liner. Scans were taken horizontally every half-inch. Examples of C.T. scans of the aluminum tubes are shown on figure 1. Voids were found at the interface between two of the ceramic liners, CS-50 low modulus and BS-25, and the aluminum cast. These defects are located near the molten metal pouring zone. It appears that the aluminum solidified too fast and did not wet the entire ceramic surface. Cracks

in the ceramic were found for CS-50 low modulus in the region where the aluminum was very deformed, stress concentration due to localized clamping of the metal must be responsible for the ceramic failure. The thermal shock and thermal stresses generated during aluminum casting did not otherwise damage the ceramic liners. New tubes have been cast with higher temperature molten aluminum and will be evaluated during the next period. Examples of C.T. scans of port-liners with porous compliant layer and fibrous compliant layer are shown respectively in figure 2 and in figure 3.

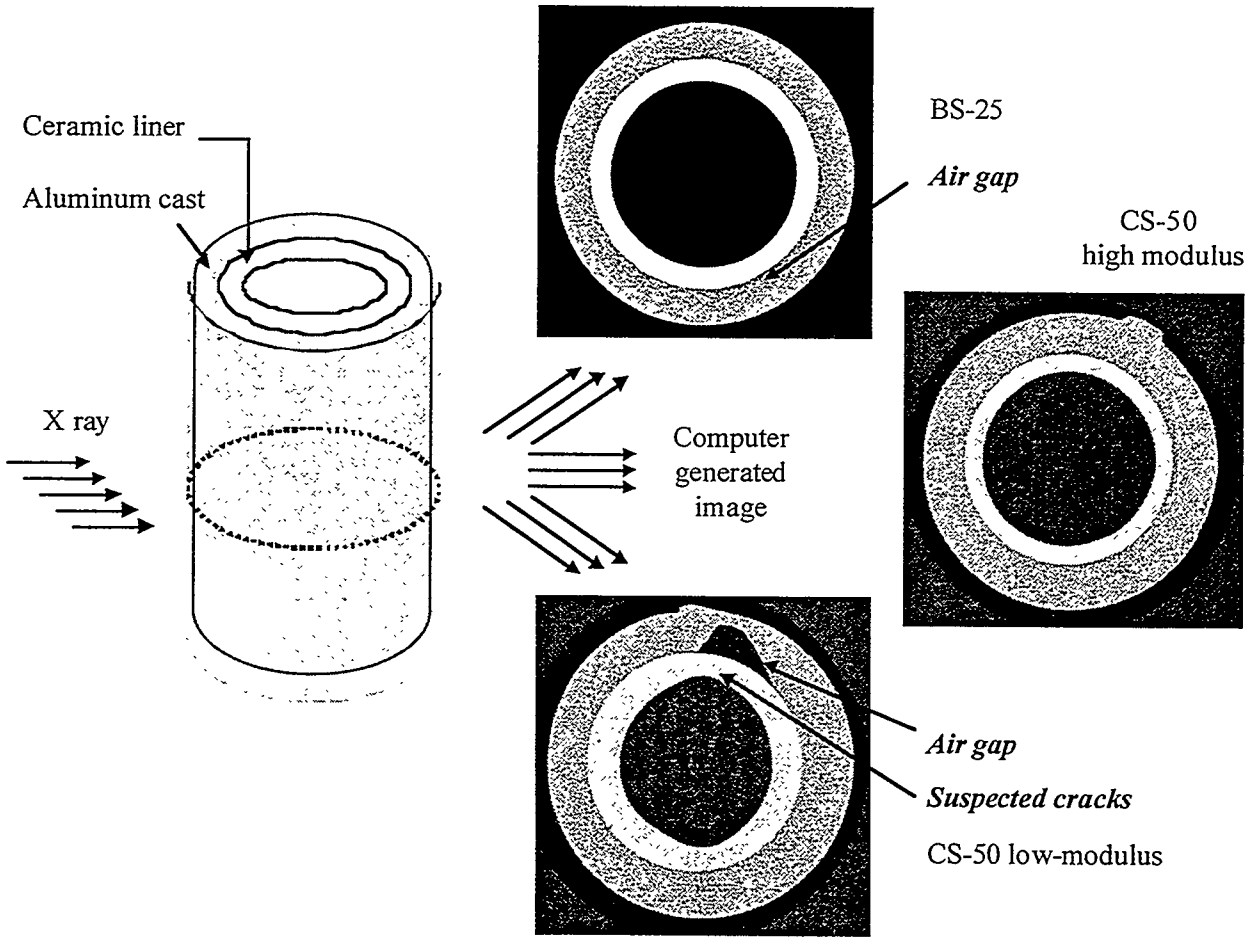

Figure 1: CT scans of aluminum cast portliners

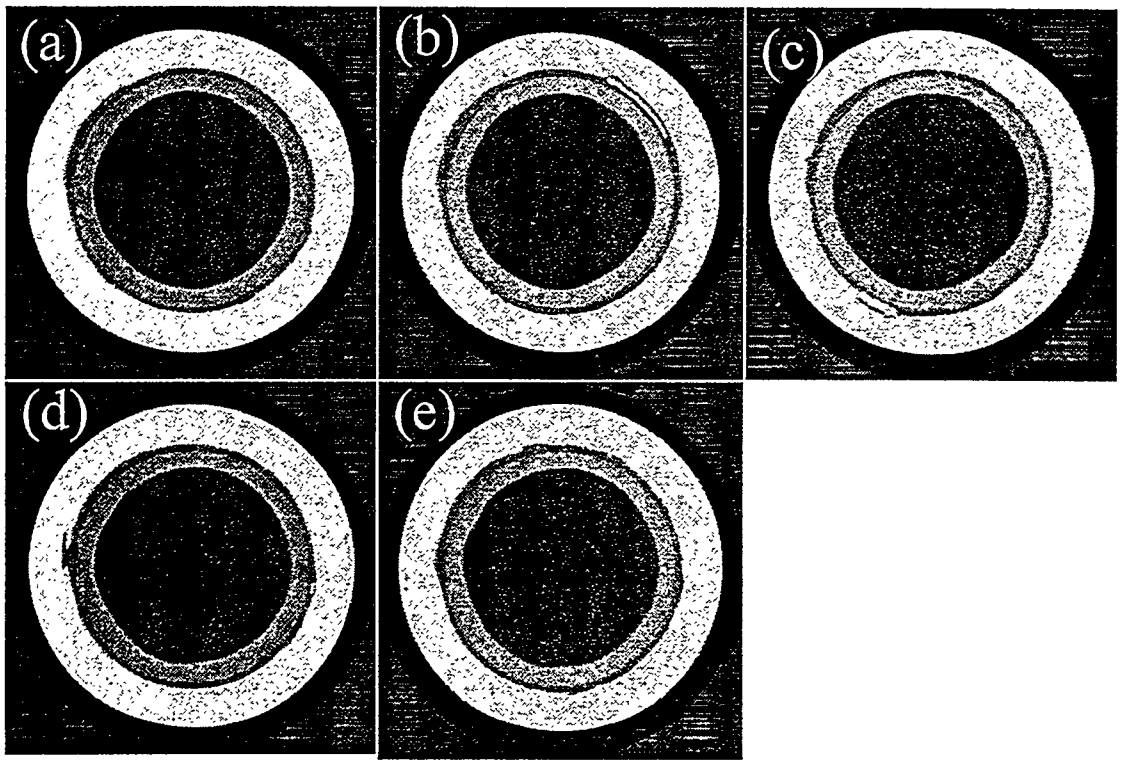

Figure 2: C.T. scans of CS50 medium density port-liner with porous compliant layer

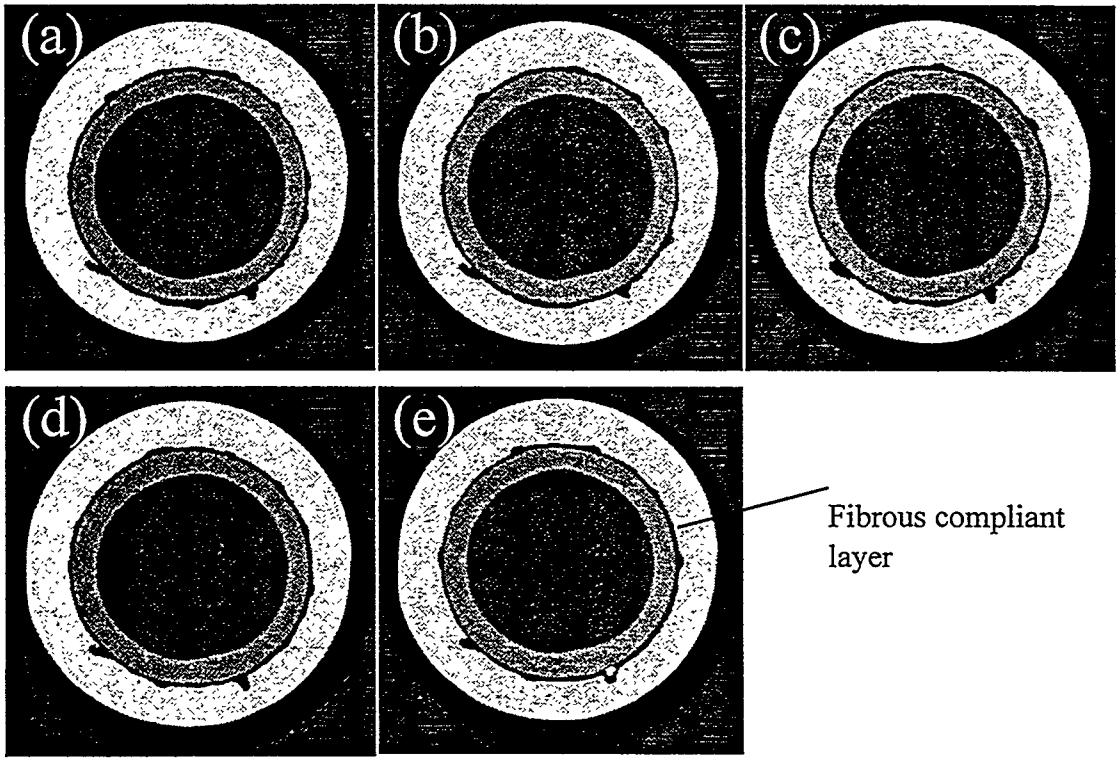

Figure 3: C.T. scans of CS50 medium density port-liner with fibrous compliant layer

For both port-liners no cracks were found in the ceramic liner. The compliant layers prevented failure of the ceramic liner by diminishing compressive stresses during cooling and by preventing direct contact between the liner and the molten metal during casting. However, in figure 1 (b) and (c), iron can be found very close to the ceramic liner, which in case of direct contact would have induced its failure. Increasing the density of the compliant layer would ensure a better protection of the ceramic from the molten metal. Though, the density should not be too high for the layer to still be compliant under the compressive stresses created by the metal as it cools.

In figure 2, we can see that the ceramic liner is intact and well protected from the metal cast. When in contact with heat, the fibrous compliant layer expands, preventing any molten metal from touching the ceramic liner. Buckling of the compliant layer indicates that the fibrous material expanded too much. Thinner compliant layer should result in less expansion, less buckling and better clamping of the ceramic liner inside the metal port.

Dye penetrant evaluation of the ports revealed two cracks on the aluminum surface for the port with CS-50 low modulus liner. However, these cracks could not be found with computed tomography. Non-destructive evaluation of the ceramic could not be performed by dye penetrant because the ceramic was porous and the penetrant could not be washed off.

During an attempt to remove the straight-walled portliners by cutting open the aluminum cast, the ceramic liner broke and separated from the aluminum. The ceramic surface presented few spots of aluminum indicating a poor wetting of the liner by the molten metal. The portliner was then successfully extracted by slowly melting down the aluminum. The iron-casts were cut open and the ceramic tubes remained intact after this operation. Mechanical properties of the port-liner will be remeasured and compared to the as-fabricated material in order to determine possible damage of the material. Any degradation of the mechanical properties resulting from metal casting would indicate that the thermal stresses were too high.

Characterization of the straight-walled portliner by computer tomography was very encouraging. There was no destructive crushing of the ceramic during cooling of the molten aluminum. However, the casting temperature needs to be increased to obtain a better wetting of the ceramic. Additionally, we need to evaluate the thermal insulation capacity of the NZP liners to insure that there will be no thermal degradation of the aluminum at operating temperature. C.T. scans also showed that there was no destructive crushing of the ceramic during cooling of the iron cast, and it pointed out possible improvements of the compliant layers. Optimization of the compliant layer/portliner combination will continue next period.

Development of NZP-Ceramic Based "Cast-in-Place" Diesel Engine Port Liners

Rama Nageswaran, Justin Cassell and Santosh Y. Limaye (LoTEC, Inc.)

Objective/Scope

The overall objective of this research is to develop sodium-zirconium-phosphate (NZP) ceramic based "cast-in-place" diesel engine port liners. Specific objectives are: (1) Development and optimization of the overall insulation system, (2) Refinement of the compliant layer formation process around the ceramic insulation system, (3) Development and adaptation of cost-effective powder and material fabrication processes, and (4) Creation of database of high temperature properties (stability in diesel exhaust environment, thermal cycling, thermal shock.)

Technical Progress

During the last semi-annual period, the final metal casting trials of straight tubes cast in aluminum and cast iron were completed. Particular attention was devoted to the casting of higher strength and higher density CS-50 cast in aluminum and cast iron. Furthermore, the casting of a solid cylinder in aluminum without a compliant layer was completed. Results from ORNL of CT scans conducted on straight tube port liners were received and analyzed. A few straight tubes cast in aluminum were sent to Cummins for diesel engine testing.

Finite element analyses of metal casting of BS-25 and CS-50 in gray iron and aluminum were conducted for complex S and Y-shaped exhaust ports. In all, 8 different model combinations were generated using MSC Nastran. With respect to the complex shapes, the much anticipated successes were achieved in metal casting trials involving both cast iron and aluminum. These trials included several successful castings of Y-shaped and S-shaped NZP port liners having 2 or 3 mm thick compliant layers. Yet again, the importance of a suitable compliant layer in obtaining crack-free "cast-in-place" complex shaped tubes was clearly inferred. Based on the results of finite element and metal casting iterations that paved the way for successful complex-shape exhaust port castings, a presentation was made at the American Ceramic Meeting in Cocoa Beach, FL. The following describes some of these activities in greater detail.

Metal Casting Trials

Straight Tubes:

The casting of straight tubes with cast iron or aluminum was concluded during this reporting period. The completion of straight tube casting served to satisfy three main objectives: 1) the final verification of finite element analysis, 2) the qualitative assessment of the new ceramic mat as a

stress mitigating compliant layer and an effective thermal barrier, and 3) the replication of "crack-free" CS-50 tubes of regular and high strength cast with two different types of aluminum(ductile and less ductile).

Previous FEA modeling yielded results which predict the failure of the NZP tubes when cast in aluminum without a compliant layer. Likewise, the aluminum was predicted to crack due to tensile stresses. As was noted, the highly ductile behavior of the A356 aluminum that has been used to cast the straight tubes is believed to cause the deviation from FEA predictions. A less ductile yet stronger aluminum and one that displays more linear elastic behavior was used to cast CS-50 medium strength tubes of 5 mm wall thickness. As a result of the lower ductility, the casting produced results that were in accordance with the FEA; both the CS-50 tube and aluminum surrounding the tube cracked. It was found, however, that a stronger CS-50 (high strength) can withstand the shrinkage stresses of the less ductile aluminum and thus produce crack-free ports. A CS-50 HD straight tube cast in such aluminum without a compliant layer is depicted in Figure 1.

From FEA analysis, it has been found that the tensile shrinkage stresses of the cooled metal increase as the ceramic wall thickness increases. In an effort to examine the behavior of aluminum at extreme tensile stresses, a solid NZP cylinder was cast in A356 aluminum. It was found after casting that the aluminum cracked while the NZP solid cylinder remained crack-free. Figure 2 exemplifies this situation. (In Fig. 2, the tubular appearance at the top is due to a 1" cut-out that was made for holding the solid cylinder in place during casting.) Through this exercise, it was determined that the tensile limit of the aluminum can be exceeded when cast, and thus shows a limit of the ability of A356 aluminum to yield around an NZP tube / solid rod. Such results corroborate with the stress analysis that determined survival of the NZP, where the compressive stresses of 211 MPa on the BS-25 MD cylinder were vastly lower than its compressive strength of 330 MPa. On the other hand, the model predicted the aluminum to fail, owing to tensile stresses of 251 MPa for the A356 aluminum that has a tensile strength of 235 MPa.

Included in the final straight tube casting trials was the refinement of casting straight tube port liners in cast iron with the commercial ceramic mat compliant layer. It has been established through numerous casting trials that straight tube NZP tubes can be cast in cast iron successfully using the commercial mat. In fact, several variations of the commercial compliant layer have been used to cast straight tubes in cast iron, and furthermore, all types have proved successful at producing "crack-free" tubes. These mat materials also have comparable physical, mechanical, and thermal properties with those of the LoTEC compliant layer. The optimum thickness of the mat compliant layer was ~3 mm also for the casting iron around ~ 4mm thick NZP tubes. (This requirement was established through finite element analysis of the metal casting situation also.)

Characterization and Testing of Cast-in-Place NZP Straight Tubes

An aluminum-cast CS-50 lined straight tube exhaust port without a compliant layer was sent to ORNL for CT scanning at various depths into the casting. The objective behind the CT scans was to determine if there was any cracking of the NZP, metal or both after casting. It was found from the CT scans that the NZP was not cracked, yet one scan did display that there was some cracking of the aluminum surrounding the NZP. A crack was found at the interface between the NZP and the aluminum, and it extended radially to the middle of the aluminum wall. (This is in agreement with FEA predictions of tensile stresses in the metal which are highest at the interface). Although the crack did not extend all the way to the exterior of the aluminum, it was surmised that the ductility of A356 aluminum does not fully insure against tensile cracking of the aluminum beyond a threshold. However, more detailed examination of the CTscan of this A-356 aluminum-cast CS-50 straight tube revealed that the crack originated from a casting defect (air gap) located at the interface between the CS-50 and the aluminum.

To verify that such cracking was indeed due to casting aberrations and not actually due to the excessive tensile stresses, more successfully cast tubes were sent to ORNL for further scanning. Subsequent CT scans of successfully cast-in-place NZP tubes with aluminum (A-356) and cast-iron around showed no signs of interior cracks. Figures 3(a) and (b) show CT scans of crack-free CS-50 tubes cast in aluminum and iron, respectively. It can be seen from these figures, that there are no cracks in the metal either. This result suggests that the origin of cracking in A356 was most likely due to pressure from unexpected outgassing (which manifests itself as the air gap in the CT scan) during the casting process.

Finite Element Analysis and Metal Casting of Complex Shaped Tubes

It may be recalled that attempts to cast metal around the complex shaped port liners, without a compliant layer, were not successful even for the case of ductile A356 aluminum casting. FEA modeling was undertaken to obtain stress predictions in order to enhance the success rate of crack-free castings with aluminum as well as cast-iron. Two principal complex shaped port liners are of particular interest to engine companies: i) the S-shape and ii) the Y-shape. The metal casting situation of both complex shaped port liners were modeled using FEA. Solid models of these complex shapes were generated using PT/Modeler and the FEA done using MSC-NASTRAN. For the FEA, ten-noded tetrahedral solid elements were generated using the auto mesher.

S-Shaped Port Liner

Due to the inherent simplicity of the S-shape port liner as compared to the Y-shape, the S-shaped port liner was used first for FEA and metal casting. FEA was conducted on BS-25 and CS-50 S-shaped port liners cast in either gray iron or aluminum without compliant layers, totaling four different cases. Material properties for the FEA analysis are in Table 1. In all cases, FEA predicted

failure of NZP due to excessive compressive stresses. As an example, it was found that for the case of a BS-25 S-shaped port liner cast in A356 aluminum, compressive stresses in the BS-25 were 385 MPa which exceeds its compressive strength (330 MPa). These results are summarized in Fig. 4.

To verify the FEA results, a BS-25 S-shaped port liner that was cast in aluminum without a compliant layer was examined carefully. As was predicted by the FEA, the ceramic port liner had barely cracked in the regions of highest compressive stresses. For the S-shaped port liner, the areas of high compressive stress were those at the regions of geometric transition. This is evident in comparing the stress contour plots of the FEA in Figure 4a (see arrow) of the S-shape with that of the actual metal casting in Figure 4b. As with aluminum, it was determined that the S-shaped port liners would fail when cast in gray iron without a compliant layer. It has since been verified that compliant layers of at least 3 mm thickness are needed for an S-shaped NZP port liner to be cast successfully in aluminum or gray iron. Figure 5 shows three S-shaped NZP port liners that were successfully cast in gray-iron with compliant layers. Based on stress predictions from FEA of the complex shapes, an appropriate compliant layer thickness, for preventing failure of the ceramic tube, is thought to be between 2.5 and 3.5 mm.

Y-Shaped Port Liner

The ability to model and cast S-shaped exhaust port liner was extended to that of the Y-shaped port liner. As was the case with the S-shape, the same four cases were modeled using FEA for the Y-shape. The Y-shape also exhibited regions of excessive compressive stresses. The results from FEA led to the conclusion that the Y-shaped port liner must certainly be cast with a compliant layer in order to mitigate catastrophic stresses. The regions that had the highest stresses were, expectedly, those with significant geometric transitions. One specific example is the zone where the two passages are separated and where the passages blend into one (see Fig. 6(b) that depicts Al. cast around NZP).

The following general observations could be made as far as the aluminum casting of the BS-25 and CS-50 tubes:

- Compressive stresses in the NZP were highest at regions of stress concentration.
- Tensile stresses in the A356 aluminum are below its failure limit (235 MPa).
- The extent of cracking corresponded to the magnitude of the FEA predicted stresses.

In comparing the S_{xx} normal stress contour plots of a BS-25 Y-shape cast in aluminum (Figure 6) with that of an actual BS-25 Y-shape cast in aluminum, it is evident that the regions of cracking are to be expected. Based on these results and previous metal castings, it was decided that a reasonably thick compliant layer would have to be used. Yet again, the 3mm thick compliant mat was used successfully to prevent failure of the BS-25 ceramic that was cast both in aluminum and

iron. Recently, a few more castings have been successfully made in order to confirm this result. Figure 7 shows three crack-free Y-shaped NZP lined exhaust ports that were cast in gray-iron.

Future Work

Final report in progress.

References

1) C.S.C. Lei, W.E.Frazier, and E.W Lee "The Effect of Hot Isostatic Pressing on Cast Aluminum," *JOM*, vol. 47 [11], 38-39 (1997).

Status of Milestones

Program on schedule.

Communications/Visits/Travel

1) Rama Nageswaran and Justin Cassell traveled to Cocoa Beach, FL to present a paper at the 22nd Annual meeting of American Ceramic Society.

Problems Encountered

None.

Publication/Presentation

1) R. Nageswaran, J. J. Cassell, S. Y. Limaye, and D. Stinton, "Fabrication of NZP-Ceramic/Metal Diesel Engine Exhaust Ports Using Finite Element Analysis as a Guiding Tool", Presented at the 22nd Annual Meeting of the American Ceramic Society held at Cocoa Beach, FL in Jan. 1998.

   A conference proceedings paper is also in the making.

Table 1: Measured / Compiled Material Properties Used for the FEA.

Properties	BS-25	CS-50	Aluminum A356 alloy	Gray Iron	Compliant Layer
Density, ρ (g/cc)	2.80	2.91	2.75	7.00	0.15
Elastic Modulus, E (GPa)	55.0	70.0	70.0	172.0	0.5
Poisson's ratio, ν	0.24	0.24	0.33	0.28	0.1
Tensile Strength, σ_t(MPa)	--	--	235	370	--
Compressive Strength, σ_c (MPa)	330	390	--	830	--
Thermal Expansion, α (ppm/°C)	1.0	3.0	21.4	12.1	3.18
Stress Free Temperature (°C)	--	--	300	800	--

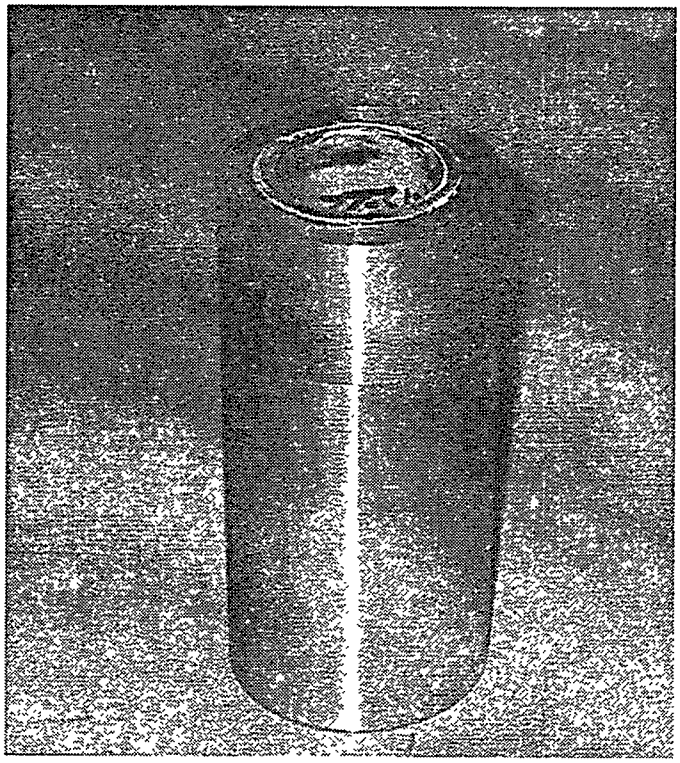

Figure 1. A 4 mm wall thickness CS-50 high strength tube that was successfully cast in ductile A-356 aluminum without a compliant layer.

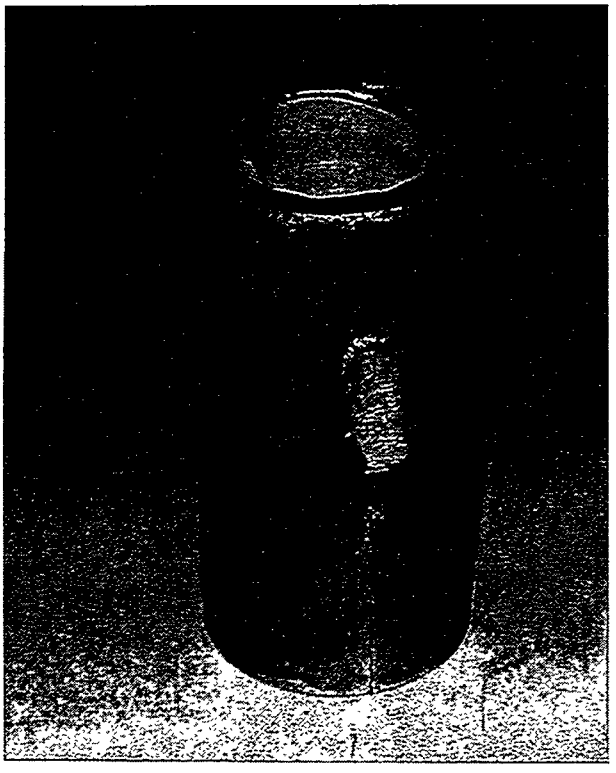

Figure 2. A crack-free BS-25 ***solid cylinder*** cast in aluminum showing cracking of aluminum due to excessive tensile stresses.

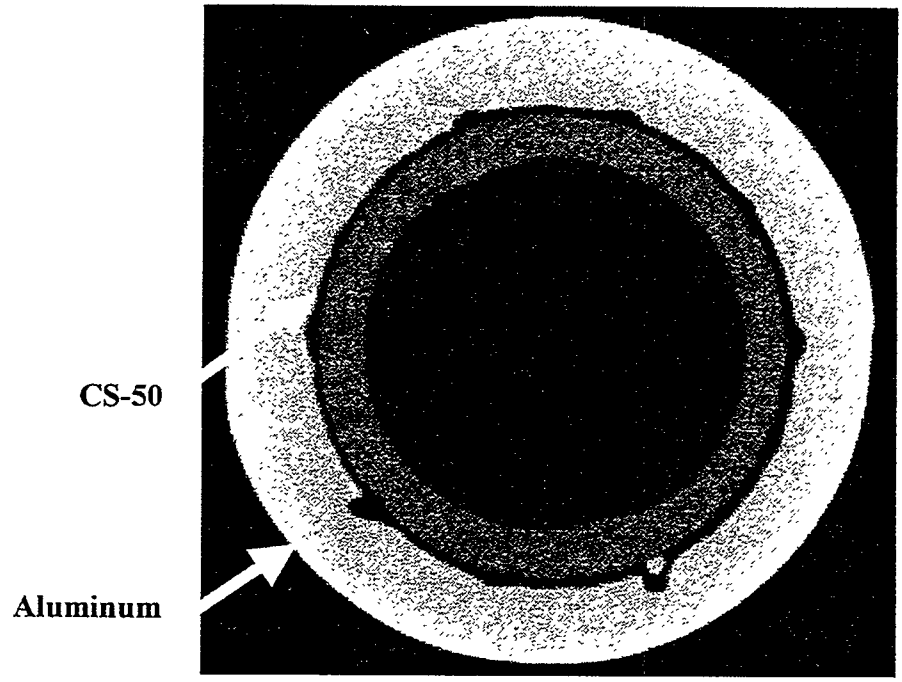

Figure 3a. CT Scan of CS-50 cast in aluminum without a compliant layer.

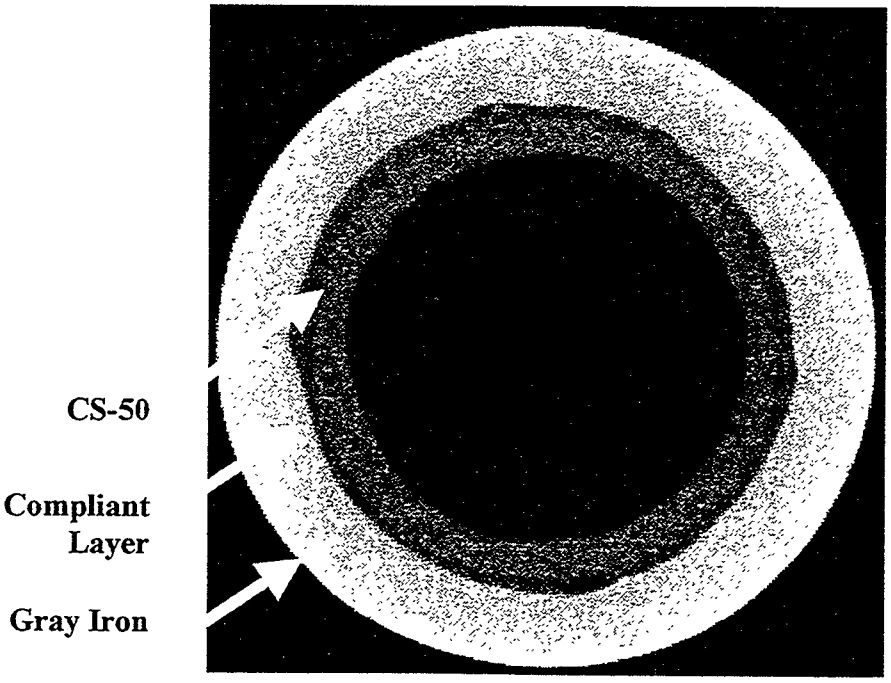

Figure 3b. CT Scan of CS-50 cast in gray iron with a 3 mm compliant layer.

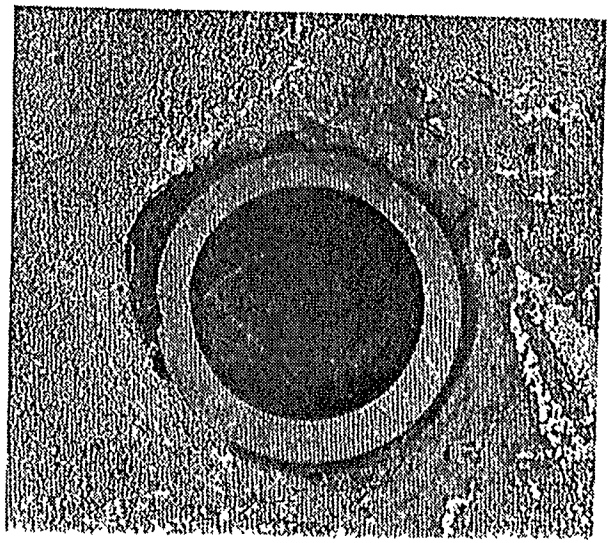

BS-25 cast in aluminum

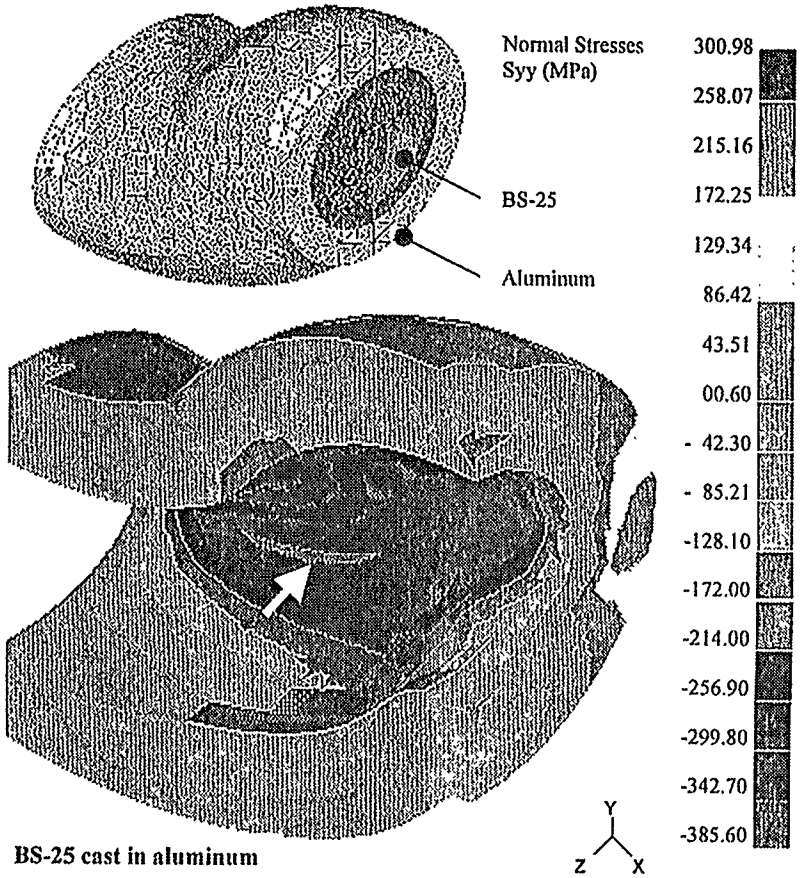

BS-25 cast in aluminum

Figure 4. (a) Actual S-shaped port liner casting exhibiting cracking at areas of high compressive stress as predicted by FEA; (b) Stress contour plot of a BS-25 S-shaped port liner cast in aluminum (arrow indicates region of maximum stress.)

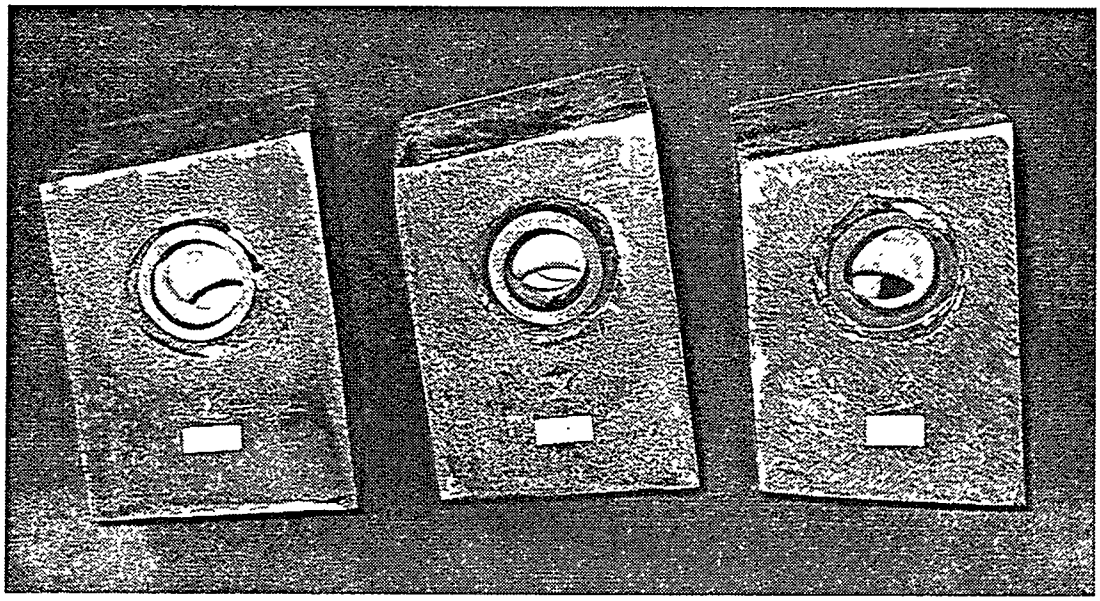

Figure 5. Evidence of crack-free gray-iron castings involving S-shaped NZP port liners with ~3mm thick compliant mats.

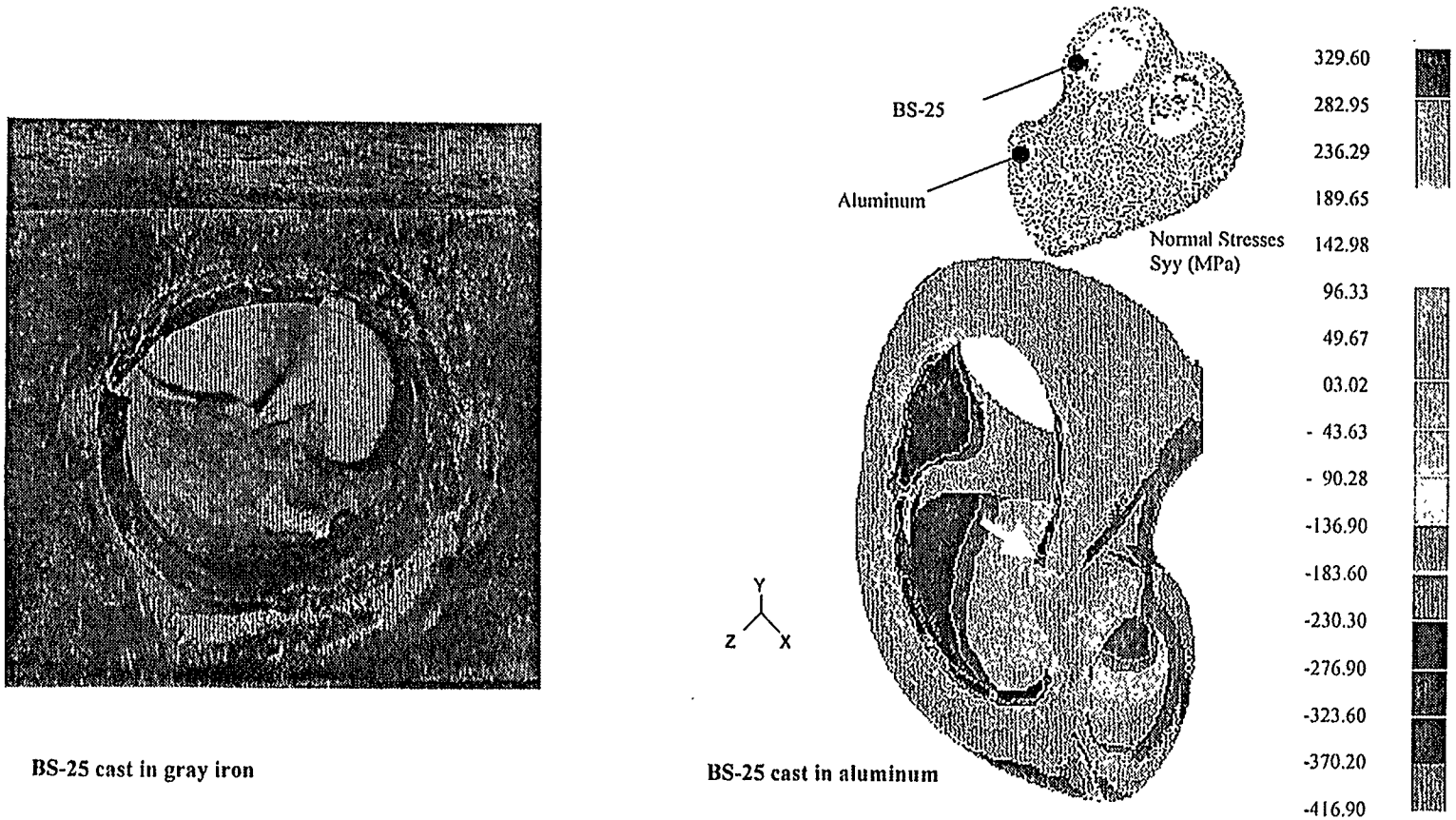

Figure 6. (a) Actual Y-shaped port liner casting exhibiting cracking at areas of high compressive stress as predicted by FEA; (b) Stress contour plot of a BS-25 Y-shaped port liner cast in aluminum (arrow indicates region of maximum stress.)

Figure 7. Evidence of crack-free gray-iron castings involving Y-shaped NZP port liners with ~3mm thick compliant mats.

ADVANCED MANUFACTURING TECHNOLOGY

DEVELOPMENT OF ADVANCED CERAMIC MANUFACTURING TECHNOLOGY

Subcontract No. 86X-SP234C

C.Burk, T.P. Leo, L.D. Lynch, B.J. McEntire - SGIC, Norton Advanced Ceramics
Y. Kalish, R. Begin - Detroit Diesel Corporation
C. Bida, M. Hauptman, L.E. Mains - Deco Grand, Inc.
M. Tricard, J. Hagan, D. Graham, J. Picone - Norton Company, World Grinding Technology Center
J. Kellogg - Centorr/Vacuum Industries
V.K. Pujari, W.T. Collins - SGIC, Northboro R&D Center
P. Parrish - BDM Federal, Inc.
T. Zahrah, S. Hollo - MATSYS, Inc.
A.E. Mascarin - IBIS Associates, Inc.
D. Wittmer - Wittmer Consultants

Report Prepared by
Vimal K. Pujari

Saint-Gobain Industrial Ceramics, Inc.
Northboro Research and Development Center
Goddard Road
Northboro, MA 01532

Semi-annual Technical Progress Report
October 1997 - March 1998

Objective/Scope

The objectives of this program are to design, develop and demonstrate advanced manufacturing technology for the production of ceramic valves. A production manufacturing process for a ceramic exhaust valve for DDC's Series 149 diesel engine is being developed under this program. Specific objectives are: (1) To reduce manufacturing cost by at least an order of magnitude over current levels; (2) To develop and demonstrate process capability values (C_{pk}) of 0.7 or less for all critical component attributes; and (3) To validate performance, durability, and reliability of this ceramic valve in rig and engine testing.

Technical Highlights

Task 1 - Component Design and Specification

This task has been completed.

Task 2. Component Manufacturing Technology Development

2a) Environmental Safety and Health

This task has been completed.

2b) Process Cost Modeling

This task has been completed.

2c) Process Control

i.) Milling and Spray Drying Process Control

This task has been completed.

ii) Continuous Sintering

This task has been completed.

iii) Machining

This task has been completed.

2d) Intelligent Process Control

This task has been completed.

Task 3 - Inspection and Testing

The viability of the three cost effective machining procedures, discussed in the previous bi-monthly reports (Task 2), is being evaluated by performing engine durability tests employing the mine haul cycle.

Consequently, 33 valves machined at Vendor A have been engine tested. After a few early failures (100-400 hours), attributed to relatively rough surface finish on the valve head (verified by subsequent fractography of the failed valves), the remaining 16 valves successfully completed the required 1000 hours of durability testing using the mine haul cycle. Based upon these tests, the surface finish specification on the valve head region has been modified with the concurrence of DDC. The same surface finish will now be required from all other machining vendors for the production demonstration set valves.

Seventeen valves machined by Vendor C have been supplied to DDC for engine durability testing following metrology and proof testing at NAC. These valves meet the newly defined surface finish specifications described above. DDC continued the rig testing with 16 Vendor A and 16 Vendor B valves to accumulate additional hours, and to evaluate various seat materials. Based upon the results of this testing effort, valve sub-assembly design features were optimized.

Task 4 - Process Demonstration

4a) This task has been completed.

4b) Final Demonstration

Production Demonstration of Ceramic Valves

As described in the previous bi-monthly report, the production demonstration set of NT551 valves have been finish machined at three vendor locations as stated below:

Vendor A - 150 valves
Vendor B - 100 valves
Vendor C - 30 valves

(a) Vendor A - CNC Profile Grinding
One hundred and fifty valves have been finish-machined using this approach. Briefly, this technique involves a high speed (>80m/sec) rough grinding to remove approximately 93% of the stock, followed by finish-machining using a superabrasive wheel. All 150 valves have been fully inspected and proof tested in accordance with DDC specifications. Based upon these measurements, process yield and reproducibility data have also been established.

(b) Vendor B - Centerless Grinding
One hundred fully finished valves have been received from Vendor B. Per DDC specifications, these valves have also undergone full inspection and proof testing. Eighty-seven fully qualified valves from this machining campaign are being shipped to DDC to initiate an additional 1000 hours of engine durability testing.

(c) Vendor C - Peel Grinding
Thirty Series 149 diesel valves finished in accordance with DDC specifications have also been received from Vendor C. These valves are in the process of being inspected/proof tested.

In addition, as a part of the production demonstration set, 30 (fully finished) valves each from Vendors "A" and "B" were previously supplied to DDC in order to (a) optimize various valve sub-assembly features, and (b) perform 1000 hours of engine durability tests which were successfully completed.

Thus, to date a total of 340 finish-machined valves have been produced and inspected. Hence, this completes Milestone #6 (fabricate 320 final design valves).

The total machining times at Vendor "A" and "B" have also been documented in order to estimate the process improvement and corresponding cost reduction.

Communications/Visits/Travel

Communication on regular basis with WGTC, Chand Kare Technical Ceramics and Detroit Diesel Corporation.

Problems Encountered

None.

Durability of Diesel Engine Component Materials

Peter J. Blau, R. L. Martin, and B. DuMont
Oak Ridge National Laboratory

Objective/Scope

The objective of this effort is to enable the development of more durable, low-friction moving parts in diesel engines for heavy vehicle propulsion systems by conducting friction, lubrication, and wear assessments and analyses on advanced materials, surface treatments, and coatings. The scope of materials and coatings is broad and includes any metallic alloy, intermetallic compound, ceramic, or composite material which is likely to be best-suited for the given application. Parts of current interest include valves, valve guides, and fuel injector plungers. The major technical approach of this work is to use bench-scale simulations of the rubbing conditions in diesel engine environments to study the accumulation of surface damage, and to correlate this behavior with the properties and compositions of the surface species. The effects of mechanical, thermal, and chemical factors on wear and friction are being determined and will be used to refine material selection strategies for durability-critical engine components.

Technical Highlights

Evaluation of the friction and wear of candidate valve guide materials. To achieve the objectives of this task, we are making use of the tribology laboratory at ORNL which contains a number of specialized friction, lubrication, and wear bench-tests designed to help study the relationship between the properties of materials and their performance under surface contact conditions. Some of these testing systems are designed to simulate specific types of operating conditions, others are designed for fundamental studies of friction and wear, and still others conform to ASTM wear testing standards. A commercial reciprocating wear testing machine has been specially modified to study the response of diesel engine valve stems to rubbing contact with candidate valve guide materials.

A schematic illustration of the testing geometry we have developed is given in Fig. 1. This testing geometry evolved incrementally over the last six months based on an extensive series of tests first using a single flexure bar-on-cylinder geometry. That configuration had alignment problems which produced uneven wear damage, and the new twin-bar-on-cylinder arrangement shown in Fig. 1 has proven more stable. The upper bar fixture has been modified to improve the supply of lubricant to the specimens during the tests.

Diesel engine valves have been obtained from Caterpillar, Inc., and cut sections of them are being used as one half of a rubbing pair against silicon nitride materials. Tests are being conducted both dry and in the presence of heated diesel engine lubricants in order to establish the range of behavior ranging from lubricant-starved conditions to well-lubricated conditions. In addition to the silicon nitride materials, we have obtained samples of ceramic composite materials developed by Ford Motor Company, Scientific Research Laboratory, and will be evaluating them as well.

Dr. Brigitte Dumont joined this project in December 1997. Dr. Dumont was appointed a post-doctoral fellow by the Oak Ridge Institute of Science and Engineering (ORISE). She has a doctorate in Physics and Chemistry from the University of Burgundy, Dijon, France, and has

worked as an engineer at the Creusot-Loire Industrie, Center of Materials Research. Her background includes experimental wear studies of hard coatings for cutting tools and the use of acoustic emission in monitoring wear. Her task is to help develop valve guide materials screening methodology, including the precision measurement of wear by various techniques.

Future Plans

a) We plan to conduct a series of twin-bar-on-cylinder friction and wear tests on candidate valve guide materials both lubricated and dry, to simulate starved conditions.

b) A visit is planned to Cummins Engine Company, Columbus, Indiana, to identify and define future cooperative research efforts in materials tribology aimed at other parts of the valve train and the fuel injection system.

Status of Milestones

On schedule.

Communications/Visitors/Travel

None

Problems Encountered

None

Publications and Presentations

None

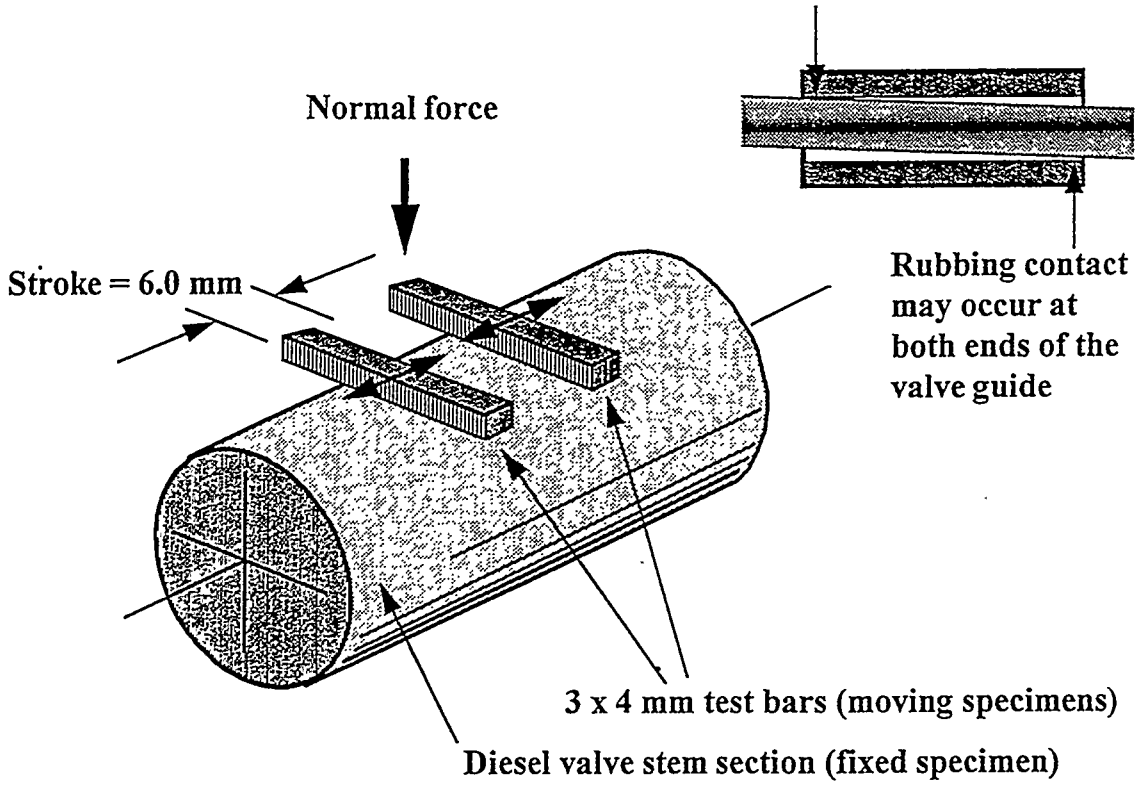

Figure 1. The twin-bar-on-cylinder test configuration simulates the concentrated contact conditions that a valve might experience due to axial misalignment with its guide. The advantage of this test configuration is that it uses standard ceramic flexure specimens along with actual valve stem sections.

HIGH-SPEED, LOW-DAMAGE GRINDING OF ADVANCED CERAMICS

Joseph A. Kovach
Michael A. Laurich
Eaton Manufacturing Technologies Center
Willoughby Hills, Ohio 44094

Stephen Malkin
University of Massachusetts
Amherst, Mass. 01003

Objective/Scope

The overall objective of the **H**igh **S**peed **L**ow **D**amage (HSLD) grinding project is to develop a single step, roughing-finishing process suitable for producing high-quality advanced ceramic components at high material removal rates and at substantially lower cost than traditional, multi-stage grinding processes. Initial implications from Phase I have suggested that HSLD grinding of Si_3N_4 is technically feasible. Accordingly, to achieve the overall program objective, the Phase II effort is focused on:

1.0 Continued expansion of the HSLD science base

2.0 Further development of the enabling HSLD technologies required for successful implementation, and

3.0 Economic analysis of the HSLD production cost drivers.

Technical Progress

This semi-annual report summarizes technical progress achieved during the period from October 1, 1997 to March 31, 1998. The report describes activities at the Eaton Manufacturing Technologies Center. A technical overview is presented in the following areas:

1.0 Economic analysis of the HSLD production cost drivers

Model Overview

The model will predict finishing costs for a single OD plunge grinding operation over a range of material removal rates and wheel speeds. Other parameters are treated as constants. The model is constrained to find the maximum number of parts that can be produced on one machine in the total number of hours available.

Outputs from the model as functions of material removal rate and wheel speed include:

- Total cost per piece
- Wheel cost per piece
- Labor cost per piece
- Overhead cost per piece
- Capital cost per piece (10 year depreciation)
- Wheel cost per piece
- Dressing roll cost per piece
- Number of pieces produced
- Number of pieces per dress
- Number of wheels required
- Grind time per piece
- Total cycle time per piece

Model Development

A total cost per piece is determined as a function of the various costs associated with the manufacturing process: capital, labor, and consumables. Two approaches can be taken to constrain the model based on capacity. One method is to set a production target and then determine the number of machines required. This model, instead, was constrained by fixing capital at one machine and determining the number of pieces that could be produced.

Following is the development of the expressions used to compute the costs per piece and maximized production on one machine. The equations were subsequently coded in Matlab and integrated with a graphical user interface to create an interactive cost model.

The first expression is the grinding time required for one piece. For an OD plunge operation, the expression is simply the amount of material to be ground away divided by the material removal rate.

$$t_{grind} = \frac{\pi \cdot RadialStockEnvelope \cdot (InitialWorkDiameter - RadialStockEnvelope)}{SpecificMaterial\,\mathrm{Re}movalRate}$$

Intuitively, the higher the material removal rate, the less time is spent grinding the part. However, increasing the material removal rate also accelerates the rate at which the wheel wears away. Increasing the wear rate then requires more frequent dressing and wheel changes - - reducing the amount of time available to make parts and increasing costs. Therefore, it is important to understand the relationship between process parameters and the wheel wear rate. Relating the amount of material ground away to the amount of wheel wear is the G-Ratio (grinding ratio).

$$G-Ratio = \frac{VolumeMaterialGroundAway}{VolumeWheelWornAway}$$

G-Ratios were determined experimentally for an OD plunge of NT551 with a 240 grit resin bonded wheel [D240-100-UI841]. A water soluble oil, Cincinnati Milacron CX-270 (an experimental version of the fluid now sold as Quantalube

270) diluted at a ratio of 12:1 was used as the grinding fluid. Fluid was supplied at 9.7 GPM at 33 PSI using a standard nozzle design.

A schematic of the approach used to determine wheel wear is presented in Figure 1. The grinding wheel had a width of approximately one half inch. The grinding contact width was kept at 0.400 inches to allow a portion of the wheel to remain untouched and serve as a datum to measure wheel wear (Step 1). To avoid grinding off the datum, each subsequent plunge into the specimen was stopped 0.005 inches radially from the previous cut. After a grinding test, the entire wheel width was then lightly plunged into a S/RBSN bar (Step 2). If the wheel had worn during the test, a step would be imprinted onto the bar. This step was measured on an optical comparator to determine the gross radial wheel wear (Step 3). G-Ratio values were calculated after grinding away 3.0 in^3 of material.

Table 1 and Figure 2 illustrate the G-ratio data over a range of material removal rates and wheel speeds. Notice that as material removal rate is increased, the G-Ratio goes down. However, as wheel speed is increased, the G-Ratio can be improved by 3X, even at high material removal rates. From this data, an expression to predict the G-Ratio as a function of material removal rate and wheel speed was derived:

$$G-Ratio = [-31.408 \cdot MaterialRemovalRate + 44.713] \cdot e^{(0.0001 \cdot WheelSpeed)}$$

Using the G-Ratio equation based on wheel speed and material removal rate, and the requirement that the wheel should be dressed after a maximum amount of radial wheel wear has been achieved, the number of pieces per dress can be calculated.

$$NumberofPiecesperDress = G-Ratio \cdot \frac{InitialWheelDiameter^2 - WornWheelDiameter^2}{InitialWorkDiameter^2 - FinalWorkDiameter^2}$$

The total time to make one piece is comprised of loading and unloading the part, an average value for setting up the machine, time actually spent grinding the part, and an averaged time spent dressing the wheel:

$$TimeperPiece = t_{loadtunload} + \frac{t_{setup}}{LotSize} + t_{grind} + \frac{t_{dress}}{NumberofPiecesperDress}$$

Given the total number of hours available to make parts and the just determined total time per piece, the number of pieces that can be produced in a year is:

$$TotalPiecesMade = \frac{TotalTimeAvailablefor\,Production}{TimeperPiece}$$

TotalPiecesMade represents the total number of pieces that were processed on the machine. To determine the number of good parts produced, this number must be modified by the scrap factor.

$$NumberofGoodPieces\,\mathrm{Pr}oduced = (1 - ScrapRate) \cdot TotalPiecesMade$$

Further utilization of the G-Ratio equation can predict the number of wheels that will be required in grinding the total production run.

$$NumberofWheels = \frac{TotalPiecesMade}{G - Ratio} \cdot \frac{InitialWorkDiameter^2 - FinalWorkDiameter^2}{InitialWheelDiameter^2 - FinalWheelDiameter^2}$$

Depending on the efficiency and other requirements of the dressing process, it may require several "dressing media" per wheel. The exact number would be based upon dressing method and experience.

$$NumberofRolls = NumberofRollsperWheel \cdot NumberofWheels$$

The capital, wheel and roll costs per piece are functions of the cost of each respective item, the number of each required (recall that capital was constrained to one machine) and the number of good pieces produced. Capital cost per piece is also dependent on the depreciation rate, which was assumed to be 10 years for this model.

$$CapitalCostperPiece = \frac{MachineCost}{DepreciationRate \cdot NumberofGoodPieces\,\mathrm{Pr}oduced}$$

$$WheelCostperPiece = \frac{WheelCost \cdot NumberofWheels}{NumberofGoodPieces\,\mathrm{Pr}oduced}$$

$$RollCostperPiece = \frac{RollCost \cdot NumberofRolls}{NumberofGoodPieces\,\mathrm{Pr}oduced}$$

Labor and overhead costs are functions of the amount of time spent making a part. Multiplying the *TimeperPiece* by the appropriate cost rate gives the labor and overhead costs per piece. This model assumed that one operator would be assigned to the one machine.

$$LaborCostperPiece = TimeperPiece \cdot LaborRate$$

$$OverheadCostperPiece = TimeperPiece \cdot OverheadRate$$

Finally, a total cost per piece can be calculated by summing the individual contributing costs:

$$TotalCostperPiece = CapitalCostperPiece + WheelCostperPiece + RollCostperPiece + LaborCostperPiece + OverheadCostperPiece$$

Input Data

Table 2 details the input variables to the model and values selected to represent a nominal operating condition. A centerless plunge operation using a 240 grit resin wheel grinding Norton NT551 was selected for this scenario.

While all of the assigned values are arbitrary, they were selected as reasonable values for a one shift operation to grind blanks that are either *near net* or have been processed leaving a *finishing* stock envelope. Also, it was assumed that one operator would be assigned to the one machine.

The total number of hours was based on one annual shift (2080 hours total available). After subtracting out vacations, holidays, downtime and other non-production periods, 1,600 hours remain. A value of 1,600 hours is on par with industrial engineering studies of typical manufacturing environments representative of this scenario which indicate that a machine is utilized roughly 400 minutes out of every 480 minute shift.

It should be cautioned that the G-ratio data used in the model is specific to this wheel grit size and bond type, material, coolant type and supply. Further, the model should be limited to the range of wheels speeds [6,000 - 18,000 ft/min] and material removal rates [0.1 - 1.0 in^3/min/in] evaluated experimentally.

Sensitivity to the following parameters was investigated:
Labor Rate:

1. $10 / hour, 0% overhead rate (low)
2. $15 / hour, 80% overhead rate (nominal)
3. $20 / hour, 150% overhead rate (high)[1]

Dressing Time

4. 20 seconds (low)
5. 2 minutes (nominal)
6. 15 minutes (high)

Results

Tables 3 and 4 with Figures 3 through 12 summarize the cost per piece and annual throughput data for the six cases.

Figures 3 and 4 present graphs of the costs per piece and production rates for the nominal case (2 minute dressing time, nominal labor rate). Figure 3 illustrates that at conventional wheel speeds (6,000 ft/min), the faster material is removed, the more it costs. Increasing the material removal rate from a conventional level (0.1 in^2/min) to a high material removal rate (1.0 in^2/min) results in more than a doubling of the cost per piece. However, as wheel speed is increased, cost go down. At the high material removal rate, by going from conventional wheel speeds (6,000 ft/min) to 18,000 ft/min reduces the cost by

[1] Recognize that all of these overhead values are low when compared to typical industrial values. However, since this cost model already includes many overhead components, these values are appropriate.

more than half. Observe that the slopes of the curves are different for each material removal rate. The least cost approach is to grind at 0.5 in^2/min using wheel speeds over 13,000 ft/min.

Figure 4 illustrates the number of pieces that can be produced on one machine at the various material removal rates and wheel speeds. Of interest again is the effect of material removal rate at the conventional wheel speed of 6,000 ft/min. The highest material removal rate results in the fewest number of pieces being produced on an annual basis. Insight into an explanation is given by the G-ratio relationships as presented in the form of parts per dress summarized in Table 5.

Parts per dress is a measure of the number of pieces that are ground between wheel dressings. In this model, a dressing operation is required when the wheel has been worn away some radial distance. This indicator relates to a dulling of the grains or gross bond fracture due to excessive forces that could be remedied by dressing. From the experimental wheel wear data, G-ratios were determined as functions of material removal rate and wheel speed. Using G-ratios, stock envelope, wheel diameter and part diameter, the number of pieces per dress can be predicted.

Table 5 indicates the dressing frequency is three times as often for the high versus lowest material removal rate. The lowest material removal rate, of course, wears the wheel the least and has the highest pieces per dress. The lowest material removal rate, in general, resulted in more pieces produced than the high material removal rate, but less than the middle removal rate. A material removal rate of 0.1 in^3/min/in is too slow to make a lot of parts. It appears as if at 0.5, there is a good balance between dressing frequency and wear rate, hence the highest production rate.

It is important to recognize, however, that only 48 pieces per dress could be achieved using conventional conditions (0.1, 6,000 ft/min). However, by increasing wheel speed to 18,000 ft/min, the material removal rate could be increased 10 times while still obtaining 51 pieces per dress.

Increasing the wheel speed to 18,000 ft/min illustrates how the pieces per dress can be increased by more than three times at all three material removal rates. Once again, at the lowest material removal rate, dressing is not the production limiting issue when compared to the relatively slow pace of grinding. Referring to Figure 4, at approximately 11,000 ft/min, the material removal rate can be increased from 0.1 to 1.0 because the wear rate has been reduced through higher wheel speeds, increasing production. Although from cost per piece and production perspectives, it is still cheaper and more productive to grind at 0.5. Closer examination of the data with a finer step in material removal rate indicates that about 0.7 in^2/min is the ideal material removal rate for this scenario in terms of quantity parts produced and total cost per part.

Effects of Dressing time

By increasing wheel speed, the rate at which the wheel wears out decreases. As expected, increased wheel life results in more pieces per dress, higher output and lower per piece cost. However, depending on the speed of the dressing procedure, the per piece costs and annual production rates can vary significantly.

By changing from a two minute dressing cycle (Figure 3) to a 20 second dressing cycle (Figure 5), costs are reduced, on average by 10-12% (Table 3). Significant gains can be realized in production (Table 4, Figure 6 compared against Figure 4), especially for a setup that requires extensive dressing (6,000 ft/min, 1.0 in^3/min/in). For this case, the number of pieces produced can be increased a factor of nearly three.

In many applications, the dressing time can approach the 15 minute limit. Compared to the nominal dressing time of two minutes (Figure 3), the cost per piece (Table 3, Figure 7) nearly doubles at the high material removal rate while the production quantity (Table 4, Figure 8 compared against Figure 4) is reduced by 20-25%.

Effects of labor rate

Figures 9 and 10 document the total cost per piece for low and high labor rates respectively. As described previously for the nominal labor rate case, as wheel speed was increased, it became cost effective to increase the material removal rate. Comparing Figures 9 (low labor rate) and 10 (high labor rate) with Figure 3 (nominal labor rate), shows that the wheel speed required to increase material removal rate varies. To illustrate why this is so, refer to Figures 11 and 12.

Figures 11 and 12 are plots of costs (total cost per piece, labor cost per piece, consumables cost per piece and capital cost per piece) versus material removal rate for 6,000 and 18,000 ft/min respectively. Figure 11 shows that for low wheel speeds, the consumables cost is the dominant contributor to the total cost per piece. This behavior was also observed for the low and nominal labor rates at each of the three wheel speeds. Also, notice the minimal contribution of the capital costs.

As the wheel speed was increased to 18,000 ft/min at the high labor rate (Figure 12), for low material removal rates, labor costs dominate since the wheel is being utilized effectively. Once the material removal rate becomes sufficiently high to cause rapid wheel wear, consumables begin to dominate. By increasing material removal rate, the production rate is sufficient to cost effectively utilize labor, however, the consumables content of the total price increases continuously. Therefore, it is critical to increase wheel speed to extend the life of the wheel.

Further analysis of Figure 12 shows that the minimum cost occurs at a material removal rate of 0.5 in^2/min. The trade-off of speed versus wheel life appears to

be balanced at this point. However, should improvements be made in the process (more durable wheel bond systems, improved coolant and delivery, etc.), high material removal rates could be cost-effectively achieved.

Summary

The feasibility of a high-speed, low-damage grinding process for silicon nitride has been demonstrated. As illustrated in Figure 13, at sufficient wheel speed, material can be removed with no resultant degradation in strength - - at high material removal rates. (Provided that the grinding system - - bond type, grit size, balancing, coolant, etc. - - have been properly setup.

In general, increasing wheel speeds will:

- Reduce grinding forces
- Improve surface finish
- Increase wheel life
- Reduce bulk workpiece temperatures
- Allow for high material removal rates
- Meet or exceed all baseline material properties

From the economic analysis of the HSLD production cost drivers, as presented in this report, it was shown that by merely increasing the material removal rate from 0.1 to 1.0 in^3/min/in without increasing wheel speed, more than doubles the cost per piece while reducing production by over 25%.

For a material removal rate of 1.0 in^3/min/in, increasing wheel speed from 6,000 to 18,000 ft/min:

I. Decreases total cost per part by 67%
II. Increases production rate up to 3X
III. Allows cost effective labor utilization in high labor rate environments

Therefore, high wheel speeds must be employed.

In examining the graphs of cost per part and annual production versus material removal rate, it appears as though even greater benefits could be realized by increasing wheel speed beyond 18,000 ft/min. During development of the HSLD science base, wheel speeds as high as 25,000 and in certain cases, 35,000 ft/min were evaluated. However, 18,000 ft/min appears to be an upper wheel speed limit for readily available resin and vitrified bonded wheels. Above 18,000 ft/min, these bond types are subject to failure modes such as exceeding the hoop strength or thermally softening. While metal bonds can be stronger and less thermally sensitive, they are difficult to dress. With advances in bond technology, higher wheel speeds should be attainable, further reducing costs and increasing production.

Realize however, that when approaching these high speeds, extra attention must be paid to the entire grinding system - - machine capability including stiffness and damping, extremely fine balancing, precise truing, and sufficient coolant introduction. Failure of any one of these "support" technologies will prevent realizing the benefits of high speed grinding.

2.0 Final Report

The Phase II final report is currently being assembled and should be completed by July 31, 1998.

Status of Milestones

In an effort to complete the final report, a no-cost extension has been granted to continue the program until July 31, 1998.

Communications/Visits/Travel

J. Kovach attended the Annual CCM meeting in Dearborn, October 28 - 30, and presented a summary of the HSLD Phase II program activity.

Problems Encountered

Eaton is in the process of "phasing-down" the Manufacturing Technologies Center. This has slowed program progress, but should not affect completion of the final report.

Publications

"High-Speed, Low-Damage Grinding of Advanced Ceramics" - Extended abstract and presentation published in the Annual CCM proceedings, October 28 - 30, 1997.

Wheel Speed (ft/min)	Material Removal Rate (in^3/min/in) 0.1	0.5	1.0
6,000	65	49	
12,000	163	98	65
18,000	195	163	140

Table 1. Experimental G-Ratio data as function of wheel speed and material removal rate (240 Resin, NT551).

Model Variable	Nominal Value
Machine cost	$350,000
Wheel Type	240 Resin
Wheel Cost	$20,000
Wheel speed - low	6,000 ft/min
Wheel speed - high	18,000 ft/min
Wheel diameter	12 inch
Bond thickness	1/4 inch
Dressing roll cost	$1,200
Number of rolls/wheel	1
Dressing frequency	0.0001 inch
Dressing time	2 min.
Material type	NT551
Radial stock envelope	0.005 inch
Final part diameter	0.375 inch
G-Ratio	Calculate as function of Vs, Q'w
Material removal rate - low	0.1 in^2/min
Material removal rate - high	1.0 in^2/min
Scrap rate	5%
Lot size	N/A
Number of hours per year	1,600
Setup time	N/A
Load+Unload time	2 sec
Labor rate	$15/hour
Overhead rate	80% O.H.

Table 2. Variables in cost model and values for the nominal case.

	0.1 in^2/min	0.5 in^2/min	1.0 in^2/min
	Nominal case - 2 minute dressing cycle, nominal labor rate		
6,000 ft/min	$0.29	$0.35	$0.70
12,000 ft/min	$0.19	$0.21	$0.40
18,000 ft/min	$0.14	$0.13	$0.23
	20 second dressing cycle		
6,000 ft/min	$0.26	$0.30	$0.62
12,000 ft/min	$0.18	$0.18	$0.35
18,000 ft/min	$0.13	$0.12	$0.21
	15 minute dressing cycle		
6,000 ft/min	$0.51	$0.66	$1.40
12,000 ft/min	$0.32	$0.38	$0.78
18,000 ft/min	$0.21	$0.23	$0.44
	Low labor rate		
6,000 ft/min	$0.25	$0.32	$0.66
12,000 ft/min	$0.16	$0.18	$0.37
18,000 ft/min	$0.11	$0.11	$0.21
	High labor rate		
6,000 ft/min	$0.34	$0.39	$0.77
12,000 ft/min	$0.24	$0.24	$0.44
18,000 ft/min	$0.18	$0.15	$0.27

Table 3. Total cost per piece as functions of dressing cycle and labor rate.

	0.1 in^2/min	0.5 in^2/min	1.0 in^2/min
	Nominal Case - 2 minute dressing cycle		
6,000 ft/min	0.71	0.91	0.56
12,000 ft/min	0.83	1.23	0.86
18,000 ft/min	0.91	1.52	1.22
	20 second dressing cycle		
6,000 ft/min	0.96	1.74	1.57
12,000 ft/min	0.99	1.89	1.87
18,000 ft/min	1.01	1.99	2.09
	15 minute dressing cycle		
6,000 ft/min	0.24	0.19	0.09
12,000 ft/min	0.36	0.33	0.17
18,000 ft/min	0.51	0.53	0.29

Table 4. Parts produced per year (in millions) as function of dressing cycle.

	0.1 in^2/min	0.5 in^2/min	1.0 in^2/min
6,000 ft/min	48	33	15
12,000 ft/min	87	61	28
18,000 ft/min	159	111	51

Table 5. Pieces per Dress - Nominal Case

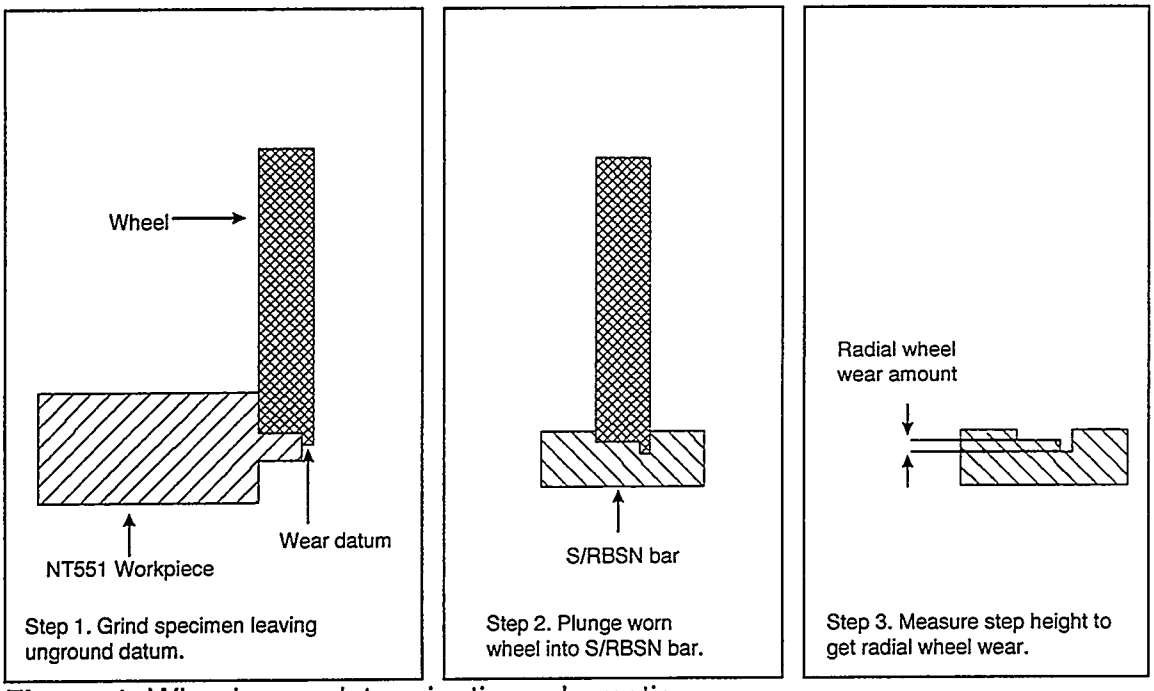

Figure 1. Wheel wear determination schematic.

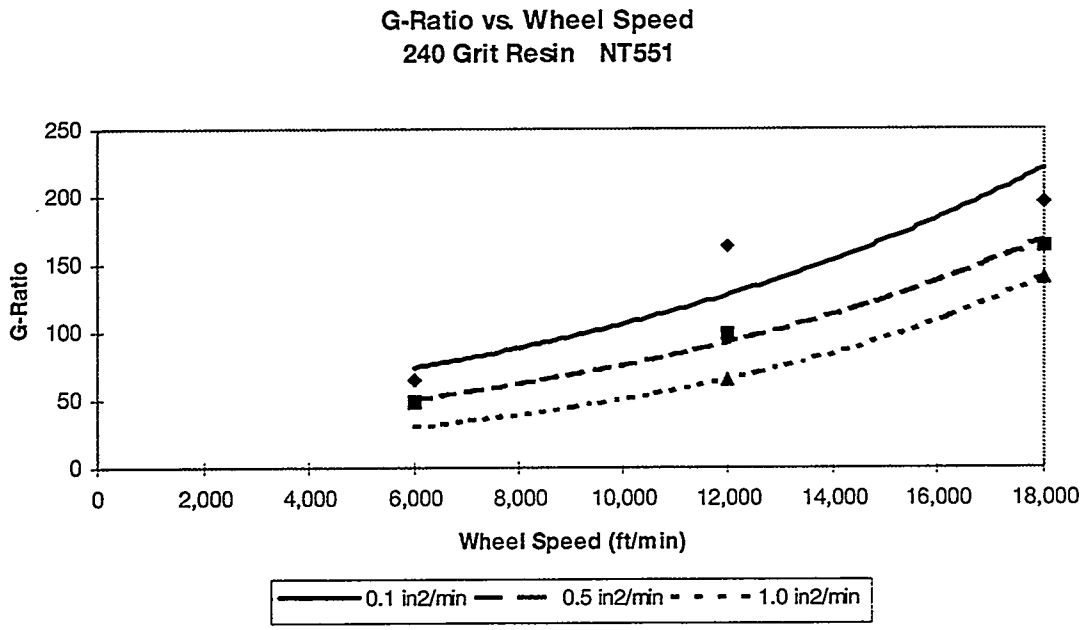

Figure 2. Experimental G-Ratio data as function of wheel speed and material removal rate (240 Resin, NT551).

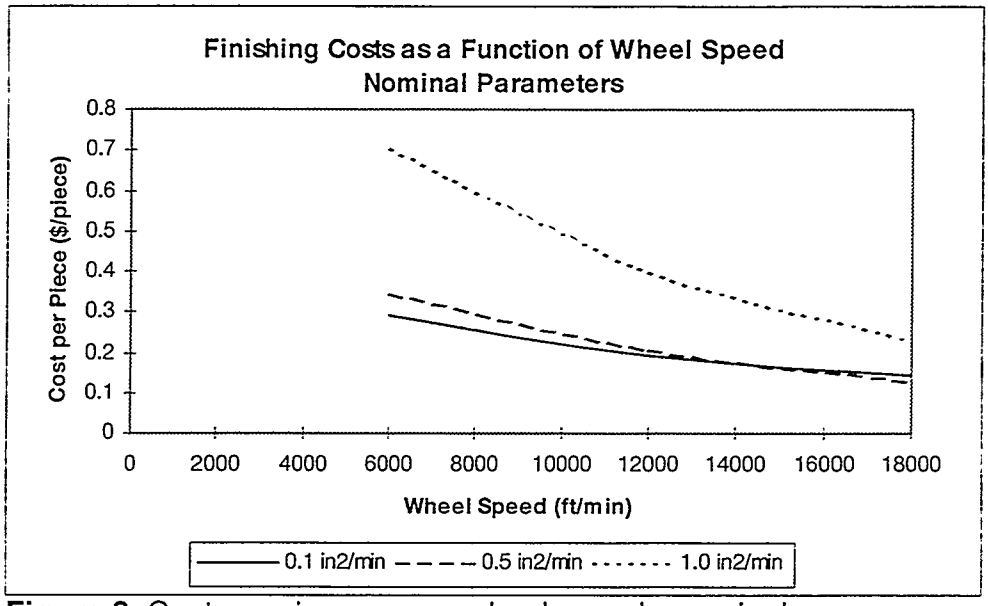

Figure 3. Cost per piece versus wheel speed - nominal case.

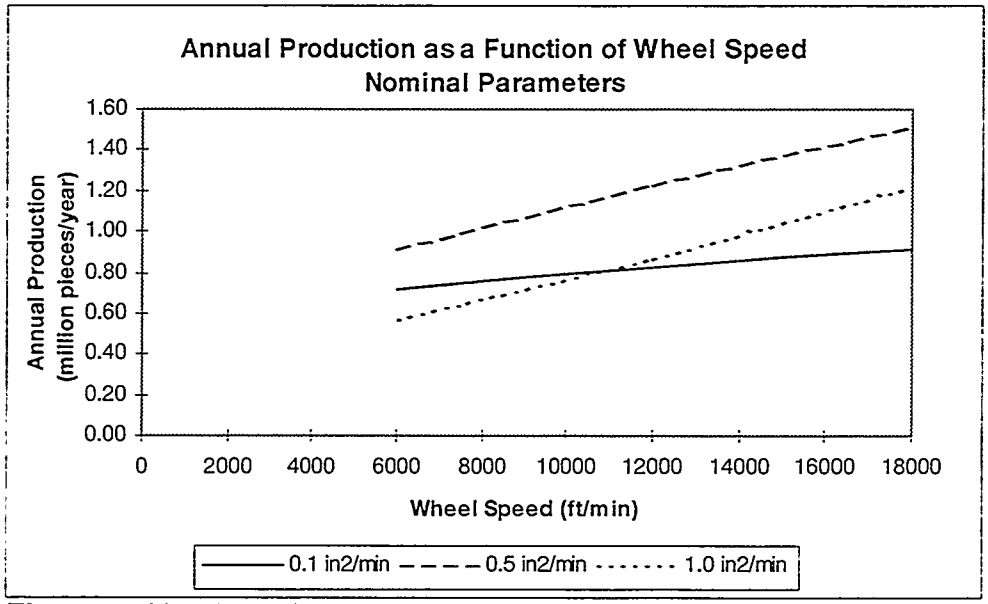

Figure 4. Number of pieces produced versus wheel speed - nominal case.

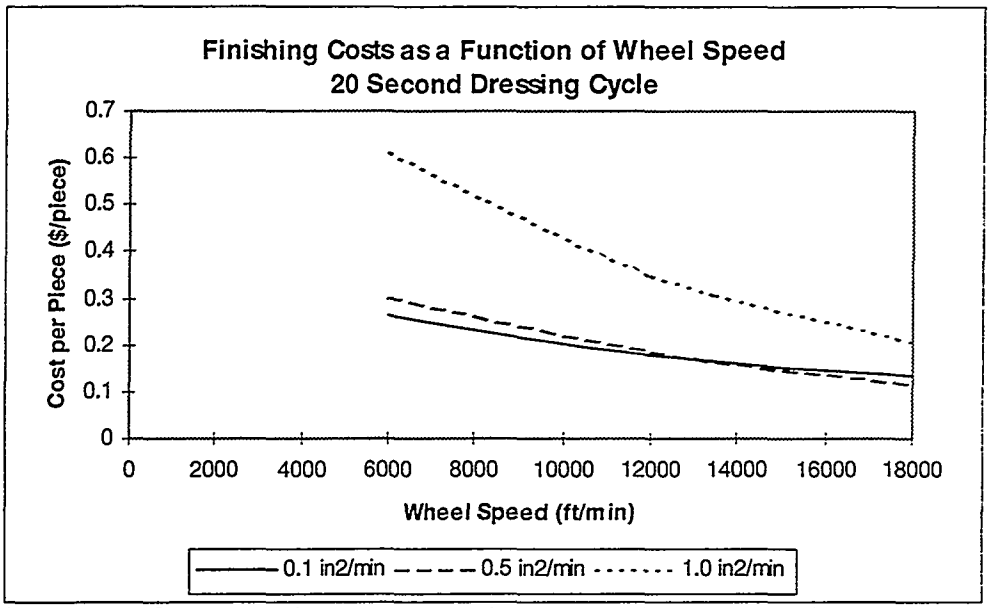

Figure 5. Cost per piece versus wheel speed -20 second dressing cycle.

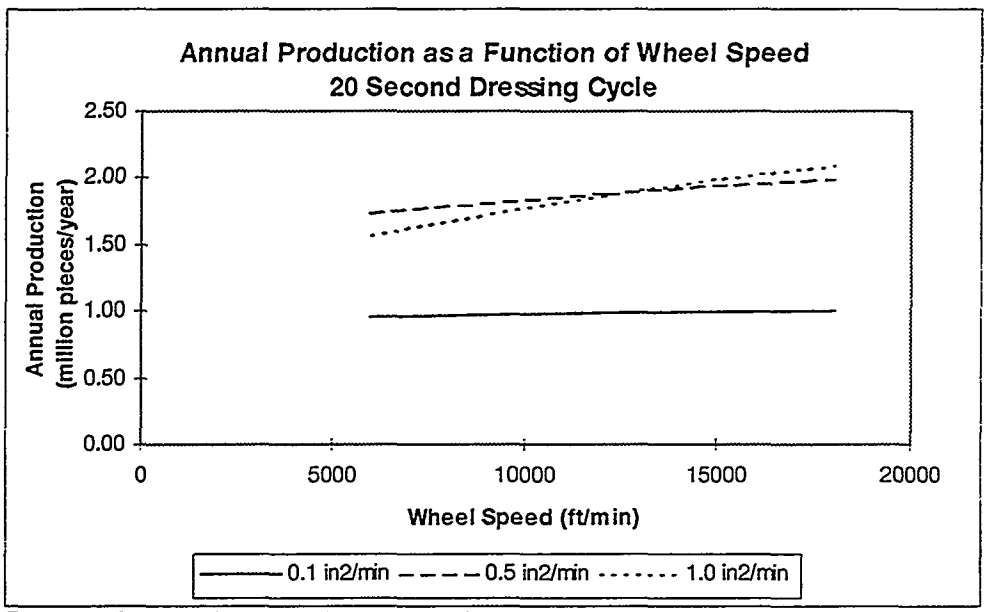

Figure 6. Number of pieces produced in one year versus wheel speed - 20 second dressing cycle.

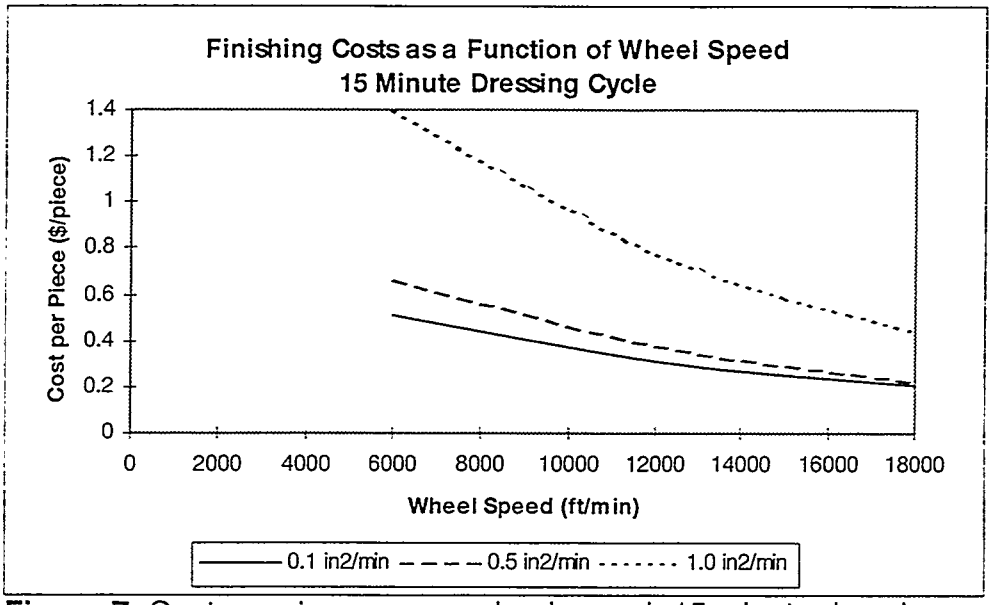

Figure 7. Cost per piece versus wheel speed -15 minute dressing cycle.

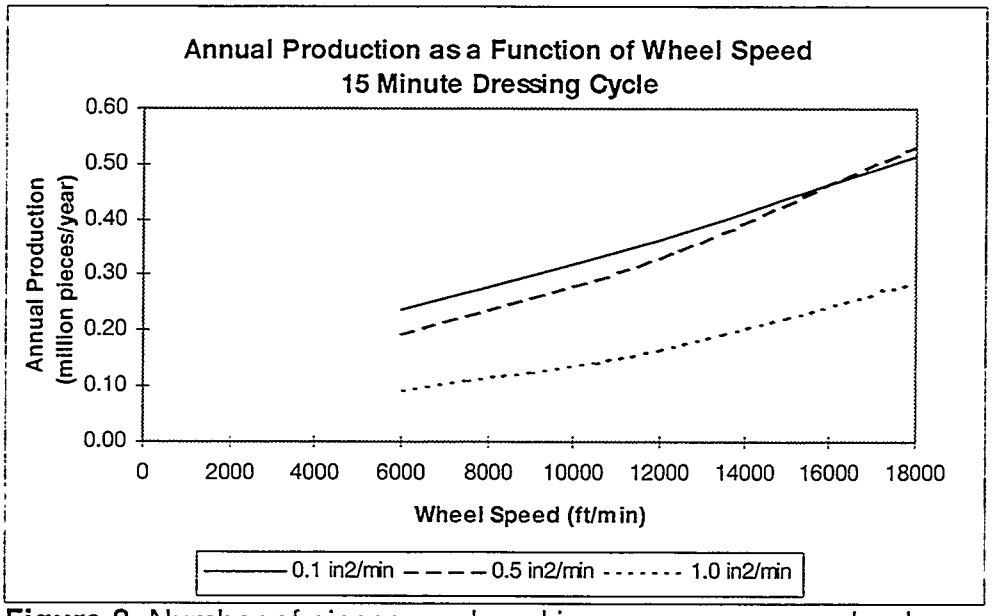

Figure 8. Number of pieces produced in one year versus wheel speed - 15 minute dressing cycle.

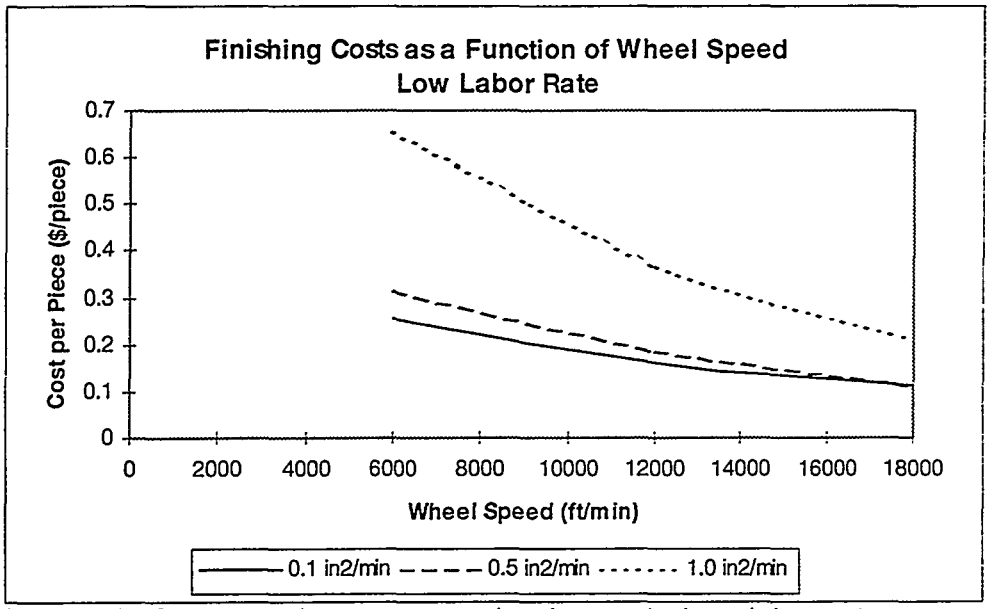

Figure 9. Cost per piece versus wheel speed - Low labor rate.

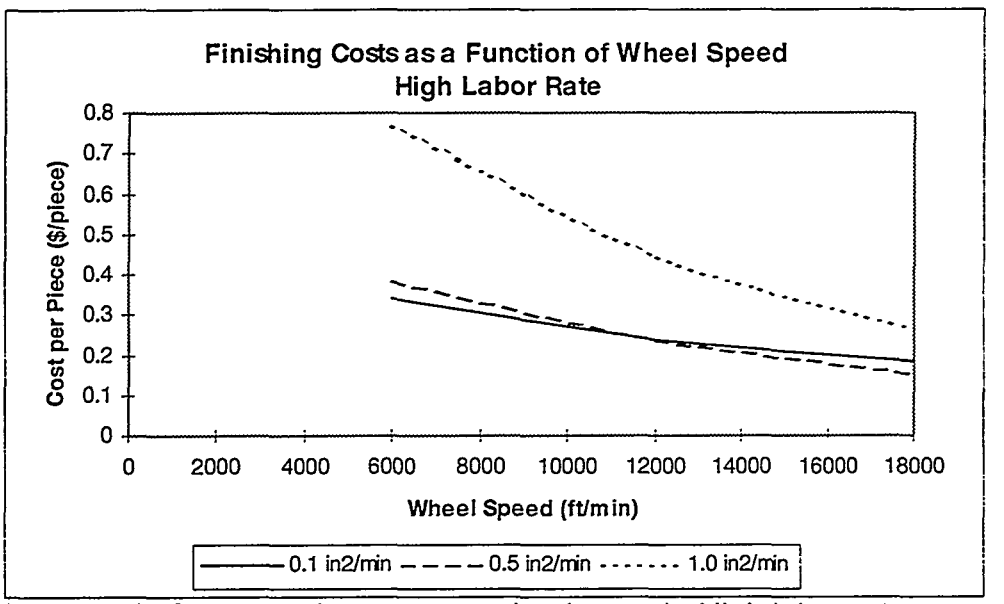

Figure 10. Cost per piece versus wheel speed - High labor rate.

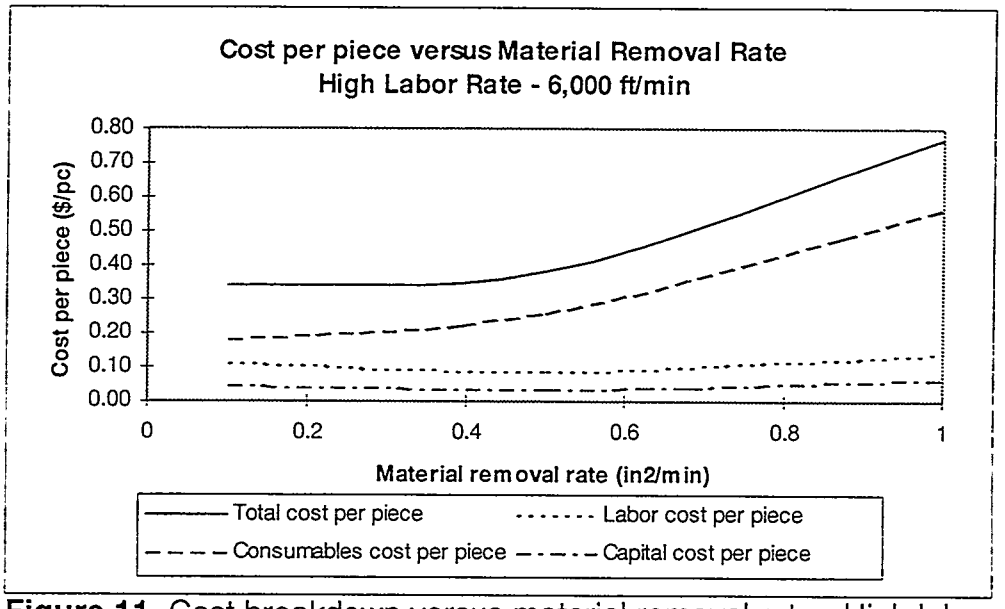

Figure 11. Cost breakdown versus material removal rate - High labor rate at 6,000 ft/min.

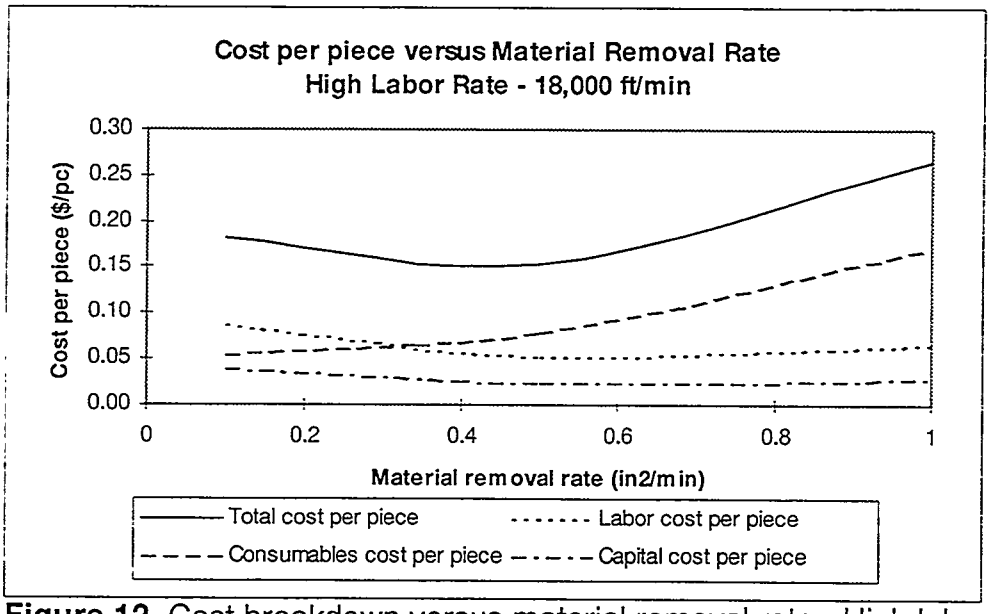

Figure 12. Cost breakdown versus material removal rate - High labor rate at 18,000 ft/min.

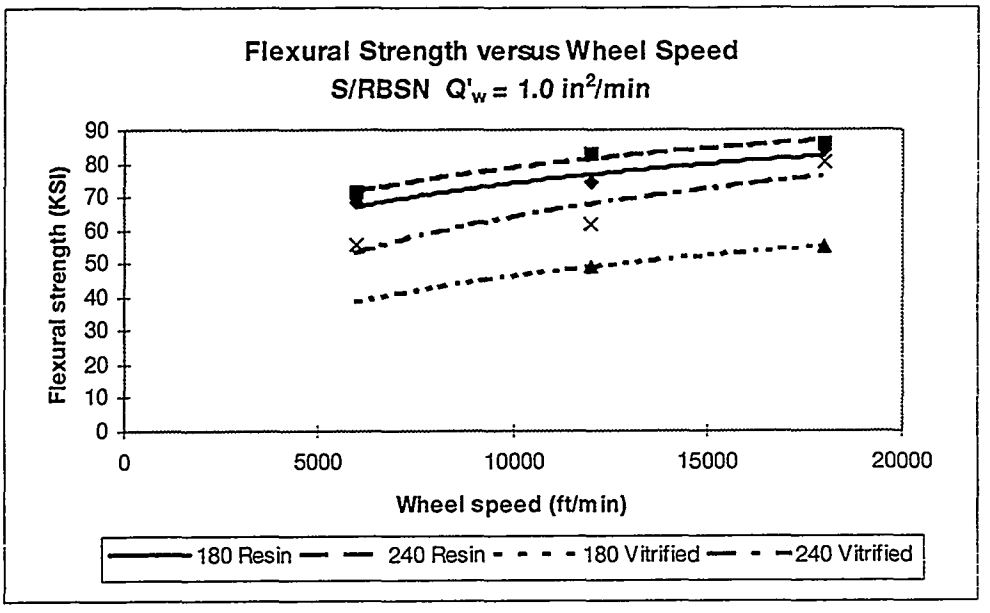

Figure 13. Flexural strength as a function of wheel speed for various wheel types.

NEXT GENERATION GRINDING SPINDLE FOR COST-EFFECTIVE MANUFACTURE OF ADVANCED CERAMIC COMPONENTS

Joseph A. Kovach
Michael A. Laurich
Eaton Manufacturing Technologies Center
Willoughby Hills, Ohio 44094

Objective/Scope

The overall objective of the Next Generation Grinding Spindle (NGS) program is to design, develop, test and demonstrate the operation of a next-generation, high-stiffness spindle to be used for centerless grinding of ceramic components. More specifically, the goals lead to the demonstration of a 50 hp, twin-grip, centerless grinding spindle capable of using 12-14" diameter by 8-12" wide grinding wheels with at least 7,000 rpm capability in a through-feed or in-feed grinding mode. The spindle stiffness is to be at least 2,000,000 lb/in. Program activities involve the development of a spindle bearing arrangement as well as an integral spindle/motor package. Accordingly, to achieve the overall program objective, this Phase I effort is comprised of the following six (6) major Tasks:

1.0 Spindle Design and Verification Testing
2.0 Motor Development
3.0 Wheel Hub Development
4.0 Wheel Balancer Development
5.0 Sensors, Sealing and Support Hardware Development
6.0 Final Assembly, Testing, and Demonstration

Technical Progress

This semi-annual report summarizes technical progress achieved during the period from October 1, 1997 to March 31, 1998. The report describes activities at the Eaton Manufacturing Technologies Center. A technical overview is presented in the following areas:

Technical Highlights

1.0 Spindle Design and Verification Testing

The custom built tilting pad bearings have been received and efforts are currently underway to modify an existing test rig at Case Western Reserve University. With the exception of the bearing side plates, all remaining design details have been completed.

2.0 Motor Development

Motor design has been completed. Integration of the shaft, cooling sleeve, laminations, wire leads and associated hardware has also been finalized. As such, purchase orders for the rotor and stator components have been submitted. The custom rare-earth magnets have been received. The motor drive unit is also nearing completion. Testing of the brushless DC motor will probably occur at the spindle drive unit vendor

3.0 Wheel Development

Engineering design has been completed on the grinding wheel. Based on discussions with several vendors, the graphite-epoxy composite hub is to be fabricated using a filament winding approach. Vitrified bonded 240 grit diamond segments will be bonded onto the periphery of the hub to complete the grinding wheel.

Status of Milestones
Program is basically on schedule.

Communications/Visits/Travel
A meeting has been scheduled to review program status in Oak Ridge on April 22, 1998.

Problems Encountered
Eaton is in the process of "phasing-down" the Manufacturing Technologies Center. This has slowed program progress and may require some modification of the anticipated deliverables.

Publications
None

Development of an "Intelligent Grinding Wheel" for In-Process Monitoring of Ceramic Grinding

S. Malkin, R. Gao, C. Guo, B. Varghese and S. Pathare
Department of Mechanical and Industrial Engineering
University of Massachusetts
Amherst, MA 01003-2210

Introduction

This is the third semi-annual report for the project "Development of an Intelligent Grinding Wheel for In-Process Monitoring of Ceramic Grinding." This report covers the period from September 1, 1997 to February 28, 1998.

The overall objective of this project is to develop sensor-integrated "intelligent" diamond wheels for grinding of ceramics. Such wheels will be "smart" enough to monitor and supervise both the wheel preparation and grinding processes without the need to instrument the machine tool. Intelligent wheels will utilize re-useable cores integrated with sensors: to measure the acoustic emission (AE) and grinding force. Signals from the sensors will be transmitted from a rotating wheel to a receiver by telemetry. Wheels will be "trained" to recognize distinct characteristics associated with truing, dressing and grinding.

Technical Progress

This overall project is divided into six tasks as follows:

1. Development of miniaturized sensors and data transmission system,
2. Wheel design and sensor configuration,
3. Calibration of the sensor integrated wheel,
4. Training of the intelligent wheel,
5. Grinding tests,
6. Prototype demonstration.

The technical progress is summarized in this report according to the tasks. All activity during this third period has been concerned with the first two interrelated tasks, which need to be completed before undertaking the remaining tasks.

Task 1. Development of Miniaturized Sensors and Data Transmission System

As stated in the previous semi-annual reports, a number of miniaturized piezoceramic sensors are being integrated into the "intelligent" grinding wheel core to measure force and acoustic emission (AE) for in-process monitoring of the wheel condition. Criteria taken into consideration for selecting the number and location of the sensors included the wheel geometry and its rotational speed, required measurement resolution, signal sampling and transmission rate, bandwidth required, complexity of the electronics, and space limitation for wheel integration. In addition, configuration of the bonded abrasive material on the wheel periphery also needed to be considered. The original wheel core design for force measurement included a total of sixteen sensors at the wheel periphery. However, the abrasive manufacturer (Norton Company) recommended that the abrasive on the grinding wheel be built up from twenty-two segments glued to the periphery. In order to maintain a symmetrical sensor arrangement, the number of abrasive segments should be a whole multiple of the number of force sensors. Therefore it was decided to use eleven piezoceramic sensors on the periphery of the wheel core for force measurement. For acoustic emission measurement, a minimum of three AE sensors are needed in order to pinpoint the circumferential location of the acoustic emission source at the wheel periphery by signal triangulation. In order to provide some system redundancy and

increased measurement accuracy, it was decided to use four AE sensors mounted on the face of the grinding wheel near its bore. Therefore, a total of fifteen sensors are used for both force and AE measurement.

The electronic circuit has been designed to handle inputs from all of the fifteen sensors in a time-multiplexed fashion. As shown in Fig. 1.1, the circuit consists of three functional blocks:

- An analog signal conditioner for sensor interface;
- An analog-to-digital signal converter (ADC) and a digital signal processor (DSP);
- An RF transmitter for telemetric data transmission.

This circuit was designed and initially implemented on breadboards. Based on the verification of its functionality, a circuit layout featuring both standard DIP (dual-in-line package) and SMD (surface mount device) components was developed for printed circuit board (PCB) implementation. The layout design was accomplished using a combination of manual and auto-routing techniques. The PCB was then fabricated by an external vendor, with the final size being approximately 4" x 5". Components were placed on the PCB by manual soldering under a special magnifier designed for SMD components handling.

This circuit board was then interfaced to a DSP evaluation kit, which contains a TMS320C542 Digital Signal Processor from Texas Instruments. The DSP kit was then connected to a PC by an emulator, which provides access to internal memory and registers of the DSP. This entire circuit was operated with a single J size 6-Volt battery 48 x 36 x 9

mm in size. The flat shape of the battery is particularly suitable for integration into the grinding wheel. The DSP was programmed to acquire the data from test signals fed to various sensor channels. Various data acquisition software was used to sample data from the ADC (Analog-to-Digital Converter). Multiplexing among the sensors was found to be successful. The analog signal conditioner and the DSP kit has exactly the same functionality required for data acquisition, except for a DSP-emulator connection which is needed for programming the DSP and data retrieval.

For the planned RF telemetric data transmission, tests were conducted independently by using signals with voltage levels compatible to those of the DSP serial port data output. Data was transmitted on the 900 MHz, FCC license-free ISM (Instrumentation, Science, and Medical) band. Various digital signal test patterns (ASCII strings) were transmitted and received without any error over a distance of about 8 meters at a rate of 9,600 bits per second.

Upon successful testing of each of the electronic functional blocks, the entire circuit will be mounted, together with a battery, on an "L" shaped bracket and attached to the face of a grinding wheel. A photograph of the assembled electronic circuit is shown in Fig. 1.2. The wheel-integrated electronics will be tested with the grinding wheel rotating first at relatively low speeds. The DSP will transfer the acquired data through its serial port to the RF transmitter, which then transmits the data wirelessly to the external receiver.

Each sensor being integrated into the wheel was calibrated by applying loads on an Instron

testing machine and measuring the output using a Kistler charge amplifier. The calibration information, along with the wheel rotating speeds, will provide realistic data on the required functionality for the final circuitry. Based on this information, the functional blocks of the circuit will be modified and miniaturized to fit on a PCB 2.5" x 3.5" in size. The RF transmitter will be fabricated separately on a PCB of 1.5" x 1". The RF transmitter will be physically isolated from the sensitive analog electronics to ensure that the signals from the sensors are not corrupted by EMI (Electromagnetic Interference). The circuit boards will also be individually shielded by aluminum foil to protect them from external EMI.

During grinding as the wheel-workpiece contact sweeps past an embedded force sensor, an impulse output signal is generated which is proportional to the force acting on the grinding wheel. For a sensor of width w and peripheral wheel velocity v_s, the time duration of the impulse is approximately $T = w/v_s$. For example, a wheel velocity of 60 m/s and sensor width of 3 mm would give $T = 50$ ms. This corresponds to a signal frequency centered at 20 kHz. The force sensors also respond to AE signals having a larger bandwidth. To derive the force component from the recorded signals, it is necessary to implement a bandpass filter centered at the frequency of the force component, e.g., 20 kHz. The filtering operation will be conducted by the DSP. The block diagram of the signal processing to derive the force signal is shown in Fig. 1.3. Implementation of the bandpass filter requires accurate information of the wheel speed in order to calculate the pulse width T of the force signal. Once the pulse width is known, the bandpass filter parameters can be fixed to derive the force value.

Task 2. Design of Grinding Wheel and Adapter Plate

Structural modification of the wheel core was necessary in order to accommodate the fifteen force and acoustic emission sensors. Space also was needed for the data processing and transmission electronics. For this purpose a special adapter plate was designed. This section describes the design of the grinding wheel and the adapter plate.

The wheel core design and sensor locations are shown in Figure 2.1. In order to utilize standard abrasive segments provided by Norton Company, the design of the wheel core was changed to include twenty-two abrasive segments on the periphery of the aluminum wheel core. This resulted in an effective wheel diameter of 14 inches. Based on results from the static tests (see previous report) and in order to maintain a symetrical arrangement with the abrasive segments, it was decided to use eleven force sensors equally spaced 32.76 degrees apart around the wheel periphery. The sensors were placed sufficiently far away from the joints between the abrasive segments, and cemented into eleven slots machined on the periphery of the wheel core. In additional to these force sensors, four acoustic emission sensors were symmetrically placed around the wheel closer to the bore, as described under Task 1.

In order to minimize structural modifications to the wheel core and facilitate access and maintenance of the electronic circuitry, it was decided to mount the electronic circuitry, the leads, the RF transmitter, and the power supply on an adapter plate attached to the face of the wheel as shown in Figure 2.2. A similar "dummy" plate will also be fastened to

the opposite wheel face in order to maintain symmetry and balance. This modular (re-configurable) design also provides flexibility enabling use of the same adapter plate with other sensor-embedded wheels differing somewhat in size and abrasive content. It furthers allows easy maintenance of the electronic circuitry/components and programming of the DSP without dismounting the wheel from the machine spindle. The wheel may be used for regular production while electronic maintenance is being undertaken.

An annular recess in the adapter plate will be used to house the electronics required for signal conditioning, processing, and transmission. The electronics will be anchored to the adapter plate by means of screws. A cover (gasket) will be sandwiched between the adapter plate and the wheel to protect the electronics from environmental disturbances such as grinding fluids. Two dowel pins embedded in the wheel core will be used to precisely locate the adapter plate with respect to the wheel core. The adapter plate will be fastened to the wheel by screws. Furthermore, the outer face of the adapter plate will be shielded from outside electrical noise by means of aluminum guards (shields). Connector terminals are provided on the adapter plate for every sensor. These connectors will be secured to the leads by bolts to provide good electric contact. The leads from the connectors will be laid out in the shallow grooves at the bottom face of the annular recess running directly under the electronic circuitry. Finally the electronic circuitry will be sealed to insulate it from grinding debris that may seep in during grinding.

Both the wheel core and the adapter plate have been manufactured. Abrasive segments will be bonded on to the wheel core during the first week of April. The final electronic

circuitry is expected to be ready by May. Afterwards preliminary tests will be conducted with the wheel rotating at slow speeds. The wheel, together with the associated electronics, will be mounted on the spindle of the grinding machine. The performance of the ADC, signal processing and telemetry equipment will be evaluated by rotating the wheel against a friction plate (or roll). The results of this test will help to establish a basis for miniaturization of the various electronic circuits.

Publications

- Sumukh Pathare, Robert Gao, Biju Varghese, Changsheng Guo, and Stephen Malkin, "A DSP-Based Telemetric Data Acquisition System for In-Process Monitoring of Grinding Operation," accepted for publication in *Proc. 1998 IEEE Instrumentation and Measurement Technology Conference* (IMTC/98), St. Paul, Minnesota, May 18-21, 1998.

Trips and Meetings

None to report during this period.

Personnel

- Stephen Malkin, Sc.D., Distinguished Professor, Principal Investigator

  Overall project management, grinding test and analysis.

- Robert Gao, Ph.D., Assistant Professor, Co-Principal Investigator

  Design of miniaturized sensors, telemetry, and microelectronics; testing and prototype demonstration.

- Changsheng Guo, Ph.D., Senior Research Fellow, Co-Principal Investigator

  Mechanical design, setup, testing and prototyping of grinding wheel.

- Biju Varghese, Graduate Research Assistant, Ph.D. Student

  Mechanical design, calibration, training and testing of the grinding wheel prototype

- Sumukh Pathare, Graduate Research Assistant, M.S. Student

  Sensor development, electronic circuits design, implementation, and testing

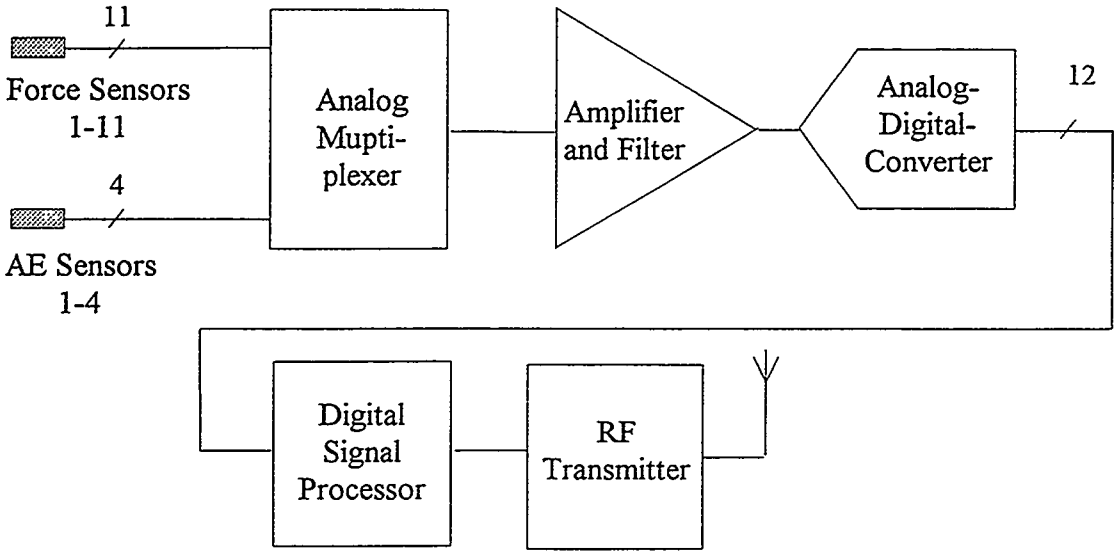

Figure 1.1. Block diagram of the wheel-integrated sensors and electronics

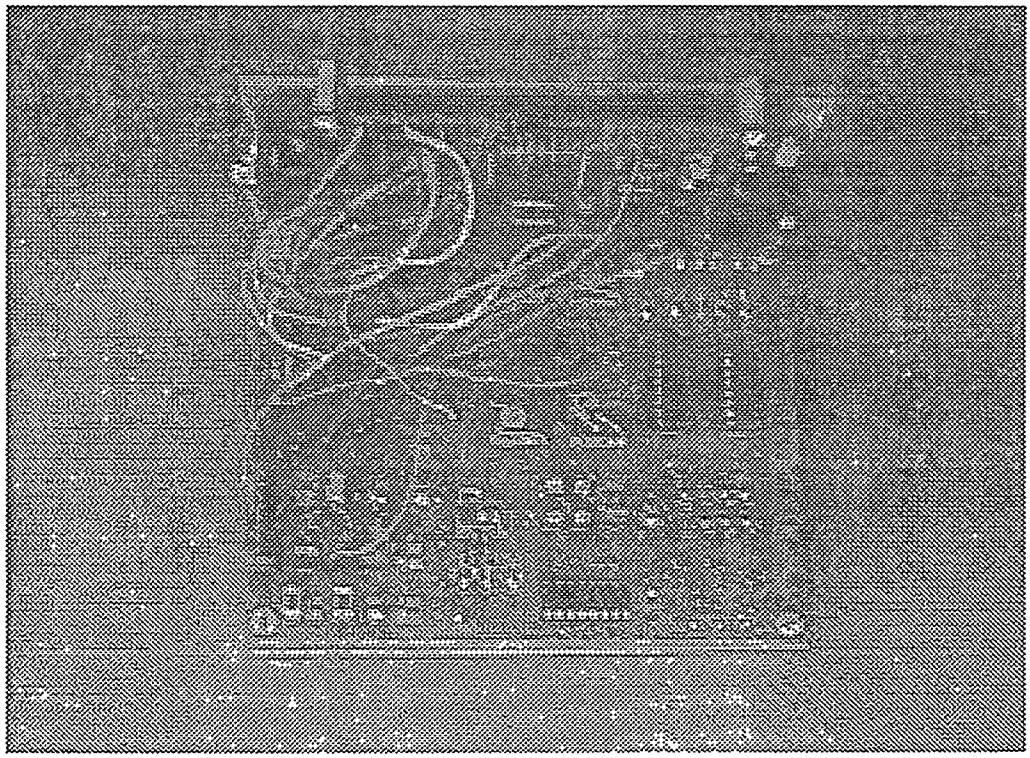

Figure. 1.2. Photograph of the wheel electronics

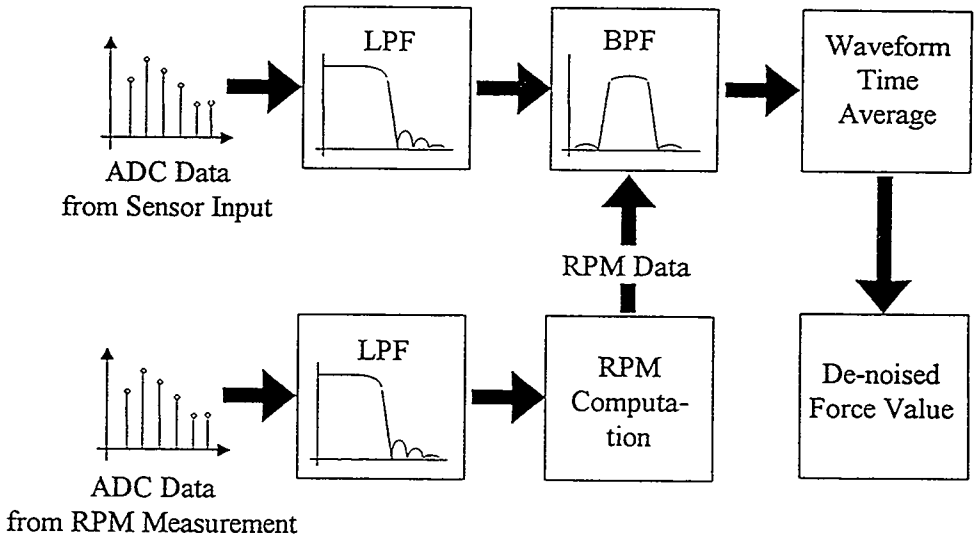

Figure. 1.3. Filtering of force signals

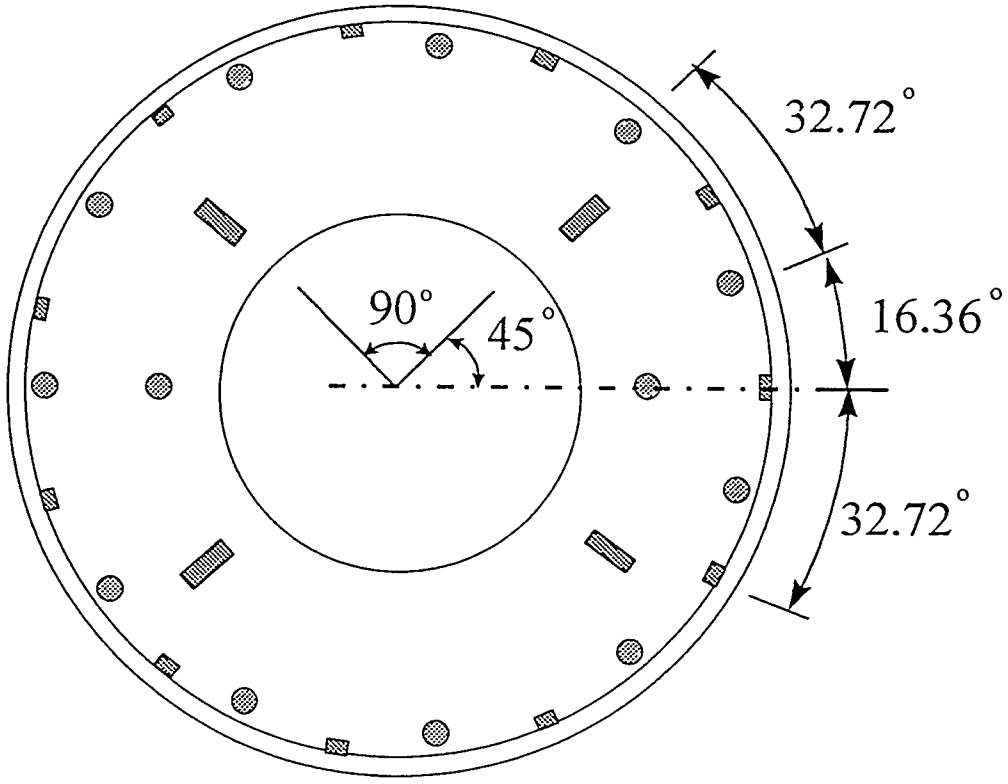

Figure. 2.1. Sensor arrangement in wheel core

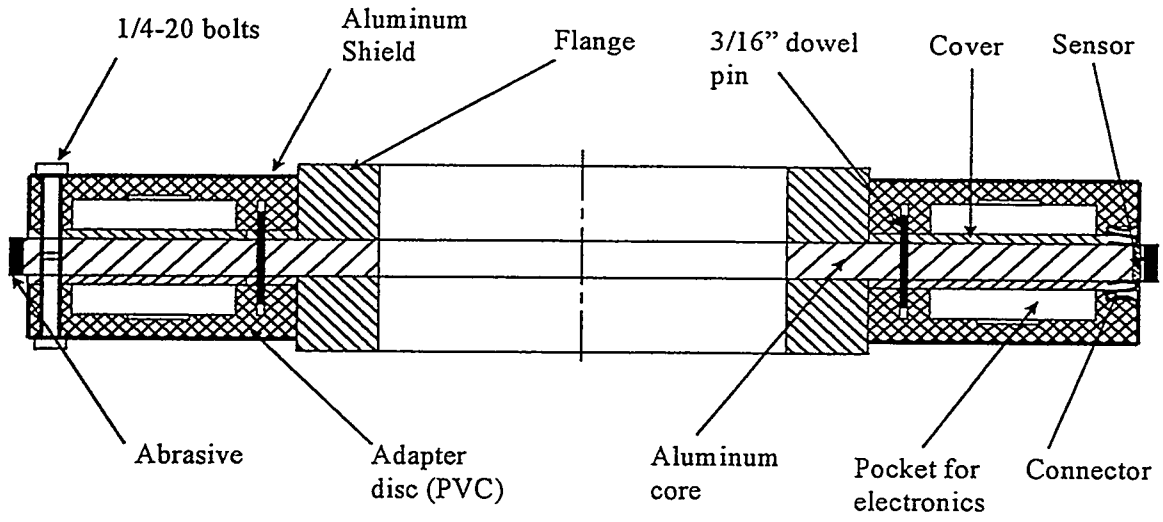

Figure. 2.2. Cross sectional view of the wheel core assembly

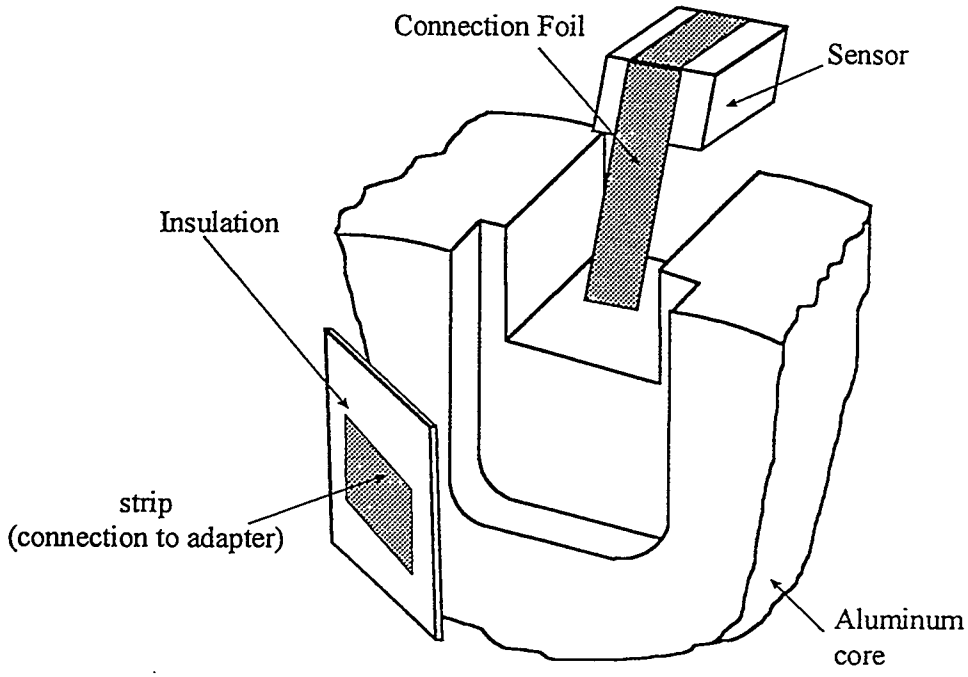

Figure. 2.3. Connection of the sensors to the wheel core

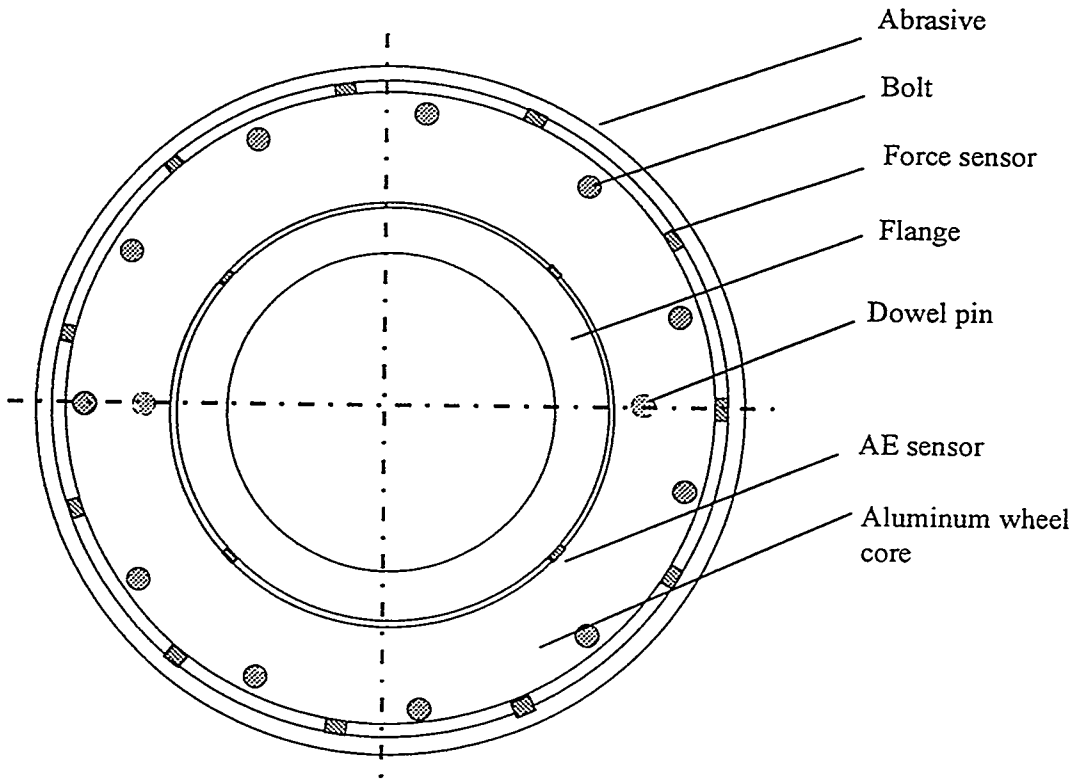

Figure. 2.4. Cross sectional view of the wheel assembly

Laser Scatter Methods for Detecting Subsurface Machining Damage in Ceramics – Jiangang Sun, William A. Ellingson, (Argonne National Laboratory), Michael C. Long, Michael H. Haselkorn, and Charles J. Anderson (Caterpillar Inc.)

Objective/scope

The primary objective of this program is to develop a laser scattering procedure that would provide a direct (near-real-time) indication of changes in the subsurface (and surface) during machining. These changes include machining-induced damage (such as median crack formation) and surface roughness. A second objective is to evaluate dye penetrant technology as an off-line indicator of surface-breaking cracks. The laser program is being executed in three steps. The first is evaluating optimization of the laser scattering procedure to examine specimens machined by innovative techniques. The second step will involve correlation of the laser scattering results with mechanical properties in "real" machined ceramic specimens. The final step will be to develop a prototype instrument to be evaluated for on-line implementation in a production environment. The investigation into dye penetrants for surface-defect detection is being conducted in three steps: review of literature, off-site visits to appropriate current users (e.g., Norton) and vendors (e.g., Sherwin, Inc.), and laboratory experiments.

Technical progress

1. Elastic Optical Scattering Results

1.A Caterpillar Samples

We continued the effort to establish correlations between the elastic optical scattering data and the surface microstructure and machining damage. A set of diamond-ground specimens was obtained from Caterpillar, Inc. and are being used for this study. They are GS44 and Ceralloy Si_3N_4 ceramics and were machined by diamond grounding at high and low material removal rate (MRR). The machining conditions are listed in Table 1.

Figure 1 shows the elastic optical scattering images of GS44 and Ceralloy specimens at low and high MRR. For GS44 specimens, there is a distinct difference between the optical scatter images. However, the difference is not too drastic for Ceralloy specimens. It is suspected that surface roughness could play a role to the optical scattering.

Table 1 List of diamond-ground specimens and their machining conditions

Test No.	Wheel specification	Specimen ID	Material	MRR	Wheel wear	Grinding force initial/last pass
6	99304007-Vit/150Grit /125/non-friable	CAT6B	GS-44	High-12"/min	0.0054mm	20/135 lbs
		CAT6D	Ceralloy	High-12"/min	0.0052mm	20/35 lbs
7	99304008-Vit/100Grit /125/non-friable	CAT7B	GS-44	Low-6"/min	0.0036mm	20/80 lbs
		CAT7D	Ceralloy	Low-6"/min	0.0105mm	20/60 lbs
8	99304008-Vit/100Grit /125/non-friable	CAT8B	GS-44	High-12"/min	0.0062mm	10/50 lbs
		CAT8D	Ceralloy	High-12"/min	0.0070mm	20/50 lbs
9	99304010-Vit/150Grit /75/friable	CAT9D	Ceralloy	High-12"/min		5/50 lbs

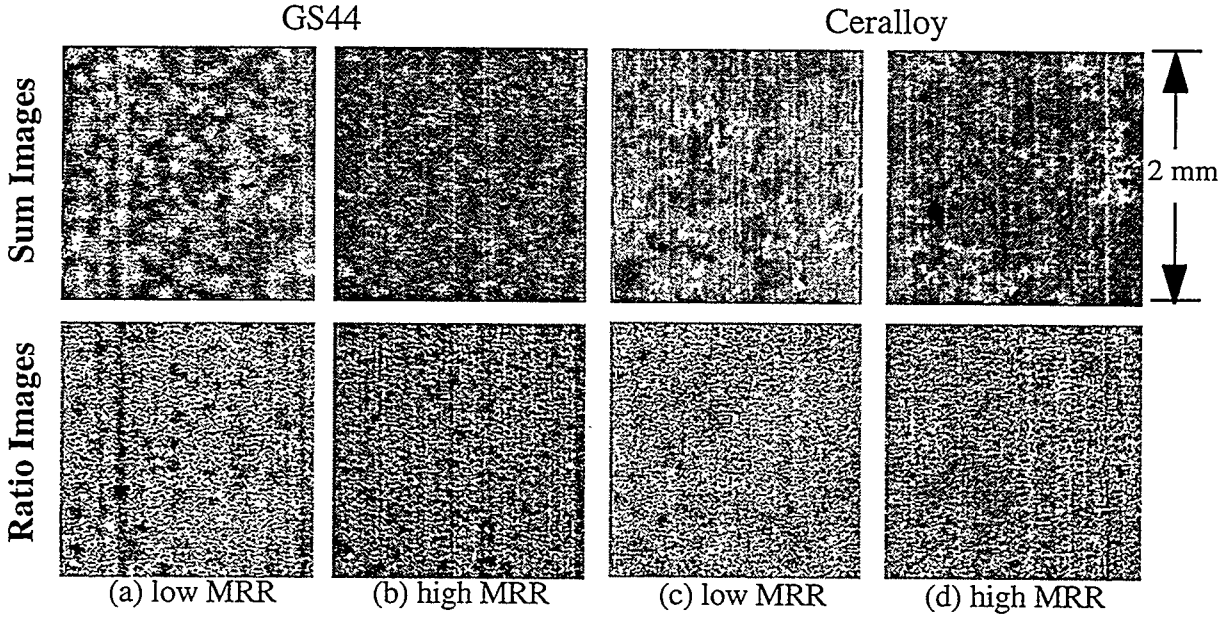

Figure 1 Scatter images of GS44 specimens at (a) low MRR (CAT7B) and (b) high MRR (CAT8B), and of Ceralloy specimens at (c) low MRR (CAT7D) and (d) high MRR (CAT8D).

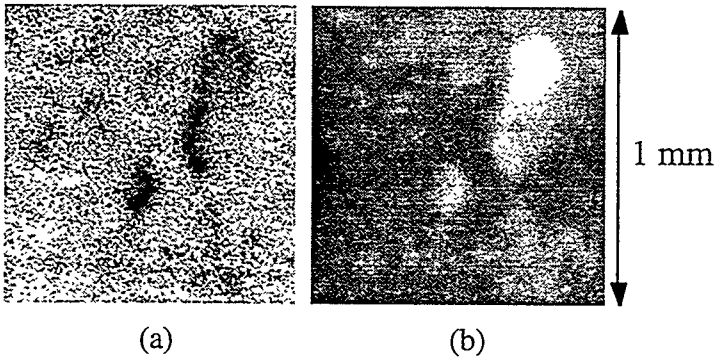

Figure 2 Elastic optical scatter (a) ratio and (b) sum images of a diamond-ground GS44 specimen (CAT8B).

The elastic optical scatter images were compared with the surface photo micrographs. The diamond-ground GS44 specimen CAT8B was used in the comparison which has a high material removal rate as listed in Table 1. In this study, we focused on some specific features observed from the laser scatter images. Figure 2 shows the scattering ratio and sum images at 1-μm resolution on an 1-mm x 1-mm region which contain two prominent defects (defects show brighter in sum image and darker in ratio image). Figure 3 shows two micrographs at 50X magnification at the same region, one obtained with a normal incident light and the other with an oblique (~20°) light. In Fig. 3a, the normal-light micrograph, the prominent defects detected in laser scatter images can be observed as darker lines of the same shape as that in the scatter images. However, there are many other darker lines (which were not detected in the scatter images) such that these two defect lines may be easily overlooked from the micrograph. In Fig. 3b, the oblique-light micrograph, however, the defects are easily observed.

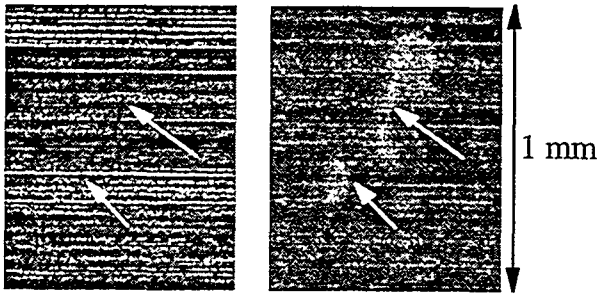

Figure 3 (a) Normal- and (b) oblique-incident-light photo micrographs (50X) for the surface of the diamond-ground GS44 specimen shown in Fig. 2.

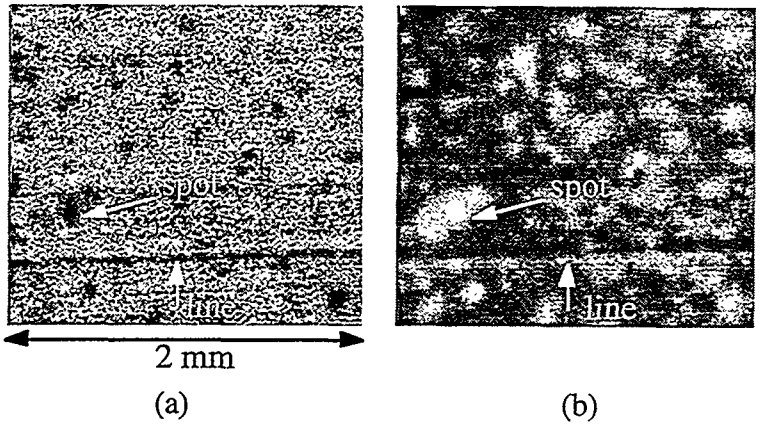

Figure 4 Elastic optical scatter (a) ratio and (b) sum images of a diamond-ground GS44 specimen (CAT8B).

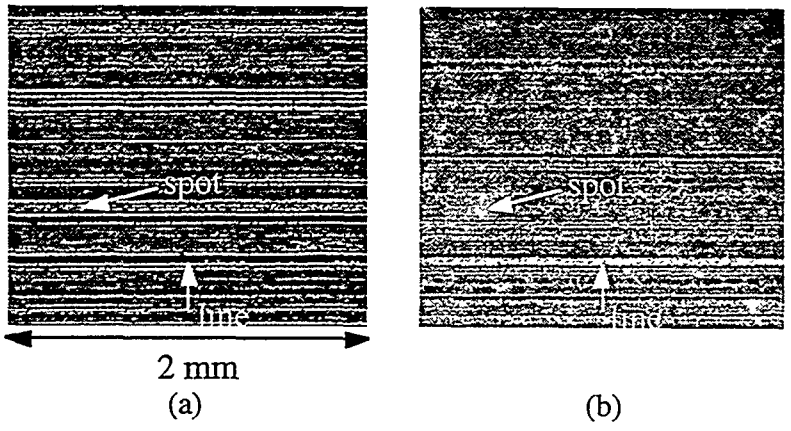

Figure 5 (a) Normal- and (b) oblique-incident-light photo micrographs (50X) for the surface of the diamond-ground GS44 specimen shown in Fig. 4.

Figure 4 shows the laser scattering ratio and sum images at 5-μm resolution on a 2-mm x 1.75-mm region. Two prominent defects are indicated, a spot about 80 μm in diameter and a line about 40 μm in width. Figure 5 shows two micrographs at 50X magnification on the same region, one obtained with a normal incident light and the other with an oblique (~30°) light. In the normal-light micrograph (Fig. 5a), the defect spot is not observed, while the defect line is shown as a

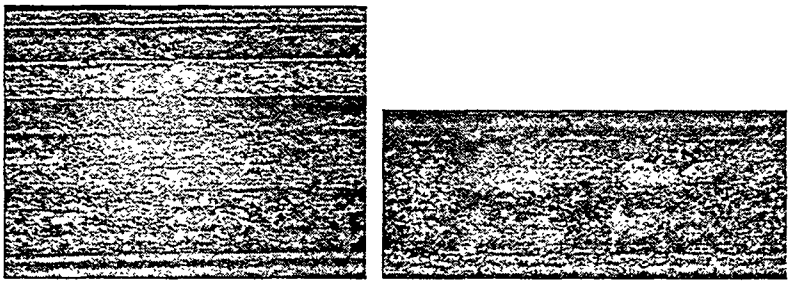

(a) (b)

Figure 6 Photo micrographs (1000X) for the surface region at (a) defect spot and (b) defect line as shown in Figs. 4 and 5.

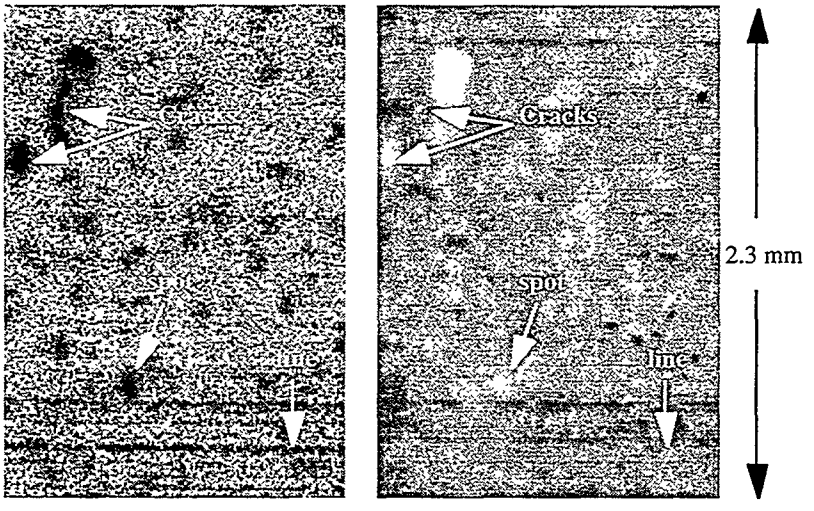

(a) (b)

Figure 7 Elastic optical scatter (a) ratio and (b) sum image of a diamond-ground GS44 specimen (CAT8B), after polishing off a layer of 20 μm from the ground surface.

darker line. In the oblique-light micrograph (Fig. 5b), these two defects are easily observed. At higher magnification (1000X), shown in Fig. 6a for the defect spot and Fig. 6b for the defect line, it is seen that there is no visible surface damage at the spot region while there is a distinctive difference of the surface microstructure at the defect-line region compared with that in its surrounding regions. These features are further investigated with a procedure by repeated polishing and re-examining of the surface.

Our technique is to sequentially do the following steps: a) obtain laser scatter data, b) obtain optical photomicrographs, c) polish to remove 10 μm of material (because voids in the GS44 specimen are typically in the order of 20 μm) and repeat the sequence. At present, a ~20 μm layer has been polished off from the specimen surface. Figure 7 shows the scattering ratio and sum images at 5-μm resolution on a polished surface region containing several prominent defects. Figure 8 shows a micrograph at 50X magnification on the same region. Two surface-breaking cracks are detected as shown on top of the scatter images. The feature identified as "spot" in the scatter images shows no surface defect from the micrograph. The feature identified as "line" is presumably due to machining damage, and it shows some microstructural irregularity on the surface. These features are continuously investigated with additional polishing and re-examining.

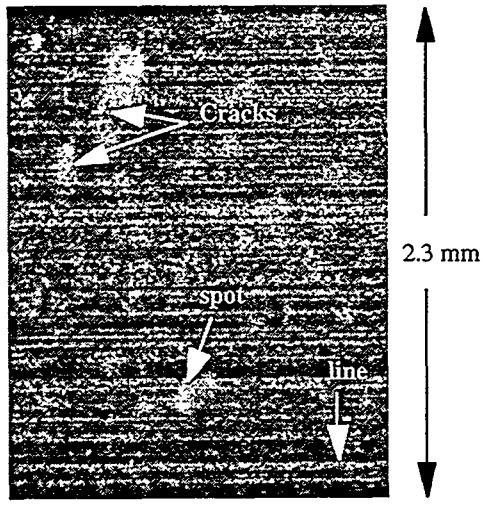

Figure 8 Photo micrograph (50X) for the same surface region of the diamond-ground GS44 specimen shown in Fig. 7. Note the direct correlation between the laser scatter image and the optical image.

1.B Eaton Samples

We have obtained ground silicon nitride specimens from Eaton Corporation, as shown in Table 2. Results of elastic optical scattering tests will be presented in future reports.

Table 2. Machining conditions of silicon nitride specimens from Eaton Corporation

Grit size	Bond type	Speed	Test #	Sample	Peak load (lbs)	Max. stress (psi)	Failure origin
180	Resin	5,000	1	1-1	117.3	67,455	Grind
180	Resin	6,000	9701-1	9701-1-1	142.6	78,591	Grind
180	Resin	10,000	2	2-4	121.6	68,742	Grind
180	Resin	12,000	9701-2	9701-2-15	134.7	71,427	Grind
180	Resin	18,000	9701-3	9701-3-7	160.6	86,150	Grind
240	Resin	6,000	9701-4	9701-4-6	128.8	69,363	Grind
240	Resin	12,000	9701-5	9701-5-2	145.3	78,635	Grind
240	Resin	18,000	9701-6	9701-6-2	161.5	85,251	Grind
240	Vitrified	18,000	9701-9	9701-9-6	145.9	78,768	Grind
180	Vitrified	6,000	9703-1	9703-1-15	108.3	58,265	Gone
180	Vitrified	12,000	9703-2	9703-2-5	93.5	50,614	Grind
180	Vitrified	18,000	9703-3	9703-3-4	93.5	50,576	Grind
240	Vitrified	6,000	9703-4	9703-4-1	77.7	42,382	Grind
240	Vitrified	12,000	9703-5	9703-5-1	116.4	63,248	Grind

2. Automation for On-Line Inspection with Optical Scattering

We did not devote any effort to this part of the project this period because we have been working to establish correlations before we continue this work.

3. Impact Acoustic Resonance Results

A nondestructive acoustic resonance spectroscopy technique is being used to experimentally determine elasticitic moduli of the rectangular samples. The technique, referred to as impact acoustic response (IAR), involves lightly tapping the test specimen with a blunt tipped force transducer and recording the dynamic response of the specimen via its radiated sound spectrum using an 1/8 inch microphone. Structural resonant frequencies of the specimen are identified. This information and geometric information about the specimen, are used to extract elastic modulus values based on plate vibration theory.

Estimated moduli of elasticity for the diamond-ground specimens are plotted in Fig. 9. They are calculated based on isotropic thin beam theory using the fundamental resonant frequency. Error bars denote ±3 standard deviations due to uncertainty in specimen dimensions and material density.

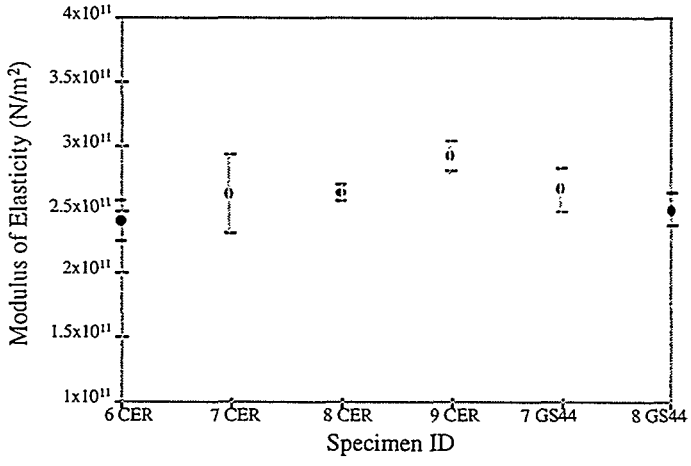

Figure 9 Estimated modulus of elasticity for diamond-ground specimens.

We are in the process of adding a scanning laser vibrometer setup so that fundamental mode shape can be correlated to the acoustic signals already received. Both Polytec and Ometron systems have been assessed. Currently we plan to buy a single head and mount on x-y stages.

Status of Milestones

All ANL milestones are on or ahead of schedule.

Communications/Visits/Travel

Travel:

1. W. A. Ellingson and J. G. Sun attended the Annual Automotive Technology Development Customers' Coordination Meeting at Dearborn, MI, Oct. 27-30, 1997.

2. J. G. Sun attended the Am. Cer. Soc's 22nd Annual Cocoa Beach Meeting, Jan. 20-24, 1997, Cocoa Beach, FL.

3. W. A. Ellingson attended the Am. Cer. Soc's 22nd Annual Cocoa Beach Meeting, Jan. 25-30, 1997, Cocoa Beach, FL.

Communication:

1. Discussions have been taking place with Eaton Corporation and St. Gobain Industrial Ceramics to obtain machined specimens with carefully controlled machining conditions.

Problems Encountered

Two milestones were rescheduled to May 15, 1998 because we do not have specimens with machining parameters to allow establishing correlations of NDE data with specimen machining conditions and mechanical properties. Efforts have been made to obtain additional specimens from Caterpillar with GS44 using only depth of cut and feed rate as variables.

Publications

None this period.

Milestone Schedule

FY97

Complete initial elastic optical scatter data acquisition on high material removal rate (HMRR) Si_3N_4 flat plate specimens.	May 30, 1997	**Completed**
Complete Impact Acoustic Resonance (IAR) data acquisition on HMRR flat plate specimens.	June 30, 1997	**Completed**
Complete microstructural analysis of HMRR specimens and correlate to optical and resonance data.	Sep. 15, 1997	Rescheduled to 5/15/98

FY98

Complete initial elastic optical scatter data acquisition on low material removal rate (LMRR) Si_3N_4 flat plate specimens.	Nov. 15, 1997	**Completed**
Obtain mechanical properties and correlate data of HMRR specimens.	Dec. 15, 1997	Rescheduled to 5/15/98
Complete IAR data acquisition on LMRR flat plate specimens.	Feb 15, 1998	**Completed**
Complete microstructural analysis, obtain mechanical properties and correlate data of LMRR specimens.	May 15, 1998	On schedule
Obtain HMRR and LMRR round specimens of Si_3N_4.	May. 30, 1998	
Complete initial elastic optical scatter and IAR data acquisition of round HMRR and LMRR specimens.	Sep. 15, 1998	

FY99

Complete IAR data acquisition on round HMRR and LMRR specimens.	Nov. 30, 1998	
Complete microstructural analysis of round HMRR and LMRR specimens.	Feb. 15, 1999	
Correlate IAR and elastic optical data on round HMRR and LMRR specimens.	Apr. 15, 1999	
Prepare limited mechanical property specimens from round specimens and correlate to NDE data.	July 15, 1997	
Complete and test set up of initial high speed optical scatter system on grinding machine.	Aug. 15, 1999	
Submit project report.	Sep. 30, 1999	

Cost Modeling Analysis of Fabrication Approaches for Silicon Nitride Components[1]

James M. Wimmer

Objective/Scope:

A number of diesel, automotive, and gas turbine engine manufacturers are interested in implementing structural ceramic components into their products due to the benefits of lower weight, reduced wear, and higher temperature capability that ceramics exhibit over current metal versions. Since a variety of fabrication approaches can be employed for any given part, guidance on the "best" fabrication approach, based on production volume, cost, delivery schedule, and performance, is very useful to ceramic component manufacturers. Although simplistic cost analyses of production costs are routinely performed, more sophisticated and comprehensive cost models are needed.

AlliedSignal Ceramic Components (CC), in conjunction with the California State Polytechnic University at Pomona (Cal Poly Pomona), refined a process cost model for the evaluation of various fabrication methods used to manufacture ceramic diesel engine and aerospace/industrial gas turbine engine components. This ceramic component cost model was configured to evaluate the benefits and trade-offs of a variety of fabrication routes for three specific components that were selected to represent a wide range of potential structural ceramic part features - a turbocharger wheel, a diesel engine cam roller follower, and an auxiliary power unit gas turbine nozzle. The cost model focused on establishing the relative benefits and trade-offs of net-shape forming versus extensive machining of simple stock shapes for each component type. The model established the potential low-cost manufacturing method and identified aspects of the manufacturing process that are cost reduction-limiting. The model can also be used to predict component cost as a function of production volume and to indicate whether customer cost targets are realistic. The final report on the process cost modeling effort has been completed.

A basic assumption of the cost modeling effort was that the slip casting, injection molding and gelcasting fabrication processes all result in equivalent yields and material properties. Since this has not been demonstrated for AlliedSignal's near-net-shape processes using AS800 silicon nitride, a new task was added to this effort. Under this task, the properties of gelcast and injection molded material will be compared with slip cast material. Taking future high temperature heat engine requirements into account, the latest composition of AS800 has been selected for this comparison. The Statement of Work for the new task is described below.

Task 5 - Evaluation of AS800 Composition 5 Material
AlliedSignal Ceramic Components has developed a higher-temperature variation of AS800 silicon currently referred to as Composition 5. The process for fabricating the slipcast version of Composition 5 is currently being scaled up and the material properties characterized under Subcontract No. 85X-SH596C. Although slipcasting is a traditional way to fabricate ceramic parts, newer net-shape fabrication approaches such as injection molding and gelcasting offer the potential for lower cost fabrication of high quantities of engine components for applications such as PNGV.

The objective of Task 5 is to apply the current injection molding and gelcasting fabrication processes developed for AS800 to the Composition 5 variation and to evaluate the mechanical properties of the resulting product. The fabrication processes, including both green forming and sintering, will be modified as required to achieve a fully dense material. Initial material property characterization will include flexural strength and stress rupture testing up to 2500°F. The data will be compared with the baseline slipcast Composition 5 as well as with standard AS800 made by similar processes.

A second level of characterization will be performed for gelcast Composition 5. Buttonhead tensile specimens will be cut from gelcast plates and stress rupture tests will be conducted at a limited number of temperatures up to 2500°F. Several material lots will be tested to assess material variability. For baseline comparison, additional tensile specimens of slipcast AS800 will be prepared and densified using the latest densification process. This will also allow an additional assessment of material property variation in standard AS800.

Technical Highlights:
Progress on Task 5, Evaluation of AS800 Composition 5 Material, continued. Mechanical testing of injection molded and machined Mil-B flexural test bars of was completed. Room temperature strength (previously reported) averaged 712 ± 34 MPa (20 bars). Strength at 1370°C (also previously reported) averaged 437 ± 25 MPa, (12 bars). Bars tested in flexural stress rupture at 1370°C at a stress of 310 MPa did not pass the 10 hour life goal. As a result, testing was conducted at lower temperatures. At 1260°C, the injection molded material met the stress/life goal.

Similar testing was conducted for machined gelcast Mil-B flexural test bars of AS800 Composition 5. Room temperature strength averaged 742 ± 54 MPa (18 bars) while strength at 1370°C averaged 522 ± 43 MPa (6 bars). These averages are similar to slipcast material. Similar to injection molded material, gelcast material passed the 310 MPa/10 hour flexural stress rupture goal at a temperature of 1260°C.

In addition to flexural testing, twenty-four (24) buttonhead tensile specimens were machined from large gelcast plates. To-date, fifteen fast fracture tensile tests have been conducted. The average tensile strength determined on ten (10) specimens tested at 1200°C was 518 ± 40 MPa. The average tensile strength determined on five (5) specimens tested at 21°C was 687 ± 53 MPa. Nine tensile specimens remain to be tested, five (5) at 1316°C in fast fracture and two (2) each at 1200°C and 1316°C in stress rupture. Although the number of tensile specimens tested is small, the room and elevated strength properties of gelcast Composition 5 material meet or exceed the room and elevated temperature strength properties of both slipcast Composition 5 and standard AS800 slipcast Composition 2 materials.

Although the flexural stress rupture results for both injection molded and gelcast material indicate a lower temperature capability than demonstrated by slipcast material, the injection molding and gelcasting processes for Composition 5 material are relatively immature and have not been optimized. The data obtained provides a good baseline for future stress rupture property improvement efforts.

Status of Milestones:
No milestones occurred during the reporting period.

Communications/Travel/Visits:
None

Problems Encountered:
None

Publications:
None

INTERMETALLIC-BONDED CERMETS

P. F. Becher and C. G. Westmoreland
Oak Ridge National Laboratory
Oak Ridge, TN 37831-6068

Objective /Scope

The goal of this task is to develop materials for diesel engine applications, specifically for fuel delivery systems and wear components (e.g., valve seats and turbocharger components). This will require materials with a minimum hardness of 11 GPa and a thermal expansion coefficient of between 10 to 15 x 10^{-6}/°C over the temperature range of 25° to 300° C. The material should also have excellent corrosion resistance in a diesel engine environment, a flexure strength in excess of 700 MPa, and a fracture toughness greater than 10 MPa$\sqrt{m}$ to ensure long term reliability. The material should also be compatible with and not cause excessive wear of the steel counter face. The upper temperature limit for fuel delivery systems applications is 540° C, and for the other wear applications, the limit is 815° C. Finally, the total material processing costs for these advanced materials should be competitive with competing technologies such as TiN or other ceramic coatings on high speed tool steels.

Technical Highlights

Based on previous studies, Cummins indicated an interest in chromium carbide as one of the potential matrix materials of interest for cermets. In addition, Cr_3C_2 has a high thermal expansion coefficient (10.3 x 10^{-6}/°C) making it attractive in efforts to match the thermal expansion of metallic alloys. As a result, cermets composed of chromium carbide with a binder phase of 20 to 30 vol. % Ni_3Al were fabricated using the melt-infiltration sintering method and characterized. Several chromium carbides exist and are available in powder form including Cr_3C_2, Cr_7C_3 and $Cr_{23}C_6$. The cermets were fabricated at temperatures in the range of 1300°C to 1400°C in vacuum or argon with 4% hydrogen.

While wetting of the various chromium carbides by the Ni_3Al and complete densification were readily achieved, cracks and defects were prevalent. X-ray analysis revealed that a single phase carbide matrix was not obtained; rather various combinations of the chromium carbide phases were found. The room temperature fracture strengths of the more defect free samples were less than 600 MPa, nearly half the values achieved with other carbide matrices. A limited evaluation of the use of FeAl as the binder phase for the chromium carbide cermets met with similar difficulties. As a result, attention is being devoted to both refining the matrix grain size (submicron) in the TiC matrix cermets and exploring other matrices.

While wear tests at Cummins Engine of the previously fabricated Ni_3Al-bonded TiC cermets demonstrated excellent wear resistance in these cermets, wear loss of the metallic alloy counter face was much higher. It can be expected that during wear processes the large TiC grain size (2 to 8 μm) in these particular cermets were less resistant to grain cleavage and fracture which would generate sharp TiC debris particles. The generation of TiC wear debris would create an aggressive abrasive media and, hence, contribute to its wear losses of the metallic alloy. Greater resistances to cleavage and fracture of the TiC grains should be possible by reducing the TiC grain size. Thus, recent efforts have centered on raw materials and processing steps to produce Ni_3Al-bonded TiC with a submicron TiC grain size.

The first approach involved attrition milling of a commercial coarse TiC powder with a particle size range of 1 to 5 microns. The particle size could be reduced to an average size of ~ 0.8 micron by attrition milling for 12 hours in isopropanol using zirconia milling media. However, the resultant submicron TiC powder was not readily wet by the Ni_3Al melt during the melt-infiltration sintering cycles for peak temperatures of 1375°C to 1600°C whether sintered in vacuum with or without 2 wt. % addition of carbon black or in argon-4% hydrogen. The carbon additions and the change to argon-hydrogen environment were undertaken to attempt to reduce any increase in surface oxides introduced during the milling of the TiC powder.

A commercially available submicron near stoichiometric TiC powder was then received, and TiC-25 vol. % Ni_3Al cermets prepared. Using melt infiltration small dense cermets samples were obtained with a 1 hour hold at 1400°C in vacuum. Microstructural analysis reveals that the resultant cermets had average TiC grain sizes of 0.5-0.9 microns. These samples contained some porosity and cracks. Larger samples have been prepared by using premixed TiC plus Ni3Al powders that were hot pressed at temperatures of 1350°, 1375°, and 1400°C using applied uniaxial pressures of 20 to 40 MPa. These samples all had average TiC grain sizes that were < 1 micron with the average grain size decreasing with processing temperature. Cummins is now evaluating the wear behavior of the first of these submicron grain size TiC-Ni_3Al cermets.

Status of Milestones

On Schedule

Communication/Visits/Travel

Jim Stephan of AMT and Kevin McNerney of Coors Ceramics visited ORNL (Dec. 10, 1997) to discuss processing and properties of intermetallic-bonded cermets being considered for diesel engine applications.

Cermet powder mixtures prepared and sent to Jim Stephan of AMT who is conducting initial processing studies at Coors facilities (January and February 1998).

Submicron grain size TiC-Ni3Al cermet sent to Cummins Engine for wear testing (March 1998).

Problem Encountered

None

Publications

None
New task started in May 1997

COST EFFECTIVE MACHINING OF CERAMIC ENGINE COMPONENTS

S. B. McSpadden, Jr.
T. O. Morris

Oak Ridge National Laboratory
Box 2008, Building 4515
Oak Ridge, Tennessee 37831-6069

Objective/Scope

To develop and demonstrate optimized, cost-effective grinding processes for the production of ceramic components for use in diesel engines.

Technical Highlights

Cooperative Research And Development Agreements (CRADA's) Established

CRADA's were implemented to cover joint efforts with Cummins Engine Company and Caterpillar, Inc. The Cummins CRADA, entitled *Precision Grinding of Components for Diesel Fuel Systems Applications*, has been signed and is nearing completion. The Caterpillar CRADA, entitled *Studying the Scuffing Resistance of Zirconia Fuel Injector Components for Diesel Engine Applications*, was recently signed and work is in progress. The total value of each CRADA is $120,000, and the performance period is one year.

High-speed Grinding on the Cincinnati Milacron Centerless Grinder

High speed centerless grinding is being investigated as a cost-effective method for producing ceramic engine components. The process is attractive because the need is eliminated for workpiece fixtures and workpiece alignment. Compared to other grinding processes, centerless grinding is fast, wheel wear rates are low (due to the large surface area of the grinding wheel), and the process produces high quality parts.

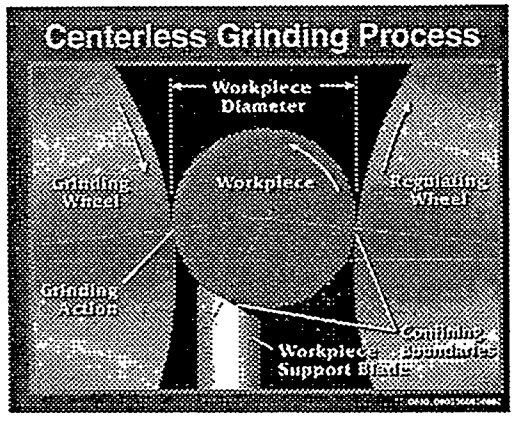

Figure 1. The centerless grinding process eliminates complicated part fixturing problems.

Recent research has demonstrated that grinding at higher wheel speeds can also dramatically reduce the cost of grinding by reducing cycle times and lowering wheel wear rates. Conventional low-speed grinding is not cost effective due to relatively high cycle times, high wheel wear, and low stock removal rates. However, there are barriers to the successful implementation of high-speed grinding. Conventional grinding machines are seldom designed and built to accommodate the higher wheel speeds associated with high

speed grinding. Maximum wheel speeds on such machines are typically 45 to 60 m/s [9,000 to 12,000 surface feet per minute]. In addition, the grinding wheels themselves are seldom designed and rated for use at high speeds.

Initial centerless grinding tests with a new-design, high-speed, vitrified-bond, diamond grinding wheel manufactured by Cincinnati Milacron indicate that drastic reductions in per-piece grinding

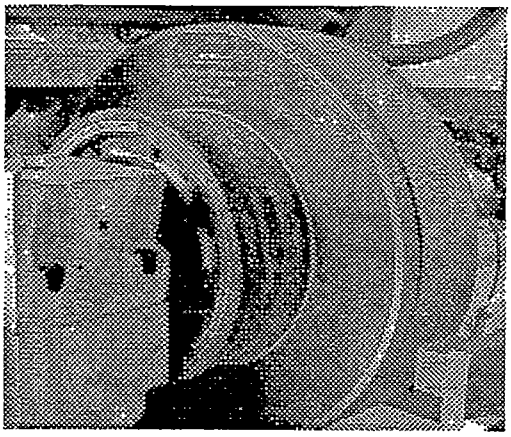

Figure 2. A light-weight, composite-core, vitrified-bond, diamond abrasive wheel is a key component for high-speed centerless grinding.

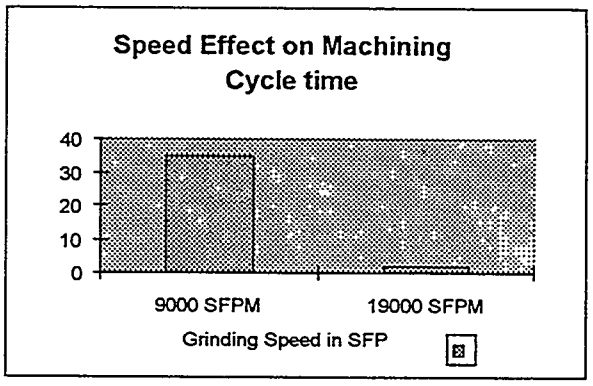

Figure 3. High-Speed cylindrical grinding offers the potential for dramatic cycle-time reductions.

cycle time can be achieved on ceramic diesel engine components such as exhaust valves. An Allied Signal GS-44 silicon nitride tensile specimen, which previously required a 35 minute cycle time to grind on a centerless grinder at conventional wheel speeds, was ground to the required finished geometry in approximately two minutes. The new wheel was operated at a surface speed of 97 m/s (19,000 surface feet per minute). Following this initial test, five specimens were ground under even more aggressive conditions to achieve a cycle time of approximately 40 seconds.

However, centerless grinding is not a simple, trouble-free process. The process is difficult to optimize and control, especially when small batches of parts are being ground. As with any high-volume process, centerless grinding works best when the equipment can be run for an extended time period without interruption. After very promising initial successes, several minor setbacks occurred during the grinding of ceramic tensile specimens, which illustrate some of the difficulties associated with the process. Despite these setbacks, valuable lessons were learned.

A group of GS-44 silicon nitride specimens was pre-ground on the Weldon cylindrical grinder to simulate near-net-shape blanks. The specimens fractured unexpectedly during the centerless grinding operation. It was subsequently discovered that their geometry was slightly different from the group that had been used previously in the successful centerless grinding work. When high stock removal rates were attempted with the accompanying higher grinding forces, the resulting bending moment became large enough to cause the ceramic blank to fracture during the grinding operation. *The lesson learned is that it is extremely important to maintain careful control of the shape of sintered ceramic blanks for the subsequent centerless grinding process.* The shape of

the ceramic blank must closely match the contours of the dressed grinding wheel, the work rest blade, and regulating wheel. Otherwise, the contour mismatch can result in unacceptably high bending moments along the surface of the blank. Although excessive bending moments are more likely to occur with a tensile specimen geometry than with an engine valve geometry, careful attention must be paid to the geometry of *any* blank used in a centerless grinding process. Efforts to produce precision blanks to "near net shape" will pay dividends in the later process of grinding the final geometry.

The uncontrolled fracture of the tensile specimen blank in the centerless grinder caused gouging of the vitrified-bond grinding wheel – resulting in a relatively expensive redressing operation. The vitrified-bond centerless grinding wheel was re-dressed to remove the minor damage sustained when the specimen fractured, and was restored to the correct shape. Two new dressing wheels containing hand-set diamonds were ordered to replace the existing wheel, which was almost completely expended by the numerous dressing cycles that were performed. The remaining blank tensile specimens were reworked to correct the problems with their contours.
After the grinding wheel was re-dressed with the new dressing wheel and the geometry of the ceramic blanks was corrected, the centerless grinding experiments resumed. Although extreme care was used to ensure that the process was set up correctly, the tensile specimens continued to break during the centerless grinding operation – in some cases, within just a few seconds of completion of the grinding cycle.

After several days of investigation, the problem was traced to excessive wear on the work rest blade. The stationary work rest blade, which supports the specimen during the grinding operation, is made of tungsten carbide. It is normally very resistant to wear. However, the material may not be adequate for centerless grinding of silicon nitride parts. Figure 3 shows an excessive wear pattern observed on the work rest blade after grinding fewer than 50 parts. It is believed that the wear is severe enough to cause the part to fracture during grinding. The worn blade is being refurbished with a diamond-coated carbide wear surface. Wear on the work rest blade is not readily apparent during normal operation of the grinder. *The lesson learned is that frequent inspection will be required when the equipment is used to grind silicon nitride material.* As with the dressing wheels described above, the work rest blade is also specialized and requires several weeks lead time to procure. For this reason, a spare blade is also being obtained. *A secondary lesson learned is that spare critical components and supplies should be ordered wherever feasible, to avoid costly delays.*

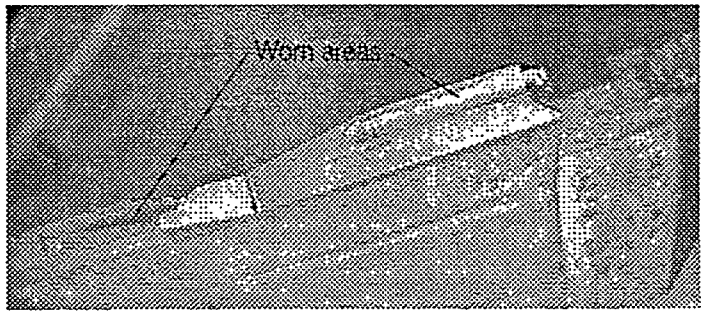

Figure 3. Excessive wear on tungsten carbide work rest blade.

High-Speed Grinding on the Weldon Cylindrical Grinder

Mr. Mike Bowling of Cummins Engine Fuel Systems Division Ceramic Technology Center machine shop spent several days at the HTML performing high-speed grinding studies on the instrumented Weldon cylindrical grinder. This was a continuation of previous work performed under the HTML user program. Additional grinding tests were run by the Machining and Inspection Research User Center staff after Mr. Bowling's visit as a part of the ongoing CRADA with Cummins. The tests were designed to measure grinding ratios (volume of workpiece material removed divided by the volume of wheel material expended) for Si_3N_4 and Zr_2O_3 specimens under various grinding conditions. A vitrified-bond, cubic boron nitride (CBN) wheel was used, and wheel speed was varied from 35 to 125 m/s. Preliminary results show a dramatic improvement in grinding ratio for the Si_3N_4 parts that were ground at 125 m/s. Grinding forces were also measured during these tests and the results are currently being analyzed.

Surface finish and roundness were measured on a series of parts using spark-out times of three and ten seconds. The inconsistency of the results was disappointing, but the experiment emphasized the need to improve the performance of the grinder. An investigation of the present condition of the grinder revealed several mechanical problems that were impacting our ability to collect reliable data and to control accurately the geometry of parts produced. These problems included mechanical backlash in the lead screws, excessive vibration and noise from unknown sources, suspected problems with digital position-readout lights, and mechanical alignment errors. Most of the problems were primarily due to normal wear and tear associated with equipment use.

Since the Weldon cylindrical grinder is potentially our most important machine, we will take whatever steps are necessary to make it as accurate as possible, consistent with our available resources. A dynamic vibration analysis was performed to determine the magnitude and source of vibration components. This will help to pinpoint mechanical components that may need to be damped, repaired, or redesigned. The mechanical alignment of the major machine components (head stock, tail stock, spindle, etc.) is being verified and corrected. If necessary, a field service technician from Weldon will perform maintenance on the spindle and leadscrew bearings and the machine controller.

Communications/Visits/Travel

Cummins Engine Fuel Systems Division personnel visited Oak Ridge and made a presentation on manufacturing processes for their current and prototype ceramic fuel system components. Cummins is making good progress with the introduction of ceramic materials into their fuel system designs. Manufacturing costs are still higher than desired but the benefits of the ceramic materials outweigh the costs. Their favorable experiences with ceramic materials to date encourage continued efforts both in reducing the costs and expanding the applications of ceramic components.

Dr. Raj Tandon of Caterpillar, Inc. visited the HTML to finalize details of the CRADA work plan.

Sam McSpadden and Tom Morris visited Cummins Engine Fuel Systems Division in Columbus, IN, to observe cylindrical grinding of ceramic specimens on the Studor grinder. Grinding ratio results obtained on this machine were similar to results obtained on the Weldon grinder at the HTML.

Sam McSpadden and Tom Morris visited Cincinnati Milacron to discuss centerless grinding problems and grinding wheel technology.

Publications

A paper on *Cubic Boron Nitride High Speed Grinding of Zirconia and M2 Steel* has been accepted for presentation at the Twenty-Sixth North American Manufacturing Research Conference (NAMRC) in Atlanta in May.

TESTING AND CHARACTERIZATION

X-Ray Computed Tomographic Imaging

W. A. Ellingson, E. R. Koehl, H. P. Engel (Argonne National Laboratory), and D. Twait (AlliedSignal Ceramic Components)

Objective/Scope

The objective of Phase III was redefined to the study of 3D density variations in slip cast GS-44 material with chopped carbon fiber. GS-44 material with chopped carbon fiber is being developed as a candidate material for diesel engine valve guides with reduced wear. Caterpillar is a cooperating partner. The selected approach to the nondestructive evaluation of this material is 3D x-ray computed tomographic imaging with an emphasis on the correlation of image data with subsequent destructive analysis of the sample.

Technical Highlights

The technical highlights will be described in four areas:
1) Completion of the AS-800 densitometry studies;
2) Discussion of the CRADA work on the new amorphous silicon detector;
3) Discussion of dual-energy x-ray CT technology; and
4) Discussion of the new GS-44 specimens.

1)-Densitometry studies of AS-800

The effort to further analyze the end anomalies shown in axial density profile curves is still inconclusive.

2)-X-Ray Detector (Amorphous Silicon) CRADA

The ANL - EG&G CRADA, signed on August 4, 1997, is testing EG&G's new amorphous silicon detector. This detector is a fast, high-sensitivity, x-ray area detector which will be used for sensing density gradients in materials such as the GS-44/chopped carbon samples being developed by Allied-Signal Ceramic Components, Torrence, CA. The agreement specifies that ANL will receive a 1024 x 1024 area detector, which ANL will use to investigate the resolution capability in ceramic materials studies.

Manufacturing problems delayed receipt of the detector until March. EG&G delivered the new area detector, model MX-1024, s/n 002, on March 17. This detector is a 2-dimensional array of 100 um pixels, 10 cm by 10 cm square with a 16-bit dynamic range (see Fig. 1). Heat dissipation methods are under development because of a need to dissipate 30 watts of heat. An aluminum frame to allow convection cooling to ambient room air has been designed and is being fabricated at ANL.

As a part of this CRADA, ANL began to develop and assemble a third x-ray imaging system for exclusive use with the new detector (see Fig. 2). This system utilizes an available Kevex 125 kVp x-ray head. The software to be used will borrow from the experience gained in the use of National Instruments LabView control software employed on earlier systems. LabView was selected to control the motion of the translation stages and

acquire the data from the detector largely because it is a relatively easy system to use and also because it has a large driver interface library. An open-frame design of the new x-y motion stages allows positioning samples as close as 10-13 cm in front of the detector plane (dependent on the sample diameter). Our x-y stages on the 160 kVp CT system allow the sample no closer than 4.5 to 4.7 cm in front of the detector plane.

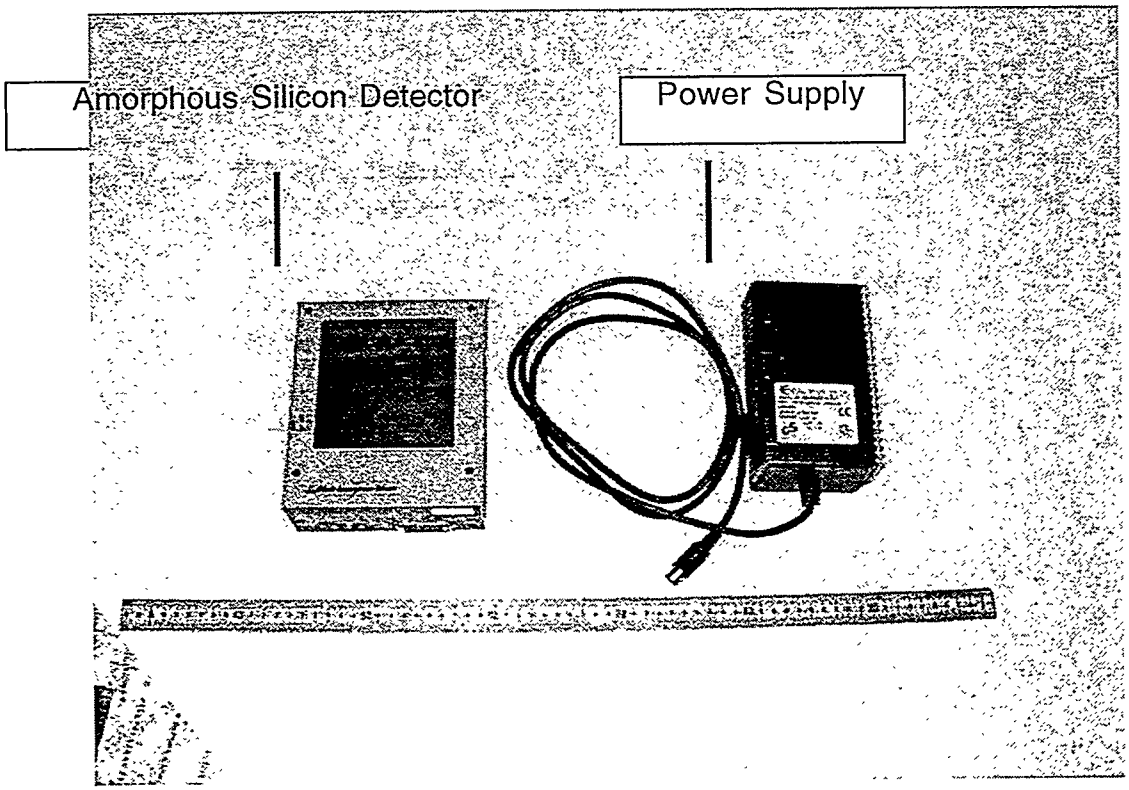

Fig. 1. Photograph showing new amorphous silicon X-Ray detector and power supply

The control CPU, software, and translation stage hardware have been assembled and the table, remote shutter all are in place.

A significant effort this period was on selection of the appropriate detector interface hardware. Candidate interface boards were considered from National Instruments, Eltech GmBH (Germany), and Dipix Technologies.

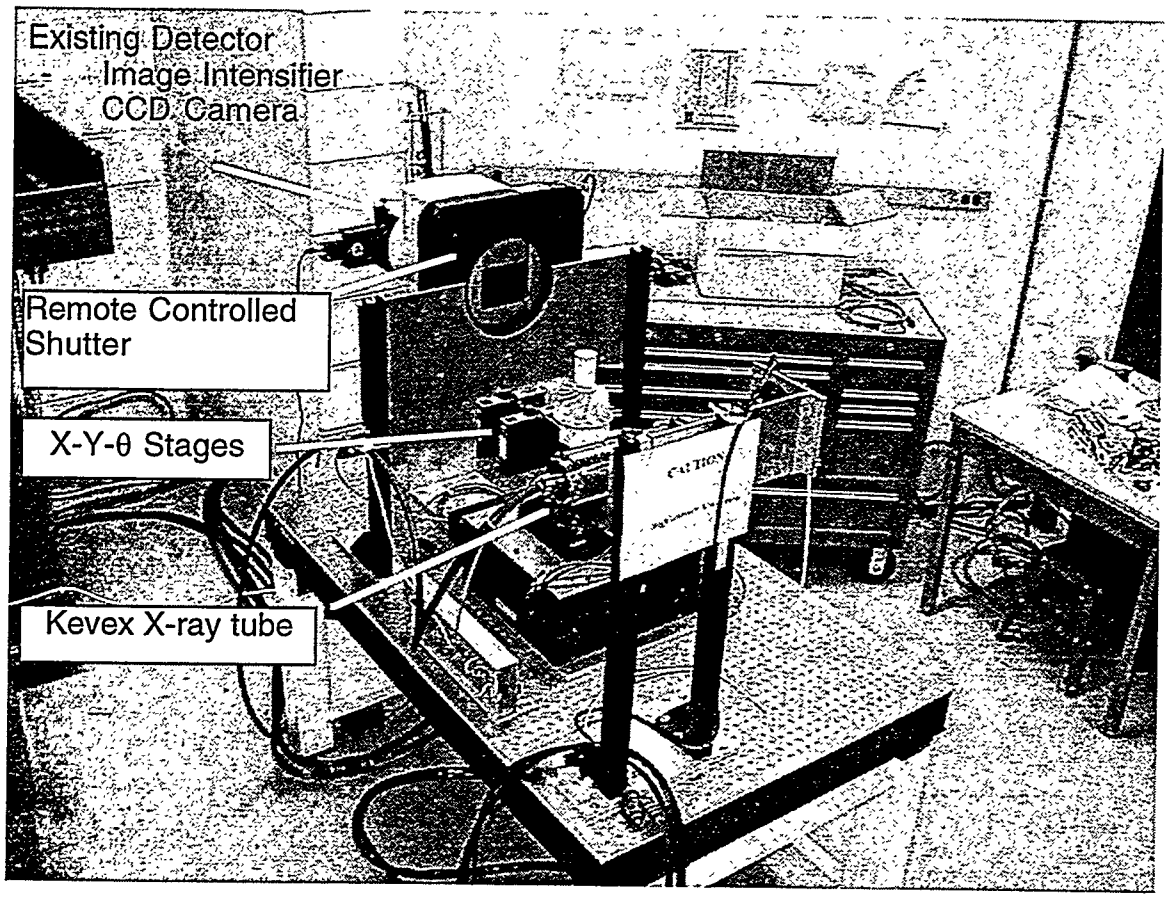

Fig. 2. Photograph of new 125 kVp microfocus X-ray for amorphous silicon detector study

National Instruments – PCI-1424

Since this is a new product, it has no track record. But it is based upon mature 8-bit digital interface technology, and readily interfaces to National Instruments LabView software. This item was voted as third choice because of cost and performance uncertainties at this time.

Eltec GmBH

Although this is used by EG&G as a customized product from Eltech GmBH in Germany, there are no standard software drivers available for this interface at present. Use of this product would require the generation of a custom virtual interface driver. Since EG&G uses this interface, they were willing to support software development. This item was chosen as option two – software development is not a desired project at this time.

Dipix Technologies – models LPG132 or XPG-1000

ANL has experience with Dipix hardware in our high-performance infra-red imaging applications. Dipix has developed a software interface control package compatible with LabView.

The XPG-1000 was chosen as the preferred interface. It is a mature, well understood, technology with a proven track record in both performance and after sales customer support.

The Dipix Technologies model XPG-1000 was selected and ordered as the detector interface hardware. This board accepts 16-bit digital input at 48 Mb/sec.

3)-Dual Energy Tomography

Dual Energy Imaging Computed Tomography (DECT) is a process that enhances reconstruction tomograms by obtaining images of the same object taken at two different x-ray energies. In the process, the x-ray imaging system needs to be calibrated using two so-called "basis" materials, which are selected to span the densities and atomic numbers of the sample materials under study. Originally, this technology was to be used on materials comprised of a mixture of silicon-based ceramics and carbon. For these samples, the atomic number for Si_3N_4 ranges from 10 to16, and for carbon as low as 6. The density of the materials to be studied ranges from about 1.5 g/cc to about 4 g/cc.

DECT procedures use step wedge "phantoms" of appropriate basis (or calibration standard) materials to obtain attenuation functions of these materials at the two x-ray energies that will be used in the study. Four basis functions (two functions for each material) model the X-ray attenuation of the basis materials as a function of their thicknesses. These attenuation functions are intended to be nearly linear.

The basis functions are used to correct a reconstructed sample tomogram, pixel-by-pixel. The results provide one sample image based on atomic number and one sample image based on density.

As part of the effort to develop the dual energy software, ANL had lucite, titanium, magnesium, and graphite step wedges produced in-house (see Fig. 3). These wedges provide the needed x-ray attenuation coefficients as a function of thickness for the materials under study.

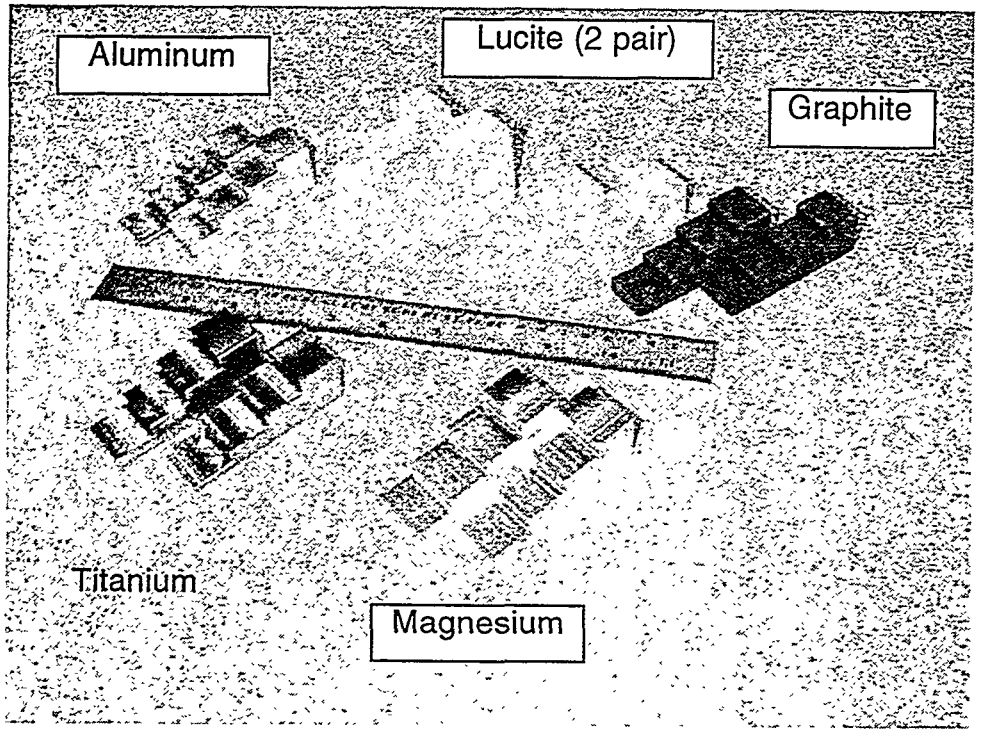

Fig. 3. Photograph of step wedges being used for dual energy algorithm development

DECT techniques and algorithms reported in the literature were coded into software routines using Research Inc., Interactive Data Language, IDL 5.0. The IDL routines also included part of the Cone Beam reconstruction code developed by Ann Sivers. At present, only a linear fit of the basis functions has been investigated.

This effort is focusing on the analysis of the GS-44/chopped carbon samples from Allied-Signal Ceramic Components. In this case, the carbon fibers have an atomic number of 6 and a density of 2.06. The GS-44 material, pre-sintered Si_3N_4, has an atomic number of about 12.3 and a mass density of 1.8-1.9.

4)-GS-44 Specimens

Initial examination of fully densified GS-44, half-cylinder specimens failed to disclose positive evidence of carbon fiber distribution. These specimens contained 10 and 12.5 vol. % chopped carbon fibers. In order to enhance spatial resolution and improve the detection sensitivity, a special 90° drive off-set motion control stage was investigated and procured. This design allows small diameter specimens to be positioned to within 25 mm of the X-ray source, thereby allowing higher magnification and improved detector sensitivity to the fiber distribution.

TESTING AND EVALUATION OF ADVANCED CERAMICS AT HIGH TEMPERATURES

J. Sankar, A. D. Kelkar and Q. Wei (Department of Mechanical Engineering, North Carolina A&T State University, Greensboro, NC 27406)

Objective/Scope

The objective of this research is to test and evaluate the long-term mechanical reliability of a Si_3N_4 at temperatures up to 1300°C.

The required research includes four (4) major tasks:

Task 1. Cyclic Fatigue Testing of PY6

Cyclic fatigue of GTE-PY6 silicon nitride shall be performed at lower temperatures to investigate 500°-1100°C characteristics of the material at this temperature range. At these lower temperatures, there may be a true cyclic fatigue effect which enhances failure compared with the static load case.

Task 2. Stress-Rupture Study of PY6

Stress-rupture testing of GTE-PY6 silicon nitride shall be performed at a lower temperature range of 500°-1100°C. Since there is little information about the time dependent behavior of this material available in this temperature regime, this task should provide some valuable data.

Task 3. Tensile Testing of GS44

Pure uniaxial tensile testing of GS44 silicon nitride will be carried out at both room and elevated temperatures up to 1200°C. The obtained data will be compared with other silicon nitride materials.

Task 4. Stress-Rupture Study of GS44

Stress-rupture testing of GS44 silicon nitride will be performed at various temperatures and stresses.

TECHNICALHIGHLIGHTS

During this reporting period, we have utilized analytical transmission electron microscopy (TEM) and high resolution transmission electron microscopy (HRTEM) to study the microstructural changes of a sintered silicon nitride, GS44, at an atomic level associated with thermal soaking in air.

GS44 has been designed as an in situ self reinforced silicon nitride ceramics. The microstructure of GS44 is characterized by elongated silicon nitride grains with an approximate aspect ratio of 11. This ceramics has high fracture toughness as compared to the conventional silicon nitride ceramics composed of equiaxial grains. The average fracture toughness can be 8.0 $MPam^{1/2}$ and up. GS 44 has been designed for applications at or below 1000°C. However, in our study, we soaked the samples at 1275°C for scientific understanding. Another reason for this study is that through creep experiment on this material, we have observed that the creep resistance of GS44 is reduced at temperatures higher than 1200°C as compared to 1000°C. The goal of this study is to have a better understanding of the changes of the microstructure, especially the behavior of the grain boundary phases, at an atomic level, as pertinent to the mechanical behavior at high temperatures of silicon nitride.

Briefly, based on the experimental observations and theoretical discussions in this work, the following conclusions can be drawn. The GS44 Si_3N_4 ceramics has been severely attacked even inside the material, most probably by oxygen, during high temperature exposure to air. The originally distinctly shaped Si_3N_4 grain boundaries and triple junctions became more rounded and the apparent volume fraction of the amorphous phases was increased due to high temperature thermal soaking. The edges of some silicon nitride grains have been turned into amorphous state. Studies on samples prepared with the electron transparent region deliberately located in various regions showed that in general the thickness of the amorphous grain boundary phase expanded due to soaking. The clear-cut atomic steps or the faceted Si_3N_4 grains that showed ledges along the grain boundaries were smeared out. All these changes could be explained on the basis of oxygen attack through fast path diffusion of oxygen species along the grain boundary phase, surface diffusion in the micropores or even through volume diffusion in the Si_3N_4 grains along specific orientations. This may contribute to a better understanding of the high temperature behavior of this material in oxidizing atmosphere.

RESULTS AND DISCUSSION

In order to understand the microstructural changes associated with the thermal soaking process of GS44, we conducted detailed observations using both high resolution and analytical transmission microscopies. It was focused on the microstructural changes along the intergranular amorphous phases and at the triple junction phases, as well as the geometry and apparent volume fraction of the amorphous phases and Si_3N_4 grains themselves. Information of these problems is crucial for the application of silicon nitride because of its importance in determining many of the high temperature mechanical and physical properties of silicon nitride fabricated via various techniques. A theoretical model proposed by Clarke and Clarke and co-workers suggests an equilibrium thickness for the intergranular amorphous film that is of the order of 1 nm regardless of the technique employed to produce the material. The origin of this "stable" thickness is shown to be the result of two competing interactions, an attractive van der Waals-dispersion interaction between the grains on either side of the boundary acting to thin the film and a repulsive term, due to the structure of the intergranular liquid, opposing this attraction, and probably one more effect from the electric double layer contribution. Clarke's model has been verified experimentally since its publication, both by conventional TEM and HRTEM observations. Recently, a more detailed and more general theoretical consideration has been proposed based upon molecular-dynamics simulation concerning the thermodynamic origin, structure and stability of the thin amorphous films found in grain boundaries in covalent ceramics like silicon nitride, with an equilibrium width slightly larger than predicted by Clarke's model. Another model experiment on the thermodynamic stability of retained intergranular amorphous films showed that a remnant amorphous layer about 1.5 nm thick can exist at equilibrium. On the other hand, there is still a paucity of information in the literature concerning the behavior of the intergranular as well as multiple junction phases at elevated temperatures. A few investigations on sintered and HIPed Si_3N_4 showed that there were certain changes in terms of volume fraction and geometry of the amorphous phases associated with high temperature annealing.

Fig. 1 is a set of TEM micrographs from the cross-sectional GS44 sample soaked at 1275°C for 40 hours. The perforation was made from the oxide scale and extended

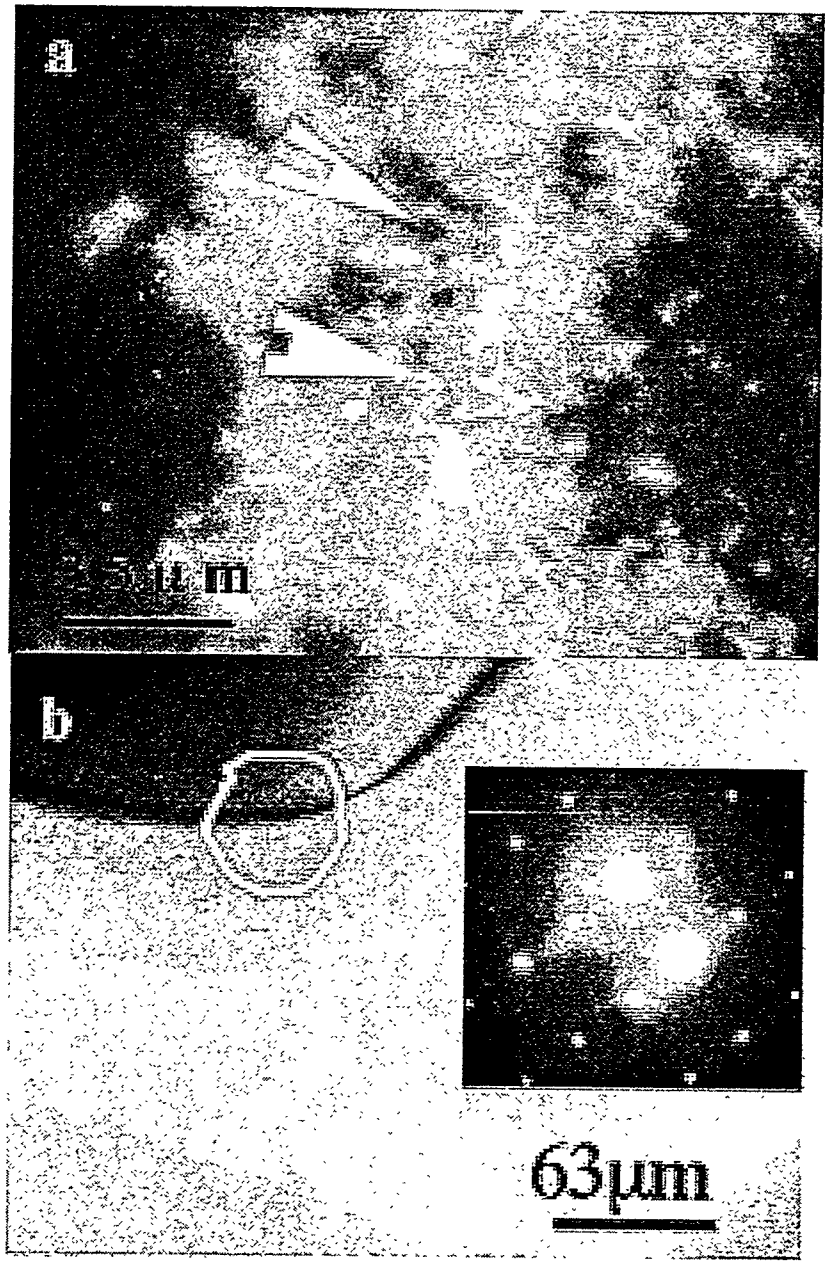
a
b
63µm

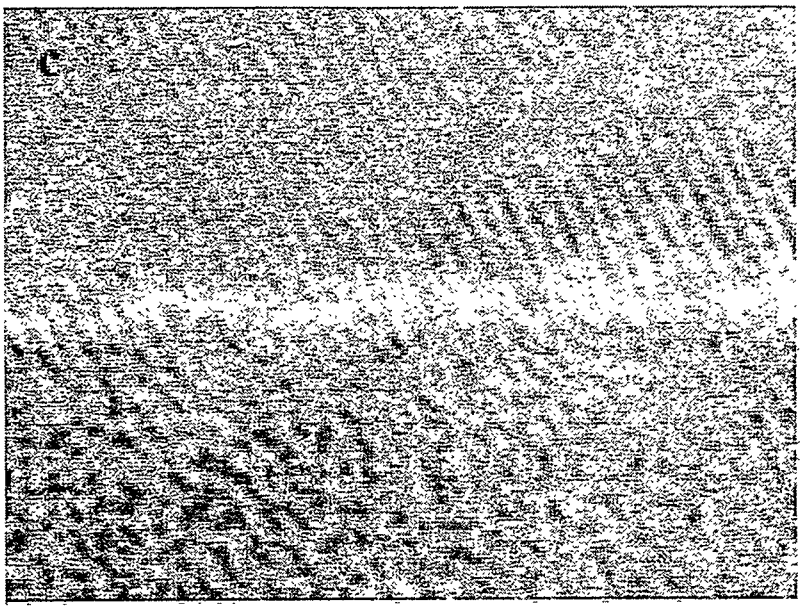

Fig.1 TEM micrographs of GS44 soaked at 1275°C for 40 hours. The electron transparent region was located in the oxide scale and extended into the interior of the material. It shows low magnification image of distinct interface between the scale region and the matrix (a), some part of the silicon nitride grains has become amorphous (b) and HRTEM lattice image (c) of the amorphous region in (b).

into the interior of the material. In Fig.1a, the bright field low magnification image, we can see a distinct interface between the scale region and the matrix silicon nitride bulk, as indicated by the arrow in the image. Also a lot of micropores are present in the sample, with some of them having worm-hole-like shape that has just been reported recently. We studied in detail one of the pore regions and found out that the Si_3N_4 grains in the region have been heavily attacked by oxygen and a considerable part of these grains have been turned into amorphous state, as shown by Fig. 1b. The inset of Fig. 1b is a diffraction pattern from the Si_3N_4 grain. This again evinces that micropores in the sintered Si_3N_4 material can play the role of oxygen transport path at elevated temperatures and will thus degrade the material. Fig. 1c is the HRTEM image of the circled region in Fig. 1b showing the vitrified silicon nitride grain edge. Also clear from this set of TEM images is that the previously distinctly shaped Si_3N_4 grains became more rounded after high temperature thermal soaking. This kind of phenomenon was first reported by Clarke. However, in that investigation, the samples were quenched from high temperatures either in N_2 or H_2 atmosphere.

Fig.2 is an HRTEM image taken from a region very close to the scale of the soaked GS44. It shows the intergranular amorphous phase of a thickness larger than 8 nm, much greater than the equilibrium thickness for grain boundary films as observed in the

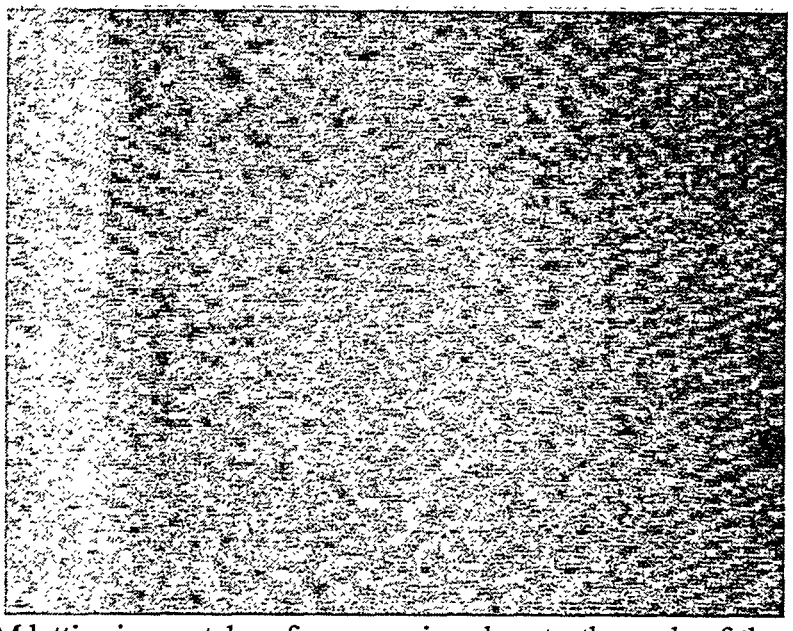

Fig. 2 HRTEM lattice image taken from a region close to the scale of the soaked GS44 showing an intergranular amorphous phase of a thickness of more than 8 nm.

as sintered samples. This expansion of the intergranular amorphous phase as a result of high temperature heat treatment of Si_3N_4 ceramics (HIPed or sintered) under various conditions has been reported also by some other authors, though contradictory result has also been reported that showed a decreased thickness of the amorphous intergranular film following oxidation. Cinibulk, et al., in their study of the effect of oxidation on the intergranular phases in silicon nitride ceramics observed intergranular phase depletion at both multigrain pockets as well as two-grain boundaries due to the outward diffusion of cations to the surface of the sample that led to a reduction in impurity concentration and resulted in the thinning of the grain boundary films. While outward diffusion of additive and impurity cations along amorphous grain boundary phases which at high temperatures usually act as rapid diffusion paths have long been recognized, its effect on the evolution of the geometry and thickness of the intergranular phases has rarely been fully understood. Therefore, more detailed studies, both theoretical and experimental, will be necessary to account for the diffusion of the cations as well as anions along the amorphous grain boundary phases and its role in the oxidation behavior at high temperatures. A reasonable presumption can be made at this point that the effect of high temperature holding of Si_3N_4 on the intergranular phases involves a competing process between the outward diffusion of the cations, which will presumably produce a reduced film thickness, and the inward diffusion of oxygen species which will attack the Si_3N_4 grains *en route*, and will tend to encroach the Si_3N_4 grains through oxidation and to expand the thickness of the intergranular films. The driving force for both of the competing processes stems from the chemical potential difference of the diffusion species. As for which of the two processes will predominate the overall reaction depends on a number of factors. Basically, the sintering additives dictate the chemical composition and morphology of the retained amorphous grain

boundary phases and multiple junction phases and combined with the processing parameters will affect the amount, type and distribution of impurity cations in the material. For example, it has been found that Y_2O_3 doped Si_3N_4 has poorer oxidation resistance than MgO doped Si_3N_4. While the amount, type and distribution of additives would have effect on the cation diffusion at high temperatures, they would also have strong effect on the inward diffusion of oxidant such as oxygen species. Thus a theoretical model should be capable of allowing for this complex, two-fold factor. This is understandable invoking the knowledge of the ionic conductivity of different oxide additives at elevated temperatures. Also crucial for the consideration of oxidation behavior of Si_3N_4 ceramics is the porosity of the material. This will in turn depend on the additives and the processing technology employed to prepare the material. The distribution, the connectivity and the number of micropores have significant effect on surface diffusion processes of oxygen into the material and will therefore affect the oxidation behavior. This may be one of the main reasons for the difference in oxidation behavior of sintered or HIPed Si_3N_4 and Si_3N_4 prepared through chemical vapor deposition(CVD) technique. They differ not only in the products of oxidation, but also in the kinetic behavior of oxidation. In the case of Si_3N_4 with micropores, the first stage is usually the transportation of oxygen through the pores into the bulk, as well as the closing of the pores by the formation of an oxide scale. This stage is usually very rapid and is followed by a largely reduced oxidation rate.

Fig. 3 is an HRTEM image taken from a region very close to the interface between the first annular ring and the interior part of normal, unchanged color. Again, an intergranular film of thickness of ~10 nm, which is much larger than the average of the virgin

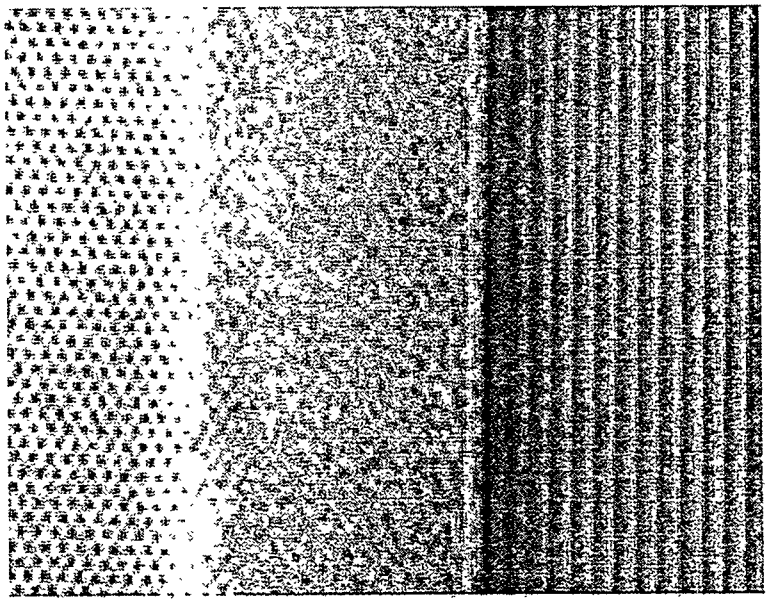

Fig. 3 HRTEM image taken from a region close to the interface between the first ring and the interior part of normal, unchanged color, showing an amorphous grain boundary phase ~10 nm thick.

sample, is observed. This expansion of the intergranular amorphous phase can be discussed with the ideology *in loc cit.* It is interesting to point out for the time being that while in the as sintered Si_3N_4 sample, distinctly faceted Si_3N_4 grains along the grain boundary phases can be frequently observed, where well defined atomic ledges can be seen clearly, it is not the case in the soaked samples. In the latter case, most of the faceted features have been smeared out, which is probably due to the oxygen attack during thermal soaking. Since the atomically sharp ledges or steps are usually of high free energy, they are therefore energetically favored for encroachment by oxygen attack. More experimental observations will be presented in the context to follow for some other regions of the soaked samples.

Fig.4 is a set of conventional TEM images with the perforation of the TEM sample deliberately located in the region between the first annular ring and the second annular ring. The color of this particular region has rarely been changed. Fig.4a is a bright field image showing the general microstructure in this region. Micropores and the so called worm-hole like pores are indicated by arrows. Fig. 4b is a higher magnification bright field image. A feature similar to that detected in Fig.1 can be observed; namely, Si_3N_4 grains with more rounded shape and increased apparent volume fraction of the amorphous phase. Fig. 4c is a dark field image showing the amorphous phase. Here we can also observe a devitrified grain boundary phase. This can be identified with the help of the fringes in the grain boundary phase which should be absent if the grain boundary phase is amorphous. While there have been some reports of the devitrification of amorphous grain boundary phases or triple junction phases in Si_3N_4 ceramics associated with high temperature post heat treatments, its occurrence in this study was not significant. Fig. 4d is a bright field image of several grains, their boundaries and triple junctions. To have a more detailed look into these boundaries and junctions, HRTEM studies were conducted. Fig. 5 shows two HRTEM lattice images taken from the triple junctions and grain boundaries from Fig. 4 (d). Though the expansion of the grain boundary phase and the triple junction phase is not remarkable in this region, the atomic ledges that were present in the virgin sample are again lost.

Fig. 6 gives two bright field TEM images of the triple junctions from the inner annular ring region. Even though it has been acknowledged that Fresnel fringe technique produces an image of the intergranular phase about 50 % larger than determined by HREM lattice fringe technique, it is still clear from the two micrographs that the grain boundary phases are much larger than observed in the virgin sample. We attribute this change in intergranular film thickness again to the oxygen attack during high temperature soaking in air.

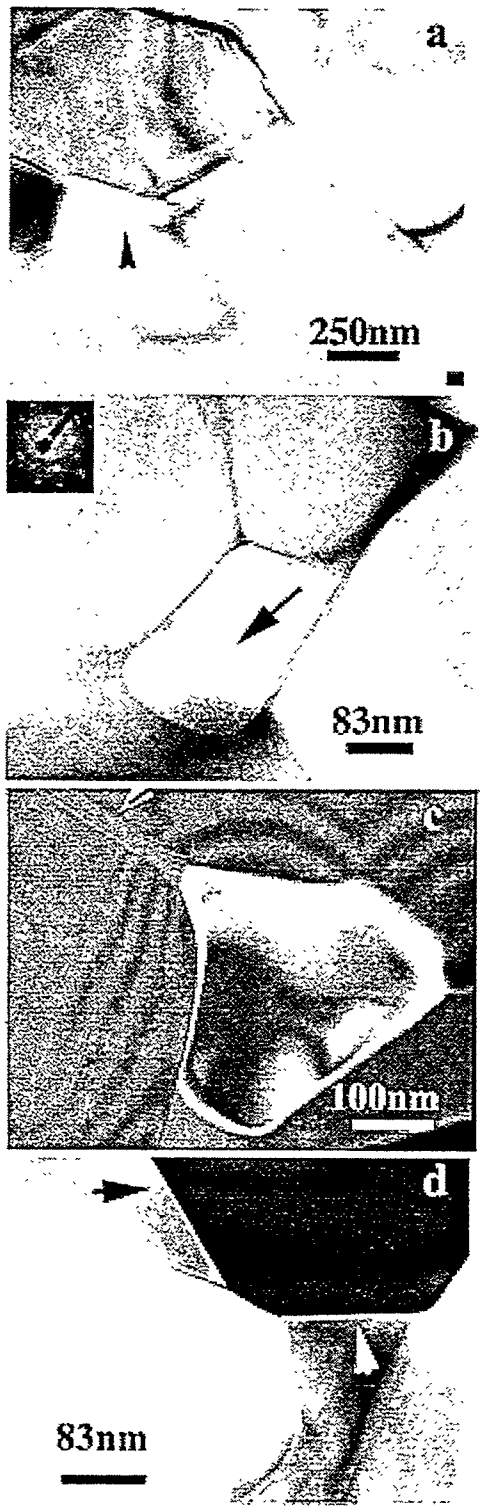

Fig. 4 Electron micrographs from the region between the first ring and the second ring, showing general view of the microstructure with micropores (a), the vitrification of Si_3N_4 grains (b), devitrification of the grain boundary phase (c) and grain boundaries and triple junctions (d).

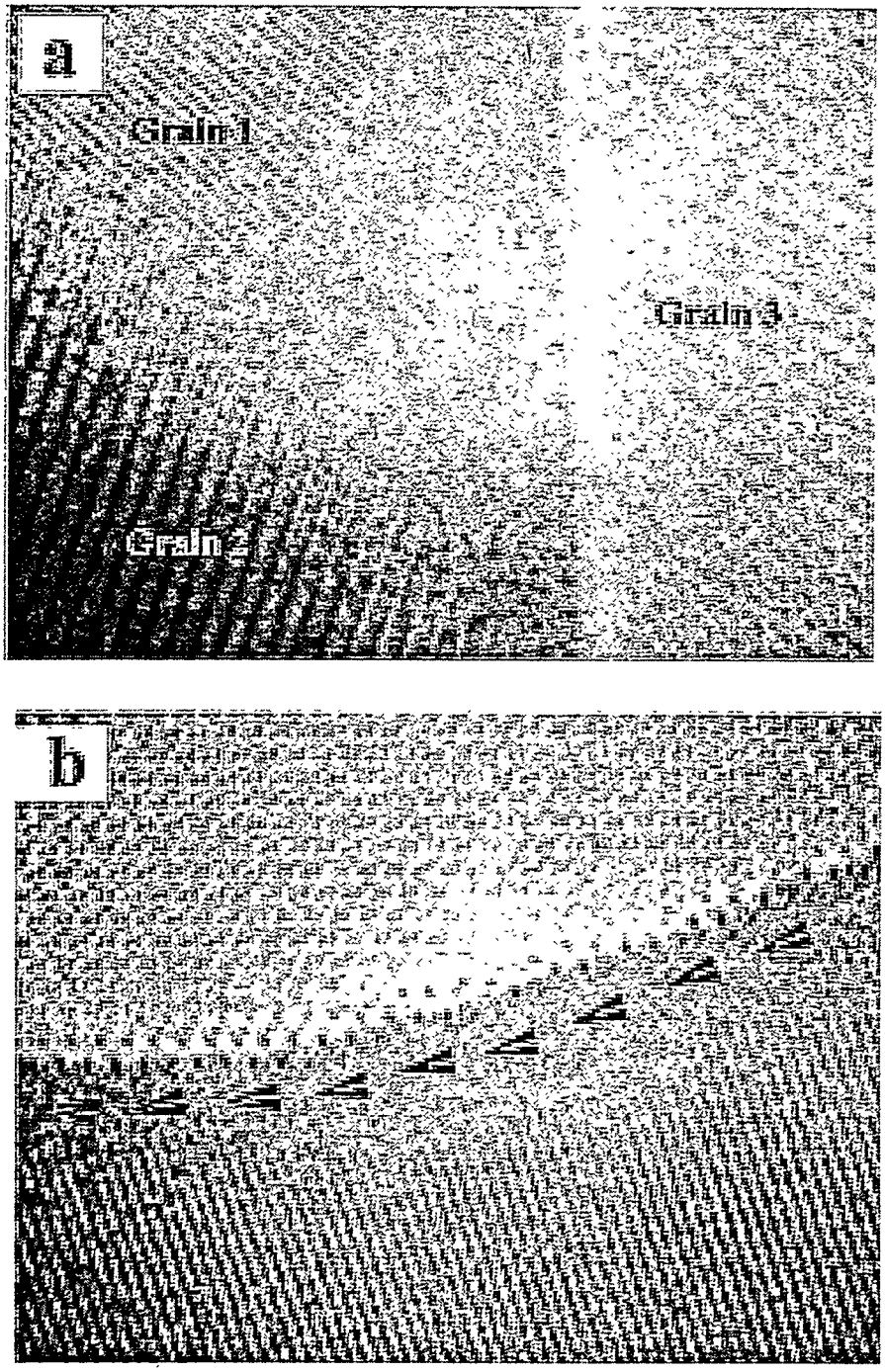

Fig. 5 HRTEM lattice images taken from the triple junction and grain boundary area of Figure 6 (d). They show smooth and relatively rounded Si_3N_4 grain edges as compared to the virgin GS44 sample.

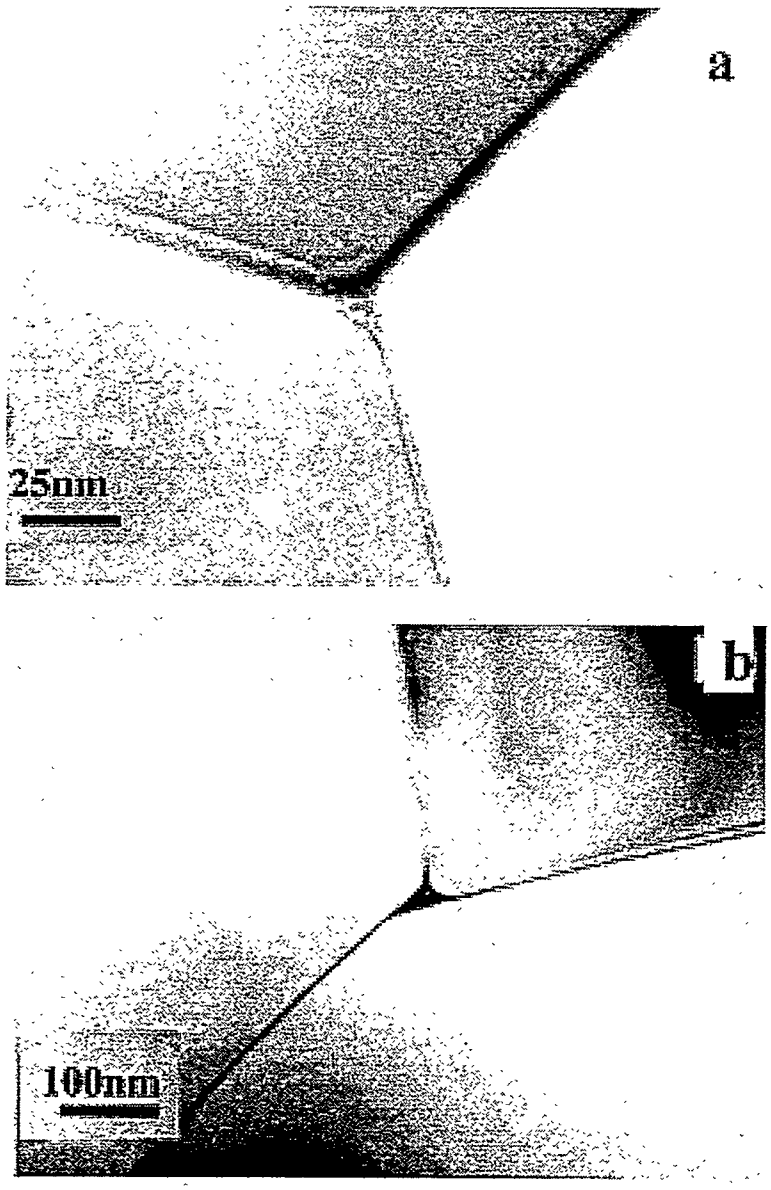

Fig. 6 Bright field TEM micrographs from the inner ring region, showing two triple junctions and the associated grain boundary phases with thickness much larger than observed in the virgin sample.

Lastly, it should be mentioned that in the β-Si_3N_4, there is a cylindrical open channel of 0.145 nm in radius along its **c** axis. This large continuous channel may enable large atoms to diffuse readily through the lattice. Oxygen species may move through the channels at high temperatures and perturb the silicon nitride grains by formation of Si-N-O bonds or even Si-O bonds to replace the strong Si-N bonds.

Status of Milestones

On schedule

Communications/Visitors/Travel

None

Publication

1. Q. Wei, J. Sankar, J. Narayan and A. Kelkar, Transmission Electron Microscopy of the Microstructural Changes of a Sintered Si_3N_4 Associated with High Temperature Soaking in Air, presented on 39th AIAA/SDM Conference, Long beach, California, April, 20-23, 1998.
2. Q. Wei, J. Sankar, J. Narayan and A. Kelkar, The effect of high temperature thermal soaking on the structure and properties of a sintered silicon nitride, presented on 22nd Annual AcerS Meeting in Cocoa Beach, Florida, January, 1998.

Problems Encountered

None

Life Prediction Verification

A. A. Wereszczak, M. J. Andrews, T. P. Kirkland, and M. K. Ferber (ORNL)

Objective/Scope

There are three central goals of the proposed structural ceramics research program: the generation of engineering data from ambient to high temperature mechanical testing; microstructural characterization of failure phenomena; and the implementation and verification of life prediction methods. Ultimately, the prediction of the high temperature mechanical performance and service life is information that is critical for the progress towards implementation of structural ceramics as components in internal combustion and automotive gas turbine engines.

The systematic study of the mechanical performance of candidate structural ceramics (silicon nitride primarily) for internal combustion engine components is undertaken as a function of temperature (< 1000°C) and time. Properties such as strength and fatigue will be characterized via flexure, tensile, and rotary bend testing.

The second goal of the program is to characterize the evolution and role of damage mechanisms, and changes in microstructure linked to the ceramic's mechanical performance at representative engine component service conditions. These will be examined using several analytical techniques including metallography, SEM, and TEM. Specifically, several microstructural aspects of failure will be characterized:

(1) the nature of slow crack growth;
(2) changes in failure mechanism as a function of temperature;
(3) edge, surface, and volume effects on strength and fatigue size-scaling; and
(4) what role residual stresses may have in these processes.

Lastly, numerical models (i.e., life prediction codes) will be used in conjunction with the generated strength and fatigue data to predict the failure probability and reliability of complex-shaped components subjected to mechanical loading, such as a silicon nitride diesel engine valve. The predicted results will then be compared to actual component performance measured experimentally in the laboratory or from field service data. As a consequence of these efforts, the data generated in this program will not only provide a critically needed base for component utilization in internal combustion engines, but will also facilitate the maturation of a design algorithm for structural ceramics subjected to mechanical loading in general.

Technical Progress

Machined ASTM C1161-B flexure specimens of Vintage #3 NT551 silicon nitride (Manufactured by Saint-Gobain Norton Industrial Ceramics, East Granby, CT) were delivered during the present reporting period. All specimens were transversely ground with a 320 grit finish grinding procedure. All edges were longitudinally ground to minimize the likelihood of edge-failures. The bend bar specimens were cleaned with a solvent, and then heated to approximately 300°C to burn off grinding fluid remnants which the solvent may have not removed. Specimen dimensions were measured and flexure testing commenced.

The ASTM C1161-B flexure testing of the Vintage #3 NT551 silicon nitride was almost completed during the present reporting period. The uncensored strength distributions for the completed sets are graphically shown in Figs. 1-12. The characteristic strength and Weibull modulus are indicated for each distribution along with 95% confidence intervals for both shown in parenthesis. The flexure strength distributions of ASTM C1161B specimens longitudinally machined and tested at 20 and 850°C are shown in Figs. 1-2. The uncensored characteristic strength and Weibull modulus are larger at 20°C than at 850°C. Strengths from longitudinally machined specimens may be viewed as representing the upper limit of material strength. The usage of such strengths are not appropriate for component design if surface maximum principal tensile stresses are orthogonal to the grinding direction; strengths measured from transversely machined

flexure bars are appropriate in this case. Consequently, the majority of uniaxial strength tests (flexure and tensile) involve specimens which were transversely machined. The flexure strength distributions of ASTM C1161B specimens transversely machined and tested at 20°C at 30, 0.3, and 0.003 MPa/s are shown in Figs. 3-5. The uncensored characteristic strength at 20°C decreases with a decrease in stressing rate. The uncensored Weibull modulus is independent of stressing rate at 20°C. The flexure strength distributions of ASTM C1161B specimens transversely machined and tested at 700°C at 30, 0.3, and 0.003 MPa/s are shown in Figs. 6-8. The uncensored characteristic strength at 30 MPa/s is larger than the two equivalent uncensored characteristic strengths at 0.3 and 0.003 MPa/s. The uncensored Weibull modulus is independent of stressing rate at 700°C. Lastly, the flexure strength distributions of ASTM C1161B specimens transversely machined and tested at 850°C at 30 and 0.3 MPa/s are shown in Figs. 9-10; specimens at this temperature and 0.003 MPa/s are currently being tested. The uncensored characteristic strength and Weibull modulus are larger-valued at 30 MPa/s than at 0.3 MPa/s at 850°C.

Ninety 5 mm diameter cylindrical vintage #3 NT551 specimens with nominal lengths of 45 mm were delivered during the present reporting period. The specimens were transversely ground and are being tested in four-point flexure (20/40 mm spans). Fixturing was designed to accommodate the specimen geometry. A total of thirty specimen sets will be tested at 30, 0.3, and 0.003 MPa/s at 20°C. The flexure strength distributions of cylindrical specimens tested at 20°C at 30 and 0.3 MPa/s are shown in Figs. 11-12; specimens at this temperature and 0.003 MPa/s will be tested during the next reporting period. The uncensored characteristic strength is larger at 30 MPa/s than at 0.3 MPa/s, while the uncensored Weibull moduli are equivalent. The cylindrical specimen flexure strength results will be used in supplement with the conventional ASTM C1161-B prismatic bend bars to predict the failure of valve stems (themselves subjected to bending from misaligned valve guides and valve seats).

Specimen machining of the tensile specimens and rotary bend specimens continued during the present reporting period. Many of the received rod-blanks from the vendor were warped, so the pre-machining of these specimens has turned out to be somewhat laborious. It is anticipated that these specimens will be delivered during the third quarter of FY98.

Polished cross-sections of the as-received vintage 3 NT551 blank stock (e.g., a randomly chosen tile, rod, and valve-blank-stem) were prepared and optically examined. All prepared specimens showed the presence of a reaction layer at all their surface perimeters. Many of the machined bend bars and cylindrical specimens contained remnants of this reaction layer, in addition to snowflake defects which were observed in earlier vintages of NT551. Examinations of earlier vintages of NT551 showed the existence of similar reaction layers, which were indeed found to detrimentally affect strength (particularly at 850°C) in those vintages.

Articles were [1] presented or [2] submitted or [3] contributed to during the present reporting period which discussed the possible apparent effects of stressing rate and temperature on the determined Weibull modulus for NT551 silicon nitride (vintage #1 material).

Flexure testing of KYON3000 silicon nitride (Manufactured by Kennametal, Latrobe, PA) was completed during the present reporting period. The uncensored strength distributions for the completed sets are graphically shown in Figs. 13-18. The characteristic strength and Weibull modulus are indicated for each distribution along with 95% confidence intervals for both shown in parenthesis. Like for the NT551, all KYON3000 specimens were ground with 320 grit machining. The flexure strength distributions of ASTM C1161B specimens transversely machined and tested at 20°C at 30, 0.3, and 0.003 MPa/s are shown in Figs. 13-15. The uncensored characteristic strength decreases with decreasing stressing rate at 20°C, while the uncensored Weibull modulus is independent of stressing rate at this temperature. The flexure strength distributions of ASTM C1161B specimens transversely machined and tested at 850°C at 30, 0.3, and 0.003 MPa/s are shown in Figs. 16-18. Like at 20°C, the uncensored characteristic strength decreases with decreasing stressing rate at 850°C, while the uncensored Weibull modulus is independent of stressing rate at this temperature.

Fractography of the NT551 and KYON3000 specimens was initiated during the present report period and this information will be used for censoring, and will subsequently be used in various failure probability prediction exercises involving internal combustion engine components.

Latest versions of AlliedSignal's ERICA and CERAMIC probabilistic computer codes were compiled during the present reporting period, and are being used. For example, CERAMIC was used to calculate the uncensored strength distributions shown in Figs. 1-18.

Status of Milestones

All milestones are on schedule.

Communications / Visitors / Travel

A. A. Wereszczak presented a poster at the ATD-CCM meeting in Dearborn, MI, Oct 28, 1997, entitled "Life Prediction Analysis of a Ceramic Engine Valve: Effects of a Changing Weibull Distribution."

A. A. Wereszczak attended the semi-annual AlliedSignal Engines Review at the ATD-CCM meeting on Oct 29, 1997.

A. A. Wereszczak, A. E. Pasto, and D. R. Johnson met with Kennametal's R. Yeckley during the ATD-CCM on Oct. 28, 1997 to discuss the line of structural ceramic materials marketed by Kennametal. R. Yeckley will be submitting a HTML User Proposal to perform mechanical tests on some of their commercially available structural ceramics.

M. J. Andrews gave a presentation entitled "Investigations of the Weibull Modulus as a Function of Stressing Rate" at the 22nd Annual Conference on Composites and Advanced Ceramics, Cocoa Beach, FL Jan. 23, 1998.

A. A. Wereszczak and M. J. Andrews visited Yuri Kalish of Detroit Diesel Corporation, Detroit, MI., on March 25 to discuss valve reliability issues and the present project's mechanical characterization analyses of the candidate NT551 silicon nitride valve material.

Problems Encountered

None.

Publications

An abstract entitled "Fast Fracture Life Prediction of a Cylindrical Component Using Standard and Nonstandard Four Point Flexure Test Specimens," by M. J. Andrews was accepted for presentation at the American Ceramic Society's 100th Annual Meeting and Exposition, May 3-6, 1998, at Cincinnati, OH.

An abstract entitled "Dynamic Fatigue Performance of a Commercial Silicon Nitride as a Function of Temperature," by T. P. Kirkland was accepted for poster presentation at the American Ceramic Society's 100th Annual Meeting and Exposition, May 3-6, 1998, at Cincinnati, OH.

"Strength Distribution Changes in a Silicon Nitride as a Function of Temperature and Stressing Rate" by A. A. Wereszczak, K. Breder, M. J. Andrews, T. P. Kirkland, and M. K. Ferber, was accepted for presentation and publication in the Life Prediction Methods Symposium at the June 1998 ASME Gas Turbo Expo, Stockholm, Sweden.

"Investigations of the Weibull Modulus as a Function of Stressing Rate," by M. J. Andrews, A. A. Wereszczak, K. Breder, T. P. Kirkland, and M. K. Ferber, In press, *Ceramic Engineering and Science Proceedings*, Vol. 19, 1998.

"Axisymmetric Tensile and Compressive Creep Deformation of Hot-Isostatically-Pressed Y_2O_3-Doped Si_3N_4," by A. A. Wereszczak, M. K. Ferber, T. P. Kirkland, A. S. Barnes, E. L. Frome, and M. Menon, was submitted for publication in the *Journal of the European Ceramic Society*. This subtask's previous emphasis "Rotor Database Generation" contributed much of the results used in this article.

References

[1] M. J. Andrews, A. A. Wereszczak, K. Breder, T. P. Kirkland, and M. K. Ferber, "Investigations of the Weibull Modulus as a Function of Stressing Rate," In press, *Ceramic Engineering and Science Proceedings*, Vol. 19, 1998.

[2] A. A. Wereszczak, K. Breder, M. J. Andrews, T. P. Kirkland, and M. K. Ferber, "Strength Distribution Changes in a Silicon Nitride as a Function of Temperature and Stressing Rate," Accepted for presentation and publication in the Life Prediction Methods Symposium at the 1998 ASME Gas Turbo Expo (June), Stockholm, Sweden.

[3] K. Breder, A. A. Wereszczak, and M. J. Andrews, "Exploration of the Weibull Modulus as a Function of Surface Preparation and Flexure Testing Conditions," In press, *Ceramic Engineering and Science Proceedings*, Vol. 19, 1998.

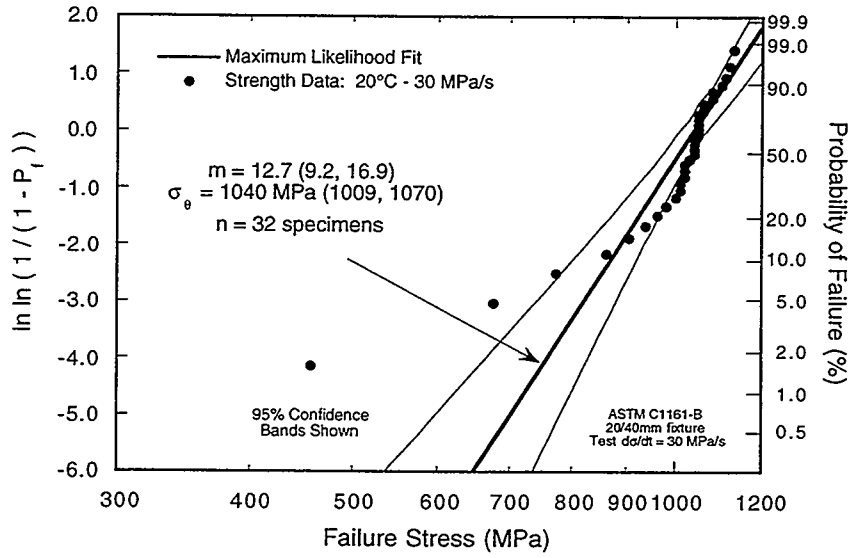

Fig. 1. 20°C : Longitudinally machined : 30 MPa/s : ASTM C1161B. Uncensored strength distribution of vintage #3 NT551.

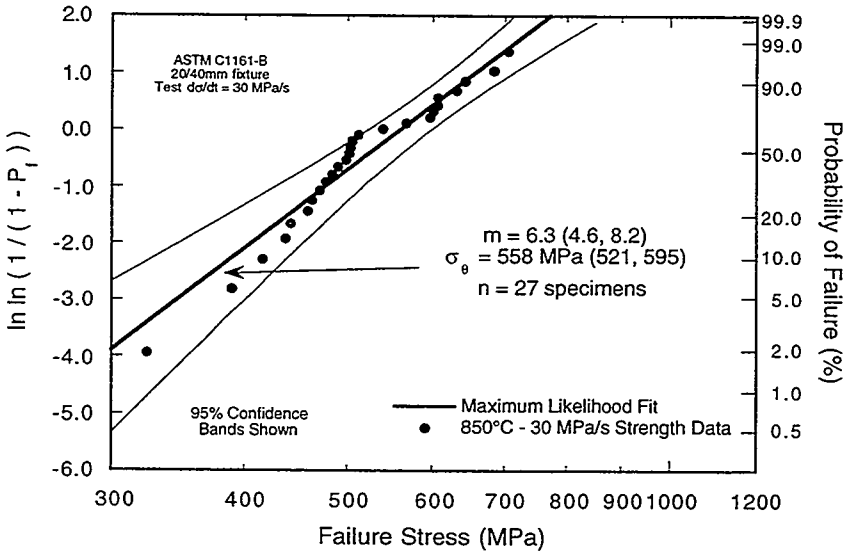

Fig. 2. 850°C : Longitudinally machined : 30 MPa/s : ASTM C1161B. Uncensored strength distribution of vintage #3 NT551.

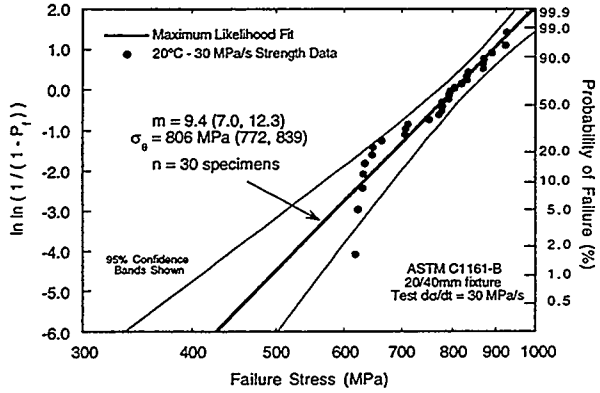

Fig. 3. 20°C : Transversely machined : 30 MPa/s : ASTM C1161B. Uncensored strength distribution of vintage #3 NT551.

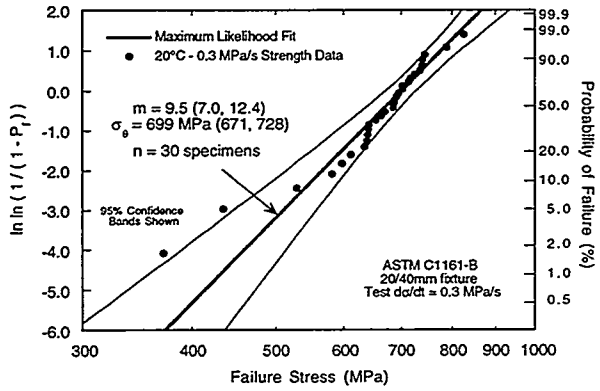

Fig. 4. 20°C : Transversely machined : 0.3 MPa/s : ASTM C1161B. Uncensored strength distribution of vintage #3 NT551.

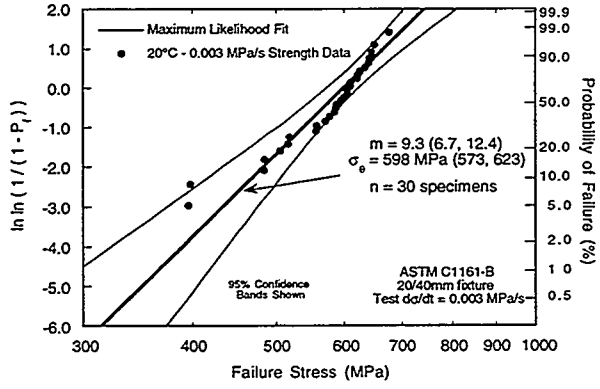

Fig. 5. 20°C : Transversely machined : 0.003 MPa/s : ASTM C1161B. Uncensored strength distribution of vintage #3 NT551.

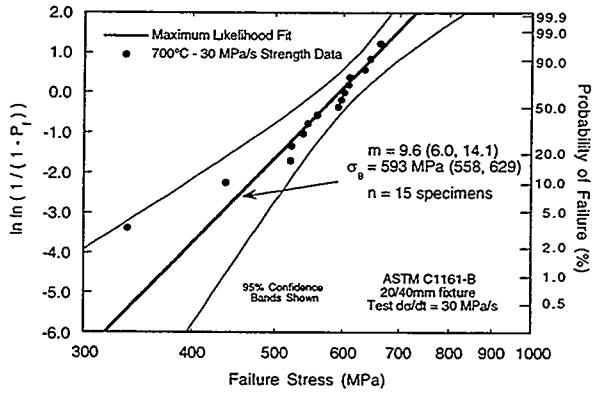

Fig. 6. 700°C : Transversely machined : 30 MPa/s : ASTM C1161B. Uncensored strength distribution of vintage #3 NT551.

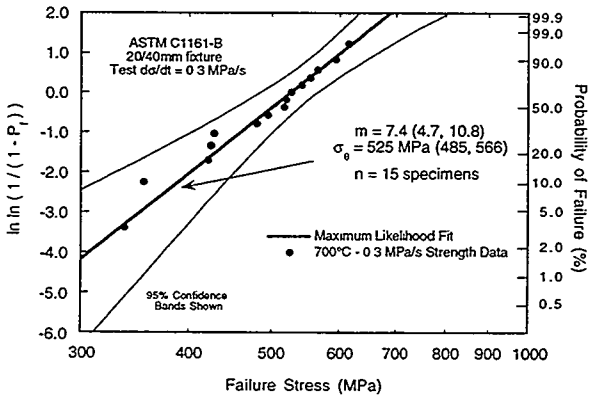

Fig. 7. 700°C : Transversely machined : 0.3 MPa/s : ASTM C1161B. Uncensored strength distribution of vintage #3 NT551.

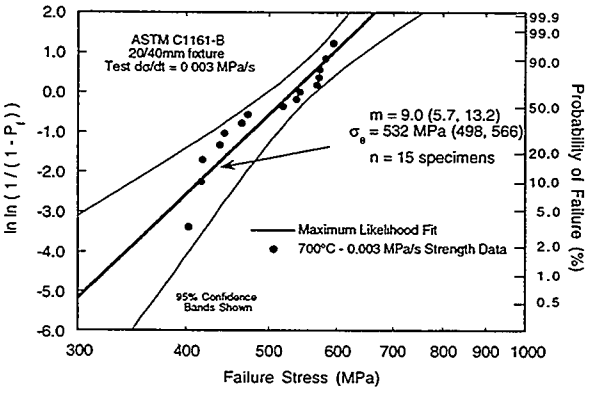

Fig. 8. 700°C : Transversely machined : 0.003 MPa/s : ASTM C1161B. Uncensored strength distribution of vintage #3 NT551.

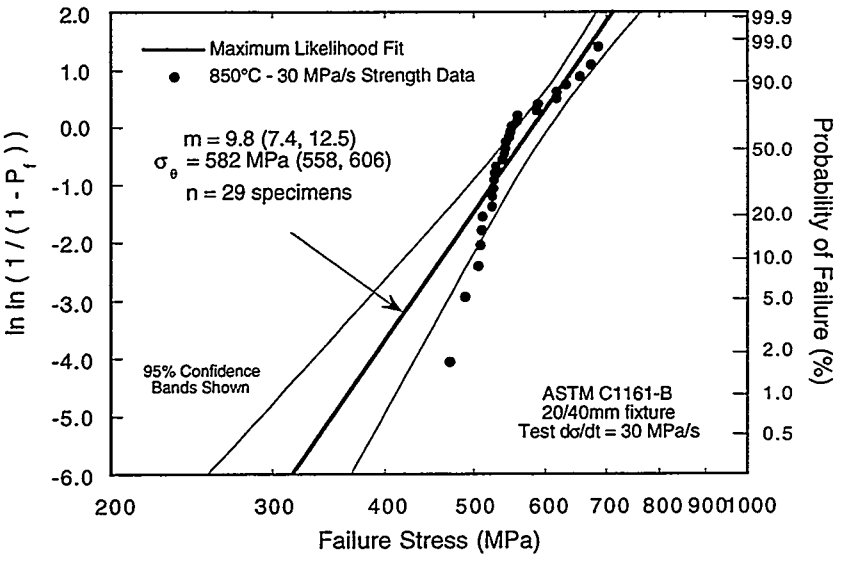

Fig. 9. 850°C : Transversely machined : 30 MPa/s : ASTM C1161B. Uncensored strength distribution of vintage #3 NT551.

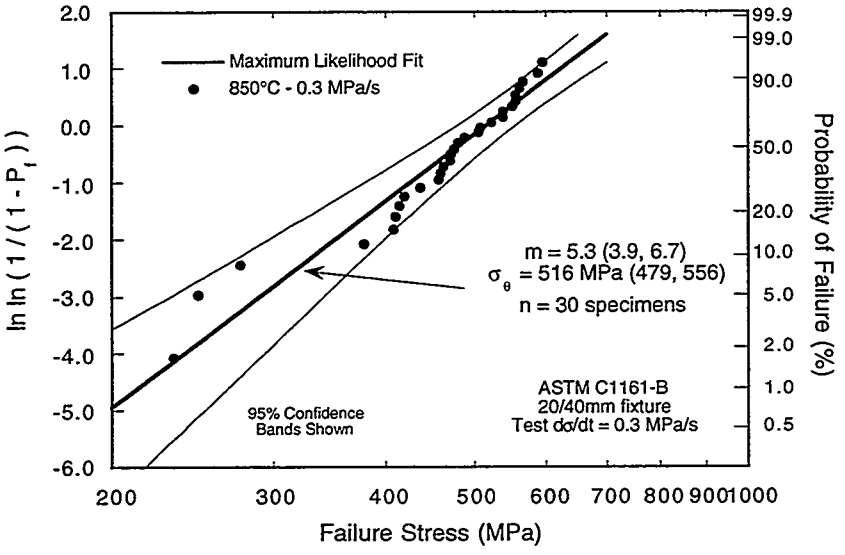

Fig. 10. 850°C : Transversely machined : 0.3 MPa/s : ASTM C1161B. Uncensored strength distribution of vintage #3 NT551.

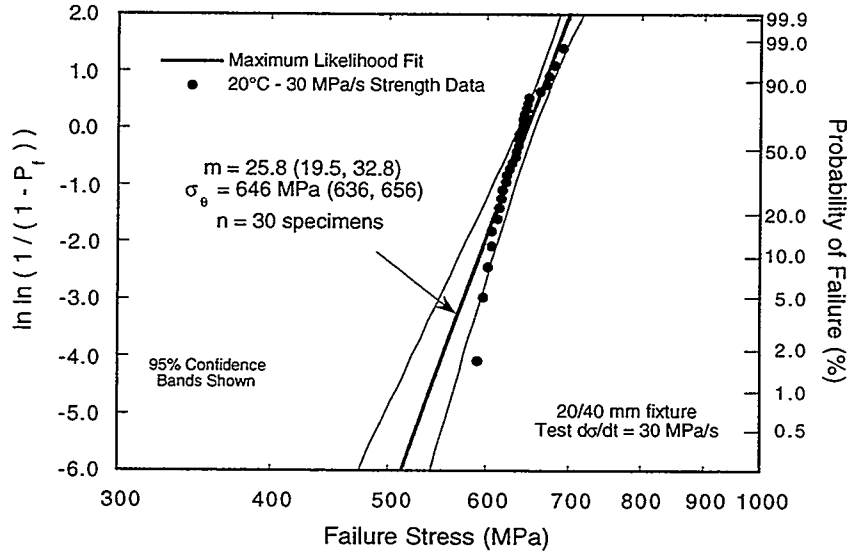

Fig. 11. 20°C : Transversely machined : 30 MPa/s : 5mm dia. cylinder tested in 4pt flexure. Uncensored strength distribution of vintage #3 NT551.

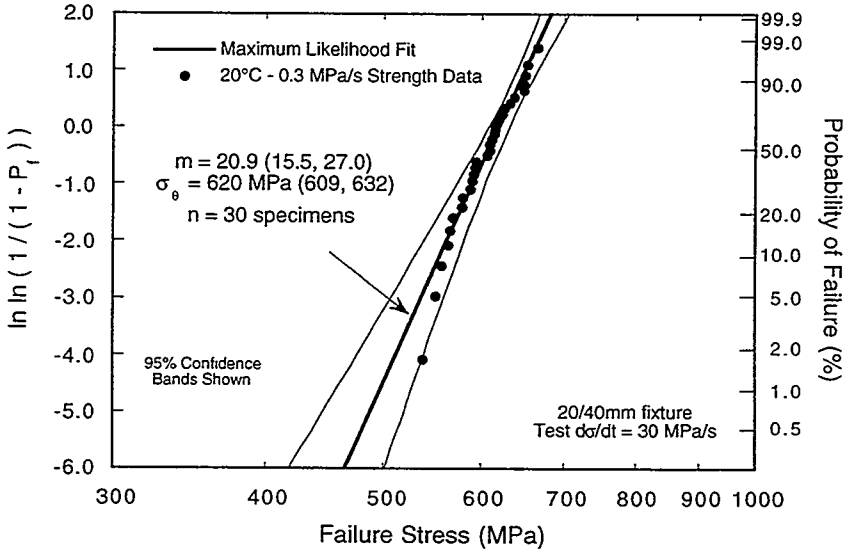

Fig. 12. 20°C : Transversely machined : 0.3 MPa/s : 5mm dia. cylinder tested in 4pt flexure. Uncensored strength distribution of vintage #3 NT551.

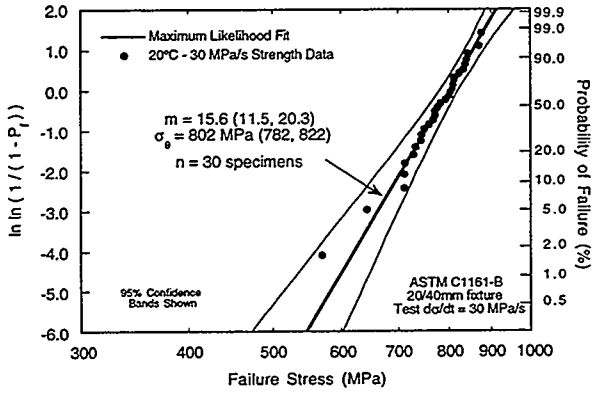

Fig. 13. 20°C : Transversely machined : 30 MPa/s : ASTM C1161B. Uncensored strength distribution of KYON3000.

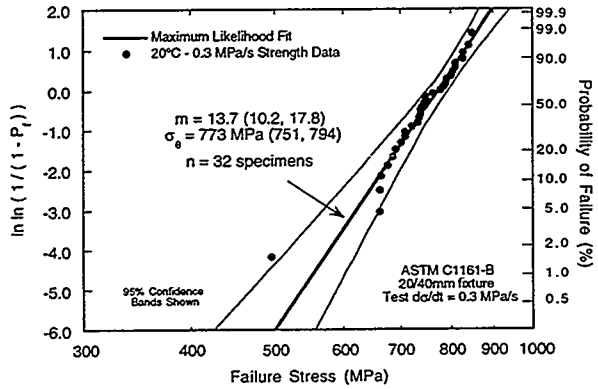

Fig. 14. 20°C : Transversely machined : 0.3 MPa/s : ASTM C1161B. Uncensored strength distribution of KYON3000.

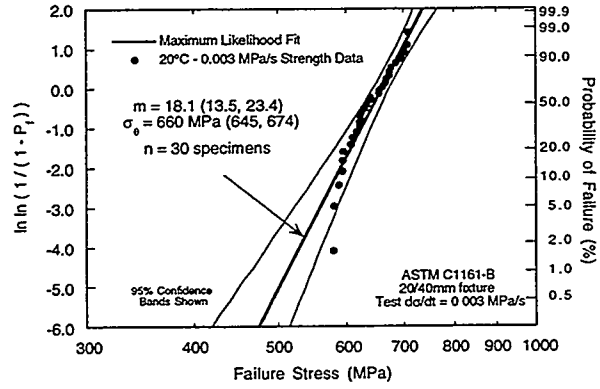

Fig. 15. 20°C : Transversely machined : 0.003 MPa/s : ASTM C1161B. Uncensored strength distribution of KYON3000.

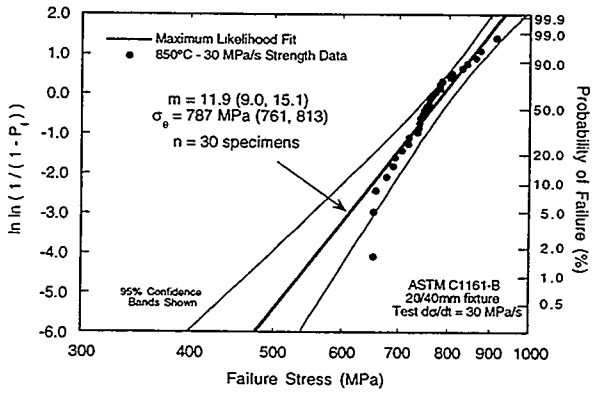

Fig. 16. 850°C : Transversely machined : 30 MPa/s : ASTM C1161B. Uncensored strength distribution of KYON3000.

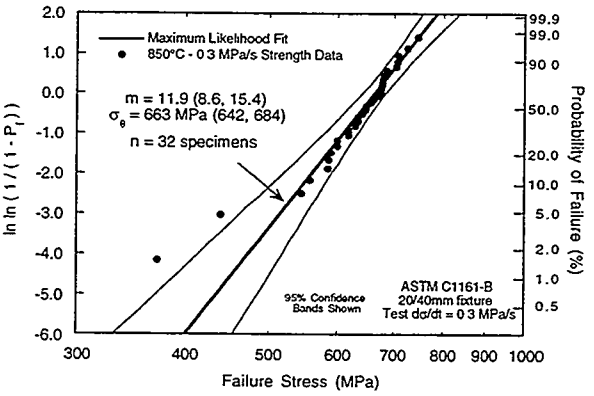

Fig. 17. 850°C : Transversely machined : 0.3 MPa/s : ASTM C1161B. Uncensored strength distribution of KYON3000.

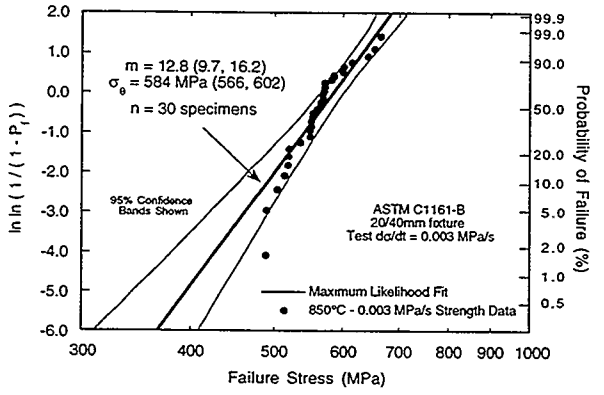

Fig. 18. 850°C : Transversely machined : 0.003 MPa/s : ASTM C1161B. Uncensored strength distribution of KYON3000.

Field Emission Analytical Electron Microscopy for Characterization of Catalyst Microstructures

L. F. Allard and T. A. Nolan

OBJECTIVE/SCOPE

The objective of the research is to use analytical and high resolution transmission electron microscopy (TEM) to characterize the microstructures of emission control catalysts. Emphasis is placed on relating microstructural changes to performance of diesel NOx reduction catalysts. The research is focused on understanding these changes through TEM studies of experimental catalyst materials reacted in an ex-situ catalyst reactor system especially constructed to allow appropriate control of the reaction conditions and the transfer of the sample between reactor and microscope.

TECHNICAL HIGHLIGHTS

Reactions have been conducted utilizing the ex-situ reactor system for the Hitachi HF-2000 field emission electron microscope in beginning studies of a series of candidate lean NOx catalysts comprising platinum group metals (PGM) supported on alumina, titania and mixed alumina-titania powders. These specimens are being provide by Dr. C.K. Narula, a collaborator at Ford Research Laboratory in Dearborn, MI. Specimens were initially reacted in 14%O_2 in N_2 at a nominal 350°C, for one hour, and then re-reacted for 15 hours. The first results showed that the holey carbon films used to support the catalyst powder were destroyed after just a few hours of reaction in an oxidizing environment, necessitating a search for a more stable holey support medium.

Successful results were obtained using our thin film ion sputter deposition system with a target of a nominal composition $LaCrO_3$, and sputtering the material onto previously prepared holey carbon films. This material is conductive and retains its conductivity at elevated temperatures. The film as-sputtered was both amorphous, featureless and conductive, as expected, because the underlying carbon support was still present. Figure 1 is an EDS spectrum of the film, showing La, Cr, O, and C, with minor elements Ca and Co also present.

Powder aggregates of Pt/alumina-titania catalyst material were dispersed over the holey support film. The film was then reacted at a nominal 450°C for 2 hours in the 14%O_2/N_2

used previously, and re-examined in the TEM. No changes were seen in the gross structure of the holey film (Fig.2), and no evidence of reaction with the alumina-titania particles was observed. The alumina-titania particles appeared to be quite stable even when the beam was focused directly onto an aggregate for high magnification observation. Figure 3 is an EDS spectrum of the film after this reaction, showing an absence of the carbon peak that indicates the carbon film reacted with O_2 forming CO and CO_2 gaseous species that resulted in its removal. The loss of the carbon film did not appear to affect the conductivity of the remaining $LaCrO_3$ film, as there was no evidence of the build-up of residual electrical charge causing the catalyst particle aggregates to be repelled from the film.

A second reaction treatment under the same oxidizing conditions again showed no noticeable changes in film structure, and still no evidence of any tendency for the catalyst particles to react with the film. The EDS spectrum from the film was identical to the one taken after 2 hours of reaction. This excellent result offers promise as an adequate solution to the problem of providing a stable, conductive holey support film for further studies of NOx reduction catalysts based on oxide supports.

The newly developed conductive holey support film was used for additonal reaction treatments on Pt/alumina-titania catalysts. Examination of the first set of specimens indicated that Pt was not adequately dispersed over the surface of the oxide support particles. Acordingly, a new technique was tried at Ford and a better result was obtained. Images such as Figure 4a at high magnification showed the dispersion of Pt clusters on the TiO_2 surface. Some clusters are clearly only about 0.5 nm in diarmeter, as is evidenced by comparison to the resolved lattice fringe spacings which are about 0.25 nm in width. The smallest clusters contain as few as 10 atoms of Pt. This specimen was then reacted at 450°C in $14\%O_2/N_2$ for two hours, then re-installed in the microscope to study the effects of the reaction treatment on the specimen morphology.

Figure 4b shows the same sample area after the reaction treatment. The TiO_2 particles show significant sintering effects, but the most striking morphological change is the apparent growth of Pt clusters into discrete particles ranging up to the 2-3 nm size range. It is results such as this that give promise that our technique development allowing such studies will pay off with critical information important to fully understand mechanisms of catalyst performance and degradation.

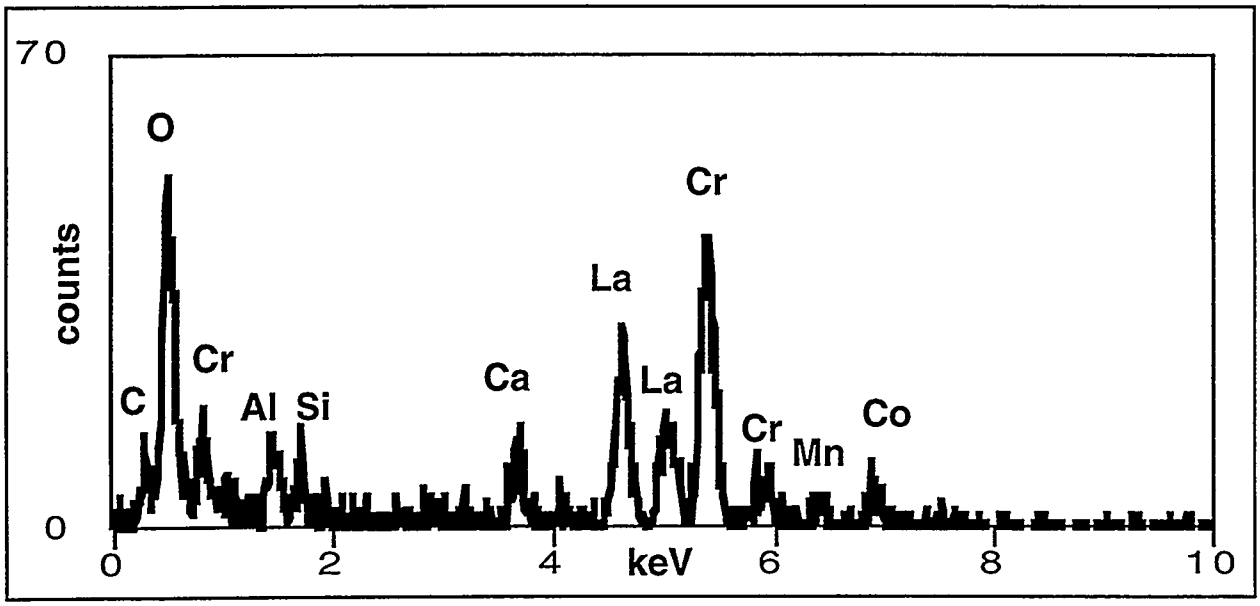

Fig. 1. EDS spectrum of the $LaCrO_3$ film as-deposited onto a holey carbon support film. The carbon peak from the holey support film is clearly present, as are peaks from the minor constituents Ca and Co. Al and Si result from sputtering of the target support structure, and Mn is an impurity in the film. Aquisition time = 50 sec.

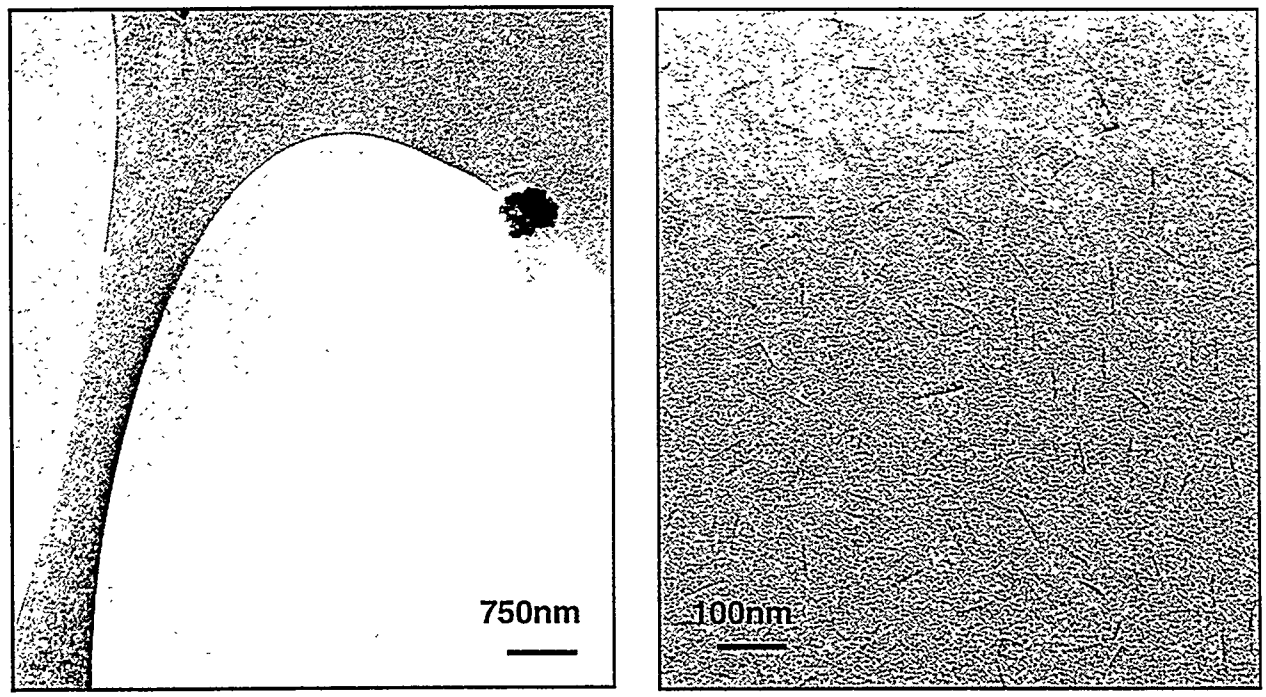

Fig. 2. a) $LaCrO_3$ holey film after 2h reaction in 14% O_2 in N_2 at a nominal 450°C. b) Rod-shaped features appeared, but film retained its amorphous character and no compositional differences were noted in EDS spectra.

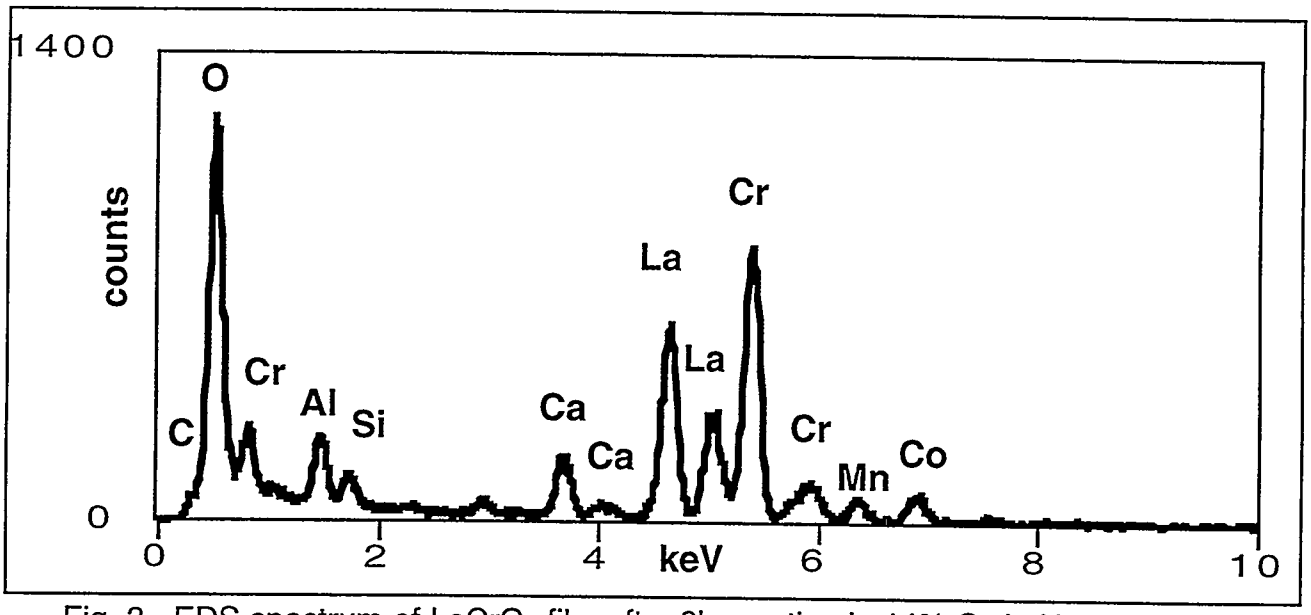

Fig. 3. EDS spectrum of $LaCrO_3$ film after 2h reaction in 14% O_2 in N_2 at a nominal 450°C. Note loss of carbon peak, indicating disappearance of carbon support film. Acquisition time = 300 sec.

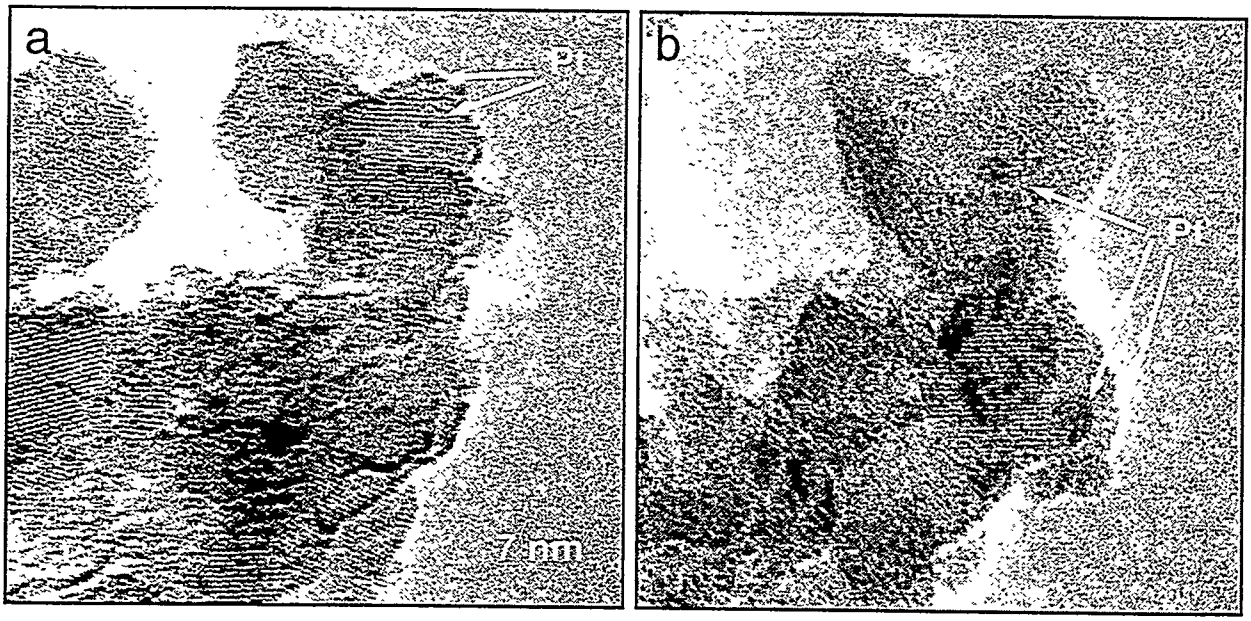

Fig. 4. Pt/TiO_2 as-prepared (a) and after reaction () at 450°C for 2 h in $14\%O_2/N_2$. Note particularly the growth of Pt clusters from 0.5 nm to 2-3 nm size range. The TiO_2 shows significant sintering even at this relatively low temperature.

MATERIALS AND TESTING STANDARDS

IEA ANNEX II Management (October 1, 1997-March 31, 1998)

M. K. Ferber and K. Breder (Oak Ridge National Laboratory)

Objective/Scope

The purpose of this task is to organize, assist, and facilitate international research cooperation on the characterization of advanced structural ceramic materials. A major objective of this research is the evolution of measurement standards. This task, which is managed in the United States by ORNL, now includes a formal IEA Annex agreement identified as Annex II between the United States, Germany, Sweden, Japan, and Belgium. The original annex included four subtasks: (1) information exchange, (2) ceramic powder characterization, (3) ceramic chemical and physical characterization, and (4) ceramic mechanical property measurements. In the United States, a total of 13 industrial and government laboratories have participated and contributed their resources to this research. The research in Subtasks 2, 3, and 4 is now complete. In 1990, research in two new subtasks was initiated, including Subtask 5, Tensile and Flexural Properties of Ceramics, and Subtask 6, Advanced Ceramic Powder Characterization. The research in Subtasks 5 and 6 was completed in 1993 and the reports were distributed. Two new tasks (Subtask 7 on Ceramic Machining and Subtask 8 on Ceramic Powder Characterization) were proposed in late FY 1993 and the research is completed (1996). Subtask 7 in the United States included eight companies and three federal laboratories. The report on the results from research performed in the United States on Subtask 7 is complete (a final draft report has been compiled of all the international research). Subtask 8 included six companies. The final report for Subtask 8 is complete. In 1996, research in two new subtasks was initiated, including Subtask 9 - Thermal Shock and Subtask 10 - Ceramic Powder Characterization, and work in these subtasks is presently ongoing.

Recent Developments

The meeting of the Executive Committee of the IEA Annex II, IEA Cooperative Programme on Ceramics for Advanced Engines and Other Conservation Applications, was held on 20 October 1997, at Sasebo-City, Japan. There were 13 people (15 including the translators) in attendance including the Executive Committee members.

Germany agreed to host the next Executive Meeting in conjunction with Materials Week in Munich to be held October 12 through 15, 1998.

A Working Group Meeting (Subtask 9) has been scheduled for May 5, 1998, in Cincinnati, Ohio, to be held in conjunction with the 100th Annual ACerS Meeting.

The Draft Progress Report for the 1998 Committee on Energy Research and Technology (CERT) Review has been submitted to the IEA Discussant for our Agreement (Dr. Peter van Luyt, The Netherlands).

Technical Highlights

Subtask 7, Machining Effects on Strength of Structural Ceramics

The summary report for Subtask 7 of all countries research is complete and is being reviewed (March 12, 1998).

Current Subtask 9 Technical Efforts

The thermal and mechanical properties data sheets for the silicon nitride (AS800) have been sent to the participants. Each country has been requested to evaluate the thermal shock stress for 5 to 10 specimens (which were furnished by the United States) and results will be compared at the upcoming Subtask 9 Workshop to be held at the Annual American Ceramic Society Meeting in Cincinnati on May 5, 1998.

Letter Report (IEA Milestone, 411526) - February 27, 1998

The development of new and improved ceramic materials, design methods for brittle materials, and life prediction methodology is of vital importance to the successful utilization of structural ceramics in combustion engine applications to improve their energy efficiency. In order to address these issues on an international level, a cooperative research agreement was initiated by several countries under the International Energy Agency (IEA). The original effort was initiated in 1979 through an Implementing Agreement for a Program of R&D on High-Temperature Materials for Automotive Engines. This agreement was completed in FY 1985, with DOE serving as Operating Agent for the United States. In this first agreement entitled, "Annex I-Ceramics for Automotive Gas Turbine Engines," the United States and Germany conducted information exchange and experimental ceramic materials and test results on those materials via participation of industrial and government laboratories in both countries.

Annex II-Cooperative Programme on Ceramics for Advanced Engines and Other Conservation Application is the current IEA agreement under which this international research is conducted. The current participants are Germany, United States, Sweden, Japan, and Belgium. The United States Department of Energy is the Chairman of the Executive Committee and Operating Agent for Annex II. The active subtasks are (1) Subtask 9 - Development and Verification of Advanced Thermal Shock Techniques and (2) Subtask 10 - Characterization of Ceramic Powders. Subtask 7 represents a follow-on effort from the previous Subtask 5 on mechanical properties of silicon nitride.

In Subtask 9, advanced thermal shock techniques for structural ceramics are being examined by each of the participating countries. All of the thermal shock methods will utilize a thin disk specimen which is centrally heated by either a laser, a gas torch, or a high intensity lamp. As shown in Figures 1-3, this heating arrangement results in a steep radial temperature gradient which generates high tensile stresses along the specimen edge. The temperature profile at fracture can be used to calculate the thermal fracture stress. In order to compare the data produced by the various heating approaches, specimens fabricated from a candidate structural ceramic (AS800 silicon nitride manufactured by AlliedSignal Ceramic Components in Torrance, CA) will be distributed to each of the participating countries. The resulting values of the fracture stress will be used as the primary correlating parameter.

Figure 4 illustrates the experimental thermal shock equipment used in the United States. In this setup, a gas torch centrally heats the ceramic disk. In order to generate a temperature gradient which is sufficiently steep to cause fracture, the outer edge of the specimen is supported by a water-cooled holder. To initiate a test, the torch is first positioned away from the sample holder. The ceramic disk is then placed on the water-cooled support block and the temperature allowed to equilibrate for 15 minutes. Air cylinders are used to position the torch directly over the specimen. An infrared (IR) camera is used to view the specimen and provide quantitative temperature information. A video cassette recorder is used to record the output of the IR camera during the entire test.

Preliminary tests with aluminum oxide, silicon nitride, and silicon carbide have been successful. Of the three materials the silicon nitride was most difficult to shock due to it's high fracture strength. Figure 5 illustrates the IR images obtained from a thermal shock test conducted on a 20 mm diameter silicon nitride specimen. The failure of this specimen leads to the formation of several pie-shaped fragments. This type of fracture morphology is expected for the centrally-heated disk specimen.

Subtask 8, Characterizing Ceramic Powders

Major responsibility for this subtask in the United States is at NIST, and a detailed report of progress on this subtask is provided in the section of this report submitted by NIST.

Status of Milestones - Milestone 411530 was completed by having the Executive Committee meeting on 20 October 1997. Milestone 411526 (Complete thermal shock technique development and issue letter report - Subtask 9) was delayed until February 1998 due to decisions that would be decided upon at the Executive Committee Meeting (completed on February 27, 1998). Other Milestones are on schedule.

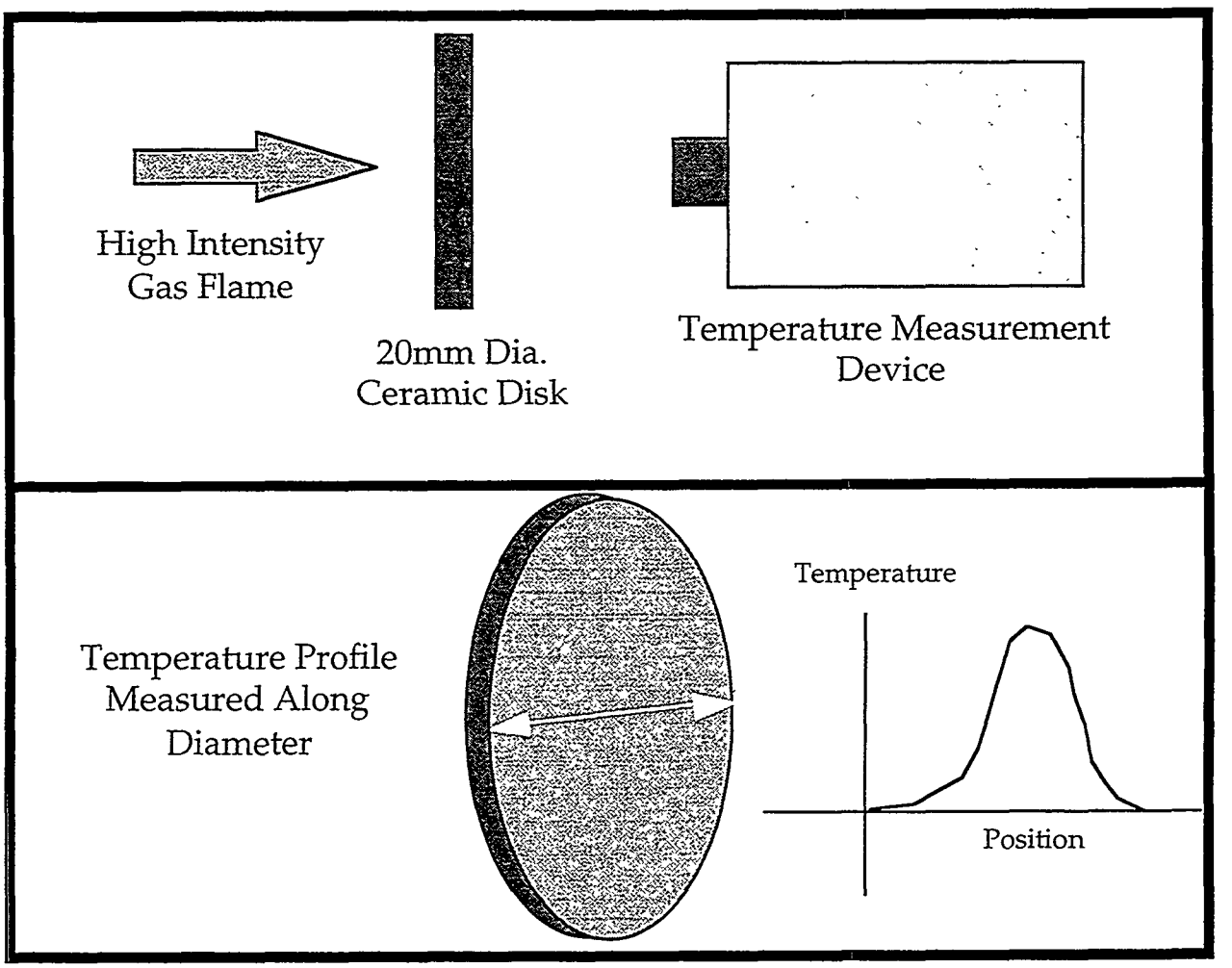

Fig. 1. Schematic illustration of the heating geometry used for the centrally-heated thermal shock disk specimen.

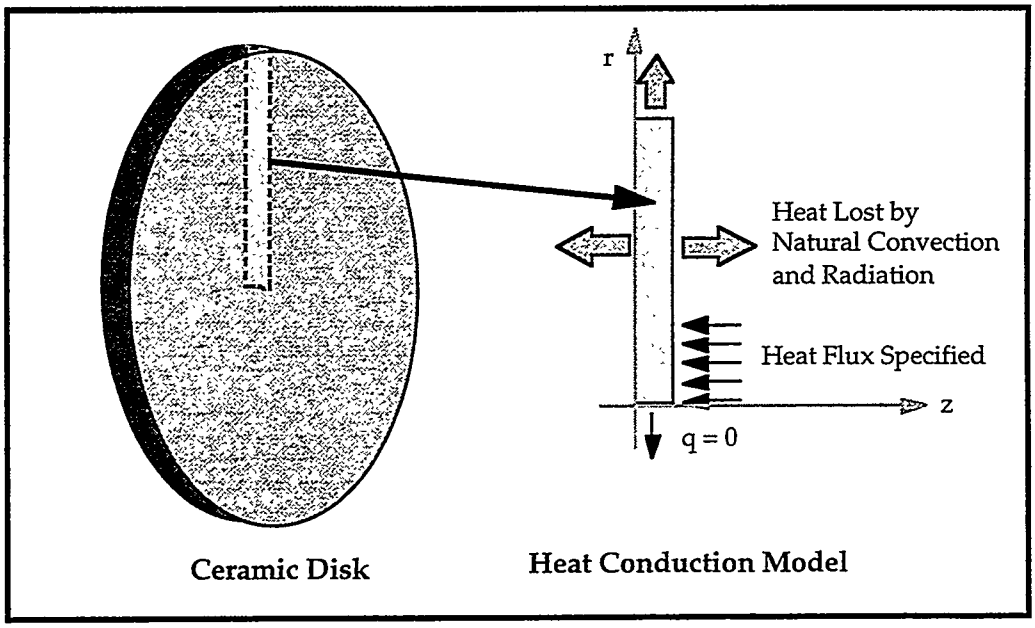

Fig. 2. Boundary conditions used to calculate the temperature profiles in a centrally-heated disk specimen.

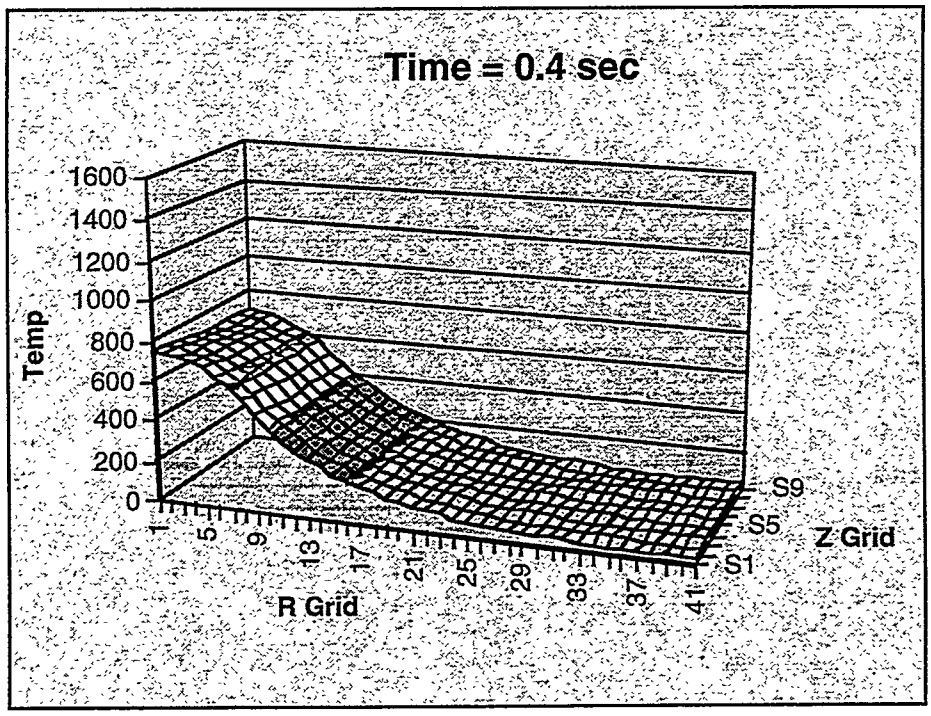

Fig. 3. Typical temperature profile calculated for the boundary conditions specified in Fig. 2.

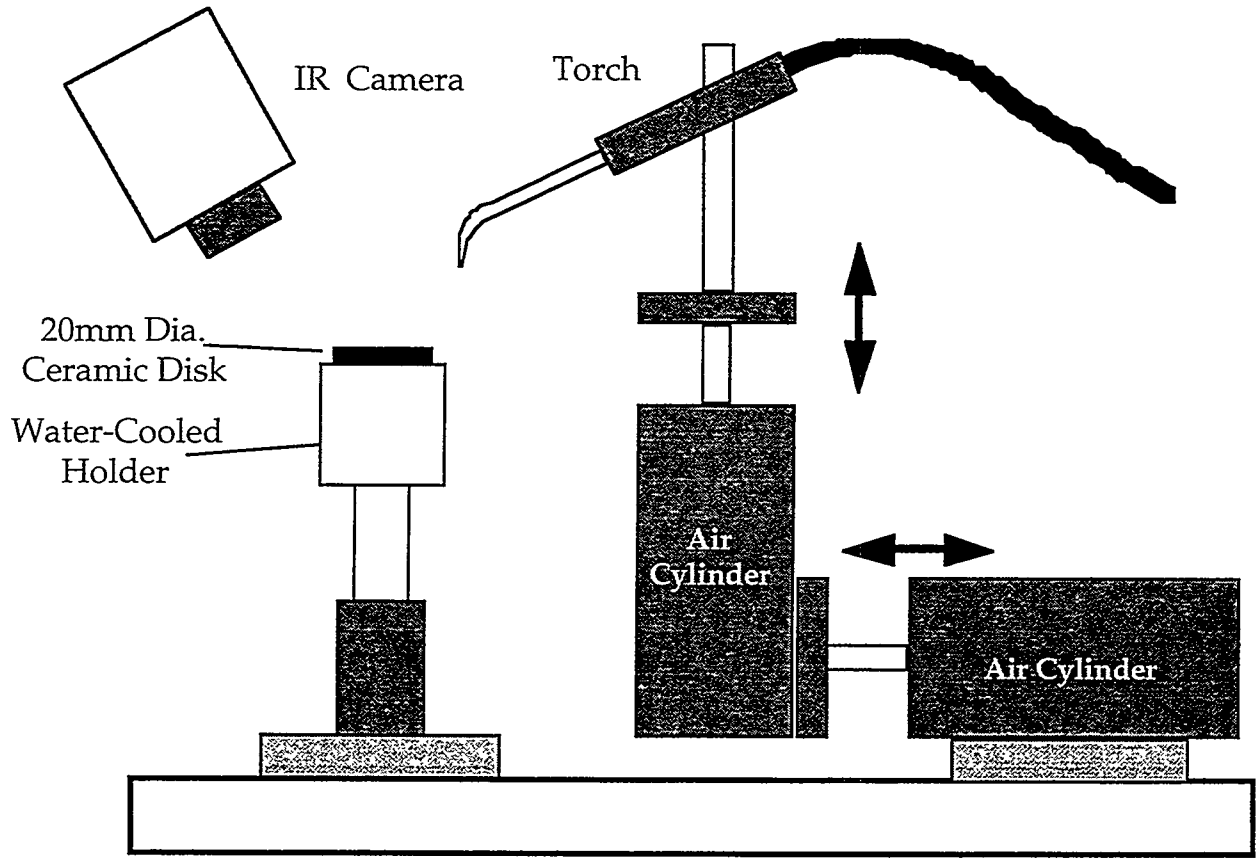

Fig. 4. Schematic representation of thermal shock setup used in the United States.

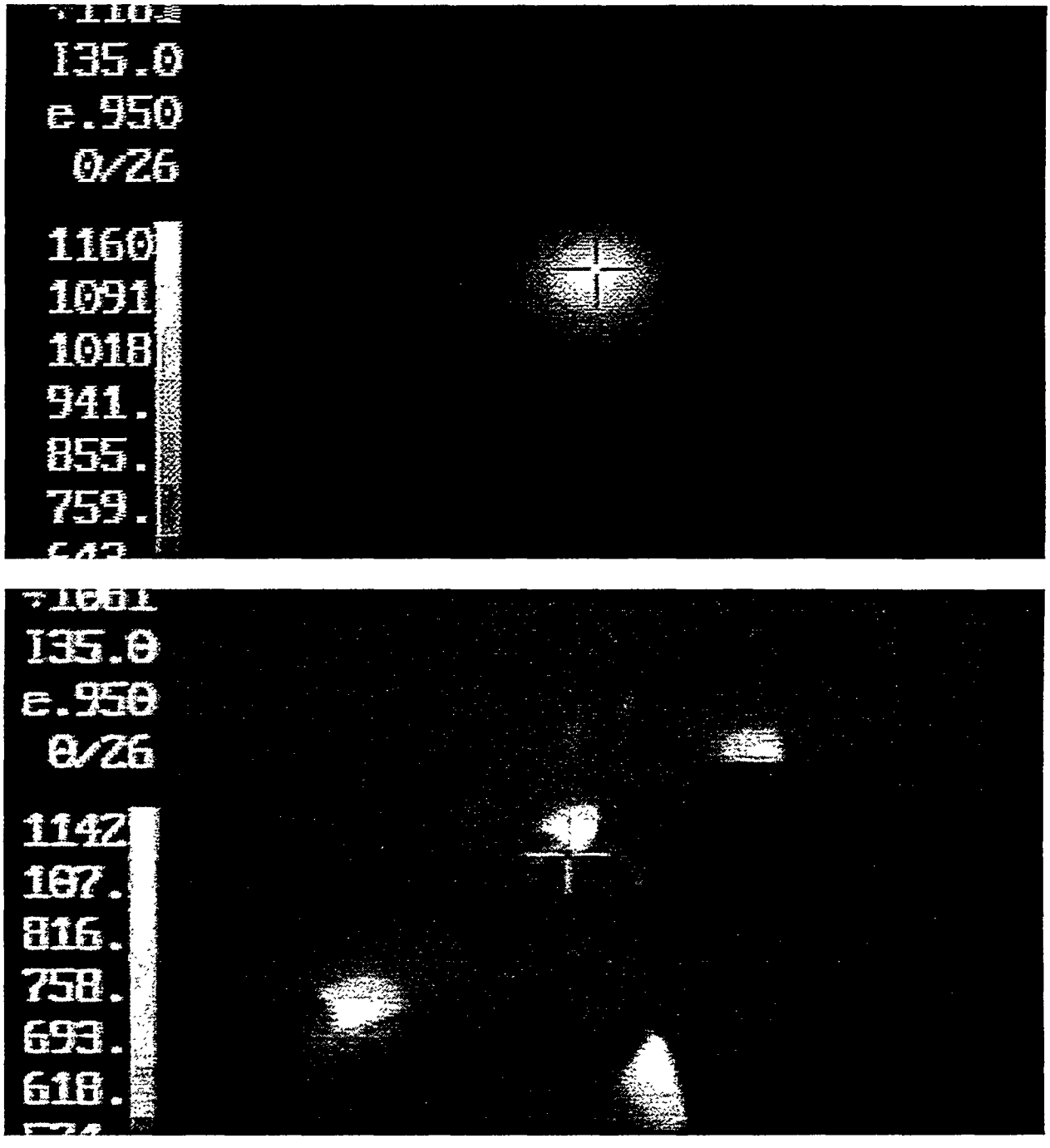

Fig. 5. IR images of thermal shock test of a silicon nitride ceramic showing specimen just prior to (top) and during (bottom) fracture.

Communications/Visits/Travel - Matt Ferber attended and presented updates on Subtasks 7 and 9 at the annual Executive Committee Meeting held October 20, 1997, at the Sasebo Washington Hotel, Sasebo-City, Japan, and the 6th Intl. Symposium on Ceramic Materials & Components for Engines, Arita, Japan (October 19-24, 1997).

Kristin Breder attended the ASTM C-28 meetings in Cocoa Beach January 17-20, 1998, and the American Ceramic Society Conference on Ceramics and Composites in Cocoa Beach January 20-24.

Publications and Presentations - K. Breder,* M. K. Ferber, and R. D. Ott (Oak Ridge National Laboratory, Oak Ridge, Tennessee, USA), "Grinding of Silicon nitride by Creep-Feed Grinding and Conventional Surface Grinding," presented and pp. 388-393 in Proceedings of the 6th International Symposium on Ceramic Materials & Components for Engines, eds. K. Niihara, S. Kanzaki, K. Komeya, S. Hirano, K. Morinaga, Arita, Japan, October 19-24, 1997 (1998).

J. P. Erauw,* W. Hendrix and E. Van. Hoof (VITO, Mol, Belgium); K. Breder and M. K. Ferber (Oak Ridge National Laboratory, Oak Ridge, Tennessee, USA), "Machining of Silicon Nitride: Process Parameters - Mechanical Properties Relationship," presented and pp. 394-399 in Proceedings of the 6th International Symposium on Ceramic Materials & Components for Engines, eds. K. Niihara, S. Kanzaki, K. Komeya, S. Hirano, K. Morinaga, Arita, Japan, October 19-24, 1997 (1998).

M. K. Ferber,* A. A. Wereszczak and E. Lara-Curzio (Oak Ridge National Laboratory, Oak Ridge, Tennessee, USA), "Time-Dependent Failure of Structural Ceramics and Ceramic-Matrix Composites at Elevated Temperatures," presented at the 6th Intl. Symposium on Ceramic Materials & Components for Engines, Arita, Japan (October 19-24, 1997).

M. Mizuno and Y. Nagano* (Japan Fine Ceramics Center, Japan), "Machining Conditions and the Strength of Silicon Nitride Ceramics, presented at the 6th International Symposium on Ceramic Materials & Components for Engines, Arita, Japan (October 19-24, 1997).

"Standard Testing Methods for Ceramics Matrix Composites (Summary)," PEC-TS CMC 01-14 - 1997, Petroleum Energy Center, Japan, March 1997.

Kristin Breder,* Andrew A. Wereszczak, and Mark J. Andrews, "Exploration of the Weibull Modulus as a Function of Surface Preparation and Flexure Testing Conditions," presented at American Ceramic Society Conference on Ceramics and Composites in Cocoa Beach January 23, 1998.

The following reports were distributed at the Executive Committee in Japan (October 20, 1997).

Japan distributed the following reports:

(1) New Sunshine Project, brochure prepared by New Energy and Industrial Technology Development Organization, Tokyo, Japan.

(2) Hironori Arakawa, Takayuki Suzuki, Kazufumi Saito (MITI), and Shigeru Tamura, Shinsuke Kishi (NEDO), Research and Development of 300 kW Class Ceramic Gas Turbine Project in Japan, presented at the International Gas Turbine and Aeroengine Congress and Exhibition in Orlando, Florida, June 2-5, 1997, ASME Pamphlet 97-GT-87.

(3) Research and Development on Ceramic Gas Turbine (300 kW class). FY 1996 Annual Report, published by New Energy and Industrial Technology Development Organization, May 1997, Tokyo, Japan.

Germany distributed the following reports:

(1) Annual Report 1996/97, Part: High Performance Structural Ceramics, published by Project Management Organization New Materials and Chemical Technologies, NMT, Forschungszentrum Jülich GmbH for the Federal Ministry of Education, Science, Research and Technology (BMBF), Jülich, Germany.

(2) Report of the Federal Government on Research 1996, published by the Federal Ministry of Education, Science, Research and Technology (BMBF), Bonn, Germany.

(3) Technology Centers for Solution Based Coating, brochure describing research facilities involved in coating technology.

Belgium distributed the following reports:

(1) Scientific Report 1996, published by Vlaamse Instelling voor Technologisch Onderzoek (VITO), Mol, Belgium.

(2) Annual Report 1996, published by Vlaamse Instelling voor Technologisch Onderzoek (VITO, Mol, Belgium.

The Preprints were mailed (December 15) to the Executive Committee and National Representatives:

Preprints of the Annual Automotive Technology Development Customers' Coordination Meeting, Volume I: Advanced Automotive Technologies, Volume II: Heavy Vehicle Technologies, Volume III: Automotive and Heavy Vehicle Technologies Poster Session, Dearborn, Michigan, October 27-30, 1997.

NDE Standards for Advanced Ceramics

R. W. McClung

The development of standards is important for the establishment of reliability and acceptance of advanced structural materials. Committee C-28, on Advanced Ceramics, has been organized in the American Society for Testing and Materials (ASTM) to address this issue. One of the activities of the C-28 committee is nondestructive examination (NDE). The Section C-28.02.02 on NDE is reviewing existing standards on NDE (primarily developed for metals) to determine potential applicability for ceramics, as well as drafting original standards. Use of existing or modified standards, if available, is more efficient that generation of new documents and will assure the input of a large body of NDE expertise. Close liaison has been established with ASTM Committee E-7 on Nondestructive Testing, and documents are in various stages of review, recommendations for change, modification, and balloting. R. W. McClung is a subcommittee chairman in both committees and the official liaison.

Technical Highlights

Liaison and technical support have been continued between ASTM committees C-28 and E-7. To date, forty-two E-7 NDE standards identified as having potential relevance to ceramics have been reviewed in detail with recommendations made to E-7 for modifications to identified documents. Successful action is complete on 37 documents; three are being addressed by E-7; others require action by C-28.

A revision to standard C-1212 (on fabricating reference specimens with seeded voids) to incorporate improvements from a newly approved standard C-1336 (on fabricating reference specimens with seeded inclusions) received society approval. An additional set of comments with an affirmative ballot was reviewed and a revision prepared for a concurrent subcommittee/committee ballot.

A limited amount of data has been identified for establishing radiographic equivalence factors for advanced ceramics. Additional specimens will be sought for experimental radiography to develop additional data. A volunteer for the radiography has been recognized. The intent of this action is to provide data for a table in an E-7 standard E-94 on the radiographic method. Other work in progress includes an amplified outline for a draft standard for reference specimens containing laser-drilled holes and a possible standard on determination of porosity in ceramics using ultrasonic velocity.

Following a successful main committee ballot on a revision to C-1175 (the guide to existing NDE standards that have been selected as having relevance and applicability to ceramics), the standard received society approval on December 16, 1997. The revision adds five additional E-7 NDE standards: E-94, Guide for RadiographicTesting; E-1570, Practice for Computed Tomographic (CT) Examination; E-1647, Practice for Determining Contrast Sensitivity in Radioscopy; E-1672, Guide to Computed Tomography (CT) System Selection; and E-1695, Test Method for Measurement of Computed Tomography (CT) System Performance.

A number of new or revised E-7 NDE standards with current or potential relevance to ceramics were reviewed and comments prepared on E-7 committee and subcommittee ballots. The topics included new standards for calibrating and measuring density by computed tomography (CT), for determining contrast discrimination visual acuity of radiographic interpreters, and reference radiographs for evaluating performance of radiographic digitization systems. Revisions balloted included a guide for CT imaging, a guide for storage of radiographic film, a practice for determining contrast sensitivity in radioscopy, and a guide to radiography (the last was revised in response to comments and requests from Committee C-28).

During meetings of Committee E-7 in January 1998 (sequential with meetings of C-28), participation by McClung as C-28 liaison included meetings of the subcommittees on radiology and ultrasonics. Significant activity is ongoing in both subcommittees that will result in standards of interest and value for advanced ceramics. Several of the revisions and ballots are based, in part, on requests from C-28. Radiographic standards in various stages of drafting, revisions or balloting include standards for image quality response of film at low energies, practice for radiographic examination, total image unsharpness in radiology, contrast sensitivity in radioscopy, computed radiology, computed tomography (CT) measurement of density, volumetric CT, a guide to radiographic examination, storage of radiographs and film, and calibration of transmission densitometers.

Subcommittee E7.06 on Ultrasonic Methods has many standards in different stages of preparation or ballot. Ultrasonic standards in process include resonant ultrasonic spectroscopy (currently used for ceramic bearings and other materials), evaluation of flaws by immersed techniques, characterization of instruments and search units, detection and evaluation of flaws by contact techniques, and immersed examination.

Several standards from both subcommittees are in different stages of presentation, balloting, or adoption by the international Committee ISO TC-135 on Nondestructive Testing. These include several on CT, ultrasonic immersion examination, and characterization of ultrasonic equipment.

IEA Subtask 10 - Ceramic Characterization and Standards for Heat Engines

George Onoda and Lin-Sien Lum
National Institute of Standards and Technology
Bldg 223, Room A256, Div. 852
Gaithersburg, MD 20899

Objective/Scope

The objective of Subtask 10 is to tighten and finalize procedures for the characterization of secondary properties of powders. There are four focus areas relating to the secondary properties: dispersion of powders for slurry preparation, slurry preparation, spray-dried powders, and green body evaluation.

Subtask 10 will involve participants from Belgium, Germany, Japan, Sweden, and the United States.

Technical Progress

The robustness testing of the procedures for the measurement of dispersion of powders and rheology has been completed. Compilation of the final procedures for the measurement of dispersion powders and rheology has been completed. The robustness testing of the procedures for evaluation of green bodies and spray-dried powders has been completed. Compilation of the final procedures for the measurement of spray dried powders and green bodies has been completed.

Milestones

The next Subtask 10 technical leader's meeting will be in Cincinnati, Ohio, on May 5 at the annual meeting of the American Ceramic Society.

Prepare and distribute samples to participants by NIST for round robin testings—3/98

Complete round robin testing—9/98

Communications/Visits/Travel

Reports of the Subtask 10 were presented to the IEA Executive Committee at Arita, Japan, in October 1997.

Publications/Presentations

Presentation of the IEA Subtask 10 was given at the NIST Ceramic Processing Characterization Consortium business meeting in December 1997.

References

None

Problems Encountered

None

Ceramic Mechanical Property Test Method Development

George D. Quinn
(National Institute of Standards and Technology)

Objective/Scope

This task is to develop mechanical test method standards in support of the Propulsion Systems Materials Program. Test method development should meet the needs of the DOE engine community but should also consider the general USA structural ceramics community as well as foreign laboratories and companies.

Draft recommendations for practices or procedures shall be developed based upon the needs identified above and circulated within the DOE ceramics engine community for review and modification. Round-robins will be conducted as necessary, but shall be well-focussed, limited in scope, and complementary to IEA round-robins. Procedures developed in this program will be standardized by ASTM and/or ISO.

Technical Highlights and Results

Summary
Work continues on developing a full-consensus fracture toughness standard in ASTM to supersede the provisional standard PS 070-97. In support of this work, we are refining the SCF test method by exploring dye penetrants as a means to make the cracks easier to detect and measure. Preparation of a reference material with certified fracture toughness continues at NIST as a separate project. Two ISO standards on fracture toughness are under development.

Two ISO flexure strength standards are being written. These will carry over the ASTM procedures into an international level. We also are cooperating in the creation of a world ISO standard for Vickers and Knoop hardness and we are pleased to note that it conforms in most details to the ASTM methods.

Research investigations continue on the diametral compression test method which is a simple means of measuring strength of ceramics round or cylindrical specimens.

Currently we are working on the following draft standards:

1. ISO CD 14704 Advanced (Fine) Ceramics - Determination of Flexural Strength at Room Temperature (NIST-USA convenes)
2. ISO CD 14705 Fine Ceramics (Advanced Ceramics, Advanced Technical Ceramics) - Test Method for Hardness for Monolithic Ceramics at Room Temperature (Convened by Japan, NIST represents the USA)
3. Advanced (Fine) Ceramics - Determination of Flexural Strength at Elevated Temperature (NIST-USA convenes)
4. ISO WD 15732 Fine Ceramics (Advanced Ceramics, Advanced Technical Ceramics) - Determination of Fracture Toughness at Ambient Temperature by Single Edge Precracked Beam (SEPB) Method (Convened by Japan, NIST cooperates with ASTM Task Group for USA response)
5. ISO draft, Fine (Advanced) Ceramics - Determination of Fracture Toughness at Room Temperature by the Surface Crack in Flexure (SCF) Method (Proposed by USA-NIST)

Earlier work in this project has contributed to the following completed standards:

1. ASTM C 1161-90 "Standard Test Method for Flexural Strength of Advanced Ceramics at Ambient Temperature," G. Quinn, NIST.

2. ASTM C 1198-91 "Dynamic Young's Modulus, Shear Modulus, and Poisson's Ratio for Advanced Ceramics by Sonic Resonance," by S. Gonczy, Allied-Signal; G. Quinn, NIST; and J. Helfinstine, Corning.
3. ASTM C 1211-92 "Standard Test Method for Flexural Strength of Advanced Ceramic at Elevated Temperature," by G. Quinn with help from Mr. M. Foley, Norton; Mr. T. Richerson, Allied-Signal; and Dr. M. Ferber, ORNL.
4. MIL HDBK 790 "Fractography and Characterization of Fracture Origins in Advanced Structural Ceramics," with J. Swab and M. Slavin, U.S. ARL.
5. ASTM C 1239-94a "Standard Practice for Reporting Strength Data and Estimating Weibull Distribution Parameters," by S. Duffy, NASA-Lewis; G. Quinn, NIST; and C. Johnson, G.E.
6. ASTM C 1322-96 "Standard Practice for Fractography and Characterization of Fracture Origins in Advanced Ceramics," in cooperation with Mr. J. Swab, U.S. ARL.
7. ASTM C 1326-96 "Standard Test Method for Knoop Indentation Hardness of Advanced Ceramics."
8. ASTM C 1327-96 "Standard Test Method for Vickers Indentation Hardness of Advanced Ceramics."
9. ASTM PS 070-97 "Standard Test Methods for the Determination of Fracture Toughness of Advanced Ceramics," in cooperation with Prof. I. Bar-On, WPI; Prof. M. Jenkins, Univ. Washington, and J. Salem, NASA-Lewis.

Fracture Toughness

In this semiannual period we continued to work on the refinement of the ASTM standard. A revised document was balloted in ASTM in the Fall of 1997 and received one negative and a number of useful affirmative with comment responses. Refinements to the document have been made and it is ready for an April 1998 ballot.

We have begun to advertise the new standard in a series of lectures and presentations. It is important that the ceramic and engineering community become cognizant of the standard and start to use it. Interest is high. At the Cocoa Beach January, 1998 American Ceramic Society conference, an invited lecture was made before a packed audience. A dozen reprints were quickly snapped up and 15 more copies of the paper and the provisional standard had to be mailed from NIST upon our return.

The work to create a Standard Reference Material (SRM) for fracture toughness continues. SCF specimens from four billets of NC 132 hot-pressed silicon nitride have shown remarkable within-billet consistency. Consequently, we are proceeding with a parallel project at NIST to prepare Standard Reference Material #2100 for distribution in the fall of 1998.

Table 1

Fracture toughness of NC 132 silicon nitride by the three methods in ASTM PS-070. All data from specimens cut from billet C.

test method	location in billet	specimen #						Average MPa$\sqrt{m}$	std. dev.
		1	2	3	4	5	6		
scf	middle - set 1	4.36	4.68		4.52	4.56		4.53	0.13
scf	middle- set 2	4.31	4.84	4.68	4.49	4.62		4.59	0.20
scf	outside	4.58	4.46	4.63	4.46	4.53	4.48	4.53	0.07
cn*	middle	4.49	4.62	4.76	4.63	4.78		4.63	0.13
cn*	middle	4.55	4.48					4.52	0.05
sepb	middle - set 1	4.59	4.54	4.69	4.42	4.70	4.39	4.56	0.13
sepb	middle - set 2	4.69	4.60	4.46	4.64		4.72	4.62	0.10

* Tested by J. Salem, NASA-Lewis

In the present semiannual period, we did complementary SEPB experiments and Jon Salem at NASA-Lewis also tested a set of 10 chevron notch specimens for a direct comparison to our extensive SCF results. These are the three methods in the ASTM fracture toughness standard. Table 1 shows that the data are extraordinarily consistent! Furthermore, the results are in superb agreement with the grand average of 4.59 MPa$\sqrt{m}$ obtained from 107 SCF specimens from 20 laboratories in the 1994 VAMAS round robin. These new positive result vindicate the choice of the three methods in the ASTM standard and pave the way for the adoption of a fracture toughness standard reference material.

At the Cocoa Beach, January 1998 meeting of ASTM C-28, the committee agreed that a draft fracture toughness standard based on the SCF method should be prepared for ISO Technical Committee TC 206, Fine Ceramics. A 21 page draft was prepared and submitted to ISO TC 206 Secretariat for consideration as a New Working Item.

We started work on fluorescent dye penetration as a means to enhance precrack detectability in the SCF fracture toughness test. Our goal with this work is to make the SCF method easier and help simplify the ASTM standard. A level IV, ultra-high sensitivity fluorescent penetrant, Magnaflux grade ZL-37 was used on several alumina specimens. This work was in conjunction with a fracture toughness round robin that is underway in the VAMAS project. The round robin features the SEVNB method, but sufficient specimens were available that we could try the SCF method as well.

ZL-37 is a common ultra-high sensitivity penetrant that has been used effectively in other DOE ceramic programs. Vimal Pujari used it at Norton in 1993 to study surface cracks in silicon nitrides. Forster and Ellingson studied it as a complementary method to their more sophisticated NDE procedures and published ORNL/sub/93-SN893-1 in 1996.

Our new procedure is to apply the dye penetrant while the SCF precracked specimen is loaded to about 1/2 the expected fracture load. The specimen is then hand ground to remove the residual stresses and the specimen is penetrated once again. It is then dried overnight in a desiccator and then is fractured in four-point flexure. Common black lamp UV lamps are inadequate to illuminate small cracks, so we used a metallographic microscope that has an intense xenon lamp source with built-in UV filters. Such equipment is not exotic and is a common feature on many metallographic and biological microscopes. We hope that this equipment will be able to discern the precracks on a routine basis.

The two aluminas from the VAMAS round robin that we tested were a 99.8% pure, coarse-grained (>10 μm) grade also a 99.9%, fine-grained (1.3μm) material. The fluorescent dye worked well on the coarse-grained alumina and highlighted the precracks whereas all our normal fractographic methods were unsuccessful. We were surprised that the dye penetrant did not work in the fine-grained alumina.

We next tried ZL-37 on three of our own ceramics that were not part of the VAMAS round robin. On Coors AD-999 alumina, a fine-grained (~ 3 μm) 99.9% grade with which we have substantial experience, the dye worked reasonably well. The crack size as estimated under fluorescing conditions agreed with the white light and scanning electron microscope fractographically-measured sizes. Of interest was that our fracture experiments were done in dry nitrogen to retard slow crack growth, but much to our chagrin, halos around the precracks were evident. The dye penetrated into the halo. Either the dye caused some slow crack growth, or the precracks extended a little bit after indentation and during the dye penetration step we used. As noted above, we loaded the specimens to about half the expected break load then dye penetrated the cracks. We thought that the half load would be safe,

but perhaps it was not. The dye is an oil based product and was insoluble in water but maybe it does not completely retard SCG.

Experiments on a Coors coarse-grained (~ 12 μm) alumina, grade AD 94 were unsuccessful. The dye penetrated the connected porosity and the precracks could not be discerned against the background penetration.

Experiments on Carborundum sintered alpha silicon carbide were partially successful. The dye penetrate only one of two sepciemsn tested. It is likely that the crack opening is very small in this high elastic modulus material. A toughness of 2.7 MPa$\sqrt{m}$ was obtained for the single successful specimen; a result that is in good agreement with other data by fractographic methods.

Additional experiments are underway. Sherwin RC 88 ultra-high sensitivity penetrant is on order as is Sherwin's DP 40 visible penetrant, which Jon Salem and Sung Choi used effectively on SEPB fracture toughness specimens. (See W.B. S. Element 3.2.1.7 progress reports in mid 1996.)

Diametral Compression

The diametral compression test, also known as the Brazilian disk strength method, is a means of measuring the strength of cylindrical specimens that are loaded on the rim as shown in Figure 1.

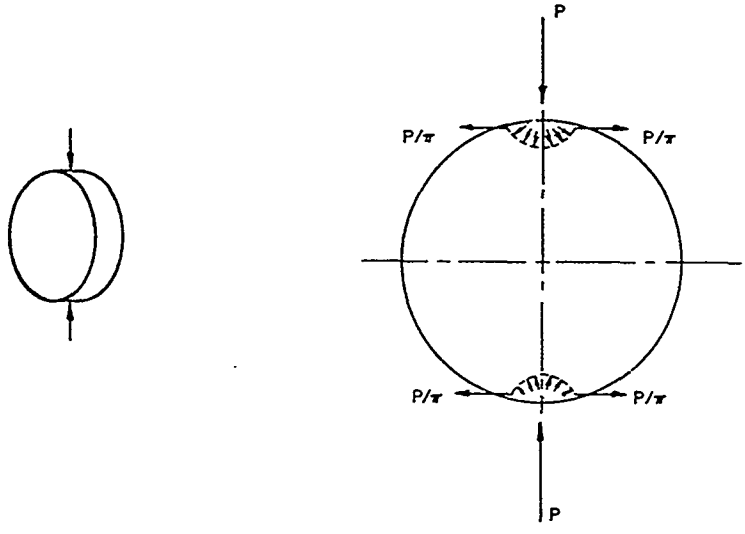

Figure 1 The diametral compression strength test

A paper on our preliminary findings from AD-99 alumina and a sintered tetragonal zirconia was presented by Jeff Swab at the Ceramic Materials and Components Conference in Arita, Japan in October. All of the specimens tested were fractured between hardened steel platens, usually with inserts cut from a thin file folder. The inserts are necessary to avoid high contact stresses and shear fractures initiating from the specimen ends. Two different specimens sizes were used: 6.4 mm diameter x 3.2 mm thick (volume = 103 mm^3), and 9.5 mm by 2.4 mm thick (volume = 170 mm^3). To further ensure even loading, small flats were machined on opposite ends of each of the larger specimens.

Results for zirconia are shown in Table 1. Fractography was feasible for the low strength AD 99 alumina and the sintered zirconia. Other tests on high strength silicon nitride specimens caused so much fragmentation that fracture origins could not be found.

Table 1 Strength of sintered Y-TZP zirconia

	Four-Point Flexure strength Size B	Diametral Compression Strength	
		Small, 6.4 mm diameter	Large 9.5 mm diameter
Number of specimens	30	30	27
Characteristic strength (MPa)	640	405	487
Weibull modulus	8.6	8.4	13.1

The primary conclusions from the work on the zirconia were:

a. Machining direction on the disk faces had no influence on strength, since the dominant flaws were volume distributed pores.
b. The diametral compression specimens were 25 - 36% weaker than size B, four-point flexure specimens. This is as expected since the diametral compression specimens had larger effective volumes than the flexure specimens.
c. Fractures originated from the midplane in the classic triple-cleft mode for all but three specimens.
d. Contrary to expectations, the larger (9.5 mm) diameter specimens were stronger than the smaller diameter (6.4 mm) specimens. Fractography was easier for the smaller specimens and 90% of origins were found. In contrast, only 50% of the larger specimen origins were found. The larger specimens had small flats machined on the ends, whereas the smaller specimens had no such flats. It is possible that the flats have altered the stress distribution, contrary to published reports in the literature.
e. Pores or porosity were the dominant flaw types. Fracture origins were usually located at the disk face surface and not scattered throughout the volume as had been hoped.

Additional Coors grade AD-99 alumina specimens were tested. This low cost ceramic is formed by extruding rods which are then sintered to ~95% of theoretical density. Our objective was to further study the influence of end shim materials. We had previously tested AD-99 specimens with inserts cut from file folder paper. We now tried some with no inserts and some with teflon pipe-thread tape. We also tried several means of specimen confinement. (Fractography is time consuming due to the fragmentation and we hoped that specimen reconstruction could be facilitated by applying tape to the flat faces or even around the rim.) The new results are shown in Table 2.

Table 2 Strength of extruded, sintered alumina Coors AD-99

	card-padded 5.8 mm diam.	unpadded 5.8 mm diam.	teflon tape 5.8 mm diam.	card-padded 9.4 mm diam.
number of specimens	11	10	10	5
average strength (MPa)	152	128	112	119
standard deviation (MPa)	17	18	16	11

As the table shows, two specimen sizes were tested. A 1/4" extruded rod was ground and then sliced to make 5.8 mm diameter x 3.2 mm thick specimens. Larger specimens were fabricated from a 3/8" rod and were machined to 9.4 mm diameter x 2.4 mm thick. The smaller specimens thus had a volume of 84.5 mm^3, and the larger specimens, 167 mm^3. Specimen end faces were surface ground in random orientations. A fractured specimen is shown in Figure 2.

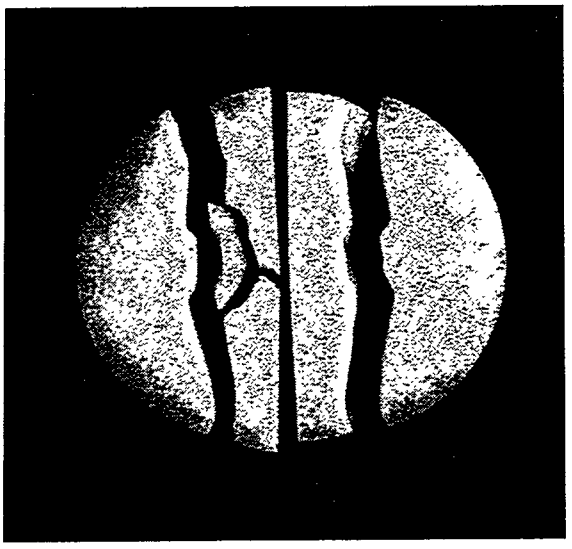

Figure 2 AD-99 alumina 5.8 mm diametral compression specimen illustrating the classic triple-cleft fracture pattern.

The primary conclusions from testing the alumina are:

a. The unpadded and teflon-wrapped specimens had much lower apparent strengths than the card-padded specimens.

b. The larger card-padded specimens were weaker than the smaller specimens, as expected from Weibull theory. *(This is the opposite of what was observed for the zirconia above.)*

c. Classic triple cleft fractures were obtained in most instances, except that a higher incidence of end fractures occurred for the unpadded or teflon tape-wrapped specimens. The teflon tape wrapping appears to be ineffective in reducing end fractures, probably because the tape was too thin. The tape may have exuded out from the contact points and also may have added an undesired splitting force to the specimens.

d. The fracture origins were frequently porous seams associated with the extrusion process. A seam or axial line of poorly-sintered material ran down just off the center of the specimens. Isolated pores also acted as strength-limiting flaws. SEM fractographic analysis is underway.

e. The extrusion seams are probably specimen-size specific. That is to say, the extrusion seams in the larger rods may be different than those in the smaller rods.

f. All fractures commenced from the disk faces and not from the volume.
(The same observation was made for the zirconia above.)

g. Machining damage may have affected the fracture origins. In several instances, the fracture origin had a slight jog that coincided with the direction of surface grinding. There appeared to be a propensity for the grinding to pull out or rip some grains from around the periphery of the porosity type origins, whether they were isolated pores or extrusion seams.
(This finding is in contrast to what we observed for the zirconia above. We surmise that the weaker alumina may have been more prone to this effect.)

h. Specimen reconstruction and fractographic analysis was much easier for the larger specimens than for the smaller specimens. *(This is the opposite of what we observed for the zirconia!)* The smaller specimens broke into smaller fragments, some of which flew away or were lost, whereas the larger specimens broke into larger, more manageable pieces that were easy to reassemble.

Five Coors AD-999 sintered alumina specimens were tested using a new specially-designed fixture with cutting tool inserts. On the five tested, only one fracture origin could be found. It was a pore, typical for this material and the same type of flaw activated by flexure tests. The five specimens had different types of confinement applied: tape around the rim, tape on the faces, or no tape at all. Despite these precautions, crack branching and crack interactions were so high that the origin region could not be found in four of the five. The single origin found was a pore, typical for this material and the same type of flaw activated by four-point flexure tests. The pore was located on the specimen circular face. An additional set of AD-999 specimens is being prepared with the notion that alternative confinement schemes will be tried in order to improve the chances of finding fracture origins.

It is distressing that the fracture origins were located on the specimen circular faces that for all three materials: the AD-99 and AD-999 aluminas, and the Y-TZP alumina. This occurred despite the fact that the origins were classic volume-distributed flaws. We had hoped than more flaws would be located in the specimen bulk. Diametral compression specimens have a high surface area to volume ratio. Fracture mechanics also suggests that a flaw experiences a higher stress intensity if it is located at a surface compared to what it would experience at the same stress level if it is in the interior.

Fractography

Ed Begley at NIST continues to help us put the flaw figures from ASTM standard C 1322-96 onto a Webb site. This will enable a broad user community to access better quality images than the sorry renditions in the ASTM book of standards. The webb site should be finished in the Spring of 1998.

Flexure Strength at Room Temperature

We designed a new set of semiarticulating flexure fixtures for room temperature testing. Through the years we have used the traditional semiarticulating fixture (with the ball) for well-machined specimens. For less well prepared or as-fired specimens, we used the patented U.S. government four-point fixture. The latter proved to be easier to use and it was felt that a new semiarticulating design could be made with the best elements of both fixture designs. We also wished to eliminate the ball from the semiarticulating design. A new set of fixtures was designed and experiments conducted to evaluate it's suitability. A new batch of AD-999 alumina specimens left over from the TTCP round robin of the mid-1980's has been tested. Fractures were uniformly distributed in the gage section and the strength values agreed with the earlier data. We conclude that the new fixture design is satisfactory. A single experiment with a strain gaged specimen was conducted and the observed strain was within 1/2% of the theoretical amount. The fixture design will be included in a future semiannual report.

Flexure Strength at Elevated Temperature, Revision to ASTM C 1211

Fifteen separate revisions to ASTM Standard C 1211-92 "Standard Test Method for Flexural Strength of Advanced Ceramics at Elevated Temperature," were balloted in ASTM Committee C-28. This standard, which was adopted in 1992, was due for an update. Most of the revisions were editorial corrections or clarifications, but several technical changes were suggested. One revision was to include in the precision and bias section, a new summary of the round robin results of IEA subtask 5 on high-temperature flexure testing. The round robin was not run in strict compliance with C 1211 (the round robin was underway as C 1211 was being developed and adopted) but useful lessons from

the project could be cited. For example, fixed-pin fixtures gave less satisfactory results than rolling-pin fixtures as specified in C 1211. The round robin also pointed out that proper specimen and fixture alignment such as specified in C 1211, is essential for good quality results.

ISO Flexure Strength Standard
A revised draft ISO room temperature flexure strength standard was prepared in December and sent to the ISO Secretariat for distribution. This document, which has nearly all the key elements of the ASTM USA standard C 1161, is in a final polishing stage. The revisions were primarily editorial in nature, although a few technical changes were made:

a. The illustration of a grinding wheel was redone.
b. The requirement to have all four edges chamfered was relaxed to require only two edges.
c. New provisions for very hard loading rollers were incorporated.

ISO High-Temperature Flexure Strength Standard
We have started to accumulate information to prepare a high-temperature flexure strength standard for ISO TC 206.

ISO Hardness Standard
The draft standard that is being prepared by a Japanese convener was thoroughly reviewed. This document borrows heavily from the ASTM standards C 1326 and C 1327. A draft was distributed in September 1997. We reviewed this document and, prompted by some comments from the Chinese delegation, conducted a survey of how "accuracy" and "precision" are handled in other world hardness standards (e.g. for metals). A set of remedial recommendations and a position paper on this topic were sent to the Japanese convener with the hope that he would implement some changes to the new ceramic TC 206 draft.

ISO Statistical Analysis of Round Robin Data
We previously had studied ASTM Standard E 691 which describes how interlaboratory round robin data may be analyzed in order to obtain estimates of precision of a test method. We successfully applied this approach to our round robin on Vickers and Knoop hardness and used the results in the new ASTM standards C 1326 (Knoop) and C 1327 (Vickers). Similarly, we helped Steve Gonczy use the same analysis for elastic modulus by the impulse excitation method when he prepared C 1259.

> *A set of notes on the use of E 691 to interpret round robin data are available at no cost upon request.*

The question is whether such statistical analyses are acceptable at an international level, or are they specific to the United States. ISO Standard 5725, parts 1-4 were reviewed and found to utilize nearly the identical analyses. This is reassuring and will enable round robin results obtained in the USA or in VAMAS to be cited in ISO ceramic test method standards.

Other Activities
We are pleased to report that ASTM Committee E-28, Mechanical testing, has cloned and adopted two of our ASTM Committee C-28 standards for elastic moduli determination.

In another remarkable development, committee F-04, Surgical and Medical Devices, has used **5 C-28 standards** in a new materials specification standards they are preparing for zirconia and alumina. If these materials are used in certain implants, they will have to meet the requirements specified in the two ASTM standards including minimum hardness (as measured by C 1327), flexure strength (C

1161 and C 1239) and elastic moduli (C 1198 and C 1259). Thus, our C-28 standards are so generic that they may be applied to broad classes of structural ceramics. This should be considered a spin-off benefit of years of work in the Ceramic Technology Project and the Heavy Vehicle Propulsion Materials Program.

A new VAMAS round robin on surface roughness characterization by diamond stylus profilometry has been proposed by the National Physical Laboratory, England. The round robin will feature conventional roughness measurements of as-sintered, ground and polished components. Kristin Breder at ORNL was contacted and agreed to participate. NIST will also participate.

Other interested DOE parties are welcome to join this project. Please contact George Quinn at NIST for further information (301 975-5765).

Status of Milestones

412123	Conduct preliminary diametral compression strength tests.	Completed
412124	Prepare comprehensive paper on hardness testing of *Defer until SRM 2831, Vickers hardness of ceramics, is finished.*	Postponed
412125	Prepare draft ISO Flexure Strength Standard	Completed
412126	Prepare and distribute to ASTM Committee C-28 members a simple statistical analysis package for interlaboratory round robin test data.	Completed
412127	Participate in a ceramic whisker-reinforced composite round round robin	Completed
412128	Conduct dye-penetrant experiments on scf fracture toughness specimens	Underway
412129	Write comprehensive report on fracture toughness evaluation by scf method *Defer in order to spend time on preparing revised full consensus fracture toughness ASTM draft.*	defer
412130	Finish ASTM fracture toughness standard	Completed
412131	Complete Phase I diametral compression testing	Completed
412132	Commence diametral compression round robin *Defer until research at NIST is completed.*	defer
412133	Prepare draft diametral compression standard for ASTM *Defer until research at NIST is completed.*	delayed
412134	Prepare review paper on diametral compression method *Defer until research at NIST is completed.*	delayed

Publications/Presentations

1. G. D. Quinn, M. Jenkins, I. Bar-On, and J. Salem, "The New ASTM Fracture Toughness of Advanced Ceramics Standard," Key Engineering Materials, Vol. 132 - 136, Part 3, Proceedings of the European Ceramic Society Conference, June 1997, eds J. Baxter, L. Cot, R. Fordham, V. Gabis, Y. Hellot, M. Lefebvre, H. Le Dousall, A. Le Sech, R. Naslain, and A. Sevagen, pp. 2115-2888.
2. J. J. Swab and G. D. Quinn, "Effect of Precrack "Halos" on K_{Ic} Determined by the Surface Crack in Flexure Method," subm. to J. Am. Ceram. Soc.
   Also Publ. as U. S. Army ARL TR 1575, December 1997.
3. J. Swab and G. Quinn, "Fractographic Analysis of Ceramic Materials Tested Using The Diametral Compression Test," subm. to International Conference on Ceramic Materials and Components for Heat Engines, Arita, Japan, Oct. 1997.
4. "SEPB Bridge Precracker" Notes by G. Quinn, NIST, Oct. 1 1997. Available upon request.
5. "Interlaboratory Round Robin Statistical Analysis by E 691," Notes by G. Quinn, 1997, Available

upon request.

6. G. D. Quinn, J. A. Salem, I. Bar-On, and M. G. Jenkins, "The New ASTM Fracture Toughness of Ceramics Standard: PS 070-97," presented at the Cocoa Beach meeting of the American Ceramic Society, to be publ. Ceram. Eng. and Sci. Proc. 1998.

Communications/Visits

1. Extensive communications were exchanged with Mike Jenkins, Jon Salem, and Isa Bar-On on the fracture toughness draft standard.
2. Mr. Quinn attended ASTM Committee C-28 meeting in Cocoa Beach in January 1998.
3. Jeff Swab of the U. S. Army Lab continues to help out with the diametral compression work.
4. Ten silicon nitride specimens were sent to Jon Salem at NASA-Lewis for chevron notch testing.

INTERNAL DISTRIBUTION

L. F. Allard, Jr.
P. F. Becher
T. M. Besmann
P. J. Blau
R. A. Bradley
K. Breder
C. R. Brinkman
T. D. Burchell
A. Choudhury
D. D. Conger
S. A. David
M. K. Ferber
R. L. Graves
H. W. Hayden, Jr.
C. R. Hubbard
M. A. Janney
D. R. Johnson (5)
R. R. Judkins
M. A. Karnitz
R. J. Lauf
K. C. Liu
W. D. Manly
S. B. McSpadden
T. A. Nolan
A. E. Pasto
M. H. Rawlins
M. L. Santella
A. C. Schaffhauser
D. P. Stinton
T. N. Tiegs
S. G. Winslow
R. E. Ziegler
Laboratory Records - RC

EXTERNAL DISTRIBUTION

Jeffrey Abboud
U.S. Advanced Ceramics Assoc.
1600 Wilson Blvd., Suite 1008
Arlington VA 22209

B. P. Bandyopadhyay
University of North Dakota
Box 8359 University Station
Grand Forks ND 58202-8359

Donald F. Baxter, Jr.
Advanced Materials & Processes
ASM International
9639 Kinsman Road
Materials Park OH 44073-0002

M. Brad Beardsley
Caterpillar Inc.
Technical Center Bldg. E
P.O. Box 1875
Peoria IL 61656-1875

Ramakrishna T. Bhatt
NASA Lewis Research Center
MS-106-1
21000 Brookpark Road
Cleveland, OH 44135

Bruce Boardman
Deere & Company, Technical Ctr.
3300 River Drive
Moline IL 61265-1792

Michael C. Brands
Cummins Engine Company, Inc.
P.O. Box 3005, Mail Code 50179
Columbus IN 47201

Donald J. Bray
Advanced Refractory Technologies
699 Hertel Avenue
Buffalo NY 14207

Walter Bryzik
U.S. Army Tank Automotive
Command
R&D Center, Propulsion Systems
Warren MI 48397-5000

David Carruthers
Kyocera Industrial Ceramics
5713 East Fourth Plain
Vancouver WA 98661

Ronald H. Chand
Chand Kare Technical Ceramics
2 Coppage Drive
Worcester MA 01603-1252

William J. Chmura
Torrington Company
59 Field Street, P.O. Box 1008
Torrington CT 06790-1008

William S. Coblenz
Defense Adv. Research Projects Agency
3701 N. Fairfax Drive
Arlington VA 22203-1714

Gloria M. Collins
ASTM
100 Barr Harbor Drive
West Conshohocken PA 19428-2959

Shawn Cooper
FEV Engine Technology
2285 Opdyke Road, Suite F
Auburn Hills MI 48326

Douglas Corey
AlliedSignal, Inc.
2525 West 190th Street, MS:T52
Torrance CA 90504-6099

Keith P. Costello
Chand/Kare Technical Ceramics
2 Coppage Drive
Worcester MA 01603-1252

Gary M. Crosbie
Ford Motor Company
P.O. Box 2053, 20000 Rotunda Drive
MD-3182, SRL Building
Dearborn MI 48121-2053

Pamela Cunningham
WETO Technical Library
MSE, Inc.
Industrial Park, P. O. Box 4078
Butte MT 59702

Sidney Diamond
U.S. Department of Energy
Office of Transportation Technologies
EE-33, Forrestal Building
Washington DC 28505

Ernest J. Duwell
3M Abrasive Systems Division
3M Center, Bldg. 251-01-34
St. Paul MN 55144

Michael Easley
AlliedSignal Engines
P. O. Box 52181
MS 551-11
Phoenix AZ 85072-2181

J. J. Eberhardt
U.S. Department of Energy
Office of Transportation Technologies
EE-33, Forrestal Building
Washington DC 20585

Jim Edler
Eaton Corporation
26201 Northwestern Highway
P.O. Box 766
Southfield MI 48037

G. A. Eisman
Dow Chemical Company
Ceramics and Advanced Materials
52 Building
Midland MI 48667

William A. Ellingson
Argonne National Laboratory
Energy Technology Division, Bldg. 212
9700 S. Cass Avenue
Argonne IL 60439-3848

John W. Fairbanks
U.S. Department of Energy
Office of Transportation Technologies
EE-33, Forrestal Building
Washington DC 20585

Ho Fang
Applied Materials
2695 Augustine Drive, MS-0962
Santa Clara CA 95054

Dan Foley
AlliedSignal Ceramic Components
MS:1/5-1, 26000
2525 West 190th Street
Torrance CA 90504

Douglas Freitag
DuPont Lanxide Composites
21150 New Hampshire Avenue
Brookeville MD 20833

Richard Gates
NIST
Bldg. 223, Rm. A-256
Rt. 270 & Quince Orchard Road
Gaithersburg MD 20899

Allan E. Goldman
U.S. Graphite, Inc.
907 W. Outer Drive
Oak Ridge TN 37830

Robert J. Gottschall
U.S. Department of Energy
Metal & Ceramic Sciences, ER-131
19901 Germantown Road
Germantown MD 20874-1290

Thomas J. Gross
U.S. Department of Energy
Office of Transportation Technologies
EE-30, Forrestal Building
Washington DC 20585

Changsheng Guo
Chand Kare Technical Ceramics
2 Coppage Drive
Worcester MA 01603

Nabil S. Hakim
Detroit Diesel Corporation
13400 Outer Drive West, A08
Detroit MI 48239-4001

Alan M. Hart
Dow Chemical Company
1776 Building
Midland MI 48674

Michael H. Haselkorn
Caterpillar Inc.
Technical Center, Building E
P.O. Box 1875
Peoria IL 61656-1875

Deborah A. Haught
U.S. Department of Energy
Ofc. of Industrial Crosscut Technologies
EE-23, Forrestal Bldg.
Washington DC 20585

Daniel Hauser
Edison Welding Institute
Microjoinint & Plastics Tech. Team
1250 Arthur E. Adams Drive
Columbus OH 43221-3585

John Haygarth
Wah Chang
P.O. Box 460
Albany OR 97321-0460

Gene Huber
Precision Ferrites & Ceramics
5432 Production Drive
Huntington Beach CA 92649-1525

Thomas A. Johnson
Lanxide Corporation
1300 Marrows Road
P.O. Box 6077
Newark DE 19714-6077

Adam Jostsons
ANSTO
PMB1
Menai, NSW, Australia 2234

Yury Kalish
Detroit Diesel Corporation
Mechanical Systems
13400 Outer Drive West
Detroit MI 48239-4001

Roy Kamo
Adiabatics, Inc.
3385 Commerce Park Drive
Columbus IN 47201

W. C. King
Mack Truck, Z-41
1999 Pennsylvania Avenue
Hagerstown MD 21740

Tony Kirn
Caterpillar Inc.
Defense Products Dept., JB7
Peoria IL 61629

Joseph A. Kovach
Eaton Corporation
32500 Chardon Road
Willoughby Hills OH 44094

Edwin H. Kraft
Kyocera Industrial Ceramics
5713 E. Fourth Plain Boulevard
Vancouver WA 98661

Arthur Kranish
Trends Publishing Inc.
1079 National Press Building
Washington DC 20045

Oh-Hun Kwon
Norton Company
Saint Gobain Industrial Ceramics
1 Goddard Road
Northboro MA 01532-1545

S. K. Lau
B. F. Goodrich Aerospace R&D
9921 Brecksville Road
Brecksville OH 44141

Elaine Lentini
Saint-Gobain Industrial Ceramics
Goddard Road
Northboro MA 01532

Stan Levine
NASA Lewis Research Center
21000 Brookpark Road, MS:106/5
Cleveland OH 44135

Robert H. Licht
Norton Company
Saint Gobain Industrial Ceramics
1 Goddard Road
Northboro MA 01532-1545

E. Lilley
Norton Company
Saint Gobain Industrial Ceramics
1 Goddard Road
Northboro MA 01532-1545

B. J. McEntire
Applied Materials Corporation
3050 Bowers Avenue
Santa Clara, CA 95054

James McLaughlin
Sundstrand Power Systems
4400 Ruffin Road
P.O. Box 85757
San Diego CA 92186-5757

Biljana Mikijelj
Ceradyne, Inc.
3169 Red Hill Avenue
Costa Mesa CA 92626

Carl E. Miller
Delphi Energy & Engine Mgmt. Systems
4800 S. Saginaw Street, MC 485-301-150
P. O. Box 1360
Flint MI 48501-1360

Curtis V. Nakaishi
U.S. Department of Energy
Federal Energy Tech. Center
3610 Collins Ferry Rd.
P.O. Box 880
Morgantown WV 26507-0880

Malcolm Naylor
Cummins Engine Company, Inc.
P.O. Box 3005, Mail Code 50183
Columbus IN 47202-3005

Dale E. Niesz
Ceramic & Materials Engineering
607 Taylor Road, Rm. 204
Piscataway, NJ 08854-8065

George Onoda
National Institute of Standards & Technology
I-270 & Clopper Road
Gaithersburg, MD 20899

Thomas J. Paglia
Coors/ACI
3315 Boone Road
Benton AR 72015

Richard Palicka
CERCOM, Inc.
1960 Watson Way
Vista CA 92083

Vijay M. Parthasarathy
Solar Turbines
2200 Pacific Highway, M.Z. R-1
San Diego CA 92186

Magan Patel
Cummins Engine Company, Inc.
Mail Code 50183
Box 3005
Columbus IN 47202-3005

James W. Patten
Cummins Engine Company, Inc.
P.O. Box 3005, Mail Code 50183
Columbus IN 47202-3005

Stephen C. Pred
Pred Materials International, Inc.
60 East 42nd Street, Suite 1456
New York NY 10165

Vimal K. Pujari
Norton Company
Saint Gobain Industrial Ceramics
1 Goddard Road
Northboro MA 01532-1545

Fred Quan
Corning Inc.
Sullivan Park, FR-2-8
Corning NY 14831

George Quinn
NIST
Quince Orchard & Clopper Road
Ceramics Division, Bldg. 223
Gaithersburg MD 20899

Harold Rechter
Chicago Fire Brick Company
7531 S. Ashland Avenue
Chicago IL 60620-4246

Jack A. Rubin
CERCOM, Inc.
1960 Watson Way
Vista CA 92083

Robert J. Russell
Riverdale Consulting, Inc.
24 Micah Hamlin Road
Centerville MA 02632-2107

J. Sankar
North Carolina A&T State Univ.
Dept. of Mechanical Engineering
Greensboro NC 27406

Maxine L. Savitz
AlliedSignal, Inc.
Ceramic Components
2525 West 190th Street
P.O. Box 2960, MS:1/5-1, 26000
Torrance CA 90509-2960

Jim Schienle
AlliedSignal Aerospace
1130 West Warner Road
M/S 1231-K
Tempe AZ 85284

Gary Schnittgrund
Transfer Technology
16401 Knollwood Drive
Granada Hills CA 91344

Robert S. Shane
Shane Associates
1904 NW 22nd Street
Stuart FL 34994-9270

Subu Shanmugham
MicroCoating Technologies
430 Tenth Street
Suite N-108
Atlanta GA 30318

Albert Shih
Cummins Engine Company
MC 50183
P.O. Box 3005
Columbus IN 47201

Charles Spuckler
NASA Lewis Research Center
21000 Brookpark Road, MS: 5-11
Cleveland OH 44135-3127

Gordon L. Starr
Cummins Engine Company, Inc.
P.O. Box 3005, Mail Code:50182
Columbus IN 47202-3005

Marian Swirsky
Cambridge Scientific Abstract
Commerce Park, Bldg. 4, Suite 804
23200 Chagrin Blvd.
Beachwood OH 44122

Victor J. Tennery
113 Newell Lane
Oak Ridge TN 37830

Malcolm Thomas
Allison Engine Company
P. O. Box 420 (W06)
Indianapolis IN 46206

Marc Tricard
Norton Company
Superabrasives Division
1 New Bond Street, MS-412-301
P. O. Box 15008
Worcester MA 01615-0008

Marcel H. Van De Voorde
Commission of the European Community
P.O. Box 2
1755 ZG Petten
THE NETHERLANDS

V. Venkateswaran
Materials Solutions International, Inc.
P.O. Box 663
Grand Island, NY 14072-0663

Michael S. Walsh
Vapor Technologies Inc.
6330 Gunpark Drive
Boulder CO 80301

Robert M. Washburn
ASMT
11203 Colima Road
Whittier CA 90604

R. W. Weeks
Argonne National Laboratory
Bldg. 362, E313
9700 S. Cass Avenue
Argonne IL 60439

Sheldon M. Wiederhorn
NIST
Building 223, Room B309
Gaithersburg MD 20899

Matthew F. Winkler
Seaworthy Systems, Inc.
P.O. Box 965
Essex CT 06426

Thomas J. Wissing
Eaton Corporation
26201 Northwestern Highway
P.O. Box 766
Southfield MI 48037

James C. Withers
MER Corporation
7960 S. Kolb Road
Tucson AZ 85706

Dale E. Wittmer
Southern Illinois University
Mechanical Engineering Dept.
Carbondale IL 62901

Egon E. Wolff
Caterpillar Inc.
Technical Center
P.O. Box 1875
Peoria IL 61656-1875

Roy Yamamoto
Ethyl Petroleum Additives, Inc.
500 Spring Street
P. O. Box 2158
Richmond VA 23218-2158

Thomas M. Yonushonis
Cummins Engine Company, Inc.
1900 McKinley Avenue
P.O. Box 3005, Mail Code 50183
Columbus IN 47202-3005

Jong Yung
Sundstrand Aerospace
Dept. 789-6
4747 Harrison Avenue
Rockford IL 61125

A. L. Zadoks
Caterpillar Inc.
Technical Center, Building L
P.O. Box 1875
Peoria IL 61656-1875

Zhenqi Zhu
Stevens Institute of Technology
Department of Mechanical Engineering
Castle Point on Hudson
Hoboken NJ 07030

Department of Energy
Oak Ridge Operations Office
Assistant Manager for Energy
Research and Development
P. O. Box 2001
Oak Ridge TN 37831-8600

For distribution by microfiche
as shown in DOE/OSTI-4500,
Distribution Category UC-332
(Ceramics/Advanced Materials).